Improving the utility of LA-ICP-MS for isotope ratio analyses of single particles with application to uranium oxide

Doctoral Thesis

Grant Craig

April 2015

Submitted in partial fulfilment of the requirements for the award of Doctor of Philosophy of Loughborough University

Abstract

The determination of the isotopic composition of single uranium oxide particles, size 0.3-2 µm, for nuclear safeguards is current performed by either thermal ionisation mass spectrometry (TIMS) or Secondary Ion Mass Spectrometry (SIMS). Laser Ablation-Inductively Coupled Plasma-Mass Spectrometry (LA-ICP-MS), a well-established analytical technique for determining the isotopic composition of solid materials, has the potential to be another method by which single uranium oxide particles can be analysed, complementing established protocol, but requires optimisation.

In this study the ability of LA-ICP-MS to determine the isotopic composition, principally $^{234}U/^{238}U$, $^{235}U/^{238}U$ and $^{236}U/^{238}U$, of glass reference materials and sub-micron uranium oxide particles is investigated. To achieve the best detection efficiency a prototype high-speed ablation cell and injector design, designed previously at Loughborough University, was coupled to a high efficiency multi collector (MC-) ICP-MS. As a result an increase in signal-to-noise ratio and a measured detection efficiency of 5-7% was achieved for a LA-MC-ICP-MS system. The capability of the LA-MC-ICP-MS system, for the determination of the uranium isotopic composition of single particles was compared to a more established low-volume ablation cell. A source of additional uncertainty, 'blind time' arising from incompatibilities with the mixed detector array of the MC-ICP-MS was identified. The impact of the additional uncertainty on isotope ratio analysis was modelled and a method developed to filter out affected data.

LA-ICP-MS and LA-MC-ICP-MS were used to successfully determine the uranium isotopic compositions of sub-micron uranium oxide particles, of a known certified composition. A sample planchet containing particles of two distinct isotopic compositions was resolved.

The utility of three data evaluation strategies to determine the isotopic composition of single uranium oxide particles was investigated. The necessity and advantages of calculating isotope ratios using the geometric mean is demonstrated, which has application for isotope ratio analysis performed on all forms of mass spectrometry.

A novel approach to prepare particulate samples for laser ablation analysis, cytocentrifugation, is described. By using as the solvent, a mixture of nail polish and acetone, dispersed particles are held in a strong film layer thin enough to allow embedded particles to be imaged by SEM-EDX. A sample of uranium oxide particles in an environmental matrix prepared using cytocentrifugation is analysed by LA-MC-ICP-MS and their isotopic composition resolved.

Acknowledgements

I would first like to thank my supervisors, Professor B. L. Sharp; Dr H. J. Reid and Dr M. S. A. Horstwood for their help and support throughout the duration of the study.

I would like to thank all those at NIGL and BGS especially Dr Steve Noble, Dr Simon Chenery, Dr Nick Roberts, Vanessa Pashley and Jeremy Rushton. Thanks also to Dr Noah McLean for all his help on the geometric mean and coding in MATLAB.

A big thank-you to all the technicians at Loughborough University, especially Jagpal Singh in the Metrology Unit. I also need to thank David Hinds from Unity Lab Services, the ever useful voice at the end of the phone for great ICP-MS advice.

Lot of thanks to the Analytical research group at Loughborough University, past and present. Special thanks to Sarah Taylor, Amy Managh, David Douglas, Pareen Patel, Tharwat Abduljabber and John Pugh, I would say you helped keep me sane, but we all know that isn't true.

I finally need to especially thank my parents, David and Evelyn Craig, and the rest of my family; if you are reading this I won't be offended if you stop here. Thanks for the enthusiasm and support and sorry I stole the kitchen table to write-up on.

List of Abbreviations

BGS	British Geological Survey
CCF	Cross-Calibration Factor
CDD	Compact Discrete Dynode
CF	Correction Factor
CPS	Counts Per Second
CRM	Certified Reference Material
DCI	Dual Concentric Injector
DRS	Data Reduction Scheme
DU	Depleted Uranium
EDX	Energy-Dispersive X-ray spectrometer
ES	Environmental Sampling
EU	Enriched Uranium
FC	Faraday Cup
FT	Fission Track
HEU	Highly Enriched Uranium
I.D	Inner Diameter
IAEA	International Atomic Energy Agency
IC	Ion Counter
ICP-MS	Inductively Coupled Plasma - Mass Spectrometry
IR	Infra-Red
IRMM	Institute for Reference Materials and Measurements
LA	Laser Ablation
LG	Large Geometry
LOD	Limit Of Detection
m/z	Mass-to-Charge
MC	Multi-Collector
NIGL	NERC Isotope Geosciences Laboratory
NUSIMEP	Nuclear Signatures Inter-laboratory Measurement Evaluation Program
O.D	Outer Diameter

OES	Optical Emission Spectroscopy
P2P	Point-to-Point
RD	Relative Difference
RSD	Relative Standard Deviation
S/N	Signal-to-Noise
SEM	Scanning Electron Microscope
SF	Sector Field
SIMS	Secondary Ion Mass Spectrometry
TIMS	Thermal Ionisation Mass Spectrometry
TOF	Time-Of-Flight
TRA	Time Resolved Analysis
TSI	Total Signal Integration
UV	Ultra-Violet

Table of Contents

Chapter 1 – Introduction

1.1 Inductively Coupled Plasma - Mass Spectrometry (ICP-MS)

Almost all mass spectrometers follow the same basic design. To begin there is a sample introduction system which can vary from, for example, a simple spray chamber, a gas chromatograph to a laser for solid sampling. Next is the means of ionisation: in mass spectrometry it is ions not neutral atoms which are detected. Once ionised the sample is then accelerated towards a mass analyser: which acts to separate out the ions by their mass-to-charge ratio (*m/z*). The final components make up the detection system.

In inductively coupled plasma mass spectrometry (ICP-MS), of the four parts mentioned above, sample introduction, ionisation source, mass analyser and detector, it is the ionisation source, the inductively coupled plasma, which is distinct from other types of mass spectrometer.

1.1.1 The Inductively Coupled Plasma and Mass Spectrometer Interface

The first use of an atmospheric ICP in analytical chemistry was not as an ionisation source for mass spectrometry[1], instead photomultiplier tubes were used to measure the optical emission (OES) from the sample atoms and ions. Regardless of application, inductively coupled plasma torches are broadly similar in design, with the Fassel torch design[2–4], the most common since its introduction.

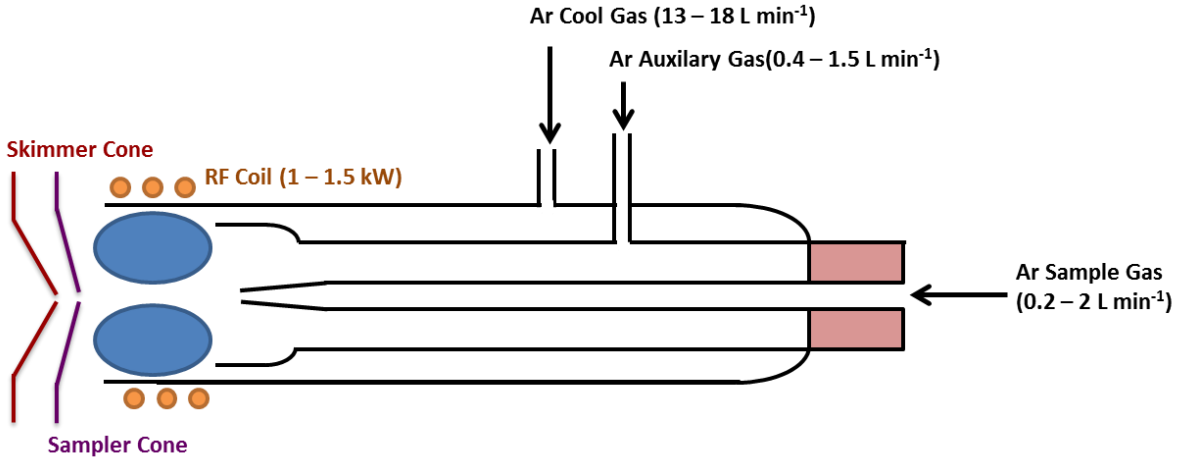

Figure 1 – Schematic of a typical Fassel design argon inductively coupled plasma torch and mass spectrometer interface.

The ICP torch consists of three concentric tubes made of quartz. The central channel is the injector, transporting the sample aerosol into the plasma. The two outer tubes transport the gas flows which both make up and cool the plasma. The argon (Ar) gas is then seeded with electrons from a tesla wire (Figure 1 - not shown). Surrounding the part of the ICP torch where the plasma is to form is a hollow copper load coil, water cooled from inside[5]. By applying a radio-frequency (RF) to the load

coil a magnetic field is generated. The magnetic field causes the seeded electrons to move energetically around the argon gas: collisions with argon atoms cause them to ionise, producing more electrons. As long as the magnetic field is maintained by the RF, ions and electrons will continue to collide, self-sustaining the plasma[2].

The spatial geometry of the torch is carefully designed to affect the shape of the plasma. As the cool and auxiliary gases are added tangentially to the plasma, a vortex is created at the plasma base: facing the injector. This vortex allows the sample gas from the injector to more easily punch though into the heart of the plasma. The location of the load coil around the torch results in the outer region of the plasma being significantly hotter than the core[2]. The temperature at the centre of the plasma is therefore highly dependent on the transfer of heat from the outer regions towards the central channel.

Some instruments come fitted with a guard electrode, a grounded metal plate placed between the plasma torch and the load coil. The guard electrode reduces the spread of ion energies, hence improving overall ion transmission for sector field mass spectrometers[4].

As the ICP is an atmospheric ion source an interface region is required to transport the generated ions into the vacuum of the mass spectrometer. A part of this interface (two cones – skimmer and sampler) is shown in Figure 1. A sample of the ions within the plasma is extracted through the orifice of the sampler cone (hence the name)[2]. The water-cooled sampler has to be made of a material with high thermal conductivity and resistance to corrosion: Ni, Al and Pt are popular. The region between the skimmer and the sampler is kept at below atmospheric pressure (2-3 mbar) by either a rotary or turbomolecular pump[5]. The skimmer design and placement needs to be correct such that the further extracted volume into the mass spectrometer is representative of the initial plasma. The pressure behind the skimmer is kept at $\approx 10^{-4}$ mbar by turbomolecular pumps, before dropping into the 10^{-7} mbar range or below further into the mass spectrometer.

1.1.2 Mass Analysers in ICP-MS

In current commercial ICP-MS systems the mass analysers' available fall into three main categories; quadrupole (Q); time-of-flight (TOF) and sector field (SF). Quadrupole based ICP-MS are the most common, followed by sector field and time-of-flight in the order of popularity.

1.1.2.1 Quadrupole Mass Analysers

The popularity of the quadrupole mass analyser is based on its combination of compact design, ruggedness and low cost relative to other types of mass analysers[6]. The quadrupoles in ICP-MS consist of four cylindrical or hyperbolic metal tube electrodes (steel or molybdenum) of typically 15-

20 cm in length and 1cm in diameter[7], arranged in parallel. This separates the electrodes into two opposite pairs. Each pair is connected to a variable DC source, one pair to the positive terminal and the other to the negative. Also applied to each pair is an AC current operating at radio frequency (2-3 MHz), 180° out of phase. By keeping the AC/DC applied potential ratio constant while increasing/decreasing both, it is possible to scan along the m/z range. Only ions of a certain m/z can pass through the centre of the quadrupole rods to the detector, all other m/z ions have an unstable trajectory and are either ejected from the quadrupole or neutralised by collision with the electrodes.

Compared to other scanning mass analysers, such as magnetic sectors, quadrupoles have high scan rates, allowing a scan of 200 m/z in fewer than 1ms[2]. This is useful for applications looking at isotopes over a large mass window. When scanning over such a range however the duty cycle needs to be taken into account. The duty cycle is the proportion of time in which the mass spectrometer is measuring each m/z[8]. For a scan window of 200 m/z the duty cycle of the mass spectrometer is 0.5 %. Low duty cycles negatively impact the efficiency of the mass spectrometer.

Many commercially available quadrupole-based ICP-MS instruments now have two or three quadrupoles in series[9–11]. Such instruments allow addition of collision and reaction gases to remove interferences.

1.1.2.2 Time-Of-Flight (TOF) Mass Analysers

Time-of-flight mass analysers work on the principle that the velocity of an ion is equal to:

$$v = \sqrt{\frac{m}{2E_k}}$$

As m is the mass and E_k is the kinetic energy, it can be concluded that if a group of ions are all accelerated with the same kinetic energy then their velocities will alter only due to their mass. In TOF mass spectrometers therefore, identically accelerated ions are passed into a drift tube of about 1 m in length, in which distance the ions separate out with lighter ions reaching the detector before heavier ions.

In order for the ions to be identically accelerated they need to be sampled simultaneously. As an ICP is a continuous ion source the ions have to be sampled, introduced into the ICP in discrete, pulsed, packets. This has been achieved by placing the TOF flight tube orthogonal to the ICP and using a quadrupole to “pulse” the ion beam into the orthogonal TOF interface[2]. The requirement for ions to be introduced in discrete, pulsed, packets has a deleterious impact on the duty cycle of the mass

spectrometer as ions are not continuously sampled. This acts to reduce the efficiency which can be achieved on a mass spectrometer with a TOF mass analyser.

The primary advantage offered by time-of-flight ICP-MS is rapid data acquisition. The entire mass range can be scanned at a rate of 20,000 Hz, exceeding the rate achievable by a quadrupole by over two orders of magnitude[12]. With such fast scanning rates spectral skew, arising from the sequential analysis of masses is eliminated[13]. This has seen the application of ICP-TOF-MS for transient signals, including aspirated single particles[14], single droplets[15] and ultrafast laser ablation[16]. A prototype time-of-flight ICP-MS (a version is now available commercially) reported a minimum time resolution of 33 μs with sensitivity approaching that achieved by quadrupole analysers[15].

1.1.2.3 Sector Field Mass Analysers

In this thesis, sector field (SF) ICP-MS will be used, employing double focussing instruments which contain two mass analysers, a magnetic sector (B) and electrostatic analyser (ESA). Although far less common than quadrupoles, they have a long history in ICP-MS, developed primarily to allow high mass resolution (R≈10,000) spectroscopy, vital to separate out isobaric masses[17].

With only a single focussing magnetic sector mass analyser, peak broadening and low resolution tend to occur as the ions produced in the source have different ion energies, depending on where in the source they originate[2]. By only allowing ions within a narrow band of kinetic energies through, the electrostatic analyser in double focussing SF-ICP-MS does not act as a mass analyser, but as an energy "filter", improving resolution[5]. Narrow electrostatic analyser slits (both entrance and exit) are another key requirement for high resolution. Slits restrict the ions passing to the analysers and detectors to only those travelling in the correct alignment. The resolution of the instrument can be changed by altering the width of the slits.

All of the ICP-MS instruments used throughout this thesis have been sector field instruments, not for the high resolution which spurred their development, but for other advantages offered by sector field ICP-MS. When considering low abundance isotopes, the sensitivity (or detection efficiency) of sector field ICP-MS, superior to both quadrupole and TOF ICP-MS, can be crucial. The increased sensitivity originates from the high energy ion beam transmission used, reducing the signal loss due to scattering of the ion beam relative to quadrupoles[2]. The second potential advantage of sector field ICP-MS is the possibility for true simultaneous measurement of different masses. The other commercially available mass analysers are unable to spatially separate ion beams of different masses into the plane of the mass analyser, unlike magnetic sectors[18]. By placing an array of detectors across the plane of the mass analyser a large number of isotopes can be simultaneously measured[4]. This category of instruments is referred to as multi collector (MC-) ICP-MS.

1.1.3 Geometries of Magnetic Sector ICP-MS

While all sector field ICP-MS instruments combine a magnetic sector and electrostatic analyser, these can be arranged in a variety of different geometries. Commercially, three geometries: Nier-Johnson; reverse Nier-Johnson and Mattauch-Herzog, are available.

Table 1 – List of available commercial sector field ICP-MS instruments and their respective geometries

Name	Manufacturer	Collector Type	Geometry
Element 2 XR™	Thermo Scientific™	Single	Reverse Nier-Johnson
Neptune *Plus*™	Thermo Scientific™	Multi	Nier-Johnson
AttoM®	Nu Instruments™	Single	Nier-Johnson
Nu Plasma II®	Nu Instruments™	Multi	Nier-Johnson
SPECTRO MS™	Spectro™ Analytical Instruments	Multi	Mattauch-Herzog

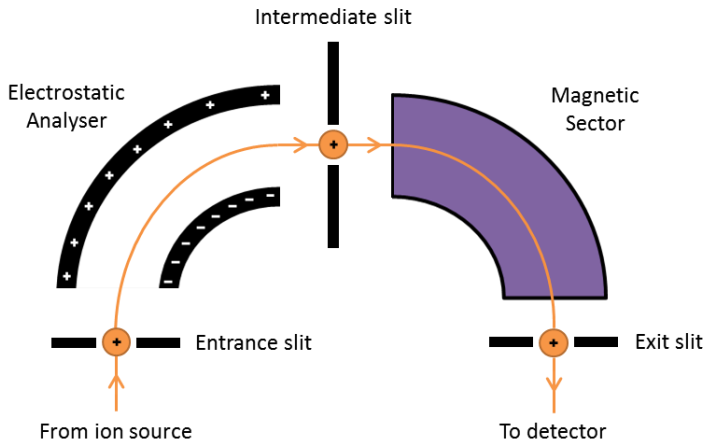

Figure 2 – The Nier-Johnson geometry for sector field ICP-MS, adapted from[19].

The Nier-Johnson geometry consists of an electrostatic sector field in front of the magnetic sector field. Both sectors consist of 90° geometries travelling in the same direction, resulting in a 180° deflection in a clockwise direction. Having the separating magnetic sector after the focussing electrostatic analyser is most useful for multi-collector instruments; the magnetic sector is in the correct location to spatially disperse ions to multiple detectors.

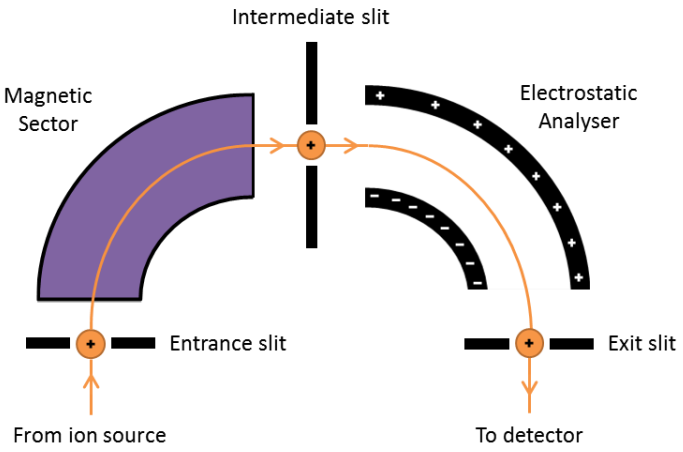

Figure 3 – The Reverse Nier-Johnson geometry for sector field ICP-MS, adapted from[19].

Conversely the reverse Nier-Johnson geometry is better for single-collector instruments as the focussing electrostatic sector field is best able to focus the analyte ion of interest onto the single available detector. The AttoM®, despite having a single detector, retains the same geometry as multi-collectors, however the reduced performance expected is mitigated by the inclusion of the proprietary FastScan ion optics either side of the magnetic sector.

The Mattauch-Herzog geometry was developed in 1935, with a photographic plate as the detector[8]. Unlike both Nier-Johnson geometries this is a dispersive rather than a scanning instrument. The 31.5° ($\pi/4\sqrt{2}$) electrostatic analyser coupled to the 90° magnetic analyser allows the separation (and detection) of the entire mass range over a single plane (on which the detector is aligned)[4].

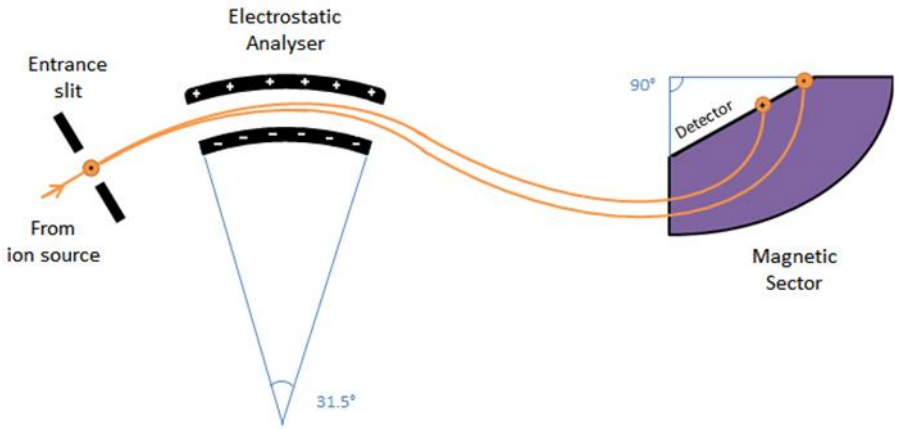

Figure 4 – The Mattauch-Herzog geometry for sector field ICP-MS, adapted from[19].

In order to make the Mattauch-Herzog geometry useful for modern quantitative mass spectrometry a detector other than a photographic plate is required. In the SPECTRO MS this detector is an array which covers the mass range from 5 to 240 a.m.u with 4800 channels (Faraday strips)[20].

1.1.4 Detectors in ICP-MS

There are two commonly used detectors in mass spectrometry; electron multipliers (EM) and Faraday cups[8]. The Faraday cup is a metal cup or cylinder with a small orifice. When ions enter and strike the walls they neutralise by accepting or donating an electron to the cup walls. This results in a current which is taken and amplified with high-ohmic resistors in the feedback loop into a signal voltage[3]: the signal voltage being relative to the ion abundance.

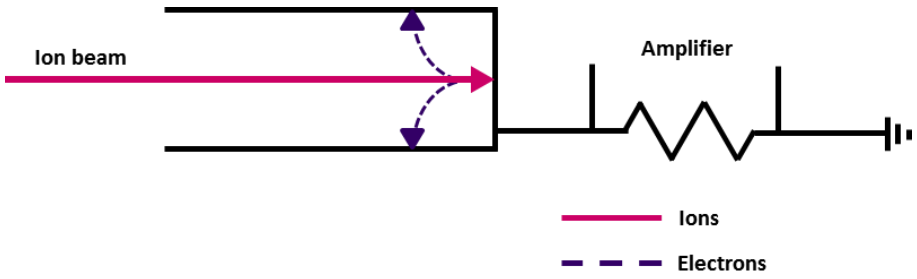

Figure 5 – Schematic of a Faraday cup and series amplifier, recreated from[8].

Many significant errors result from the generation of secondary electrons; however in current-generation instruments these are strongly suppressed. Faraday cups are robust and mass independent with a long linear range, but are limited to measuring signals with high intensities (10^4 counts per second)[3]. The limitation is due not to the Faraday cups, but to Johnson's noise (ΔV), which is generated by the high-ohmic resistor in the associated electronic circuitry[18]. This noise is best reduced with temperature control (±0.01°C). ΔV can be calculated via:

$$\Delta V = \sqrt{\frac{4k_B RT}{t_m}}$$

Where k_B is the Boltzmann constant, T is temperature, t_m is the integration time and R is the resistor value. For transient signals it is important to note the effect integration time has on the noise generated in the Faraday signal, although this effect is blunted somewhat by the square root factor. This same square root is also important in the choice of amplifier, the gain of which is proportional to R. Increasing the gain by 10 will improve the signal to noise ratio by √10 (in reality the gain is less, a factor 2, due to noise from the amplifier itself)[18].

MC-ICP-MS instruments have multiple Faraday cups in arrays, each connected to a different amplifier. Each one of these amplifiers will have a slightly different gain which, left uncorrected, will introduce biases into signal ratios between the different detectors. With current technology the limit of reproducibility of the cross-calibration of two amplifiers is 5 ppm (1 RSD)[21] and as a consequence the external reproducibility of static isotope ratio measurements is limited to about 7-10 ppm.

The electron multiplier is the detector of choice for sector field ICP-MS. In contrast to the Faraday cup the EM works best for low intensity signals. Up to 10^6 cps ion currents can be read out as single counts[3] (in this arrangement an EM can be referred to as an ion counter (IC)) and up to 10^9 cps in analogue mode which can be used to translate the ion current directly into a value in cps. Unlike the Faraday cup, electron multipliers multiply the signal intensity via a cascade effect.

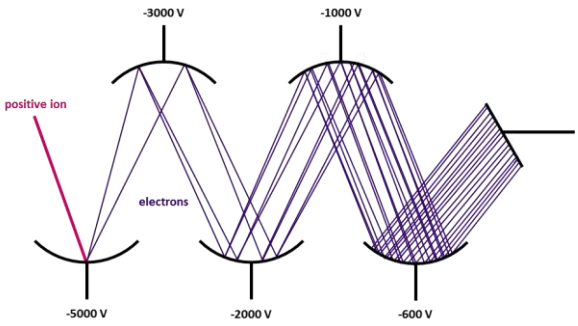

Figure 6 – Schematic of a discrete dynode electron multiplier, recreated from[8].

Electron multipliers come in a variety of slightly different types. One major difference is between discrete and continuous dynode types. In a discrete dynode multiplier, between 12 and 20 dynodes in decreasing potential are used to produce secondary electrons (electrons are produced at the primary dynode by striking ions) creating a current from a cascade of electrons[8]. This current is then increased by further electrical amplification. Continuous dynode multipliers (often called Channeltrons™) consist of one large horned, tubular-shaped dynode in which emission electrons bounce down the length of the horn producing more and more electrons. Although they have high sensitivity, they have a short lifetime and lack precision.

1.1.5 Detector Correction in MC-ICP-MS

The ability of sector field ICP-MS instruments to perform isotope ratio analysis is dependent on three important offsets (corrections) which need to be applied[22]. These three corrections are for detector dead time, which affects ion counters, mass bias and abundance sensitivity. For MC-ICP-MS a fourth offset, cross-calibration between the different detectors (often referred to as gain[21,23]) is also required.

1.1.5.1 Dead Time

With ion counters (IC's) operated in pulse-counting mode, if one ion strikes the detector whilst another ion is still being processed then this second ion is not detected[24]. This time wherein another ion cannot be detected is referred to as the detector's dead time (τ)[2]. If the dead time is known then an equation based on a Poisson distribution exists to estimate the true count rate (N_T) from the measured rate (N_0)[2,25]:

$$N_T = \frac{N_0}{1 - N_0 \tau}$$

The total dead time is made up of contributions from both the ion counters and the associated electronics. Ion counters typically have a dead time less than 10ns, a value which is swamped by the dead time of the electronics and amplifiers which correspond typically to between 20-70ns[26]. Overall in ICP-MS instrumentation the detector dead times will range between 15 and 100 ns[2].

One practical method to determine the detector dead time in ICP-MS requires a solution of known isotopic ratio[2]. Plotting the "normalised isotope ratio" (measured isotope ratio over certified isotope ratio) against dead time produces a curve. By plotting curves for solutions of different concentrations the dead time correction required can be derived from the point where the individual curves intersect.

1.1.5.2 Mass Bias

In ICP-MS mass-dependent instrumental bias is one of the most important factors affecting accuracy and external precision which originates from within the mass spectrometer[27]. This "mass bias" is caused by the preferential transmission of ions with higher masses within the mass spectrometer[28]; as a consequence the sensitivity of the mass spectrometer is not constant across the mass range, but varies depending on the mass of the isotope measured[29]. In sector field ICP-MS the mass bias effects arise prior to the separation of ions in the mass spectrometer[22] and have been assumed to mainly occur at the interface region of the ICP-MS[25,30], although ion physics suggested at least a contribution from the plasma[27].

Space charge effects occurring behind the skimmer cone (or in the field free region between the sample and skimmer cones[29]) is a well reported hypothesis for the source of mass bias effects in sector field ICP-MS[18,31–33]. When the ion beam is extracted through the sampler and skimmer cones a great body of positively charged ions are brought close together. Mutual repulsion between the positive ions causes them to diverge from axis and as lighter ions have less kinetic energy they are deflected more off-axis, causing the observed mass bias[22].

The space charge effect hypothesis is not without its detractors, the higher acceleration potential of sector field IC-MS should reduce the mass bias effect observed relative to quadrupole based instrumentation, but it has been reported that the mass bias is similar with both mass analysers[29]. Furthermore increasing the ion beam intensity should increase mass bias if space charge effects are dominant, but the opposite has been shown to be the case[22]. An alternative to space charge effects would be lateral diffusion of lighter isotopes in the plasma, resulting in the region of plasma sampled

by the interface (opposite the injector) having a lower density of lighter isotopes than would be expected. So far no consensus on the cause of mass-dependent instrumental bias in ICP-MS has been reached.

Mass bias is corrected by either an internal or external method. In the internal methodology the mass bias is determined in the sample solution itself from a known isotope ratio[29]. The known isotope ratio can be either a pair of isotopes of the analyte element that are thought invariant (e.g. $^{146}Nd/^{144}Nd$)[28] or if such a pair of isotopes is unavailable, a spike of another element containing an invariant pair can be added to the sample solution[18] (e.g. $^{205}Tl/^{203}Tl$ for Pb isotope ratio analysis)[25]. The bias determined for the known isotope ratio is then incorporated into a mathematical model to determine correction factors for the analyte isotope ratios. Three mathematical models, imported from TIMS, exist to determine the correction factors based on either a linear; power or exponential functions[25]. None of the models can be correct as they predict the mass bias is dependent on the *difference* in mass, rather than the absolute mass[29], but this is not the case, the mass bias effect is less pronounced for high mass isotopes[22]. Ingle *et al* (2003)[29] proposed using a multi-element solution to characterise the instrument response curve over as many masses as possible, rather than just a single isotope pair. A fit to the instrument response curve could then be employed to define the equation used to calculate the correction factor required.

For the external mass bias correction methodology a certified reference material containing the analyte isotope ratio of known composition is measured separately to the sample[23]. A correction factor for mass bias is calculated from the difference between the measured and certified isotope ratios[32]. The external correction methodology can be advantageous as the mass bias is determined at the masses of interest in the sample and is not reliant on a mathematical model to determine the correction factor[25].

1.1.5.3 Abundance Sensitivity and Polyatomic Interferences

Ions in the flight tube of a mass spectrometer which collide with residual gas molecules, or the edges of the entrance and exit slits, lose energy and/or slightly change their trajectory[18]. As a consequence these scattered ions appear at incorrect mass positions on the focal plane[4]. The magnetic sector deflects with a smaller radius those ions which have lost energy, causing then to build up as a 'tail' on the low mass side of the main mass peak[18]. For ratios such as $^{236}U/^{238}U$, where the ratio can often be in the 10^{-6} to 10^{-7} range for anthropogenic uranium, as the main peak is especially abundant the tail on the low mass side can be sufficient to mask the true abundance of ^{236}U. The contribution on the background signal from the tail of an intense isotope at an integer mass unit spacing (1 amu, 2 amu etc.) on the low mass side is commonly referred to as the abundance sensitivity[18]. The

abundance sensitivity can be reduced by improving the analyser vacuum[4], or by placing the ion counter measuring the low abundance isotope behind an ion deceleration filter. The ion deceleration filter improves the abundance sensitivity by filtering out ions with low kinetic energies[34], at the cost of reducing the signal achieved for the low abundance isotope[35].

The abundance sensitivity at 1 amu is normally measured as the ratio of the peak intensities at *m/z* 237 and ^{238}U for a non-highly enriched U containing solution[18,35,36]; for MC-ICP-MS this value is typically 5E-06 or 5 ppm[18]. By aspirating a solution of natural uranium (which contains no or very little ^{236}U) the abundance sensitivity at 2 amu (about 1ppm for MC-ICP-MS)[34] can be determined[35]. To gain the 'true' abundance sensitivity at 2 amu however, a correction must be made for $^{235}UH^+$, a polyatomic interference. As well as hydrides, other common polyatomic interferences in ICP-MS are oxides, argides and nitrides[17]. The determination of the UH^+/U^+ ratio is measured as the ratio of the peak intensities at *m/z* 239 and ^{238}U[37].

1.1.5.4 Detector Cross-calibration (Gain)

For each of the ion counters in a MC-ICP-MS detector array a plateau calibration curve of counts per second (cps) against voltage is created to determine the optimum operating voltage[38]. As the optimum operating voltage of each ion counter is determined individually each will respond differently to an input signal i.e. the output signal from two ion counters responding to an identical input signal will differ. To correct for such offsets a cross-calibration factor (CCF) is determined for each pair of ion counters. To determine the CCF a constant source of known abundance is directed into each ion counter and the difference between the experimental and known abundances determined. For a mixed array containing both Faraday cups and ion counters the same approach can be employed or instead a sample with a known isotope ratio can be used by placing one half of the ratio in each detector and calibrating between the experimental and known ratios[39]. This approach is identical to the methodology used to determine an external correction factor for mass bias and therefore a single correction factor is determined for both mass bias and gain[23,40,41]. If the CCF required for a Faraday cup and ion counter pair is reckoned to be too large the value on the Faraday cup is described as the "true value" and the operating voltage of the ion counter altered to reduce the size of the CCF.

1.1.6 Sample Introduction

Over time, numerous different ways have been developed for introducing samples, either of a solid, liquid or gas, into an ICP. The most common approach is to introduce liquid samples via a nebuliser and spray chamber. The argon sample gas is used to aspirate the liquid sample through the nebuliser, generating a fine mist inside the attached spray chamber. The action of the spray chamber

is to limit the size of droplets introduced into the ICP, with larger droplets typically diverted to waste.

The typical nebuliser/spray chamber arrangement is often supplemented by the addition of a desolvator. Basic desolvators such as water or Peltier cooled spray chambers facilitate the analysis of samples containing high quantities of volatile organic solvent (such as the output of a liquid chromatograph), the removal of which is vital to prevent them extinguishing the plasma[7]. More efficient desolvation, nearly removing 100% of solvent, can be achieved with a membrane desolvator. The membrane consists of tubular microporous PTFE polymer. When the sample aerosol is introduced the solvent vapour passes through the membrane, where a flow of argon gas removes it from the exterior walls. The sample vapour remains within the tubing and passes on to the ICP. Desolvating to this level improves detection efficiency, by removing solvent based interferences and lowering rates of oxide formation. Additionally as the output aerosol from the desolvator is "dry" it can be used to mimic other dry aerosol sample introduction systems, including laser ablation[42]. Although not the only way to introduce solid samples, laser ablation is commonly used to interrogate solid samples, generating a stream of particles of sufficiently small size to be wholly ionised by the ICP.

1.2 Laser Ablation

Laser ablation (LA), as a means of introducing solid samples for ICP-MS, has undergone a series of developments since its first introduction by Gray[43]. However many components of a typical laser ablation apparatus remain unchanged.

1.2.1 Standard LA Configuration

In a standard laser ablation setup the sample is placed in an ablation cell. A laser pulse is directed and focused onto the sample by mirrors and lenses[5]. Completing the instrumentation are other lenses and cameras used to allow the operator to view the sample surface. Through the ablation cell is a constant stream of gas. Upon ablation the laser pulse strikes the surface and interacts such as to produce a plume of vaporized sample. As the plume expands both the pressure and the temperature drop and the plume enters a supersaturated state. Once supersaturation occurs the constituents of the plume begin to nucleate and condense into particles[44,45]. These particles are carried by the stream of gas out of the ablation cell and towards the ICP.

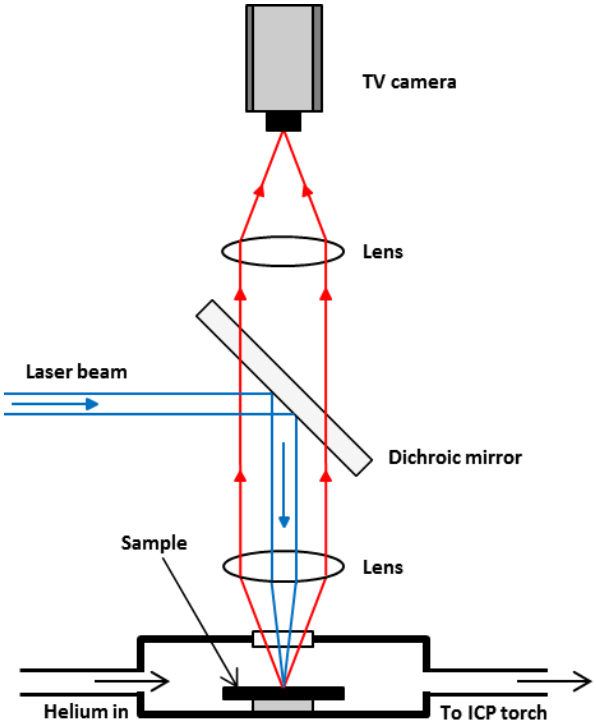

Figure 7 – Schematic of a typical laser ablation setup for ICP-MS, modified from D. Günther *et al* (1999)[46]

The main variables in system design are the type of laser, the design of the ablation cell and the quantity and composition of the ablation gas. Other factors for consideration are the opacity of the sample and the effects of vaporization[47].

1.2.2 Effect of Laser Parameters on Laser Ablation

Choosing the correct laser parameters is a key component for successful LA-ICP-MS. The variable parameters of the laser are[48]:

1. the type of laser
2. the frequency of the laser output
3. the fluence (energy density) in J/cm^2 of the laser pulse
4. the spot size of the beam
5. the irradiance
6. the pulse duration (the time over which the pulse impinges on the surface)

1.2.2.1 Varieties of Laser in Laser Ablation

Gray first used a ruby laser for laser ablation[43], but this was quickly superseded by solid-state Nd:YAG and gas-based excimer (commonly ArF) lasers[13]. The choice of laser is primarily dictated by the frequency, maximum fluence and pulse time of their output. However there are other considerations, Nd:YAG laser systems are much cheaper than ArF systems, easier to implement and require less maintenance[31]. The lasers also differ in crater profile, Nd:YAG naturally produce

Gaussian craters, excimer lasers naturally have a more flat, homogeneous profile[49]. The craters should at the very least be Gaussian[47], however flat top laser profiles, giving better lateral intensity distribution[50] and producing straight-sided craters are preferred, particularly in depth profiling[31]. Nd:YAG and Ti:sapphire (femtosecond) lasers can be modified to generate a more flat top output.

1.2.2.2 Laser Frequency

The frequencies of lasers used in laser ablation range from the infrared (IR) to the ultraviolet (UV) Over time the trend has been towards the ultraviolet, with Nd:YAG lasers being changed from their fundamental wavelength (1064 nm) to other lower wavelengths (532, 355, 266, 213 nm) by optical frequency doubling, tripling etc[31], reaching 213 nm in 1998[51]. Other wavelengths for Nd:YAG (such as 193 nm) can be reached using an optical parametric oscillator[52]. Excimer lasers are gas based and typically operate at a lower wavelength to solid-state lasers. The choice of halogen-based gas mixture determines the wavelength (e.g. 1% F_2 in Ar, ArF, λ = 193 nm).

Ultraviolet wavelengths are preferred to infrared, following the rationale provided by Jefferies *et al* (1996)[53]. At lower wavelengths better lateral resolution can be achieved, vital for determining boundaries when sample mapping[54]. Wavelength is related to resolution via:

$$R = 1.22\lambda F^*$$

Where *R* is the lateral resolution, *F** is the F-number and λ is the wavelength.

Most glasses and minerals (common samples in laser ablation[55]) are opaque to UV radiation[56]. Ablation therefore occurs mostly by the direct absorption of the laser energy. However these samples are mostly transparent to IR radiation and therefore the laser ablation mechanism relies on the presence of high concentrations of 3rd row transition metals, the energy of the d-orbitals of which appears in the IR region of the spectrum[53].

IR and UV laser ablation differ in the degree to which elemental fractionation can occur as infrared laser ablation is more reliant on thermal ablation. Fractionation is a process by which sample constituents respond differently such that one or more constituents is favoured during analysis, resulting in the experimental composition differing from the true value[49,53,57,58]. For IR laser ablation, repeated laser pulses cause a variable complex plasma layer to form above the sample surface[53]. This layer blocks further laser energy directly reaching the sample surface and with each successive pulse the plasma becomes hotter. Thermal ablation of the surface by the plasma layer occurs resulting in fractionation. Thermal fractionation is observed more for the siderophile elements e.g. Au, Zn, Tl, Pb than for lithophile elements[49,59].

1.2.2.3 Fluence and Irradiance

In laser ablation the strength of the laser pulse is quoted in terms of fluence, which is equal to the energy density in J/cm^2 impinging on the sample surface. For laser ablation to occur a *Fluence Threshold* must be breached. Below the threshold all of the laser energy is merely converted into thermal energy, but above the threshold the remaining energy is used to break chemical bonds and to give velocity to the resultant escaping particles[60]. As the fluence increases still further there becomes a point where increasing the fluence does not improve the ablation rate (µm/pulse).

Irradiance is the power density (in W/cm^2) and is the fluence related to the pulse duration. From *Energy (E) = Power (P)* time (t)* the irradiance is calculated from the fluence divided by the pulse duration. The fluence is the total amount of energy supplied by the pulse, the irradiance is the amount of energy supplied at a given time[58].

1.2.2.4 Pulse duration

Ignoring small differences in degree, the two main pulse times available in LA are nanosecond (ns) and femtosecond (fs) [45]. Nd:YAG and excimer lasers have pulse times in the nanosecond range, Ti:sapphire[61] and Nd:Glass[45] can achieve femtosecond pulse times.

The primary mechanism of ablation is different for nanosecond and femtosecond lasers. Similar to changing from IR to UV, reducing the pulse time from nanosecond to femtosecond results in an ablation mechanism more reliant on photochemical rather than thermal processes[51]. This results in a more homogeneous particle size distribution, more stable signals and suppression of elemental and isotopic fractionation[51]. Additionally the mass ablation rate is increased for femtosecond laser ablation provided the fluence remains the same[62]. The primary ablation mechanism for femtosecond lasers is still inconclusive; it has been suggested that the exact mechanism varies depending on the thermal diffusion coefficient of the sample and the fluence used[49].

The amount of fluence required for ablation is pulse time dependent. Compared to femtosecond ablation, with nanosecond pulse times the laser energy has more time to dissipate via heat conduction into the rest of the sample[63], therefore a larger fluence is required to achieve the same quantity of sample vaporisation. Consequently nanosecond lasers have a Fluence Threshold about five times higher than femtosecond lasers[64]. Femtosecond lasers can also achieve a much lower ablation rate[61] allowing greater precision during surface ablation.

1.2.2.5 Spot Size

The majority of the effects related to spot size are due to the effect it has locally on the irradiance. The smaller the spot size the more focussed the power density of the laser beam[57]. Smaller spot

sizes can be achieved without increasing the power density by masking a larger beam of lower density.

1.2.3 Coupling of LA to ICP-MS

A brief representation of how a laser ablation system is coupled to an ICP-MS is given below. The tubing used is typically ¼" o.d. Tygon® throughout, connected to the injector by means of a cup and ball joint.

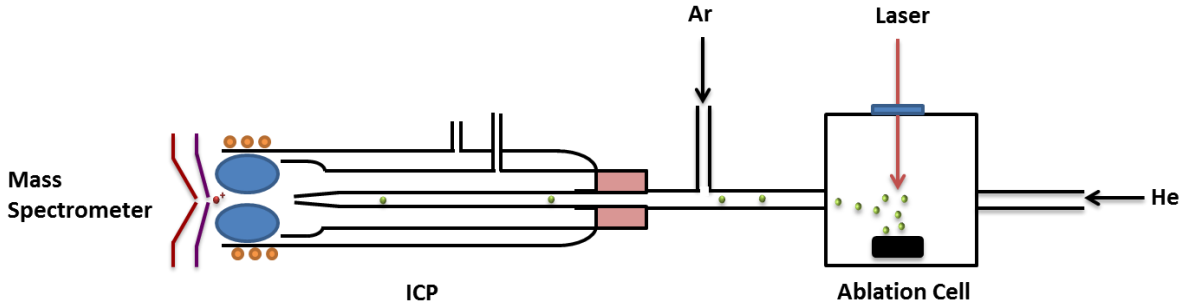

Figure 8 – Typical configuration of coupling of LA to ICP-MS, based on Kosler[65]

In the early years of LA-ICP-MS argon gas was used within the ablation cell, however this has been almost completely supplanted by helium, with argon gas mixed in before entering the ICP[47]. Using He as the ablation gas has been shown to produce better sensitivity and lower elemental fractionation over Ar, due to the reduced particle size distribution of the ablated particles[66]. Particle-size related fractionation[49,67] occurs due to volatile siderophile elements being enriched relative to the bulk composition in the smallest aerosol particles (<100 nm)[68]. These smaller particles are almost certain to be analysed[69], unlike larger particles which are more likely to be lost during transport (hence the better sensitivity with He) and to be incompletely ionised within the plasma[70], particularly for particles above 1µm for glass and 400nm for metals[69]. The high thermal conductivity of He, removes energy quickly from the ablation site, slowing condensational growth.

Using He adds a further variable, the fraction of He/Ar entering the ICP. Modelling has found higher He ratios will change both the temperature and electron density within the ICP torch[71]. This study showed increased efficiency in the ICP with a He/Ar mix and predicted an ideal ratio of between 40 to 70%. Pure He isn't used as it fails to establish a central channel through the plasma, resulting in sample particles flowing away from the central axis (recent developments suggest, instrumentation depending, pure He can be used successfully[72]).

The ideal LA-ICP-MS has been described as a scenario where; the total mass ablated has the same elemental composition as the sample and the total mass ablated is transported to the ICP[47]. 100% transport reduces fractionation and improves sensitivity. During the transport of the ablation

material to the ICP it is desirable for the maximum amount of material to reach the ICP torch. Not only does this reduce the possibility of particle-size related fractionation, but improves sensitivity. Particle losses increase with the length of tubing, with larger particles lost earlier due to selective vapour condensation on the tubing walls[57]. Therefore the length and volume of the entire transport system should be as small as possible, ablation cell included.

1.2.4 Ablation Cell Design

Each ablation cell must contain a few basic components; a sample holder; a window for the laser beam to pass through; a gas flow and a means of purging the cell[31]. Also most ablation cells move on a motorised stage to change sample location[65]. Many different cells have been developed for laser ablation, some are designed for a specific application, but others aim to improve LA-ICP-MS generally. Improvements in signal-to-noise (S/N) and transport efficiency can be achieved by reducing the residence time (washout) of the ablation plume within the cell[13,31].

1.2.4.1 Open/Closed Cells

As the ICP-MS is destabilised by the entrainment of air into the plasma, most ablation cells are closed, with the sample enclosed within. However this requirement constrains the size and shape of the sample which can be analysed[73]. This has pushed the development of open ablation cells, with the sample replacing one of the walls of the cell. However this arrangement is prone to leaks. For flat planar surfaces a non-contact cell has been reported which excludes air from the ablation surface using a micro-jet gas flow array[74,75]. Another approach has been to use atmospheric air as the ablation gas, extracting it via a diaphragm pump to a gas exchange device (GED) which exchanges the atmospheric gases for Ar and He[73,76]. Using a gas exchange device removes the requirement for either touching the sample surface or having a flat planar surface. Extracting the ablation gases with a diaphragm pump from a closed cell has also been reported, reducing re-deposition of material onto the sample surface[77].

1.2.4.2 Single Volume Cells

Early commercial ablation cells consisted of a single cylindrical volume into which the sample was placed. Gas flows across the cell from the inlet to the outlet at opposite ends of the cell. However with such cylindrical cells the transport efficiency varies depending on location, with pronounced areas of high and low efficiency[78]. Approaches to improve cylindrical cell performance have included filling in the low efficiency areas[79]; introducing a high velocity jet of gas onto the ablation site[80,81] and rotating the gas inlet at over 1,000 rpm[82].

For larger sample volumes square and rectangular cells have also been developed. One such rectangular cell consisted of two gas inlets at the extreme ends of the cell and the outlet placed at the centre[83]. The washout of this cell was characterised as 70% faster than a conventional cylindrical cell.

A recent development in single volume cells has been "tube" cells, where the tubing itself is the ablation cell. Wang *et al* (2013)[16] reported the development of one such cell where a hole was cut into the top of the tubing, for the window, and another cut into the bottom. Under the lower opening was attached the sample holder, the sample itself held 350µm from the opening. Gas flow into the sample holder lifts the ablation plume up into the tube. By keeping the sample aerosol density high pulse widths of 30ms for single shot ablation were achieved. More recently Van Malderen *et al* (2014)[72] have developed a cell with a central chamber (1.3mm) only slightly larger than the tubing (1 mm). Achieving pulse widths of 1.4ms to full width half maximum (FWTM) with a high flow of pure He, this cell represents an interesting new development in ablation cells. Both tube cells are limited to the width of the tubing in the area of sample which can be ablated.

1.2.4.3 Two Volume Cells

Improving the washout time and transport efficiency of single volume cells by restricting the ablation volume ultimately reduces the size of sample they can accommodate. This contradiction can be solved by placing a small inner cell inside a larger outer cell. The inner cell is held fixed under the laser objective, the outer cell moves to change the sample area under the inner cell. One such cell, the "Laurin" Cell, has a funnel shaped inner cell of 1-2cm^3 volume[84]. Gas flows around the inner cell keep the ablation plume within the funnel, improving washout times. The same gas flows around the inner cell have been designed to be invariant: the transport efficiency should be consistent regardless of location in the outer cell.

1.2.4.4 In-torch Laser Ablation

Several attempts have been made at in-torch ablation, where laser ablation is carried out just beneath the ICP torch[85–87]. The main advantage is to reduce both transport and memory effects to zero. The reduction in memory effects particularly allows very clean blank runs. In-torch laser ablation was first used for ICP optical emission spectroscopy[88] and developed further for mass spectrometry[85–87]. The samples were held within a recess in the injector and the laser focussed through the quartz glass of the torch. Using an ICP time-of-flight mass spectrometer, sensitivity was increased by an order of magnitude over an ablation cell: washout times reduced to 30 ms[87]. While a useful benchmark, in-torch laser ablation is impractical for routine applications, the torch needs to

be removed to change the sample and the sample needs to be small enough to fit inside the tip of the injector.

1.3 Analysis of Uranium Oxide Particles

1.3.1 Properties of Uranium and Uranium Oxides

Uranium, the heaviest naturally occurring element with a density of 19.07 $g.cm^{-3}$ [89], consists of three natural isotopes, ^{234}U: ^{235}U and ^{238}U (There are 19 isotopes of U in total). The primary use of uranium is as a fuel in nuclear reactors and in nuclear weapons[90]. Of the three naturally occurring isotopes, ^{235}U (comprising 0.72% of natural uranium) is the only isotope which can be used to sustain nuclear chain reactions[89]. Due to the low natural abundance of ^{235}U in uranium the production of nuclear weapons, and nuclear fuel for most types of nuclear reactors, requires the concentration of ^{235}U, relative to the other isotopes of uranium, be increased. The artificial concentration of ^{235}U is known as enrichment, producing the enriched uranium (EU) and by-product depleted uranium (DU). Compared to natural uranium, DU typically has a composition of 99.8% ^{238}U (natural uranium 99.283%)[89], with the remainder consisting mainly of ^{235}U with small amounts of ^{234}U. DU is contaminated with anthropogenic ^{236}U derived from reprocessed uranium[91]. The enrichment of uranium has been achieved through more than one process, these include electromagnetic isotope separation, gaseous diffusion isotope separation and high-speed gas centrifuge separation[92]. Of the processes used, gaseous diffusion isotope separation (used primarily in the period 1950-1980[92]), and high-speed gas centrifuges are the most prevalent[93].

The by-product of uranium enrichment, DU has found use in various applications, mainly exploiting the high density of uranium. Uses of DU include as counterweights on aircraft[89], as the basis of both battle tank armour and armour piercing munitions[94,95] and, despite DU being weakly radioactive itself, as a radiation shielding material[95]. Radiation is not the only health concern associated with uranium, not only is DU a weakly radioactive metal, but it is also toxic when either ingested, inhaled or embedded within the body[94]. Excepting the danger of embedded fragments (DU has been used in conflict both by American and British forces[94,95]) inhalation is the primary mechanism for exposure to DU[90]. The annual limit for DU inhalation has been set at 8.3 mg, however the particle size of the material inhaled is a key consideration as 95% of particles above 10 µm are quickly eluted via the pharynx and gastrointestinal tract, but particles below 10 µm penetrate deeper into the lungs and therefore have a much longer body retention time[90].

The danger of exposure to uranium is partly dependent on its chemical form, particularly whether or not it is soluble. Uranium tarnishes rapidly on contact with air[89] and also reacts with water[90]. This is

due to its highly electropositive nature in which it mimics the alkaline earths such as magnesium. Therefore uranium found in the environment is most likely to be in the form of an oxide[90]. Insoluble oxide forms of uranium (e.g. UO_2 and U_3O_8) concentrate in the lungs, where small particles will persist and cause radiological damage[95]. Soluble forms of uranium (e.g. UO_3[90]), however are freely able to react with biological systems, causing toxicological damage[89], Particular targets of soluble uranium are the kidneys and bones[95]. The density of UO_2 is 10.96 g cm^{-3} significantly less than pure uranium, but still considerably denser than most other species[95].

1.3.2 Environmental Sampling for Nuclear Safeguards

In 1968 the International Atomic Energy Agency (IAEA) was charged under the Treaty on the Non-Proliferation of Nuclear Weapons (NPT) to verify the commitments made for 'peaceful use' by non-nuclear weapon States[96]. Part of this verification process included safeguards which agreed that all nuclear material within the State should be subject to IAEA inspectors. However the safeguards, consisting of materials accountancy, containment and surveillance, were flawed in that they only applied to the nuclear material *declared* by the State[92]. Therefore nuclear material not declared by the State was invisible to the safeguards in place. Following the first Gulf War and the subsequent discovery of undeclared nuclear material in Iraq[92] the IAEA decided to strengthen its system of safeguards[96]. A new legal framework, The Additional Protocol was implemented as part of the effort to improve the IAEA's nuclear safeguards. As part of the Additional Protocol the IAEA was empowered to collect environmental samples (ES)[97,98] from sites beyond those areas which had been declared by the State[96].

The environmental samples collected as part of the Additional Protocol primarily consist of wipes either of cotton[92] or cellulose[99], prepared in a clean room, which are then swiped over suspect surfaces. The environmental sampling operates on the principle that the release of material from a uranium enrichment facility is inevitable, regardless of the countermeasures in place[98,99]. In both gas diffusion isotope separation and high-speed gas centrifuges the uranium material handled, most often UF_6, is released to the environment in the form of a fine particulate or aerosol[98]. The analysis of these radionuclide particles collected from the environment around a site is therefore one of the most powerful tools applied to the detection of undeclared nuclear activities[100]; with their isotopic and elemental composition being characteristic of the materials and activities occurring at the site[36]. The detection of highly enriched uranium (HEU) could indicate the presence of a weapons programme[98], as could traces of fissile plutonium[92].

The IAEA's inspection programme is not the only source of uranium particles which require analysis. The use of DU projectiles as munitions in combat has been found to produce aerosols of uranium

oxide particles (UO_x)[94]. The production of DU munitions has been associated with the release of UO_x particles into the environment at certain sites[91,95,101], as has the production of uranium metal from ore[102].

1.3.3 Analytical Methods applied to Uranium Oxide Particles

The UO_x particles, once collected in the IAEA's environmental sampling programme, undergo analysis. This analysis is separated into two components, bulk and particle analysis[98]. In bulk analysis all or most of the particle-coated sample swipe is dissolved for analysis by mass spectrometry[103]. This procedure typically involves dry ashing the swipe sample[32] in a muffle furnace[104] and then dissolving in acid[105]. This is often followed by a chemical separation, such as anion exchange chromatography[32], prior to mass spectrometric analysis[98]. The mass spectrometry used is either ICP-MS[32,105] or Thermal Ionisation Mass Spectrometry (TIMS)[98,104,106]. Although TIMS is the 'gold standard' ICP-MS is increasing used as the requirement of 20 minutes for separation and analysis is significantly less than the >50 hours required for TIMS[104].

Bulk analysis of collected particles reports the isotopic composition of the whole mass of material analysed, vital information, but the isotopic composition of each particle in the bulk sample could differ significantly from the bulk composition: particle analysis therefore has the power to return significantly more information about the sample. Using Scanning Electron Microscopy (SEM) coupled with an energy-dispersive x-ray spectrometer (EDX) to characterise the morphology of the particles (particle size, form, surface structure and composition) can give information on the history and source of samples[97,95,107,103]. Determining the isotopic composition of the UO_x particles individually rather than collectively may also reveal the presence of uranium of differing enrichment to the bulk. Hypothetically a bulk analysis which diluted a few HEU particles in a more significant quantity of DU particles could fail to identify a cause for concern.

The UO_x particles on the swipe samples range in size from 0.3-2 μm[97] and are generally in low concentrations on the swipe; the majority of the particles are dust, lead[108], or other detritus[104,103]. Therefore particles are typically extracted from the swipe to another more easily analysable, substrate. Methods for extracting particles from the swipe include vacuum impacting[108,109], rubber ball[110,98], ultrasonic agitation[111] and heptane extraction[98]. A schematic of a vacuum impactor apparatus is given in Figure 9. A vacuum pump is used to extract particles off the swipe surface through a nozzle. The substrate, often coated with an adhesive agent[109], is positioned directly behind the nozzle to best collect the particles. The air flow (containing non-adhered particles) passes around the substrate and out to exhaust.

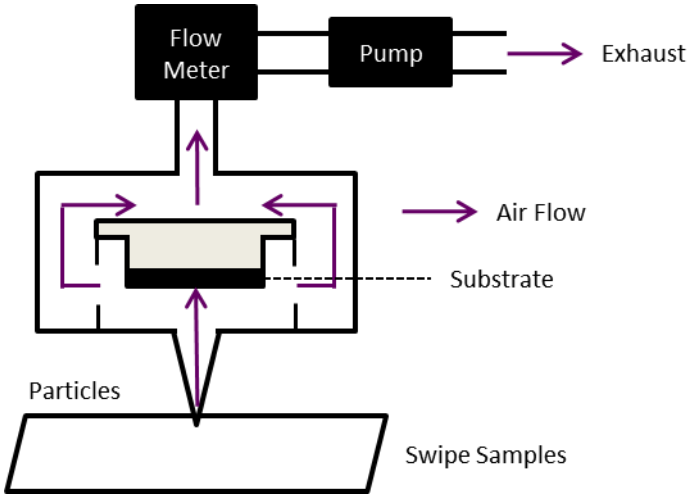

Figure 9 – Schematic of a Vacuum Impactor for collection of particles from a swipe sample onto a different substrate, recreated from Wang *et al* (2013)[111].

Both ultrasonic agitation and heptane extraction place the particles into a liquid suspension. The liquid suspension is then poured onto a solid substrate, the particles being transferred when the solvent evaporates. The particles can be embedded in a film layer by the addition of collodion to the solvent prior to evaporation[112–115,42]. Particles which have been collected on polycarbonate membranes have also been placed into a liquid suspension by dissolving the membrane in solvent[105,116,117]. No collodion is required to produce the film layer as one is created from the dissolved membrane when the solvent evaporates.

Once the particles are on the desired substrate, with or without a film layer, the uranium bearing particles are usually identified from the greater quantity of environmental particles which do not contain significant quantities of uranium. This is of particular importance for TIMS as the particles to be analysed for their isotopic composition need to be transferred from the substrate to a rhenium filament prior to analysis, one particle per filament[115,118,119]. TIMS is time consuming, and therefore in order to restrict the number of particles analysed it is most often combined with Fission Track (FT)[114,119,120]. In fission track analysis particles contained within a film layer (collodion or polycarbonate) are attached to a nuclear track detector (Makrofoil®[116] or Lexan®[114,118]polycarbonate discs) and irradiated with thermal neutrons in a nuclear reactor. The location of particles containing fissile isotopes (^{235}U, ^{239}U, ^{233}U)[115] are indicated by a cluster of damage tracks in the nuclear track detector[112,116], visible under optical microscopy. The number of fission tracks is indicative of the quantity of fissile material present; an experienced analyst can then compare the number of fission tracks to the size and appearance of the particle and determine which particles are most likely to be enriched uranium or HEU[112,116]. It is these particles whose isotopic compositions are determined by TIMS. Particles are transferred to the filament for TIMS by cutting a square around the particle with

a laser and then using a micromanipulator to move the square to the new location[115,116]. As 50 x 50 μm represents the smallest area which can be cut around the particle, the potential exists for more than one particle, of differing isotopic compositions, to be analysed simultaneously[103].

FT-TIMS, although routinely used for uranium particle analysis, is not the only approach which has been adopted[98,114,116]. FT-TIMS requires the use of an expensive rhenium filament for each particle[116], is time consuming and requires access to a nuclear reactor. An alternative to fission track is to instead use SEM-EDX to identify uranium or other actinide bearing particles. Kraiem *et al* (2012)[121] have reported using SEM-EDX to identify uranium bearing particles and then using a micromanipulator installed inside the SEM chamber to transfer particles to a TIMS filament. The higher resolution of SEM-EDX compared to fission track analysis greatly reduces the likelihood of transferring more than one particle to each filament[103], but requires the absence of a film layer over the particles. Additionally SEM-EDX only confirms the particle contains uranium, not that it has high proportions of the fissile isotopes.

By using the micromanipulator inside the SEM chamber to transfer uranium containing particles to another substrate (e.g. carbon planchet), SEM-EDX has been used to prepare uranium particles for analysis by Secondary Ion Mass Spectrometry (SIMS)[108,122]. SIMS can be used either as a focussed microprobe or as an ion microscope. In the ion microscope mode a broad primary ion beam sputters and ionises the sample surface, and the mass-filtered sample surface images generated are then projected and recorded on an ion imaging counting detector[123]. These 2D images not only provide the location of each uranium-containing particle on the surface[123], but by collecting images mass-filtered for both $^{235}U^{+}$ and $^{238}U^{+}$ and superimposing them[112], software can estimate the isotopic composition of each particle[124,125]. The focussed microprobe can then be applied to each particle, and by switching to an electron multiplier detector[108], a more precise and accurate isotopic composition obtained[125]. Using the SIMS as an ion microscope to locate the uranium particles however, is a destructive technique, reducing the number of counts which can be collected with the microprobe analysis[123], which is partly why sometimes SEM-EDX or fission track is used to identify particles for SIMS instead. Using SEM-EDX[108] or fission track[116] to isolate the particles for SIMS analysis on a fresh planchet also acts to reduce molecular ion interferences. In SIMS molecular ion interferences from other elements in or around the particle analysed easily interfere on the minor isotopes ^{234}U and ^{236}U[108,116]. These interferences negatively affect the accuracy of the $^{236}U/^{238}U$ and $^{234}U/^{238}U$ isotope ratios; which provide information on the enrichment processes and type of feed material (natural uranium or reprocessed uranium) [120].

The molecular ion interferences on the minor isotopes restrict the accuracy and precision for uranium particles which can be achieved with SIMS[112]. The molecular ion interferences on the minor isotopes can be overcome by using a high mass resolution and energy filtering techniques[126], however these act to reduce the transmission of ions through the mass spectrometer, by 95% compared to low mass resolution[120], affecting the sensitivity of the SIMS such that measurement can no longer be performed on micron-sized particles. Similar to sector field ICP-MS, SIMS instruments are double focussing mass spectrometers. Large Geometry (LG) SIMS instruments include a much larger radius magnetic sector than conventional SIMS[120]. The larger radius magnetic sector improves the transmission of ions at high mass resolution, allowing molecular ion interferences to be removed with minimal reduction in sensitivity[112,120,127]. LG-SIMS also combines the increased mass resolution with a multicollector detector array, allowing simultaneous detection of all uranium isotopes, to greatly improve the accuracy and precision of the isotope ratio measurements on single uranium particles[120,127]. Ranebo *et al* (2009)[120] found LG-SIMS performed as well as FT-TIMS (except for ^{236}U as LG-SIMS required a correction for $^{235}UH^{+}$ interferences) for uranium particle analysis in a fraction of the sample preparation time. The primary issue with LG-SIMS is cost, £3.2 million in 2010.

For nuclear safeguards timely analysis can be critical[123]. In the bulk analysis of uranium particles ICP-MS has the advantage over TIMS in this regard as sample preparation is simpler and measurement times are shorter[35]. Esaka *et al* (2013)[105] extended this advantage to particle analysis, isolating and dissolving single particles before analysing by ICP-MS. However ICP-MS can also be coupled to laser ablation systems (section 1.2), allowing solid samples to be analysed and hence the amount of sample preparation time required. LA-ICP-MS has successfully been used to analyse the isotopic composition of large (>10 µm) UO_x particles[36,101], however the majority of the particles collected on nuclear safeguard swipe samples are closer to 1 µm in size[97]. Becker *et al* (2008)[128] have reported on the analysis of micron sized and Pointurier *et al* (2011)[114] on sub-micron sized UO_x particles by LA-ICP-MS. These and subsequent analysis[109,115,118] of micron to sub-micron sized uranium particles have restricted the isotopic analysis to the $^{235}U/^{238}U$ ratio. For LA-ICP-MS to be a complementary technique to FT-TIMS or SIMS for uranium particle analysis likely improvements on what has already been reported in the literature will be required. Discounting sample preparation time, Pointurier *et al* (2011)[114] estimated the time taken to analyse 30 uranium particles by LA-ICP-MS was half the time required for SIMS and a quarter that of TIMS; including sample preparation time LA-ICP-MS was 14 times faster than FT-TIMS. Therefore improving the analytical performance of LA-ICP-MS could potentially create a powerful technique for nuclear safeguards, particularly if time is a factor in the analysis.

1.3.4 Scanning Electron Microscopy

Scanning Electron Microscopy (SEM) coupled with an energy-dispersive x-ray spectrometer (EDX) is a widely used technique for determining the size, composition and morphology of UOx particles collected from the environment[95,97,129].

The goal of any microscopy is to achieve the best possible resolution[130]. In microscopy, resolution is defined as the distance (*R*) which can be achieved between two object details which are just separable from one another. By adjusting Bragg's Law an equation can be created for resolution in terms of wavelength, λ[130]:

$$R = \frac{0.61\lambda}{sin\ \alpha}$$

Even with a perfect lens (α equal to 1) the resolution of optical microscopes are limited to 0.61 times the wavelength of visible light (400-800 nm). SEM was one of the first techniques to allow imaging without reliance on optical measures. According to the De Broglie equation the wavelength of an electron is reliant on its kinetic energy. Therefore by accelerating electrons to keV in kinetic energy a scanning electron microscope can achieve higher resolution than visible light, better than 1 nm.

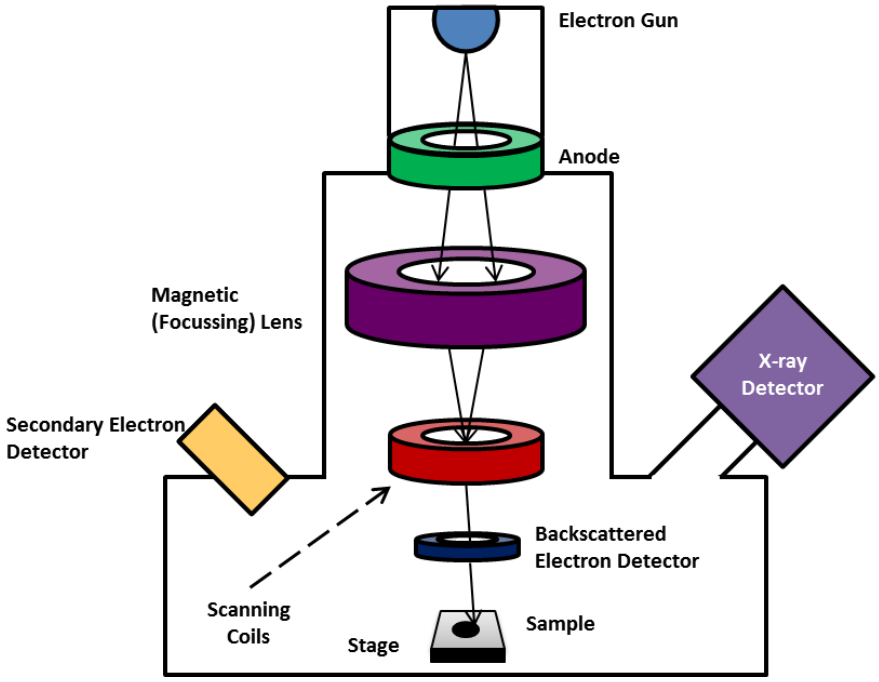

Figure 10 – Schematic of a scanning electron microscope fitted with an energy-dispersive x-ray spectrometer[131]. An Electron beam from the gun is accelerated through the anode and focussed onto the sample surface, with an arrangement of detectors around the sample stage. The chamber is under vacuum during operation.

In order to be analysed with the SEM the sample surface must be electrically conductive. If the sample surface is not conductive a thin layer of conductive material (graphite carbon, gold) can be

sputter coated onto the surface. Once the sample is made conductive it is placed on to the stage inside the SEM and the chamber sealed, a pump is then used to place the chamber under vacuum. Once at vacuum electrons are produced by a tungsten filament inside an electron gun. These electrons are accelerated through a large potential (>100 kV) and then focussed by electric and magnetic fields into an electron beam to interrogate the sample surface. The electron beam can either be held in place to examine a particular location on the sample (spectroscopy) or rastered across an area on the sample (imaging). When the electron beam interacts with the sample surface various processes occur. The primary electrons from the electron beam can be scattered back away from the sample atoms elastically and detected by the backscatter electron detector (BSE). As heavier elements backscatter electrons more than lighter elements the backscatter electron detector can be used to locate concentrations of heavy elements, such as uranium, on a sample surface. The interaction between a primary electron and a sample atom can also produce an inelastic collision which displaces a core electron from the sample atom. These secondary electrons are detected by the secondary electron detector (SE). The asymmetric orientation of the detector makes the surface condition directly under the beam critical to the number of secondary electrons detected; such differences allow the topography of the sample to be imaged.

When a core electron is displaced from a sample atom by the electron beam an electron from a higher energy orbital relaxes to take its place. This relaxation results in the release of energy as an x-ray photon. The energy of the x-ray photon released is indicative of the element of the atom. In this way the EDX detector can be used to determine the composition of the sample area interrogated by the electron beam.

For both the BSE and SE detectors the count rate of electrons is translated into brightness on the display. Unlike optical microscopes in SEM the magnification of the instrument is variable, dependent on the current sent to the scanning coils. The magnification is important as it takes into account instrumental limitations[6], such as the raster of the display used.

1.4 Aims of the PhD project

The primary aim of this project was to improve the utility of laser ablation inductively coupled plasma mass spectrometry for the determination of the isotopic composition of single micron-sized UO_x particles. To achieve this aim a few key objectives can be identified.

1.4.1 Improve Sensitivity

The restricted size of the UO_x particles provides a finite limit on the number of atoms which are available for detection. Therefore it is advantageous to maximise the percentage of those atoms

which are detected. In addition, by accelerating the transmission of the ablation plume generated from the laser ablation system to the ICP-MS the signal-to-noise ratio could be improved, further improving the limit of detection and precision on the isotope ratios. To achieve the highest signal possible from the limited sample size the main instrument utilised will be a MC-ICP-MS equipped with a high sensitivity interface. To increase sensitivity and signal-to-noise ratio further the laser ablation system and MC-ICP-MS will be coupled with a prototype ablation cell and injector design, previously designed at Loughborough University. The performance of the LA-MC-ICP-MS system using the prototype ablation cell and injector design will be evaluated for glass reference materials and sub-micron UO_x particles of known isotopic composition.

1.4.2 Compare Data Evaluation Strategies

The accuracy and precision which can be achieved for transient isotope ratio signals collected with a MC-ICP-MS is heavily dependent on the data evaluation strategy selected. The merits of three such data evaluation strategies using a mixed detector array will be investigated as will the benefits of using the geometric mean rather than arithmetic mean to determine isotope ratios. The utility of the geometric mean is shown to be applicable not just to the LA-MC-ICP-MS of UO_x particles, but to isotope ratio analysis generally.

1.4.3 Develop a Method for Preparing UO_x particles for Laser Ablation Analysis

Also required to improve the utility of LA-ICP-MS for UO_x particles is a new methodology for preparing micron-sized particles for laser ablation. The method developed will be capable of mounting micron-sized particles in an ultrathin film layer atop a clear substrate. The particle will be well dispersed across the layer, reducing the likelihood of analysing more than a single particle in each ablation.

1.4.4 Demonstration of Capability for UO_x particle analysis by LA-ICP-MS on an Environmental Sample

The final objective is to demonstrate the utility of the LA-MC-ICP-MS improvements developed on UO_x particles in an environmental sample. A soil sample from a uranium contaminated site will be obtained and a size fraction prepared and the isotopic composition of the UO_x particles measured by the LA-MC-ICP-MS system using the prototype ablation cell and injector design evaluated earlier. The isotopic composition of the UO_x particles will be compared to previously published analyses of UO_x particles collected at the same location[101].

1.5 References

1. J. W. Olesik, *Anal. Chem.*, 1991, **63**, 12–21.

2. *Inductively Coupled Plasma Spectroscopy and its Applications*, ed. S. J. Hill, Blackwell Publishing, Oxford, 2nd edn., 2007.

3. M. Tanner and D. Günther, *Anal. Chim. Acta*, 2009, **633**, 19–28.

4. N. Jakubowski, T. Prohaska, L. Rottmann, F. Vanhaecke, P. H. Roos, and T. Lindemann, *J. Anal. At. Spectrom.*, 2011, **26**, 727–757.

5. J. R. Dean, *Practical Inductively Coupled Plasma Spectoscopy (Analytical Techniques in the Sciences (AnTS)*, John Wiley & Sons Ltd, Chichester, 2005.

6. D. A. Skoog, F. J. Holler, and T. A. Nieman, *Principles of Instrumental analysis*, Saunders College Publishers, Philadelphia, 5th edn., 1998.

7. R. Thomas, *Practical guide to ICP-MS*, Marcel Dekker, New York., 2004.

8. E. de Hoffmann and V. Stroobant, *Mass Spectrometry, Principles and Applications*, John Wiley & Sons Ltd, Chichester, 3rd edn., 2007.

9. M. Wiedenbeck, R. Bugoi, M. J. M. Duke, T. Dunai, J. Enzweiler, M. Horan, K. P. Jochum, K. Linge, J. Košler, S. Merchel, L. F. G. Morales, L. Nasdala, R. Stalder, P. Sylvester, U. Weis, and A. Zoubir, *Geostand. Geoanalytical Res.*, 2012, **36**, 337–398.

10. C. Labrecque, L. Whitty-Léveillé, and D. Larivière, *Anal. Chem.*, 2013, **85**, 10549–10555.

11. M. Tanimizu, N. Sugiyama, E. Ponzevera, and G. Bayon, *J. Anal. At. Spectrom.*, 2013, **28**, 1372–1376.

12. C. J. Scadding, R. J. Watling, and A. G. Thomas, *Talanta*, 2005, **67**, 414–24.

13. D. Günther, I. Horn, and B. Hattendorf, *Fresenius J. Anal. Chem.*, 2000, **368**, 4–14.

14. O. Borovinskaya, S. Gschwind, B. Hattendorf, M. Tanner, and D. Günther, *Anal. Chem.*, 2014, **86**, 8142–8148.

15. O. Borovinskaya, B. Hattendorf, M. Tanner, S. Gschwind, and D. Günther, *J. Anal. At. Spectrom.*, 2013, **28**, 226–233.

16. H. A. O. Wang, D. Grolimund, C. Giesen, C. N. Borca, J. R. H. Shaw-Stewart, B. Bodenmiller, and D. Günther, *Anal. Chem.*, 2013, **85**, 10107–10116.

17. N. Jakubowski, L. Moens, and F. Vanhaecke, *Spectrochim. Acta Part B At. Spectrosc.*, 1998, **53**, 1739–1763.

18. M. E. Wieser and J. B. Schwieters, *Int. J. Mass Spectrom.*, 2005, **242**, 97–115.

19. FachinformationszentrumChemieGmbH, http://www.chemgapedia.de/vsengine/vlu/vsc/de/ch/3/anc/masse/ms_massenanalysator_doppelfok.vlu/Page/vsc/de/ch/3/anc/masse/2_massenspektrometer/2_4_massena 2012, (accessed Febuary 2012).

20. M. Resano, K. S. McIntosh, and F. Vanhaecke, *J. Anal. At. Spectrom.*, 2012, **27**, 165–173.

21. Z. Chu, Y. Yang, and G. Qiao, *Int. J. Mass Spectrom.*, 2006, **253**, 130–135.

22. D. C. Baxter, I. Rodushkin, and E. Engstrom, *J. Anal. At. Spectrom.*, 2012, **27**, 1355–1381.

23. A. V. Mitroshkov, K. B. Olsen, and M. L. Thomas, *J. Anal. At. Spectrom.*, 2015, **30**, 487–493.

24. C. K. Bayne, *Statistical design of mass spectrometry calibration procedures*, Oak Ridge National Laboratory Report ORLL/TM-13341, Oak Ridge National Laboratoryk, Oak Ridge, 1997.

25. I. S. Begley and B. L. Sharp, *J. Anal. At. Spectrom.*, 1997, **12**, 395–402.

26. S. Richter, a. Alonso, Y. Aregbe, R. Eykens, F. Kehoe, H. Kühn, N. Kivel, a. Verbruggen, R. Wellum, and P. D. P. Taylor, *Int. J. Mass Spectrom.*, 2009, **281**, 115–125.

27. N. J. Pearson, W. L. Griffin, and S. Y. O' Reilly, *SC40: Laser Ablation ICP-MS in the Earth Sciences: Current Practices and Outside Issues*, ed. P. Sylvester and R. Raeside, Mineralological Association of Canada, Vancouver, 2008, pp. 93–116.

28. F. Wombacher and M. Rehkamper, *J. Anal. At. Spectrom.*, 2003, **18**, 1371–1375.

29. C. P. Ingle, B. L. Sharp, M. S. A. Horstwood, R. R. Parrish, and D. J. Lewis, *J. Anal. At. Spectrom.*, 2003, **18**, 219–229.

30. T. Pettke, F. Oberli, A. Audétat, U. Wiechert, C. R. Harris, and C. a. Heinrich, *J. Anal. At. Spectrom.*, 2011, **26**, 475–492.

31. R. E. Russo, X. Mao, H. Liu, J. Gonzalez, and S. Mao, *Talanta*, 2002, **57**, 425–451.

32. R. C. B. Pestana, J. E. S. Sarkis, R. C. Marin, C. H. Abreu-Junior, and E. F. U. Carvalho, *J. Radioanal. Nucl. Chem.*, 2013, **298**, 621–625.

33. K. Newman, *J. Anal. At. Spectrom.*, 2012, **27**, 63–70.

34. S. Kappel, S. F. Boulyga, and T. Prohaska, *J. Environ. Radioact.*, 2012, **113**, 8–15.

35. S. F. Boulyga, U. Kloetzli, and T. Prohaska, *J. Anal. At. Spectrom.*, 2006, **21**, 1427–1430.

36. Z. Varga, *Anal. Chim. Acta*, 2008, **625**, 1–7.

37. A. M. Duffin, K. W. Springer, J. D. Ward, K. D. Jarman, J. W. Robinson, M. C. Endres, G. L. Hart, J. J. Gonzalez, D. Oropeza, R. E. Russo, D. G. Willingham, B. E. Naes, A. J. Fahey, and G. C. Eiden, *J. Anal. At. Spectrom.*, 2015, DOI: 10.1039/C4JA00452C

38. A. K. Souders and P. J. Sylvester, *J. Anal. At. Spectrom.*, 2008, **23**, 535–543.

39. P. J. le Roux, *J. Anal. At. Spectrom.*, 2010, **25**, 1033–1038.

40. S. F. Boulyga and T. Prohaska, *Anal. Bioanal. Chem.*, 2008, **390**, 531–539.

41. A. M. Duffin, G. L. Hart, R. C. Hanlen, and G. C. Eiden, *J. Radioanal. Nucl. Chem.*, 2013, **296**, 1031–1036.

42. C. H. Ebert, PhD Thesis, Iowa State University, 2012.

43. A. L. Gray, *Analyst*, 1985, **110**, 551–557.

44. R. Hergenröder, *Spectrochim. Acta*, 2006, **61**, 284–300.

45. S. Amoruso, R. Bruzzese, C. Pagano, and X. Wang, *Appl. Phys. A*, 2007, **89**, 1017–1024.

46. D. Günther, S. Jackson, and H. Longerich, *Spectrochim. Acta Part B*, 1999, **54**, 381–409.

47. K. Niemax, *Fresenius J. Anal. Chem.*, 2001, **370**, 332–340.

48. D. Fliegel and D. Günther, *Spectrochim. Acta Part B At. Spectrosc.*, 2006, **61**, 841–849.

49. I. Horn and F. von Blanckenburg, *Spectrochim. Acta Part B At. Spectrosc.*, 2007, **62**, 410–422.

50. J. Koch, I. Feldmann, B. Hattendorf, D. Günther, U. Engel, N. Jakubowski, M. Bolshov, K. Niemax, and R. Hergenroder, *Spectrochim. Acta Part B*, 2002, **57**, 1057–1070.

51. D. Günther and B. Hattendorf, *Trends Anal. Chem.*, 2005, **24**, 255–265.

52. M. Guillong, I. Horn, and D. Günther, *J. Anal. At. Spectrom.*, 2003, **18**, 1224–1230.

53. T. E. Jeffries, N. J. G. Pearce, W. T. Perkins, and A. Raith, *Anal. Commun.*, 1996, **33**, 35–39.

54. T. Vaculovic, P. Sulovsky, J. Machat, V. Otruba, O. Matal, T. Simo, C. Latkoczy, D. Günther, and V. Kanicky, *J. Anal. At. Spectrom.*, 2009, **24**, 649–654.

55. Y. Liu, Z. Hu, S. Gao, D. Günther, J. Xu, C. Gao, and H. Chen, *Chem. Geol.*, 2008, **257**, 34–43.

56. W. T. Perkins, N. J. G. Pearce, and J. A. Westgate, *Geostand. Newsl.*, 1997, **21**, 175–190.

57. R. E. Russo, X. Mao, and O. V Borisov, *Trends Anal. Chem.*, 1998, **17**, 461–469.

58. A. Bogaerts and Z. Chen, *Spectrochim. Acta Part B At. Spectrosc.*, 2005, **60**, 1280–1307.

59. H. Yuan, S. Gao, X. Liu, H. Li, D. Günther, and F. Wu, *Geostand. Geoanalytical Res.*, 2004, **28**, 353–370.

60. G. Gorodetsky, T. G. Kazyaka, R. L. Melcher, and R. Srinivasan, *Appl. Phys. Lett.*, 1985, **46**, 828–830.

61. K. Ozono, M. Obara, A. Usui, and H. Sunakawa, *Opt. Commun.*, 2001, **189**, 103–106.

62. X. L. Mao, A. C. Ciocan, O. V Borisov, and R. E. Russo, *Appl. Surf. Sci.*, 1998, **127**, 262–268.

63. B. N. Chichkov, C. Momma, S. Nolte, F. Von Alvensleben, and A. Tu, *Appl. Phys. A*, 1996, **115**, 109–115.

64. S. Kueper and M. Stuke, *Appl. Phys. B*, 1987, **44**, 199–204.

65. J. Košler, *Proc. Geol. Assoc.*, 2007, **118**, 19–24.

66. I. Horn and D. Günther, *Appl. Surf. Sci.*, 2003, **207**, 144–157.

67. J. Pisonero, B. Fernández, and D. Günther, *J. Anal. At. Spectrom.*, 2009, **24**, 1145–1160.

68. D. Bleiner and A. Bogaerts, *Spectrochim. Acta Part B At. Spectrosc.*, 2006, **61**, 421–432.

69. H.-R. Kuhn, M. Guillong, and D. Günther, *Anal. Bioanal. Chem.*, 2004, **378**, 1069–74.

70. M. Gaboardi and M. Humayun, *J. Anal. At. Spectrom.*, 2009, **24**, 1188–1197.

71. H. Lindner and A. Bogaerts, *Spectrochim. Acta Part B At. Spectrosc.*, 2011, **66**, 421–431.

72. S. J. M. Van Malderen, J. T. van Elteren, and F. Vanhaecke, *J. Anal. At. Spectrom.*, 2015, **30**, 119–125.

73. R. Kovacs, K. Nishiguchi, K. Utani, and D. Günther, *J. Anal. At. Spectrom.*, 2010, 25, 142–147.

74. D. Asogan, B. L. Sharp, C. J. P. O. Connor, A. Green, and R. W. Hutchinson, *J. Anal. At. Spectrom.*, 2009, **24**, 917–923.

75. D. Asogan, B. L. Sharp, C. J. P. O. Connor, A. Green, and J. Wilkins, *J. Anal. At. Spectrom.*, 2011, **26**, 631–634.

76. D. Tabersky, K. Nishiguchi, K. Utani, M. Ohata, R. Dietiker, M. B. Fricker, I. M. de Maddalena, J. Koch, and D. Günther, *J. Anal. At. Spectrom.*, 2013, **28**, 831–842.

77. T. Hirata, *Anal. Sci.*, 2007, **23**, 1195–1201.

78. D. Bleiner and D. Günther, *J. Anal. At. Spectrom.*, 2001, **16**, 449–456.

79. M. S. A. Horstwood, G. L. Foster, R. R. Parrish, S. R. Noble, and G. M. Nowell, *J. Anal. At. Spectrom.*, 2003, **18**, 837–846.

80. I. Horn, R. L. Rudnick, and W. F. Mcdonough, *Chem. Geol.*, 2000, **164**, 281–301.

81. S. E. Jackson, N. J. Pearson, W. L. Griffin, and E. a. Belousova, *Chem. Geol.*, 2004, **211**, 47–69.

82. D. Bleiner and H. Altorfer, *J. Anal. At. Spectrom.*, 2005, **20**, 754–756.

83. M. B. Fricker, D. Kutscher, B. Aeschlimann, J. Frommer, R. Dietiker, J. Bettmer, and D. Günther, *Int. J. Mass Spectrom.*, 2011, **307**, 39–45.

84. W. Müller, M. Shelley, P. Miller, and S. Broude, *J. Anal. At. Spectrom.*, 2009, **24**, 209–214.

85. M. Tanner and D. Günther, *J. Anal. At. Spectrom.*, 2007, **22**, 1189–1192.

86. M. Tanner and D. Günther, *J. Anal. At. Spectrom.*, 2005, **20**, 987–989.

87. M. Tanner and D. Günther, *J. Anal. At. Spectrom.*, 2006, **21**, 941–947.

88. X. R. Liu and G. Horlick, *Spectrochim. Acta Part B*, 1994, **50**, 537–548.

89. E. Craft, A. Abu-Qare, M. Flaherty, M. Garofolo, H. Rincavage, and M. Abou-Donia, *J. Toxicol. Environ. Health. B. Crit. Rev.*, 2010, **7**, 297–317.

90. A. Bleise, P. R. Danesi, and W. Burkart, *J. Environ. Radioact.*, 2003, **64**, 93–112.

91. N. S. Lloyd, S. R. N. Chenery, and R. R. Parrish, *Sci. Total Environ.*, 2009, **408**, 397–407.

92. D. Donohue, *J. Alloys Compd.*, 1998, **271-273**, 11–18.

93. M. May, R. Abedin-Zadeh, D. Barr, and A. Carnesale, *Nuclear Forensics. Role, State of the Art, Program Needs*, Joint Working Group of the American Physical Society and the American Association for the Advancement of Science, Washington DC, 2008.

94. V. Chazel, P. Gerasimo, V. Dabouis, P. Laroche, and F. Paquet, *Radiat. Prot. Dosimetry*, 2003, **105**, 163–6.

95. N. S. Lloyd, J. F. W. Mosselmans, R. R. Parrish, S. R. N. Chenery, S. V. Hainsworth, and S. J. Kemp, *Mineral. Mag.*, 2009, **73**, 495–510.

96. B. Autrusson, *ESARDA Bull.*, 2009, 83–84.

97. R. Kips, A. Leenaers, G. Tamborini, M. Betti, S. Van den Berghe, R. Wellum, and P. Taylor, *Microsc. Microanal.*, 2007, **13**, 156–164.

98. M. Kraiem, S. Richter, H. Kühn, E. a Stefaniak, G. Kerckhove, J. Truyens, and Y. Aregbe, *Anal. Chem.*, 2011, **83**, 3011–3016.

99. E. Kuhn, D. Fischer, and M. Ryjinski, *Enviromental Sampling for IAEA Safeguards: A Five Year Review*, IAEA Report IAEA-SM-367/10/01, IAEA, Vienna, 2001.

100. Y. Aregbe, T. Prohaska, Z. Stefánka, E. Szeles, A. Hubert, and S. F. Boulyga, *ESARDA Bull.*, 2011, **46**, 136–145.

101. N. S. Lloyd, R. R. Parrish, M. Horstwood, and S. R. N. Chenery, *J. Anal. At. Spectrom.*, 2009, **24**, 752–758.

102. R. Tortorello, E. Widom, and W. H. Renwick, *J. Environ. Radioact.*, 2013, **124**, 287–300.

103. F. Esaka, D. Suzuki, and M. Magara, *Anal. Chem.*, 2015, **87**, 3107–3113.

104. M. Liezers, S. H. Pratt, G. L. Hart, and D. C. Duckworth, *J. Radioanal. Nucl. Chem.*, 2012, 1037–1043.

105. F. Esaka, M. Magara, and T. Kimura, *J. Anal. At. Spectrom.*, 2013, **28**, 682–688.

106. S. Richter, H. Kühn, Y. Aregbe, M. Hedberg, J. Horta-Domenech, K. Mayer, E. Zuleger, S. Bürger, S. Boulyga, A. Köpf, J. Poths, and K. Mathew, *J. Anal. At. Spectrom.*, 2011, **26**, 550–564.

107. T. Shinonaga, D. Donohue, H. Aigner, S. Bürger, D. Klose, T. Kärkelä, R. Zilliacus, A. Auvinen, O. Marie, and F. Pointurier, *Anal. Chem.*, 2012, **84**, 2638–46.

108. F. Esaka, K. T. Esaka, C. G. Lee, M. Magara, S. Sakurai, S. Usuda, and K. Watanabe, *Talanta*, 2007, **71**, 1011–1015.

109. S. Kappel, S. F. Boulyga, L. Dorta, D. Günther, B. Hattendorf, D. Koffler, G. Laaha, F. Leisch, and T. Prohaska, *Anal. Bioanal. Chem.*, 2013, **405**, 2943–2955.

110. Y. Aregbe, J. Truyens, R. Kips, S. Richter, E. Stefaniak, H. Kühn, and M. Kraiem, *NUSIMEP-6 : Uranium isotope amount ratios in uranium particles*, IRMM Report EUR 23702EN, IRMM, Geel, 2008.

111. F. Wang, Y. Chen, Y. G. Zhao, Y. Zhang, T. X. Wang, J. H. Li, Z. Y. Chang, and H. P. Cui, *J. Radioanal. Nucl. Chem.*, 2013, **298**, 1865–1869.

112. *Safeguards Techniques and Equipment: 2011 Edition International Nuclear Verification Series No.1 (Rev. 2)*, IAEA, Vienna, 2011.

113. J. Messerly, PhD Thesis, Iowa State University, 2008.

114. F. Pointurier, A. Pottin, and A. Hubert, *Anal. Chem.*, 2011, **83**, 7841–7848.

115. F. Pointurier, A. Hubert, and A.-C. Pottin, *J. Radioanal. Nucl. Chem.*, 2012, **296**, 609–616.

116. F. Esaka, C.-G. Lee, M. Magara, and T. Kimura, *Anal. Chim. Acta*, 2012, **721**, 122–128.

117. F. Esaka and M. Magara, *Talanta*, 2014, **120**, 349–354.

118. A. Hubert, F. Claverie, C. Pécheyran, and F. Pointurier, *Spectrochim. Acta Part B At. Spectrosc.*, 2014, **93**, 52–60.

119. M. Kraiem, S. Richter, H. Kühn, and Y. Aregbe, *Anal. Chim. Acta*, 2011, **688**, 1–7.

120. Y. Ranebo, P. M. L. Hedberg, M. J. Whitehouse, K. Ingeneri, and S. Littmann, *J. Anal. At. Spectrom.*, 2009, 24, 277–287.

121. M. Kraiem, S. Richter, N. Erdmann, H. Kühn, M. Hedberg, and Y. Aregbe, *Anal. Chim. Acta*, 2012, **748**, 37–44.

122. F. Esaka, M. Magara, C. G. Lee, S. Sakurai, S. Usuda, and N. Shinohara, *Talanta*, 2009, **78**, 290–294.

123. P. M. L. Hedberg, P. Peres, J. B. Cliff, F. Rabemananjara, S. Littmann, H. Thiele, C. Vincent, and N. Albert, *J. Anal. At. Spectrom.*, 2011, 26, 406–413.

124. M. Betti, G. Tamborini, and L. Koch, *Anal. Chem.*, 1999, **71**, 2616–2622.

125. A.-L. Fauré, C. Rodriguez, O. Marie, J. Aupiais, and F. Pointurier, *J. Anal. At. Spectrom.*, 2014, **29**, 145–151.

126. F. Esaka, K. Watanabe, T. Onodera, C.-G. Lee, M. Magara, S. Sakurai, and S. Usuda, *Appl. Surf. Sci.*, 2008, **255**, 1512–1515.

127. P. Peres, P. M. L. Hedberg, S. Walton, N. Montgomery, J. B. Cliff, F. Rabemananjara, and M. Schuhmacher, *Surf. Interface Anal.*, 2013, **45**, 561–565.

128. J. S. Becker, H. Sela, J. Dobrowolska, M. Zoriy, and J. S. Becker, *Int. J. Mass Spectrom.*, 2008, **270**, 1–7.

129. A. Laskin and J. P. Cowin, *Anal. Chem.*, 2001, **73**, 1023–1029.

130. M. von Heimendahl, *Electron Microscopy Of Materials - An Introduction*, Academic Press, Inc., New York, 1980.

131. Scanning Electron Microscope, http://www.purdue.edu/rem/rs/sem.htm, (accessed July 2012)

Chapter 2 – Evaluation of the Utility of the Dual Concentric Injector and Enterprise Cell for Isotope Ratio Laser Ablation Multi Collector Inductively Coupled Plasma Mass Spectrometry

2.1 Introduction

This chapter describes the initial implementation of a prototype micro-volume laser ablation cell and dual injector torch design to a MC-ICP-MS. It was hoped that the prototype design would increase accuracy and precision for isotope ratio analysis by increasing the sensitivity of the LA-MC-ICP-MS system. In order to evaluate the performance of this prototype, another low volume ablation cell was used for comparison.

2.2 Experimental

2.2.1 Description of the Dual Concentric Injector and Enterprise Cell

In the optimisation of LA-ICP-MS for spatially resolved analysis, the transmission of the ablation plume from the ablation site to the ICP torch has to be both highly efficient (minimal loss of sample in transport) and as rapid as possible. By accelerating the sample transmission the signal-to-noise (S/N) ratio is increased, improving precision and limit of detection (LOD). For laser ablation imaging, accelerating the sample transmission allows the translation rate at which the sample can be analysed to be increased without affecting spatial resolution. Historically in LA-ICP-MS, the design of the laser-sample coupling mechanisms has focussed only on reducing the residence time of the sample plume within the ablation cell and not on the volume of the transport tubing beyond. However some recent coupling mechanisms have looked at optimisation beyond the cell[1,2]. As the volume of cells (or effective volume in the case of two volume designs) has decreased over time the relative impact of residence time within the transport tubing has increased. For example with a typical setup using a low volume, single-volume cell (section 2.2.5) the volume of the connective tubing used can be five times greater than the internal volume of the cell, a major contribution to pulse broadening which lowers the S/N ratio[3]. Other aspects of the sample transport also affect the transport efficiency. The necessity of adding argon to the helium ablation gas has several effects due to the introduction of a turbulent mixing point. Modelling of the mixing between Ar and He gas streams within a Y-connector by Autrique *et al* (2008)[4] demonstrated how the He carrier gas was pushed towards the walls of the tubing; introducing eddies and dissipating large amounts of kinetic

energy[5]. Furthermore smaller particulate is far more likely to remain trapped in the turbulent flow than larger particles. Smaller particles, being closer to the containing walls, were more likely to be lost in the tubing. Those smaller particles not lost to the walls have longer residence time within the tubing, due to the loss of kinetic energy, compared to the larger particulate. The increased residence time of the smaller particulate results in pulse broadening of the overall signal, and in extreme cases can lead to the pulse splitting in two; one initial response from the larger particulate and a second response from the delayed smaller particulate[4,5].

At Loughborough University a new approach to coupling a laser ablation system to ICP-MS has been developed based on (amongst others) the observations given above. A holistic approach was adopted in an attempt to improve the whole coupling mechanism (ablation cell, connective tubing and the ICP torch injector) rather than a single component. Described previously by Douglas and Managh[6] the coupling mechanism used a single length of 250 µm i.d fused silica as both transport tubing and torch injector, in order to reduce the tubing volume as much as possible and reduce turbulence. To facilitate the use of the fused silica tubing as the torch injector required the development of a support, given the in-house name 'Dual Concentric Injector' (DCI). The final part of the coupling mechanism was the ablation cell, of dual volume design, designated the 'Enterprise Cell'.

2.2.1.1 The Dual Concentric Injector (DCI)

The prototype DCI was designed to fit into the semi-demountable torch available for both the Element 2 XR™ ICP-MS and Neptune *Plus*™ MC-ICP-MS (Thermo Scientific™, Bremen, DE). For the main body of the DCI, a hollow plastic T-piece, is attached to the ICP torch via a PEEK fitting, holding the conventional 2.0 mm injector. The primary function of the DCI was to hold the fused silica tubing and injector on axis, relative to the sampler cone orifice of the ICP-MS. To this end the fused silica was contained within a hollow borosilicate rod which passes through the entire length of the main body of the DCI to a point beyond the PEEK fitting. An additional PEEK support, placed at the end of the DCI's conventional 2.0 mm quartz injector, was added to aid in keeping the fused silica on axis.

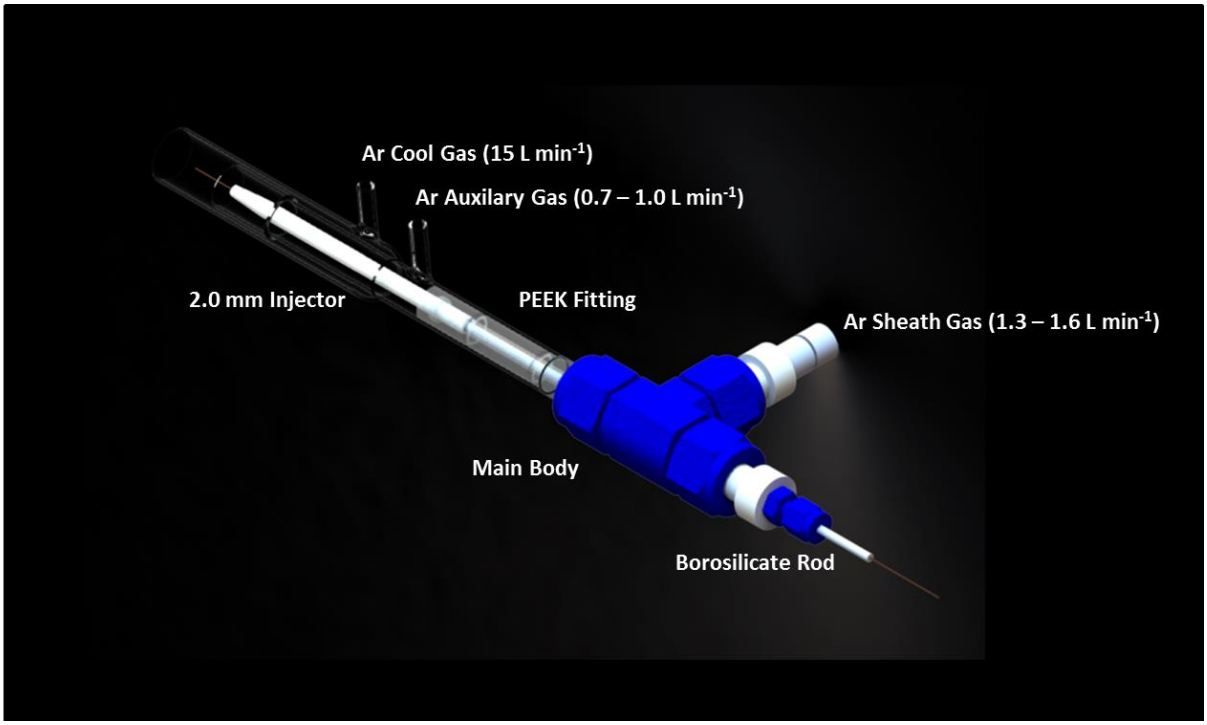

Figure 11 – Annotated rendered image of the Dual Concentric Injector in position within a semi-demountable torch, produced with Solidworks® 3D CAD software. The fused silica tubing is held within the borosilicate rod, which in turn is threaded through the main body and PEEK fitting, terminating inside the 2.0 mm injector. The Ar sheath gas upon exiting the hollow main body of the DCI forms a gas stream around the borosilicate rod and fused silica tubing. Insertion or retraction of the borosilcate rod into the main body of the DCI is used to alter the position of the fused silica tubing relative to the ICP plasma.

The secondary function of the DCI is to establish the central, stable, sample channel through the plasma which is expected from a typical, He-free, ICP torch. Without an Ar gas flow to establish the central channel the He outflow from the ablation cell will be insufficient to punch-through the outer turbulent regions of the plasma, resulting in no signal. Therefore an Ar sheath gas is added via the top of the DCI, flowing through the hollow main body, around the borosilicate rod and then out through the 2.0 mm injector to produce an Ar gas flow surrounding the fused silica injector. As the He carrier gas is contained within the fused silica there can be no disruptive mixing of the Ar and He gas streams until the He flow enters the plasma.

The final application of the DCI is to allow the fused silica injector to be extended forward of the DCI into the heart of the plasma. This application was added in response to modelling by Linder *et al* (2011)[7] which showed the potential for eddy structures at the front of the plasma, reducing analyte transport. The inference was that by adding the sample gas flow after any potential eddies, the detection efficiency could be increased.

2.2.1.2 The Two Volume 'Enterprise Cell' Comprising the Outer Cell and the Inner micro-volume 'Sniffer' Cell.

The prototype Enterprise Cell was designed by A. J. Managh to be mounted onto the ESI® New Wave Research™ (Huntingdon, Cambridgeshire, UK) UP series of laser ablation systems via an adjustable bracket (Figure 12). As a two volume cell design, the term 'Enterprise Cell' refers to the large outer cell and the smaller inner cell. The smaller inner cell is referred to as the 'Sniffer Cell'.

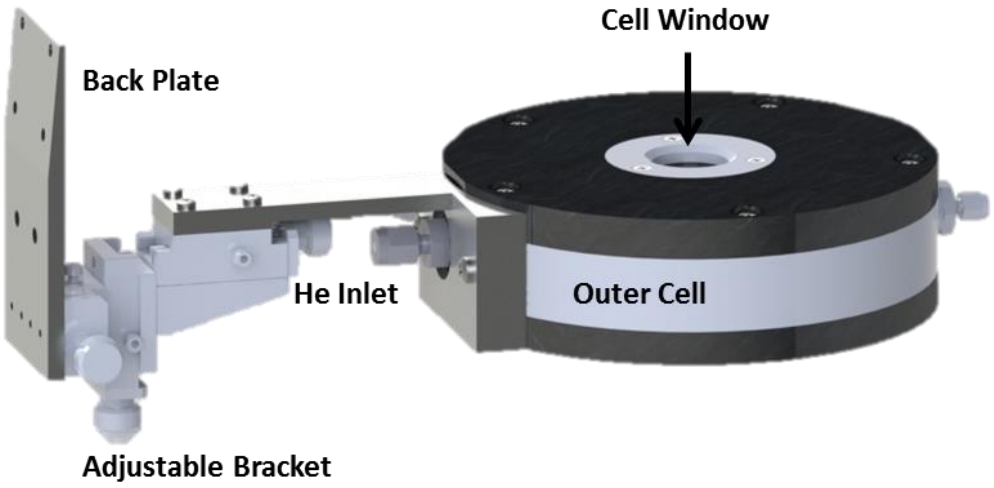

Figure 12 – Rendered image of the Enterprise Cell and adjustable bracket. The bracket (held onto the back of the laser ablation system) must be adjustable to allow the cell to be correctly positioned; as the objective of the laser ablation system must be directly over the inner Sniffer Cell.

The Sniffer Cell is held within the outer cell on a bar which sits across the cell. The bar has been carefully positioned such that the open laser port in the Sniffer Cell (Figure 14) is at the near centre of the cell, directly under the cell window. The adjustable bracket holding the outer cell must be adjusted each time In order to align the Sniffer Cell correctly under the objective.

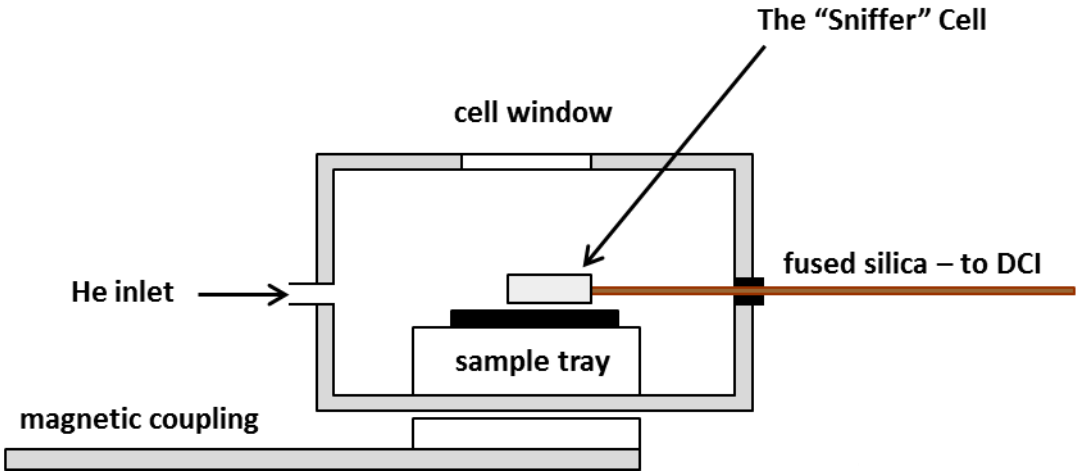

Figure 13 – Basic schematic of the Enterprise cell. The “Sniffer” Cell is held in place, 0.1 to 0.2 mm above the sample tray by a bar traversing the cell (not shown). The sample tray is moved under the stationary Sniffer Cell by magnetic coupling to an array of magnets attached by a boom arm to the UP’s XY stage.

As the position of the sniffer cell relative to the laser objective must remain fixed, the Enterprise Cell cannot be moved to change the sample position. Instead, under the Sniffer Cell in the outer cell, is a sample tray, sized to fit a 2.5 x 2.5 cm mount, which is fitted with a powerful series of magnets. These magnets are coupled to a coresponding series of magnets on an arm underneath the Enterprise Cell. By moving the exterior magnets with the XY stage, a corrersponding movement can be induced for the sample tray.

He gas is added to the cell via a port directly facing the front of the Sniffer, in a range from 10 to 150 mL/min. Due to the narrow bore of the outlet of the cell however, the outlet rate of gas from the cell is less than the range of inlet flows used. As a consequence the pressure within the cell is significantly greater than 1 atm, with typically each 10mL/min increase in He corresponding to a 1 PSI rise in cell pressure, depending on the length of tubing. Modelling and analysis by Douglas[6] has shown a correlation between the cell pressure and improved washout time and sensitivity. As the cell pressure is affected not only by the He inlet flow, but by the seal of the outer cell, reporting of the He inlet flow alone is not indicative ofthe cell performance.

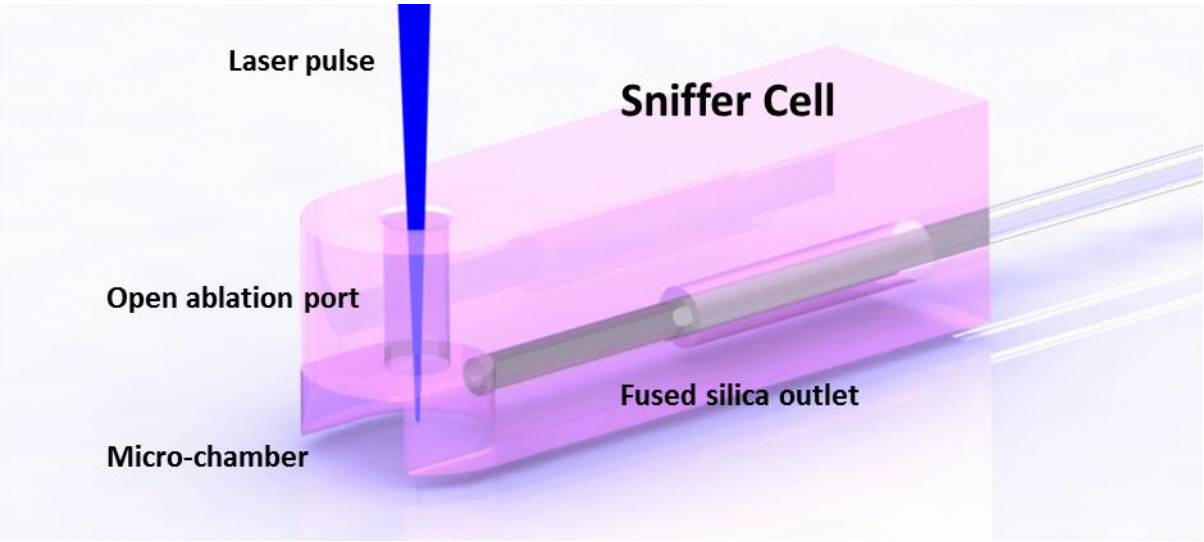

Figure 14 – Rendered image of the Sniffer Cell. Upon ablation the laser beam passes through to the small inner volume (≈0.005 cm^3) via the open laser port. The outer cell has been designed such that the gas flows direct the ablation plume down the fused silica line positioned at the back of the inner volume[8].

The actual chamber into which the ablation plume is allowed to expand is much smaller than the Sniffer itself. At the back of the micro-chamber is located the fused silica capillary outlet. The Sniffer and Enterprise Cell have both been designed to ensure that three different gas trajectories all converge at the micro-chamber:

1. A primary, high velocity, gas flow directly into the front of the micro-chamber to sweep the ablation plume into the outlet.
2. A secondary flow down the open ablation port, retarding plume formation and preventing particles escaping out of the ablation port.
3. A tertiary flow coming from under the back of the micro-chamber, between the Sniffer and the sample surface, to lift the ablation plume away from the sample surface to the height of the outlet.

To allow both smooth movement of the sample and the formation of the tertiary flow there needs to be a gap between the Sniffer and the sample. Flow modelling had suggested a 0.1 – 0.2 mm gap would give optimum performance[6].

2.2.2 Configuration of the LA-MC-ICP-MS

2.2.2.1 Instrumentation

The DCI and Enterprise Cell coupling mechanism developed at Loughborough University was transferred to NIGL, where it was used to connect the ESI® New Wave Research UP-193FX™ excimer laser ablation system to the Thermo Scientific™ Neptune *Plus*™ MC-ICP-MS (Figure 15). The Ar

sheath gas for the DCI was supplied from the outlet of a CETAC Aridus I™ desolvating liquid introduction unit.

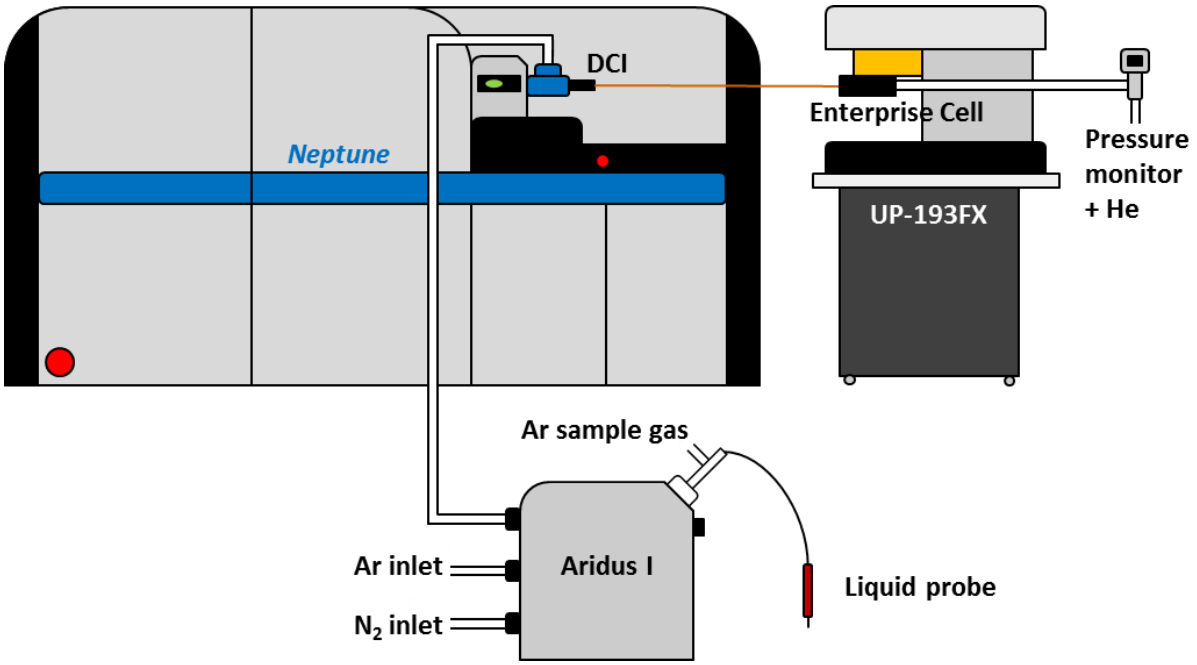

Figure 15 – Schematic of the LA-MC-ICP-MS setup with the DCI/Enterprise Cell. Due to spatial constraints the fused silica line was >1m. DCI sheath gas provided by outlet of Aridus I desolvator: allowing the addition of N_2 and aspiration of liquid reference materials.

To achieve the highest detection efficiency possible the MC-ICP-MS was configured for high efficiency by use of the Jet sampler cone and X skimmer cone. The Jet Interface™ consists of a High Capacity Dry Interface Pump and the specially designed set of cones[9]. More efficient interface pumping allows the use of a sampler cone with a larger, 1.0 mm, orifice, allowing a greater percentage of ions to be sampled from the plasma into the mass spectrometer.

Due to the physical constraints of the workspace it was not possible to juxtapose the laser ablation system optimally next to the mass spectrometer, to have either a short, or straight, transfer line between the DCI and the Enterprise Cell, both of which would be required for optimum performance. Using a 1.5 m length of tubing the volume of the system was 0.3 cm^3, with the tubing making up 98.3% of the total volume.

By using the desolvator to introduce the sheath gas to the DCI it was possible to aspirate liquid reference materials into the plasma. Liquid reference materials were used to tune the performance of the MC-ICP-MS, both at setup and after each sample change. Aspiration of reference materials of known isotopic composition yielded correction factors for detector gain, mass bias and abundance sensitivity. Addition of N_2 via a desolvator has been reported to increase the sensitivity of ICP-MS for certain isotopes by reducing the formation of metal oxides[10]. Newman has previously reported that

with the Jet Interface™ the quantity of N_2 required to achieve minimum oxide formation had a suppression effect on sensitivity[11] (others have reported signal suppression for larger quantities of N_2[10]). Addition of N_2 was therefore tuned for maximum sensitivity of uranium, not the UO/U ratio.

2.2.2.2 Method Development

The method used to determine the uranium isotope ratios was dependent on the arrangement of the detectors within the MC-ICP-MS at NIGL (Figure 16).

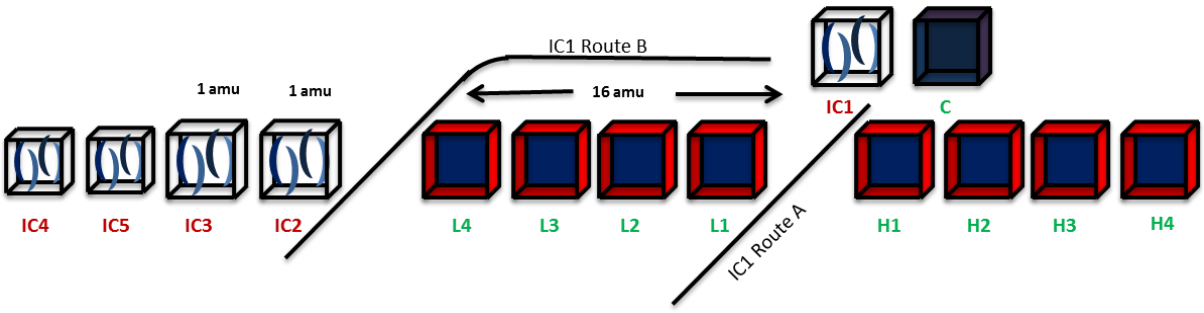

Figure 16 – Cup configuration of the MC-ICP-MS. The array consists of two mobile banks (L and H) of Faraday cups either side of an axial ion counter/Faraday cup. To the low mass side of the area are two IC's and two CDD's.

The main array consisted of eight mobile Faraday cups (FC), four either side of a fixed axial detector. The fixed axial detector could be either a Faraday cup or ion counter (IC), depending on the application. To the lower mass side of the main array was a secondary array of two ICs and two compact discrete dynode (CDD) ion counters. Given their relative abundances the minor isotopes, ^{234}U and ^{236}U, would require measurement on two ion counters and ^{238}U would need to be measured with a Faraday cup. These limitations reduced the possible cup configurations in which all of the isotopes of interest, ^{234}U, ^{235}U, ^{236}U and ^{238}U could be measured. The cup configuration selected, Method 1, is given in the table below.

Table 2 – Masses analysed in each detector, Method 1, MC-ICP-MS.

Mass (Isotope)	Detector
238 (^{238}U)	L4
237	IC1
236 (^{236}U)	IC2
235 (^{235}U)	IC3
234 (^{234}U)	IC5

Another method, Method 2, was used to determine correction factors for both the abundance sensitivity and hydride formation. It consisted of a number of sub configurations, in which three masses 236, 237 and 239 were measured on the axial IC, and 238 in H2, H1 and L1 respectively.

2.2.3 Certified Reference Materials

To initially evaluate the utility of the DCI/Enterprise Cell LA-MC-ICP-MS setup for isotope ratio analysis, a single solid certified reference material NIST SRM 611 (National Institute of Standards and Technology, Gaithersburg, Maryland, USA), containing 461.5±1.1 ppm uranium was used. The uranium used in SRM 611 has a non-natural, depleted, isotopic composition.

Table 3 – Uranium Isotopic composition of liquid and solid certified reference materials.

	$^{234}U/^{238}U$	$^{235}U/^{238}U$	$^{236}U/^{238}U$
CRM 112A[12]	5.2841e-05	7.2543e-03	-
CRM U010[13]	5.4655e-05	1.0140e-02	6.8798e-05
SRM 611[14]	9.45e-06	2.38555e-03	4.314e-05

Two other liquid reference materials were aspirated via the desolvator prior to laser analysis. A certified reference material of natural composition (CRM 112A) was analysed with Method 2, and a certified reference material (CRM U010) of non-natural composition with Method 1. The application of the correction factors determined from these certified reference materials to evaluate the laser ablation data is given below.

2.2.4 Determination of Correction Factors

The first correction factor (CF) required was for the UH/U ratio. This correction factor was determined by:

$$CF_{\frac{UH}{U}} = \frac{1}{n}\sum\left(\frac{^{239}U_{CRM112}}{^{238}U_{CRM112}}\right)$$

As natural uranium has no ^{236}U, any signal observed at masses 236 and 237 are from ^{238}U. Therefore correction factors for abundance sensitivity at 1 and 2 amu were determined by:

$$CF_{1amu} = \frac{1}{n}\sum\left(\frac{^{237}U_{CRM112}}{^{238}U_{CRM112}}\right)$$

$$CF_{2amu} = \frac{1}{n}\sum\left(\frac{^{236}U_{CRM112} - ^{235}U_{CRM112} \times CF_{\frac{UH}{U}}}{^{238}U_{CRM112}}\right)$$

As explained in the introduction to MC-ICP-MS (section 1.1.5.2), a correction factor is required for changes both in mass bias and detector response for each isotope. Using a non-natural uranium reference material correction factors were calculated by:

$$CF_{\frac{234U}{238U}} = {}^{234}U/{}^{238}U_{CRM010,\text{ certified}} \div \frac{1}{n}\sum\left(\frac{{}^{234}U_{CRM010} - {}^{235}U_{CRM010} \times CF_{1amu}}{{}^{238}U_{CRM010}}\right)$$

$$CF_{\frac{235U}{238U}} = {}^{235}U/{}^{238}U_{CRM010,\text{ certified}} \div \frac{1}{n}\sum\left(\frac{{}^{235}U_{CRM010}}{{}^{238}U_{CRM010}}\right)$$

$$CF_{\frac{236U}{238U}} = {}^{236}U/{}^{238}U_{CRM010,\text{ certified}} \div \frac{1}{n}\sum\left(\frac{{}^{236}U_{CRM010} - {}^{235}U_{CRM010} \times CF_{\frac{UH}{U}} - {}^{238}U_{CRM010} \times CF_{2amu}}{{}^{238}U_{CRM010}}\right)$$

All of the correction factors were then used to correct the laser ablation data in the following manner:

$${}^{234}U/{}^{238}U = \frac{{}^{234}U - {}^{235}U \times CF_{1amu}}{{}^{238}U} \times CF_{234U/238U}$$

$${}^{235}U/{}^{238}U = \frac{{}^{235}U}{{}^{238}U} \times CF_{235U/238U}$$

$${}^{236}U/{}^{238}U = \frac{{}^{236}U - {}^{235}U \times CF_{UH/U} - {}^{238}U \times CF_{2amu}}{{}^{238}U} \times CF_{236U/238U}$$

2.2.5 Description of a comparator system – LA-MC-ICP-MS with a low volume, single-volume cell

As a comparison to the DCI/Enterprise Cell coupling mechanism, a more traditional configuration using the low-volume, single-volume 'zircon cell' currently used at both NIGL and Loughborough was also tested. Bleiner and Günther[3] found that within a circular cell there is an area of high efficiency in the shape of a teardrop. The 'zircon cell' was created for the ESI® New Wave Research™ UP series of laser ablation systems by redesigning the circular standard cell supplied with the system[15], by restricting the internal volume to a teardrop shaped single volume of *c.a.* 3 cm^3, and here on referred to as the Zircon Cell.

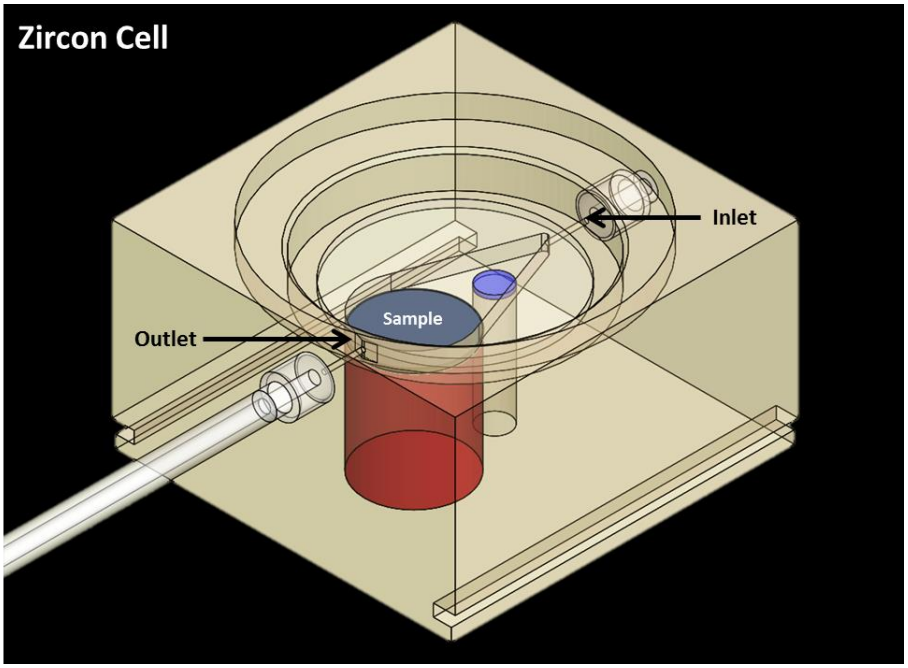

Figure 17– Rendered figure of the Zircon Cell (without lid). The gas inlet and outlet of the teardrop shape internal volume, *c.a.* 3 cm^3 are highlighted. A circular sample puck, 25 mm diameter, forms part of the chamber surface.

Instead of fused silica, all of the tubing was coated ¼" Teflon®-lined Tygon®. As with the DCI and Enterprise Cell the argon make-up gas was provided from the outlet of the desolvator with a Y-piece connector. The semi-demountable torch was fitted with the standard quartz 2.0 mm injector (Glass Expansion, West Melbourne, Victoria, Australia).

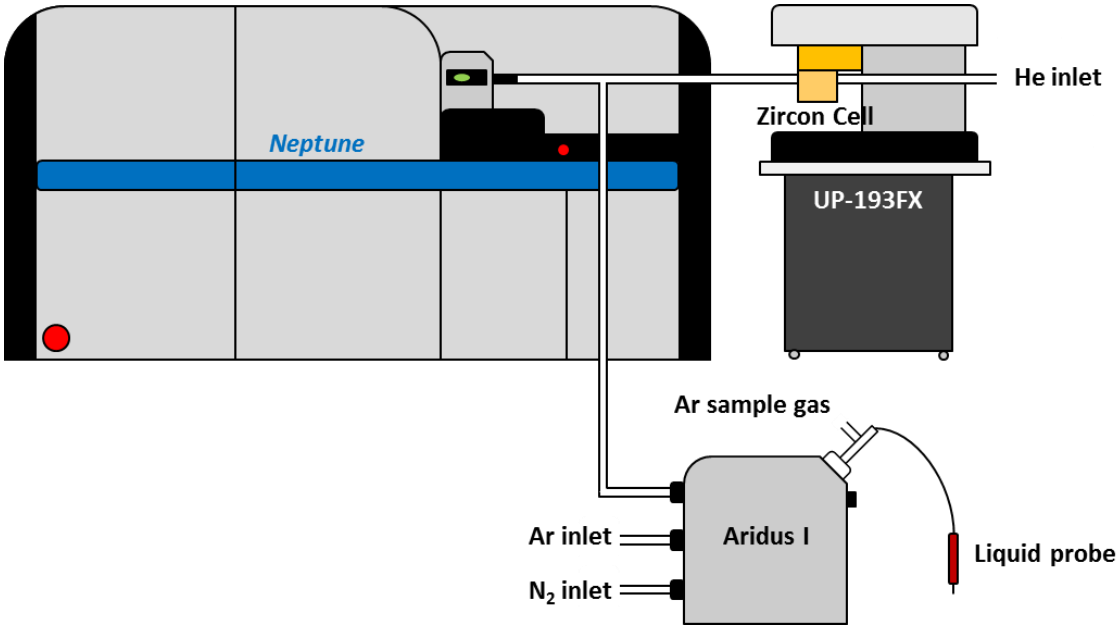

Figure 18 - Schematic of the LA-MC-ICP-MS setup with the Zircon Cell. The outlets of the Zircon Cell and desolvator are combined with a y-piece. All tubing is ¼" Tygon®.

2.2.6 Typical operating parameters

Each LA-MC-ICP-MS setup was tuned to different operating parameters. The most obvious difference was the significantly less He required by the Zircon Cell. The Enterprise Cell and DCI also required significantly more Ar and N_2 sweep gas than the Zircon Cell. One observation was that the Zircon Cell could be used in conjunction with an Aridus II™, but the Enterprise Cell and DCI could not. It was hypothesised that the DCI, due to the restrictions on flow within its body, generated a backpressure against which the Aridus II™ could not operate. Conversely the Aridus I™ could still operate, albeit at an elevated gas flow.

Table 4 – Typical operating parameters of LA-MC-ICP-MS, using both coupling mechanisms.

	Zircon Cell	**DCI/Enterprise Cell**
ESI® New Wave Research UP-193FX™ excimer laser		
Ablation mode	Single spot	Single spot
Fluence (J cm^{-2})	6	6
Repetition rate (Hz)	1	1
Spot size (µm)	20	20
He carrier gas (L min^{-1})	0.8	0.05
CETAC Aridus I™ desolvator		
Nebulizer	PFA 50	PFA 50
Sweep gas (L min^{-1})	3.51	5.40
N_2 add gas (L min^{-1})	0.07	0.09
Spray chamber temperature (°C)	95	95
Membrane temperature (°C)	160	160
Thermo Scientific™ Neptune Plus™ HR MC-ICPMS		
RF power (W)	1170	1170
Cool gas (L min^{-1})	15	15
Aux. gas (L min^{-1})	0.9	0.9
Skimmer cone	X (Ni)	X (Ni)
Sampler cone	Jet (Ni)	Jet (Ni)
Sample Gas (L min^{-1})	0.725	0.725
Extraction (V)	-2000	-2000
Resolution *m/Δm*	300	300
Cell pressure (psi)	≈0	11.5
Tubing length (m)	1.5	1.5

2.3 Evaluation of Detection Efficiency of the System

The evaluation of the performance of an ICP-MS is often reported in terms of signal intensity, quoted in units of counts per second per parts per million (cps/ppm) for a given isotope. However quoting the signal intensity in this manner is not necessarily the best unit of comparison. The signal intensity registered on an ICP-MS is heavily dependent on the rate at which the sample is introduced. The sample introduction rate is not consistent between different ICP-MS setups, but can vary by over one order of magnitude[16,17]. Evaluating the performance of an ICP-MS in terms of the signal intensity per ppm does not account for different sample introduction rates between two ICP setups.

A better approach to evaluate the performance of different ICP-MS setups would take the variable sample introduction rates into account. One such unit is the detection efficiency, which is calculated by:

$$\text{Detection Efficiency}(\%) = \frac{\text{Number of ions detected}}{\text{Number of atoms sampled}} (\times 100)$$

As both the number of ions detected and the number of atoms sampled will ideally vary identically with the sample introduction rate, the detection efficiency is identical regardless of the sampling rate selected. The number of ions detected is equal to the signal intensity in counts per second multiplied by the integration time of the mass spectrometer. In order to determine the number of atoms sampled the volume of reference material, either liquid or solid (in the case of laser ablation), must be measured. From the volume, given that the concentration and isotopic composition of the reference material is known it is possible to calculate the number of atoms sampled during the analysis.

Although the detection efficiency is independent of the sampling rate, it is still dependent on the choice of isotope. This is due in part to two different factors, the mass response curve of the mass spectrometer and the different ionisation potentials of each isotope in the plasma.

2.3.1 Determination of the Detection Efficiency by Aspiration of Solution

Prior to laser ablation of analysis, the detection efficiency of the LA-MC-ICP-MS setup was initially estimated via the aspiration of a natural uranium solution of known concentration into the argon sheath gas. The volume of the solution was measured before and after each timed analysis: as the concentration of the solution was known the number of moles aspirated during the time period could be calculated from the volume. Multiplying the number of moles by Avagadro's Number gave the number of atoms sampled by the MC-ICP-MS setup.

Table 5 – Detection efficiencies of each LA-MC-ICP-MS setup, determined by solution

Setup	Detection Efficiency (%), Determined by Solution
DCI and Enterprise Cell/Aridus I™	0.97
Zircon Cell/Aridus I™	2.82
Aridus II™ Solution Only[18]	4

The DCI and Enterprise Cell consistently lowered the detection efficiency of the aspirated solution by almost two-thirds relative to the standard Zircon Cell coupling mechanism. As it is a prototype, the most likely explanation may be the main body of the DCI is not being correctly sealed, allowing part of the argon sheath gas to leak to atmosphere. Due to the scale of the losses a leak may not be the whole explanation and therefore it was hypothesised that the body of the DCI, into which the sheath gas is introduced, may be responsible for turbulence, causing further sample losses to the chamber walls.

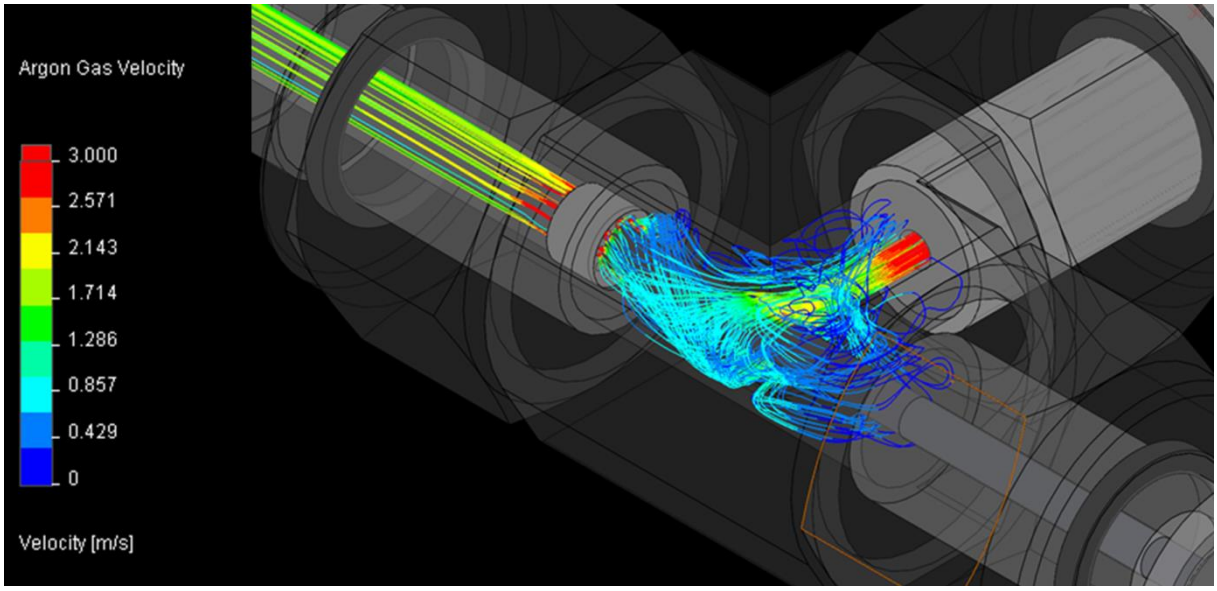

Figure 19 – Flow model of the Ar sheath gas within the main body of the DCI, determined using Solidworks 2011 (Educational Edition).

To support this hypothesis, modelling of the Ar gas flow within the DCI was performed. The model was produced in Solidworks® 2011 (Dessault Systèmes SOLIDWORKS Corp, Waltham, MA, USA) 3D computer aided design (CAD) software using the Flow Simulation package. The Flow Simulation package is used to investigate various fluid flow and heat transfer phenomena. The governing equations are the Navier-Stokes Equations, which are applicable for both laminar and turbulent flows.

The DCI was created in the CAD software. The inner surface of the body of the DCI was used as the boundary of the computational area. The boundary was defined to be adiabatic, such that no energy could be absorbed by the walls in the form of heat. The boundary had one inlet and one outlet (the end of the injector. A flow of 1.45 L min^{-1} argon was applied to the inlet. Both the inlet and outlet were set to an initial temperature of 293.20 K and a pressure of one atmosphere (the inductively coupled plasma is an atmospheric source). A full report of the initial and final conditions of the model can be found in appendix III.

The output of the modelling revealed significant contact between the gas flows and the walls of the DCI, alongside eddies and other areas of turbulent flow (Figure 19). The desolvator introduces dry plasma; the sample material is in the form of small particulate. The turbulent gas flows in the body of the DCI would increase the residence time of the particulate within the chamber. It is therefore probable that significant signal losses could occur by adherence of particulate to the walls of the main body of the DCI.

The adherence of materials to the body of the DCI could potentially affect sample measurement by laser ablation. During sample measurement, material adhered to the body of the DCI could be re-introduced to the gas stream, mixing with the sample material, affecting the isotopic composition determined. To reduce the potential impact of 'memory effects' on sample measurements after each passing of liquid reference materials through the desolvator, blank acid was aspirated to 'washout' any retained material from the desolvator. Furthermore a time delay was left between the aspiration of the blank acid into the desolvator and beginning laser ablation, to allow time for more retained material to be washed out of the system. The uranium signal during the washout period was monitored by MC-ICP-MS measurement.

2.3.2 Signal Pulse Profiles

By accelerating the transport of material from the ablation site to the ICP the DCI and Enterprise Cell should have an increased S/N ratio compared to the Zircon Cell. To evaluate this expected increase in S/N ratio single laser shots were ablated into the surface of SRM 611 to generate pulse profiles for each isotope. The number of data points in each profile was maximised by using the lowest possible integration time, 8 ms.

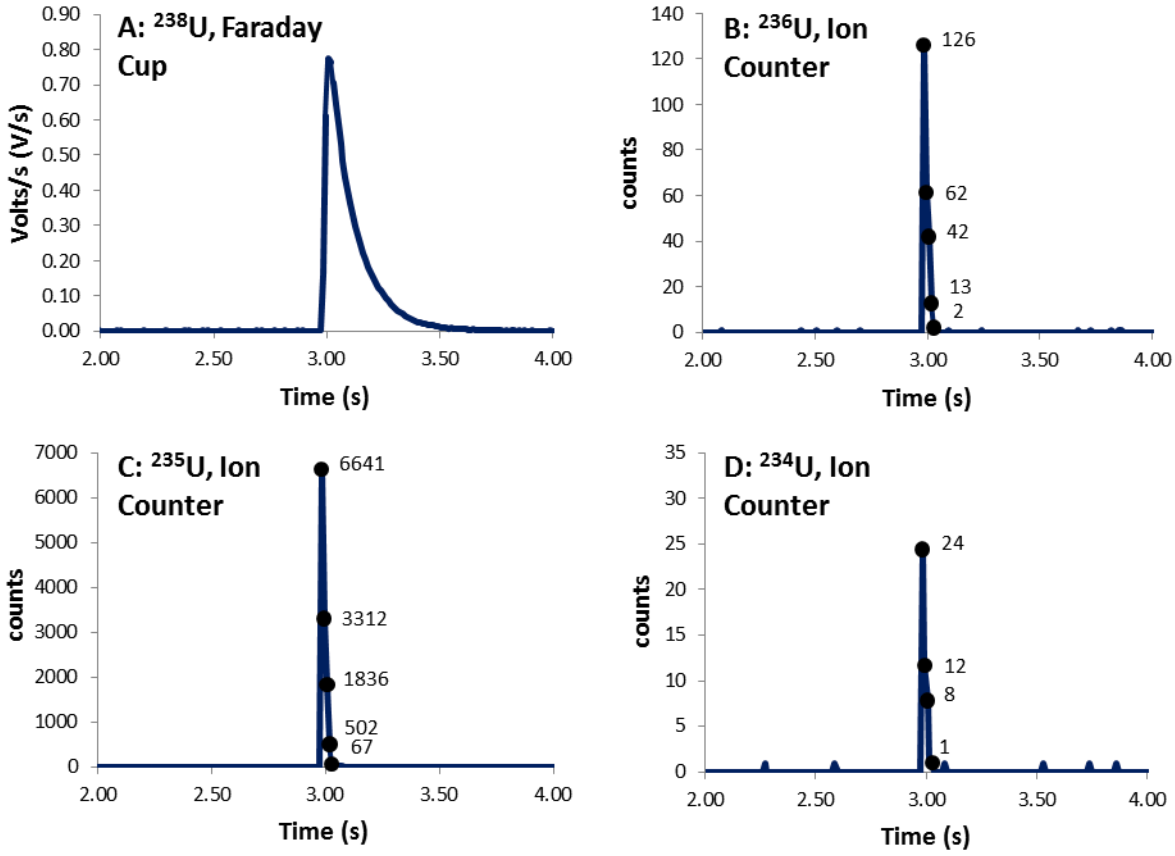

Figure 20 – Pulse profiles of U isotopes for SRM611, DCI and Enterprise Cell coupling mechanism. Integration time = 8 ms. Laser conditions: Fluence = 6 J cm^{-2}, Spot size = 20 µm, Ablation type – singleshot. A. Pulse profile of ^{238}U, measured on a Faraday Cup, in volts per second. B. Pulse profile of ^{236}U, measured on an ion counter in counts. C. Pulse profile of ^{235}U, measured on an ion counter in counts. D. Pulse profile of ^{234}U, measured on an ion counter in counts. Each black point describes each integration on the pulse profiles, values are in counts.

Typical single-shot pulse profiles on SRM 611 for all four uranium isotopes are given for the DCI and Enterprise Cell (Figure 20) and the Zircon Cell (Figure 21). The pulse profile of ^{238}U measured on a Faraday cup is significantly different to the profiles of the minor isotopes, measured on ion counters. The output of the amplifier boosting the Faraday cup response lags behind the input (ion signal), following a change in beam intensity[19], but the same is not true of the ion counters which respond to the change in beam intensity almost instantly. The pulse profile of ^{238}U does not describe the true input signal, but instead maps the tau decay of the Faraday cup amplifier, the effect of which is to spread the signal out over time. The stark differences in pulse profiles between the major and minor isotopes will have a significant impact on isotope ratio analysis which is discussed later in the chapter. Independent of any effect on isotope ratio measurements, the key advantages for the DCI and Enterprise Cell over the Zircon Cell are: an increase in the S/N ratio, improved definition of the ^{234}U and ^{236}U responses and an overall increase in signal intensity.

2.3.2.1 Increase in the signal to noise ratio

Averaging 30 pulses, the duration of the ^{235}U pulse, baseline to baseline, with the DCI & Enterprise Cell was 109ms, RSD 16.6%. The corresponding value for the Zircon Cell, again averaging 30 pulses, was 506ms, RSD 7.85%. Averaging the ^{235}U pulse maxima for the above 30-pulse measurements, the change in S/N ratio between the two coupling mechanisms is 6.2 times: the average pulse maximum for DCI & Enterprise Cell is 4,100 counts compared to 660 for the Zircon Cell.

Overall an approximately five fold increase in the S/N ratio can be reported for the DCI & Enterprise Cell over the Zircon Cell. It was expected a corresponding increase in isotope ratio precision could be expected for the prototype coupling mechanism.

2.3.2.2 Improved definition of ^{234}U and ^{236}U

With the Zircon Cell the responses from ^{234}U and ^{236}U are hard to distinguish from the baseline noise, due to the low number of counts. Any attempt to calculate an isotope ratio from these responses has a much greater likelihood of incorporating background ions and detector noise into the analysis.

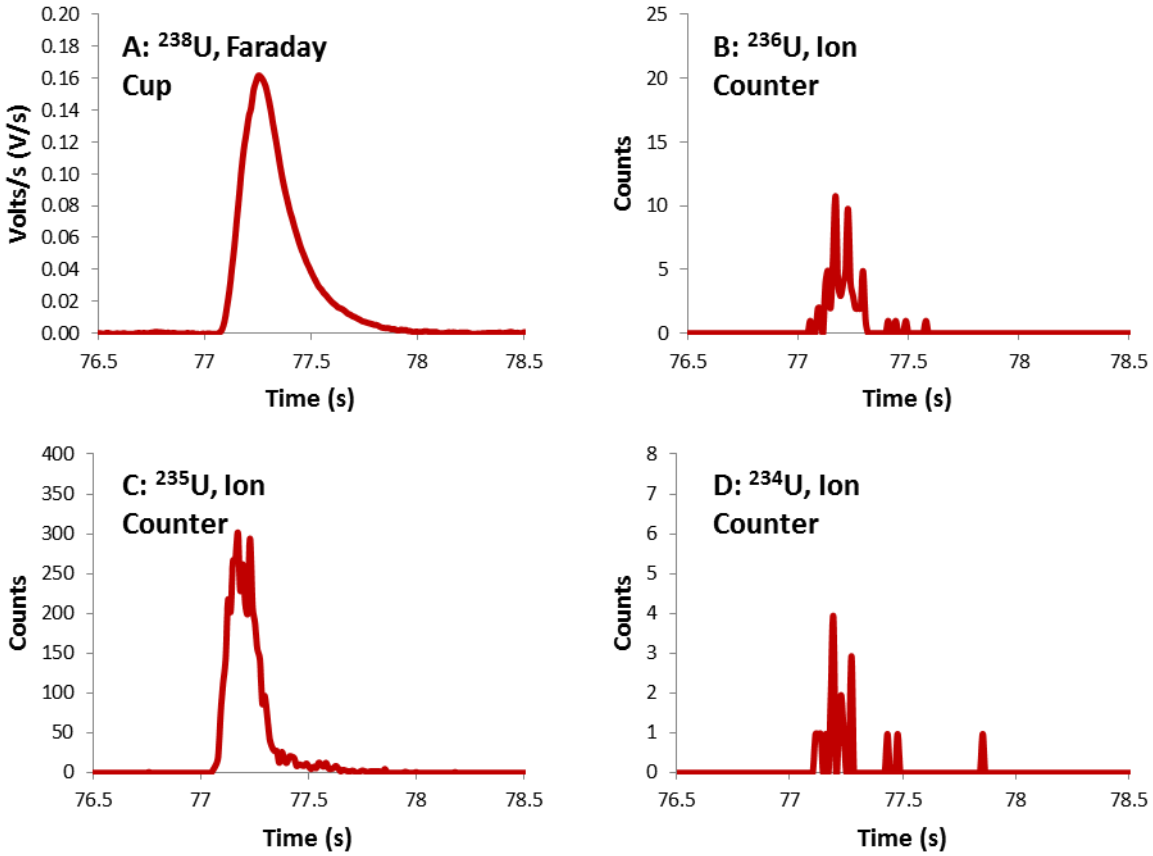

Figure 21 – Pulse profiles of U isotopes for SRM611, Zircon Cell coupling mechanism. Integration time = 8 ms. Laser conditions: Fluence = 6 J cm^{-2}, Spot size = 20 µm, Ablation type – singleshot. A. Pulse profile of ^{238}U, measured on a Faraday Cup, in volts per second. B. Pulse profile of ^{236}U, measured on an ion counter in counts. C. Pulse profile of ^{235}U, measured on an ion counter in counts. D. Pulse profile of ^{234}U, measured on an ion counter in counts.

2.3.2.3 Increase in signal intensity

While it has already been stated above that signal intensity is not the best unit of measurement for comparing between different ICP-MS setups, it is worth noting that with the DCI & Enterprise Cell a small increase in signal intensity was observed. Although the S/N ratio improved fivefold, the amount of extra material transported to the ICP-MS by the DCI & Enterprise Cell relative to the Zircon Cell was a more modest 28%.

2.3.3 Determination of the Detection Efficiency by Laser Ablation

The increase in signal intensity achieved using the DCI & Enterprise Cell was 28%, less than had been expected. The DCI & Enterprise Cell, when used to couple to a single collector ICP-MS, had reported increases of 8-14 fold in single intensity[6], when compared to a single volume ablation cell. To investigate why the increase in signal intensity was less than expected the decision was taken to determine the detection efficiency of each system by laser ablation. Deep craters were ablated into the surface of the SRM 611 by firing 100 shots at a rate of 1 Hz, fluence 6 J cm^{-2}. Spot sizes used varied from 15 to 50 µm, positioned in a geometric pattern to aid identification. The volume of the craters was measured using an Aliconia Imaging InfiniteFocus™ 3D microscope (SN 017010809808) from the Metrology Unit within the School of Mechanical and Manufacturing Engineering at Loughborough University.

The 3D microscope uses the principle of Focus-Variation. It operates by shining a coaxial light beam through the optic and down to the sample surface. The light beam is reflected off the sample surface and back to the optic which contains a digital sensor. To generate 3D images the optic is moved stepwise in the z-axis. At each step the digital sensor measures the sharpness at each location on the surface. The changes in sharpness at each z-position are used to generate 3D images within the microscope software.

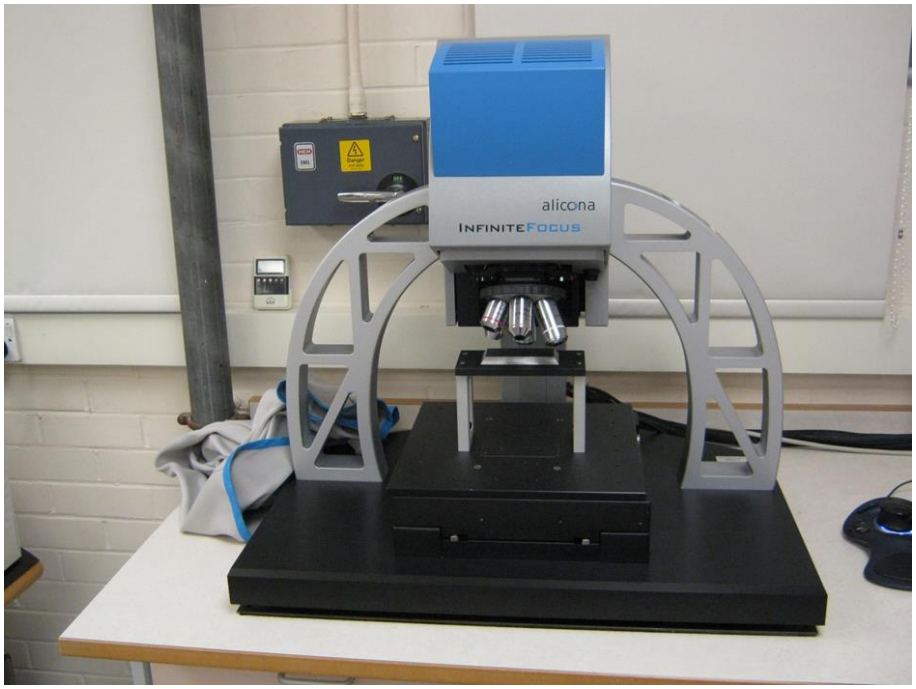

Figure 22 – The Aliconia InfiniteFocus™ 3D Microscope. Samples are placed onto the elevated stage underneath the lenses.

Using a 50x magnification, the vertical resolution of the microscope was set to 20 nm and the lateral resolution to 1 µm. Although the microscope was capable of finer resolution, it is not recommended at the chosen magnification.

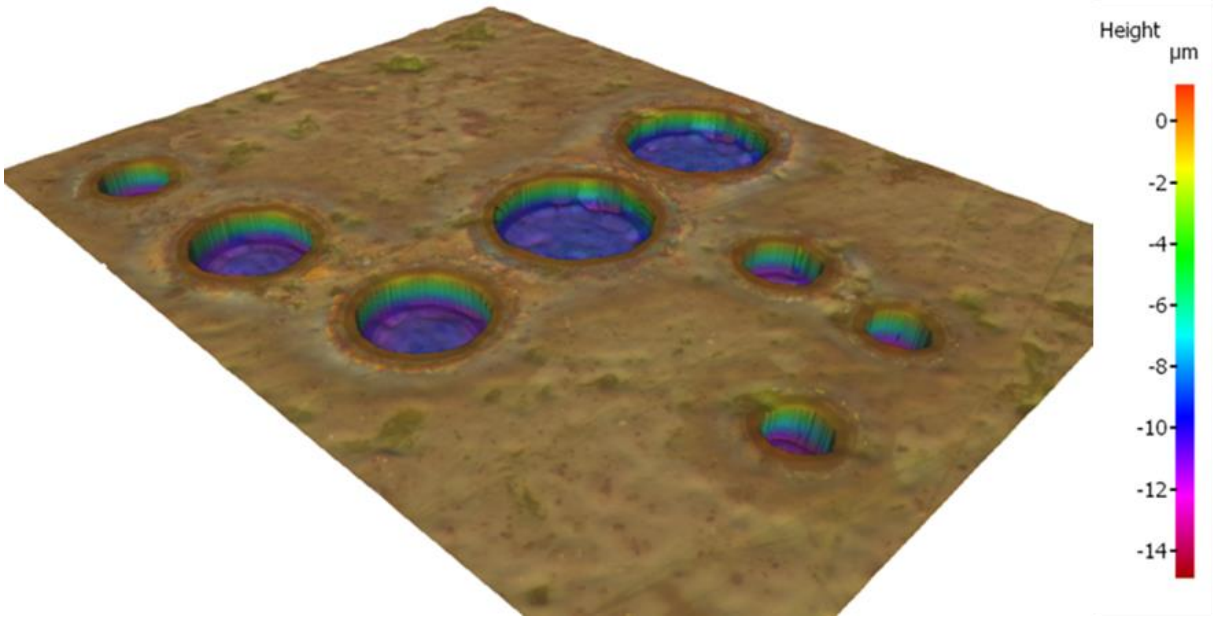

Figure 23 – 3D image of ablated craters (2 x 50 µm, 2 x 35 µm, 2 x 25 µm, 2 x 20 µm) in the surface of SRM611 created with the InfiniteFocus 3D microscope. The area imaged was 286.99 µm by 217.72 µm. The surface plane of the SRM611 glass was set to 0 µm height.

A typical example of the 3D craters is given above. Due to the homogeneous nature of the ArF excimer laser beam the floors of the craters are relatively flat, with smooth high sided walls. Using the software provided with the 3D microscope the volume of each crater and hence the volume of material ablated, was determined. The volume of material ablated (*V*) was used to calculate the mass of material (*m*) ablated as:

$$m = \rho \times V$$

The density (ρ) of SRM611 was calculated from the volume and mass of the bulk material. As the concentration of uranium in SRM611 is known, the mass of uranium was calculated from the total mass of material ablated. The number of atoms of uranium was determined by dividing the mass by the molecular weight of uranium, then multiplying the resulting number of moles by Avogadro's Constant. The known isotopic composition of SRM611 was then used to determine the number of atoms of ^{238}U sampled. The detection efficiency could then be calculated, from the ratio of the number of ions of ^{238}U measured by the MC-ICP-MS to the number of atoms of ^{238}U sampled.

Table 6 – Detection efficiency values of the LA-MC-ICP-MS system for 5 different spot sizes, both DCI & Enterprise Cell and Zircon Cell.

Spot Size	Volume (µm^3)		No. Atoms Sampled		No. Ions Detected		Detection Efficiency (%)	
	DCI & Enterprise	Zircon Cell	DCI & Enterprise	Zircon Cell	DCI & Enterprise	Zircon Cell	DCI & Enterprise	Zircon Cell
50 µm	1.3E+04	1.6E+04	3.7E+10	4.7E+10	1.3E+09	1.1E+09	**3.50**	**2.45**
50 µm	1.3E+04	1.6E+04	3.7E+10	4.5E+10	1.3E+09	1.2E+09	**3.61**	**2.58**
35 µm	6.5E+03	9.4E+03	1.9E+10	2.8E+10	8.8E+08	7.3E+08	**4.63**	**2.67**
35 µm	7.4E+03	9.6E+03	2.2E+10	2.8E+10	8.6E+08	7.4E+08	**4.01**	**2.65**
25 µm	2.4E+03	3.8E+03	6.9E+09	1.1E+10	3.8E+08	3.2E+08	**5.42**	**2.86**
25 µm	3.0E+03	3.5E+03	8.8E+09	1.0E+10	3.9E+08	3.2E+08	**4.44**	**3.09**
20 µm	1.7E+03	2.4E+03	4.8E+09	7.0E+09	2.6E+08	2.0E+08	**5.29**	**2.86**
20 µm	1.7E+03	2.4E+03	5.0E+09	6.8E+09	2.5E+08	2.0E+08	**5.09**	**2.93**
15 µm	7.4E+02	1.1E+03	2.2E+09	3.2E+09	1.4E+08	1.1E+08	**6.32**	**3.59**
15 µm	7.3E+02	1.1E+03	2.1E+09	3.2E+09	1.3E+08	1.1E+08	**6.31**	**3.53**

The difference in detection efficiency between the DCI & Enterprise Cell and the Zircon cell was between 41% and 79%, depending on spot size. Regardless of spot size the improvement in detection efficiency is greater than the 28% improvement in signal intensity reported earlier. The increase was due to a change in ablation volume: despite using the same laser conditions the craters

generated in the surface of SRM611 were shallower (Table 6) when using the DCI & Enterprise Cell compared to the Zircon Cell. This suggests that with the Enterprise Cell a proportion of the laser energy is lost before it reaches the sample surface. The Enterprise Cell, due to its pressurised operating state, has a cell window three times thicker than the Zircon Cell and this could be the cause of the lost energy. Another potential source of energy loss is the Sniffer Cell. The diameter of the laser beam as it passes through the open port in the Sniffer Cell is much wider than the spot size at the sample surface. If the laser beam was not aligned to pass straight through the centre of the open port, part of the laser beam could touch the Sniffer Cell itself. This would reduce the energy of the laser beam which impacts the sample surface.

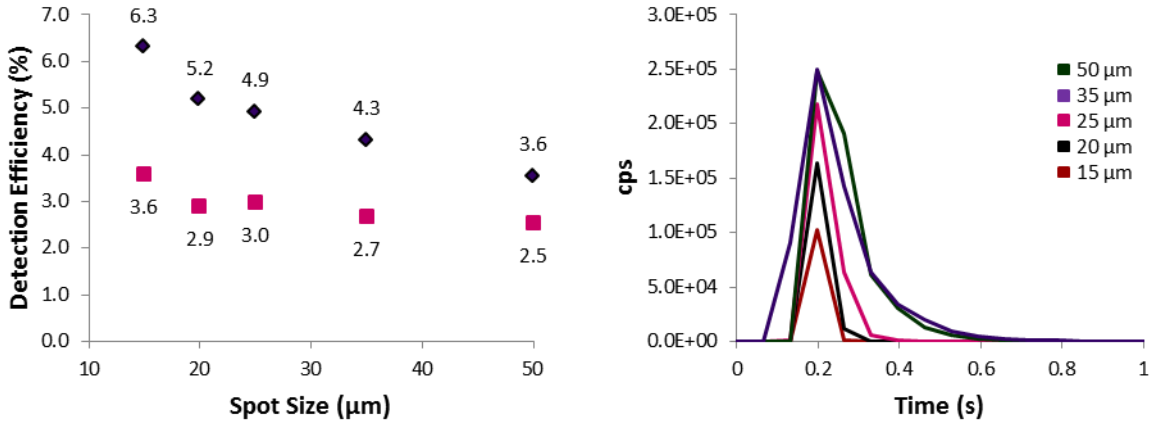

Figure 24 – A. Detection efficiency against spot size for Zircon Cell (Pink) and Enterprise Cell (Purple). B. Typical pulse profiles of different spot sizes on SRM611 using the DCI & Enterprise Cell.

Another feature of the detection efficiency measurement with the DCI/Enterprise Cell is that the determinations vary with spot size (Figure 24A). The Zircon Cell also exhibits the same tendency, but to a lesser degree. A linked phenomenon is an increase in the signal pulse duration with spot size (Figure 24B). Above 25µm the S/N ratio does not improve, but instead additional counts go towards pulse broadening until the performance of the Enterprise Cell begins to mirror that of the Zircon Cell. The cause of the pulse broadening is as yet unknown, but two possible causes can be hypothesised. The first hypothesis is that there is a limit to the particle density which the fused silica can accommodate. In this case the larger spot sizes generate a plume of material which breaches this limit. As a consequence part of the particulate is “held up” in the micro-chamber until the particle density in the tubing drops to allow it to continue towards the ICP. In the other scenario the larger spot sizes are responsible for generating a larger shockwave on ablation. This shockwave is sufficient in magnitude to force part of the particle plume outside of the micro-chamber. In this case the pulse broadening is a representation of the time taken for the particles to return to the micro-chamber from the outer cell. In both cases the detection efficiency will drop. If the particulate is retained

within the micro-chamber losses can occur to the walls of the micro-chamber or redisposition onto the sample surface. If the particulate is ejected from the micro-chamber it is highly unlikely all of the material will be re-entrained, but instead some particles will be lost to the outer cell.

Despite the pulse broadening the detection efficiency of the DCI and Enterprise Cell at 50µm was still equivalent to the best that the Zircon Cell achieved. At lower spot sizes the detection efficiency rapidly increased beyond the 4.0% best maximum previously reported by the manufacturer (Table 4) and on to an efficiency of 6.3% at 15 µm. To confirm such a claim the experiment was subsequently repeated with better than 5.0% achieved consistently. During validation prior to the analysis of the Colonie soil sample (Chapter 7) an average detection efficiency of 7.5% was achieved for a 25 µm spot size. For all spot sizes 25 µm and below the detection efficiency averaged 7%.

2.3.4 Extending the fused silica injector

As reported in the experimental section 2.2.1.1, the DCI has the ability to extend the fused silica injector forward. All the work previously shown was generated with the end of the fused silica flush with the 2.0mm injector used for the sheath gas. It has been reported[6] that extending the fused silica beyond the 2.00 mm injector can improve both the S/N ratio and the signal intensity, which can be obtained with the DCI and Enterprise cell coupling mechanism.

Table 7 – Laser parameters used with the ESI UP-193FX laser ablation system. 30 shots of 20 µm spot size were ablated at the same location, at a rate of 1 Hz.

Parameter	Value
Ablation mode	Single spot
Fluence (J cm^{-2})	6
Repetition rate (Hz)	1
Spot size (µm)	20
Number of shots	30

In order to evaluate the merit of extending the fused silica beyond a position flush with the sheath gas injector, single spots were again ablated into the surface of SRM611. At each location on the SRM611 glass 30 pre-ablation shots were used to condition the surface, followed by 30 analysed shots. For each extension, signal pulses were collected at two different positions on the glass surface. Extending the DCI, as it involved physically touching the injector, could alter the X and Y location of the torch. Therefore after each change in extension, solution was aspirated via the desolvator to check the instrument sensitivity. If required, changes were made to the torch position or sweep gases to restore the instrument sensitivity to its previous value. Over the course of the

experiment, changes of up to 100 µm were required, to both X and Y positions, and 40 ml/min of Ar to the sweep gas. More minor corrections were required for N_2.

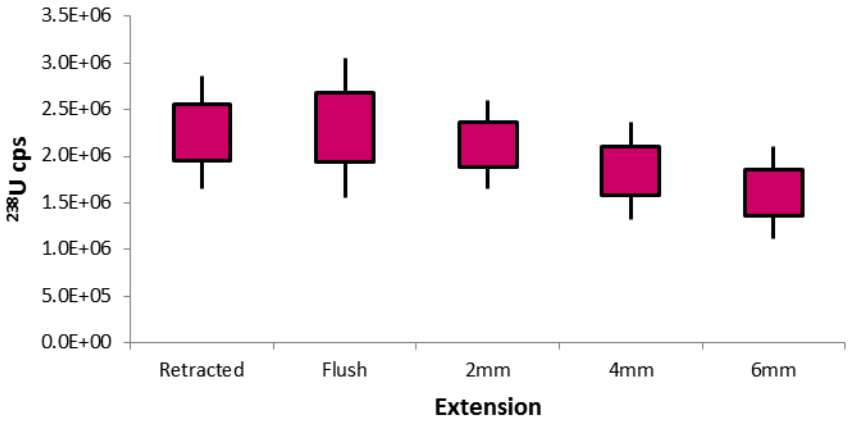

Figure 25 – average ^{238}U counts for 60 shots on SRM 611 at 5 different fused silica extensions. Each box denotes 1RSD and error bars 2RSD.

Five different extensions were tested, flush, 2mm extended, 4mm extended; 6mm extended and retracted back approximately 5mm into the outer injector. Unfortunately extending the fused silica beyond the flush point did not result in any increase in signal intensity, but instead a gradual decline was observed. Interestingly returning the injector to the flush position from 6mm extended did not fully recover the signal intensity previously observed. There is therefore the potential for other effects to be sufficient to mask any changes occurring only from the extension of the fused silica. One possible interfering effect could be the changes to the gas flows within the Enterprise Cell, caused by the reorientation of the sample tray under the Sniffer Cell when moving to a new sampling site. It is also likely that on extension the fused silica tubing goes off axis effecting efficiency, although moving back to the flush point should have restored the tubing to axis.

Although further work would be required to conclude definitively, it is also possible that no improvement in signal intensity may be possible from extending the fused silica. The extension experiment was designed to inject the sample beyond a highly turbulent region which modelling had suggested existed in front of the plasma. However Lindner *et al* (2011)[7] state that the turbulent region is most pronounced at low sample gas flow rates containing a high percentage of He. Further modelling seemed to suggest that at flows above 1.0L min^{-1} recirculation ceased to occur for the injector gas[20]. With the DCI and Enterprise Cell conditions used, neither of those conditions holds and extending the fused silica may only result in reducing the ionisation efficiency of the particles in the plasma.

2.3.5 Comparison between the 'Normal' and 'Jet' Cones

As the diameter of the fused silica injector was far less than the diameter of the sampler cone orifice (250um vs 1.00mm respectively), it was hypothesised that the use of the 'Jet' cones may not contribute greatly to the detection efficiency of the DCI and Enterprise Cell coupling mechanism. Using a 2mm injector to add sample to the plasma, increasing the sampler cone orifice can be expected to increase the proportion of the sample ions 'sampled' by the mass spectrometer interface. However with an injector much narrower than the sampler cone orifice, assuming the sample ions do not diffuse too much in the plasma, the entirety of the sample ions may be captured by the sampler cone. In order therefore to gauge the contribution of the Jet Interface to the detection efficiency, the detection efficiency was calculated using both the 'Normal' sampler and 'Jet' sampler cones.

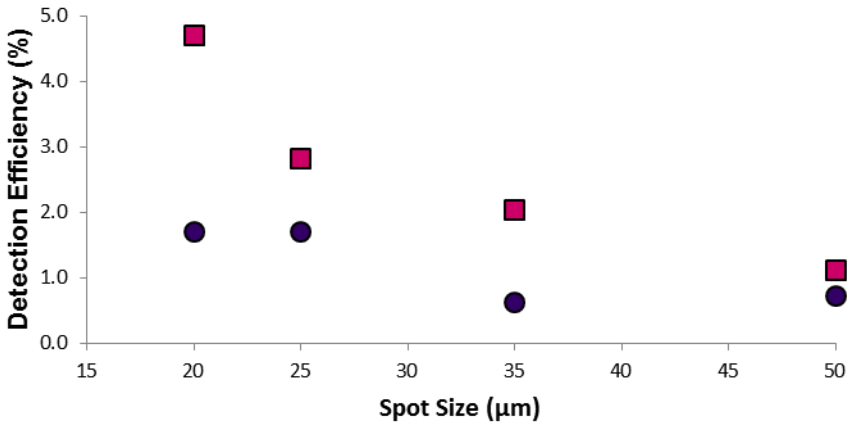

Figure 26 – Detection efficiency against spot size for the Enterprise Cell. A. Jet Cones (Pink Squares) and B. Normal Cones (Purple Circles). All measurements were performed on alternate days, with each reported value an average of two individual replicates.

The detection efficiency with the Jet cones describes the curve shown earlier in the section. However with the Normal Cones the detection efficiency plateaus, with both the 20 and 25 µm spot sizes exhibiting the same value. The Jet Cones have a very large impact on the sensitivity of the interface and were retained for all subsequent experiments.

2.4 Initial Determination of the Uranium Isotope Ratios of NIST SRM611 glass

Before the uranium isotope ratios could be calculated for the single shot ablations of SRM 611 a data evaluation strategy had to be chosen. Kappel *et al* (2013)[21] recently tested and evaluated three different data evaluation strategies for LA-MC-ICP-MS of single uranium particles. These three data evaluation strategies were:

- Point to Point (P2P)
- Linear Regression
- Total Signal Integration (TSI)

The utility of these three data evaluation strategies for the data generated by both the DCI & Enterprise Cell and Zircon Cell were investigated.

2.4.1 Point to Point (P2P) Data Evaluation

The P2P data evaluation strategy is historically the method by which isotope ratios have been determined in ICP-MS. The isotope ratio is determined for each data point (integration) in the signal window of interest and from these values a mean and uncertainty are derived. With the DCI and Enterprise Cell however there is a problem implementing the P2P methodology. As was described earlier with the pulse profiles in section 2.3.2, the pulse profile of ^{238}U, measured on a Faraday cup, is different to the profiles of the minor isotopes, measured on ion counters. As the output of the Faraday cup amplifier response lags behind the input signal, and the ion counter response does not, the isotope ratio changes across the transient signal, a source of error defined as spectral skew. Spectral skew is defined for a single collector mass spectrometer as an error in relative signal levels for several m/z values across a transient signal, that arises from the need to scan a spectrum, while the input sample concentration is changing[22]. Therefore for a single collector ICP-MS spectral skew occurs due to non-simultaneous measurement of the isotopes. However for a multi-collector, simultaneous measurement, mass spectrometer, spectral skew has also been defined as the error on an isotope ratio due to the differences in time taken for each detector to output the input signal, especially with a detector array containing a mixture of Faraday cups and ion counters[23]. This form of spectral skew is present with both the DCI & Enterprise Cell and Zircon Cell however the effect is more pronounced for the new prototype (Figures 20 and 21). Cottle *et al* (2009)[23], when using a similar mixed detector array of Faraday cups and ion counters, noted a 0.15 s delay in the time taken for the Faraday cups to respond to the initiation of signal, relative to the ion counters. If a similar delay were to occur for the pulses generated by the DCI & Enterprise Cell, with average pulse duration of 109ms, the signal on the ion counters would be over before the Faraday cup even begins to register a response and indeed for some pulses this was the case. Furthermore due to the tau decay of the Faraday cup amplifier, when the Faraday cup does respond the pulse generated is over a greater time frame than the input signal mapped by the ion counters. For these reasons the P2P data evaluation strategy is inappropriate to use with the DCI & Enterprise Cell coupling mechanism using MC-ICP-MS.

Although the Zircon Cell is also affected by the same spectral skew which makes the P2P data evaluation strategy inappropriate for the DCI & Enterprise Cell, as the pulse duration is nearly five times greater than its competitor the delay in response of the Faraday cup relative to the ion counters is insufficient to entirely divorce the signal pulse profiles from each other. Unlike the DCI & Enterprise Cell, where the output signal pulse profile using a Faraday cup can be almost entirely attributed to the tau decay of the amplifier, with the Zircon Cell the input signal has a much longer wavelength (*ca.* 500 ms) and makes a much greater contribution to the output signal pulse profile from the Faraday cup amplifier. The output signal pulse profiles from both the ion counters and Faraday cups therefore occur over roughly the same time frame. It was therefore decided that the Zircon Cell could be used to evaluate the performance of the P2P data evaluation strategy. In order to do so 100 individual 20µm laser shots were ablated into the surface of SRM611 (fluence = 8 Jcm^{-2}, integration time = 66ms). Instead of using P2P across the entire duration of the pulse, baseline to baseline, only the main body of the pulse was used. To define the main body of each pulse an integration window was drawn limited to only those data points for which the ^{235}U signal was greater than 5,000 cps. This limit was selected as it was sufficiently great to filter out those values at the beginning of each pulse, where due to the delay discussed above, the Faraday cup had yet to respond.

Table 8 – Uranium Isotope Ratios for SRM611, Zircon Cell, P2P. The average isotope ratios determined are more than twice the reference values for SRM611

Method		**$^{234}U/^{238}U$**	**$^{235}U/^{238}U$**	**$^{236}U/^{238}U$**
P2P	**R_{mean}**	2.196e-05	4.888e-03	9.379e-05
	(RSD)	(42.9%)	(24.0%)	(31.0%)
	RD	132.4%	104.9%	117.4%

The average ratios, R_{mean}, of the 100 pulses are given in Table 8. Also reported are the relative standard deviation (RSD) of the 100 pulses and the relative difference (RD) of the mean to the expected value. The reporting method has been selected to mirror that used in various publications describing the isotope ratio analysis of uranium oxide particles[24–28,21]. For all three ratios both the RSDs and RDs are unacceptably high. In all three cases the reported R_{mean} is more than twice the expected value for SRM611, i.e. the RD is more than 100%.

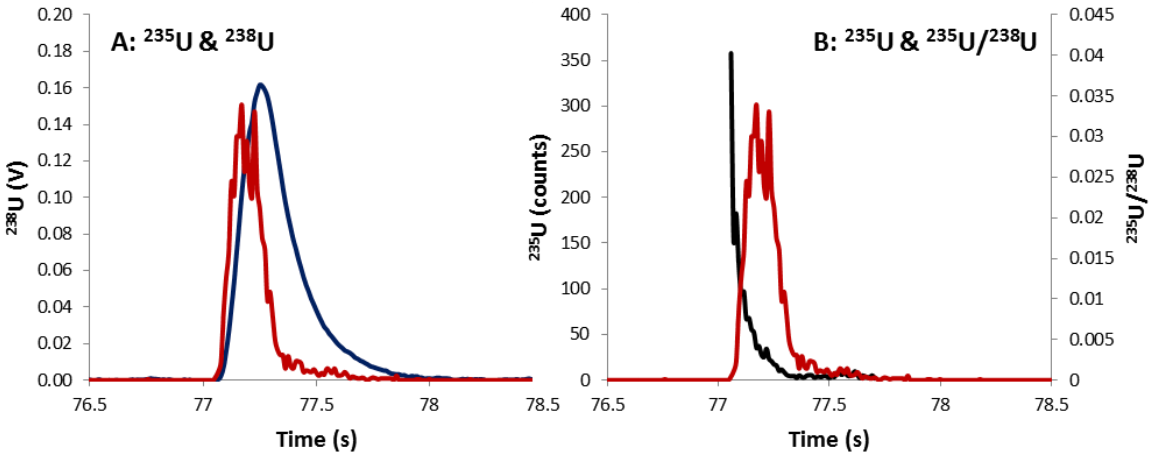

Figure 27 – A. Pulse profiles of ^{235}U & ^{238}U for SRM611, Zircon Cell. Integration time = 8 ms. Laser conditions: Fluence = 6 J cm^{-2}, Spot size = 20 µm, Ablation type – singleshot. B. $^{235}U/^{238}U$ (in black) across the pulse, superimposed on ^{235}U signal pulse profile from Figure 21. The isotope ratio describes a curve across the lifetime of the pulse.

For a uranium oxide particle reference material Kappel *et al* (2013)[21] reported a RD of only 0.5% from the certified value using P2P. In that instance only two isotopes, ^{235}U and ^{238}U, were monitored on Faraday cup detectors. While for the Zircon Cell the ion counters and the Faraday cup signal pulse profiles are similar in duration, the rate at which they respond to the input signal is not. Consequently the two sets of profiles are not in alignment and the corresponding isotope ratios therefore show a trend from high to low values across the pulse. Su *et al* (2014)[29], measuring erbium particle ratios, reported the isotope ratio could not be detected by P2P with a mixed array of detectors.

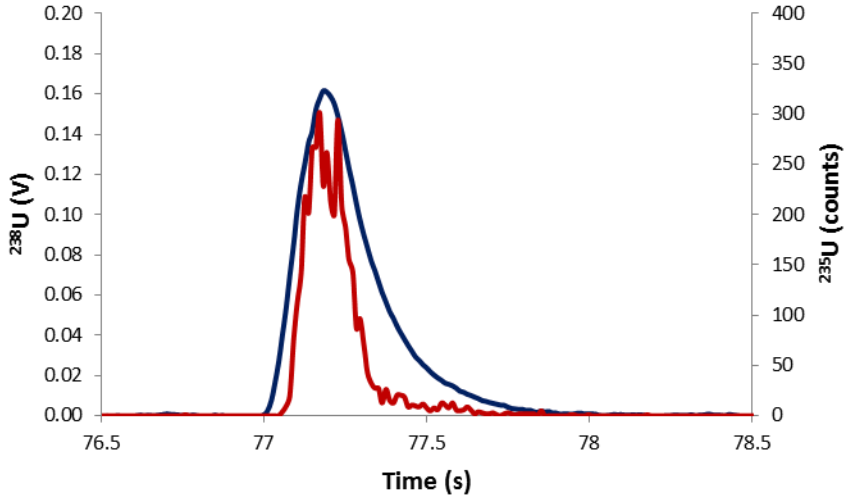

Figure 28 – Pulse profiles of ^{235}U & ^{238}U for SRM611, Zircon Cell. Integration time = 8 ms. Laser conditions: Fluence = 6 J cm^{-2}, Spot size = 20 µm, Ablation type – singleshot. The pulse profile of ^{238}U has been shifted forward in time to better align with the minor isotopes.

One possible solution to the misalignment of the Faraday cup and ion counter signal pulse profiles would be to move the ^{238}U pulse profile forward in time whilst processing the data such that there is better overlap between detector responses. In Figure 28 the pulse profiles from Figure 27A have been brought into better alignment by shifting the ^{238}U signal forward in time. In the data from the 100 laser shots generated earlier, the ^{238}U data were brought forward, first by one 66ms integration and then by two to see if the P2P data evaluation strategy could be improved.

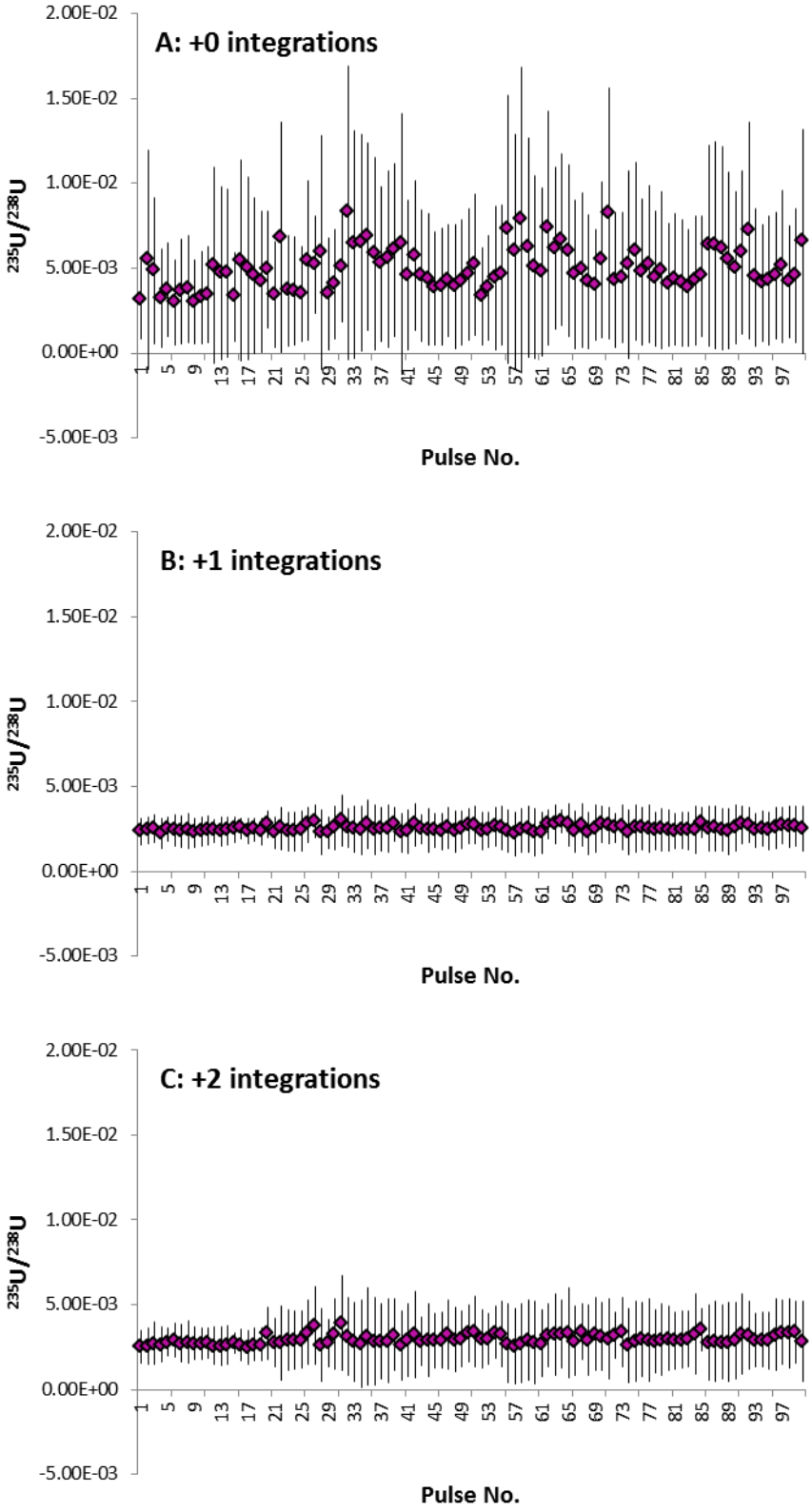

Figure 29 – $^{235}U/^{238}U$ for 100 single pulse calculated by P2P, Zircon Cell, error bars are 1RSD. A. Unaltered P2P. B. ^{238}U brought forward by one 66ms integration. C. ^{238}U brought forward by two 66ms integrations.

Moving the ^{238}U signal forward in time by one integration clearly had a dramatic effect, reducing both the RSD and the RD closer to the true value. Although moving the ^{238}U signal forwards by two

integrations was still an improvement on the original uncorrected version it is an overcorrection when compared to moving the ^{238}U signal forward by one integration.

Table 9 – Uranium Isotope Ratios for NIST611, Zircon Cell, P2P+1integration. Both the RSD and RD are significantly improved over the P2P results in Table 8.

Method		$^{234}U/^{238}U$	$^{235}U/^{238}U$	$^{236}U/^{238}U$
P2P+1integrations	**R_{mean}**	1.069e-05	2.461e-03	4.631e-05
	(RSD)	(20.3%)	(7.0%)	(12.7%)
	RD	13.2%	3.2%	7.4%

While the improvements in both the RSD and RD for P2P+1 (hereafter referring to the dataset where the ^{238}U signal has been moved forward by one integration in time) compared to the original uncorrected P2P are significant, both values are still far greater than what it had been hoped could be achieved, given the instrumentation available.

2.4.2 Linear Regression Data Evaluation

The second data evaluation strategy, linear regression was first developed by Fietzke *et al* (2008)[30] for LA-MC-ICP-MS with the aim of improving the precision, relative to P2P, for the same dataset. In this method the simultaneously collected isotopes are plotted against one another as an x-y scatter plot. When a linear fit is then plotted through the points using the least squared method, the isotope ratio is equivalent to the gradient and, by using the LINEST function in MSEXCEL, the standard error of the gradient can be derived as a measure of the precision.

In time-resolved analysis (TRA) LA-MC-ICP-MS we can split the dataset into two sections:

1. The windows of interest around the sample pulses
2. The remaining background signal.

With the P2P data evaluation strategy only the signal integration windows selected are used when evaluating the data, the parts of the data where only background signal is recorded are discarded. Additionally, all of the data points within the signal integration windows selected are assumed to be statistically equal[30], but the number of counts detected within each integration can vary by several orders of magnitude in TRA. The number of counts has a direct relation on the uncertainty of the isotope ratio determined for each integration. Instead with the linear regression strategy the whole dataset is evaluated; no signal integration windows need to be selected. The linear fit is dominated by the largest signals, heavily weighting the isotope ratio towards those values which should have

the best precision. The included background and low count integrations have little significance on the final isotope ratio.

For our analysis however, linear regression has the same flaw as P2P, it requires simultaneous responses from all of the detectors and therefore is not appropriate for the DCI and Enterprise Cell coupling mechanism.

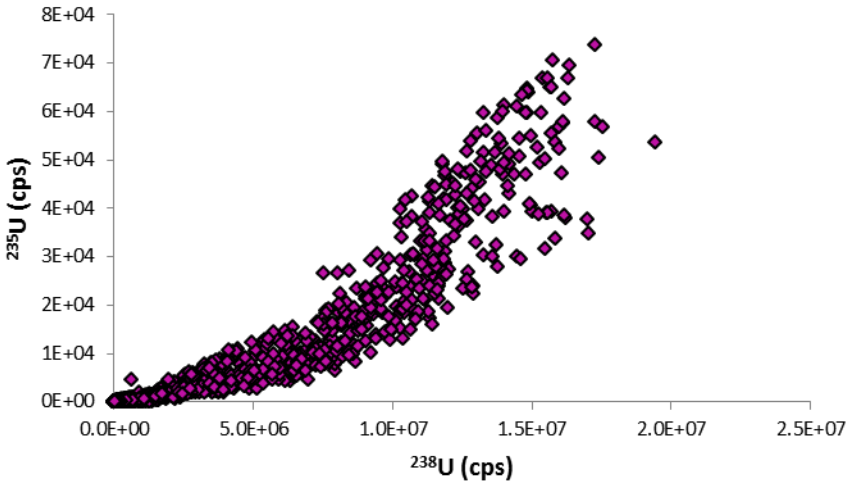

Figure 30 – ^{235}U (cps) plotted against ^{238}U (cps), for 100 single pulses, P2P+1, Zircon Cell. Every integration collected (including baseline) is plotted. The points cannot be fitted onto a single straight line; instead two intersecting lines appeared to be the best fit.

Using the same 100 pulse Zircon Cell dataset from the evluation of the P2P data processing strategy, a plot of ^{235}U against ^{238}U is given above (Figure 30), with again the ^{238}U pulse profile moved forward by 1 integration to bring it more into alignment with the pulse profiles from the ion counters. In the figure, a single linear fit could not be plotted through the data points, but instead it appears there are actually two intersecting linear fits, with the point of crossover at around ten million cps of ^{238}U. The linear fit which best describes low count rate signals is depleted in ^{235}U compared to the bulk composition of SRM611. The other linear fit best describes high count rate signals and is subsequently enriched in ^{235}U relative to the bulk. This reveals that moving the ^{238}U pulse profile has not eliminated all of the spectral skew. Relative to ^{235}U a greater percentage of ^{238}U counts are in the tail of the pulse, as a consequence the apex of the pulse is enriched in ^{235}U, the tail depleted. The RSD of a single linear fit through the data in Figure 30 gives an uncertainty for the determination of ^{235}U/^{238}U of 39.3%, less precise that using the P2P data evaluation starategy, the determination for which had already been discarded as unacceptable.

2.4.2.1 Determination of $^{236}U/^{235}U$ by Linear Regression

Although $^{234}U/^{238}U$, $^{235}U/^{238}U$ and $^{236}U/^{238}U$ could not be measured by linear regression with either the DCI & Enterprise Cell or Zircon Cell, both $^{236}U/^{235}U$ and $^{234}U/^{235}U$ could be measured as the three ICs respond indentically. Due to the greater abundance of ^{236}U than ^{234}U in SRM611, $^{236}U/^{235}U$ was chosen to evaluate the utility of linear regression for an array consisting of similar detectors.

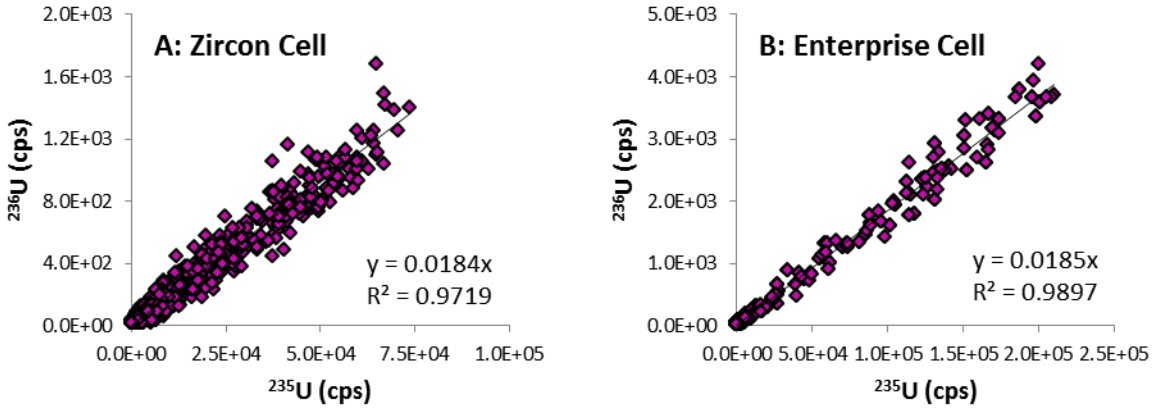

Figure 31 – ^{236}U (cps) plotted against ^{235}U (cps). A. 100 pulses, Zircon Cell. B. 90 pulses, DCI and Enterprise Cell. Laser conditions: Fluence = 6 J cm^{-2}, Spot size = 20 µm, Ablation type – singleshot.

Plotting ^{236}U against ^{235}U for datasets containing multiple single-shot laser ablation pulses on SRM 611, a good linear fit was achieved for both coupling mechanisms. The data collected with the Zircon Cell had a greater degree of scatter, with an RSD of 16.7% compared to 10.0% for the Enterprise Cell, a reflection of the lower S/N ratio achievable with the more conventional coupling mechanism.

Perhaps the largest disadvantage of using the linear regression data evaluation strategy for determining the isotope ratio of single particles is it requires a population of data from which to determine an isotope ratio; in this case more than a single particle. For nuclear particles where the sample material is limited, a crucial composition may be missed due to its low abundance in the whole population and ideally a composition assessment needs to be obtained on each individual particle.

2.4.3 Total Signal Integration (TSI) Data Evaluation

The third data evaluation strategy, total signal integration (TSI) was first applied to the laser ablation of zircons by Johnston *et al* (2009)[31] to eliminate both errors due to laser signal noise and the requirement to correct for U-Pb fractionation. It was further applied to single-shot laser ablation by Cottle *et al* (2009)[23], to correct for the inaccuracies caused by the time-offset between the Faraday cups and ion counters. In this approach the isotope ratios are not calculated for each integration, but are instead calculated from the sum of the total number of counts for each isotope. By summing

from baseline to baseline for each individual isotope the time-offset problems which beset P2P and linear regression are eliminated. Therefore this was the only method which could evaluate the data generated by the DCI and Enterprise Cell. The most significant drawback of TSI is, similar to linear regression; it does not provide uncertainties for each individual isotope measurement[32]; a problem if we wish to report a composition from a single particle.

2.4.3.1 TSI Data Evaluation of Single Shots on SRM611 using the Zircon Cell

To evaluate the TSI data evaluation strategy for the Zircon Cell coupling mechanism, 300 single shot ablations were carried out with SRM611. The laser fluence was 8 J cm^{-2} and the spot size 20µm. The integration time of the mass spectrometer was 66ms. The TSI data evaluation was performed in MSEXCEL.

Table 10 – Mean uranium isotope ratios for 300 single shot ablations with TSI, Zircon Cell.

Method		$^{234}U/^{238}U$	$^{235}U/^{238}U$	$^{236}U/^{238}U$
Zircon Cell	**R_{mean}**	1.04E-05	2.35E-03	4.55E-05
TSI	**(RSD)**	(17.0%)	(1.34%)	(7.66%)
	RD	9.64%	-1.50%	5.29%

Comparing the results in Table 10 to the best data evaluation strategy so far employed (P2P with the ^{238}U signal moved forward by one integration) there was a discernible improvement in each measurement. The greatest improvement was in the RSD of $^{235}U/^{238}U$, reducing from 7.0% to 1.34%. Regardless of its utility to the DCI & Enterprise Cell therefore TSI would still have been the data evaluation strategy of choice for this project.

2.4.3.2 TSI Data Evaluation of Single Shots on SRM611 using the DCI and Enterprise Cell

To evaluate the TSI data evaluation strategy for the DCI & Enterprise Cell, 10 x 30 single shot ablations were carried out with SRM611. The laser fluence was 6 J cm^{-2} and the spot size 20µm. The integration time of the mass spectrometer was 66ms. The TSI data evaluation was performed in MSEXCEL.

Table 11 – Mean uranium isotope ratios for 10x30 single shot ablations with TSI, DCI & Enterprise Cell.

Method		$^{234}U/^{238}U$	$^{235}U/^{238}U$	$^{236}U/^{238}U$
DCI & Enterprise Cell	**R_{mean}**	1.05E-05	2.34E-03	4.56E-05
TSI	**(RSD)**	(14.1%)	(2.93%)	(7.92%)
	RD	10.39	-1.93	5.53

Comparing the results for the two different coupling mechanisms in the two tables (10 and 11) above, some points are worthy of further discussion. The RD for $^{234}U/^{238}U$ and $^{236}U/^{238}U$ were consistently high using both the DCI & Enterprise Cell and Zircon Cell. For the $^{234}U/^{238}U$ ratio the literature is not consistent on a reference value for SRM611. The values used to calculate the RDs of all three isotope ratios were from the most recent publication, comparing MC-ICP-MS, MC-TIMS and SIMS analysis of SRM611[14], however in a previous publication the $^{234}U/^{238}U$ isotope ratio determined for SRM 611 was higher[33]. Using the $^{234}U/^{238}U$ ratio from the previous publication to calculate the RD reduced the measure to 5.60% (DCI & Enterprise Cell), a similar bias to $^{236}U/^{238}U$. However of key importance was despite the improvements in S/N ratio and detection efficiency for the DCI & Enterprise Cell over the Zircon Cell this is not reflected in the isotope ratio analysis. Indeed instead of the expected improvement in precision the RSD of $^{235}U/^{238}U$ for the DCI & Enterprise Cell was more than double the value achieved by the Zircon Cell with the same data evaluation strategy. The RSD of $^{234}U/^{238}U$ was improved by a few percentage points by the new prototype coupling mechanism; the RSD of $^{236}U/^{238}U$ was barely affected. Why the expected improvements in RSD using the DCI & Enterprise Cell failed to materialise, with the possible exception of $^{234}U/^{238}U$, required further investigation.

2.5 Investigation into Sources of Error in TRA LA-MC-ICP-MS

2.5.1 Determination of the Scale of Additional Uncertainty in the System via Counting Statistics

As the DCI & Enterprise Cell had demonstrated a fivefold improvement in S/N ratio alongside a spot size dependant increase in detection efficiency over the Zircon Cell, it was expected the RSD and RD of the $^{235}U/^{238}U$ ratio would be similarly improved. However the opposite proved to be the case with the RSD of $^{235}U/^{238}U$ for the DCI & Enterprise Cell more than double the value achieved for the Zircon Cell. It was inferred therefore that using the DCI & Enterprise Cell coupling mechanism may be introducing a new unexpected source of additional uncertainty into the LA-ICP-MS system.

In order to investigate the source of the additional uncertainty on the $^{235}U/^{238}U$ ratio it was decided to first determine its scale. At first the scale of the additional uncertainty was estimated, by subtracting the RSD achieved with the Zircon Cell from the RSD achieved with the DCI & Enterprise Cell, but this assumed the Zircon Cell uncertainty was unaffected by the new source of additional uncertainty. The possibility that the RSD calculated for the Zircon Cell included a contribution from the source of the additional uncertainty identified with the DCI & Enterprise Cell could not be discounted.

The TSI data evaluation strategy does not provide uncertainties for each individual isotope analysis, however Cottle *et al* (2009)[23] assigned to each isotope ratio a limiting uncertainty, calculated from counting statistics on the minor isotope. Mass spectrometry is subject to a fundamental noise, due to the particulate nature of the matter detected, which cannot be eliminated[34]. This fundamental noise therefore places a limit on the precision which can be achieved. The limit on precision, counting statistics, is due to the random arrival of ions at the detector, and hence is governed by the Poisson distribution. By adopting counting statistics the difference between the expected RSD from the limiting uncertainty and the experimental RSD determined for each coupling mechanism, could be used as an estimate of the scale of the additional uncertainty. To calculate the limiting uncertainty, a Monti Carlo simulation in MATLAB® (MathWorks®, Natick, MA, USA) was used to simulate a random Poisson distribution around the number of counts for each isotope. The determination of the standard deviation for each Poisson distribution was used to calculate the limiting uncertainty on each isotope ratio analysis.

Table 12– Mean uranium isotope ratios for 300 single shot ablations with TSI, Zircon Cell, limiting RSD. The experimental RSD are within 1% of the limiting RSD for all three isotope ratios.

Method		$^{234}U/^{238}U$	$^{235}U/^{238}U$	$^{236}U/^{238}U$
Zircon Cell	R_{mean}	1.04E-05	2.35E-03	4.55E-05
TSI	**(RSD)**	(17.0%)	(1.34%)	(7.66%)
	RD	9.64	-1.50	5.29
	Limiting (RSD)	(16.8%)	(1.11%)	(8.18%)

Table 13– Mean uranium isotope ratios for 10x30 single shot ablations with TSI, DCI & Enterprise Cell, limiting RSD. The experimental RSD for $^{235}U/^{238}U$ is further from the limiting RSD, than for either $^{234}U/^{238}U$ or $^{236}U/^{238}U$.

Method		$^{234}U/^{238}U$	$^{235}U/^{238}U$	$^{236}U/^{238}U$
DCI & Enterprise Cell	R_{mean}	1.05E-05	2.34E-03	4.56E-05
TSI	**(RSD)**	(14.1%)	(2.93%)	(7.92%)
	RD	10.4	-1.93	5.53
	Limiting (RSD)	(15.1%)	(0.99%)	(7.28%)

By subtracting the experimental RSD from the limiting RSD the size of the additional uncertainty on $^{235}U/^{238}U$ can be estimated as 1.94% with the DCI & Enterprise Cell and 0.23% with the Zircon Cell. This suggests that the source of the additional uncertainty on $^{235}U/^{238}U$ is also present with the Zircon Cell, but to a lesser extent. It was noted here that the scale of the additional uncertainty on

$^{235}U/^{238}U$ with the DCI & Enterprise Cell was almost identical to the RD: suggesting the additional uncertainty may be due to a systematic error, a constant bias towards a lower value.

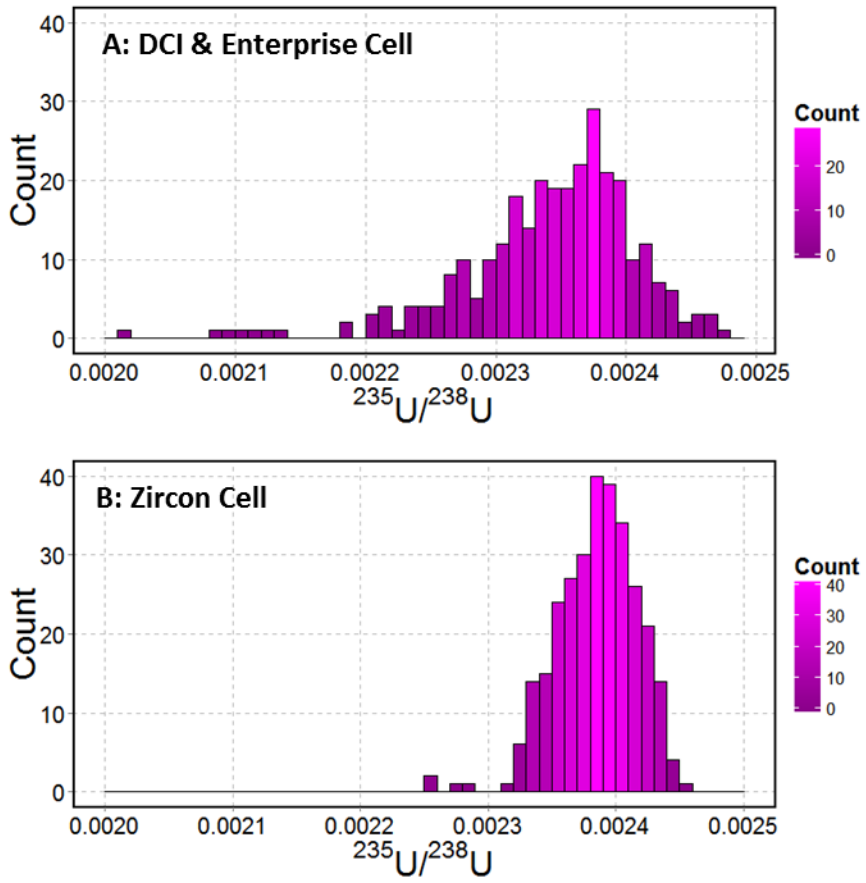

Figure 32 – Histograms of $^{235}U/^{238}U$ for 300 single shot ablations of SRM611. A. DCI & Enterprise Cell. B. Zircon Cell. The Zircon Cell exhibited less scatter around the mean than with the DCI & Enterprise Cell.

Plotting histograms of the $^{235}U/^{238}U$ values for all 300 pulses, both coupling mechanisms, it is clear the distribution with the DCI & Enterprise Cell is not Gaussian, especially when compared to the Zircon Cell. As predicted the deviation from Gaussian behaviour is towards lower $^{235}U/^{238}U$ values, suggesting the additional uncertainty and the bias in the RD have the same source. In Figure 32 the bin widths were kept constant at 1e-05 as was the range at 5e-04. Consequently it is possible to observe the count maxima for both the DCI & Enterprise Cell and Zircon Cell occur simultaneously. If the additional uncertainty could be removed the RD values should be identical for both coupling mechanisms.

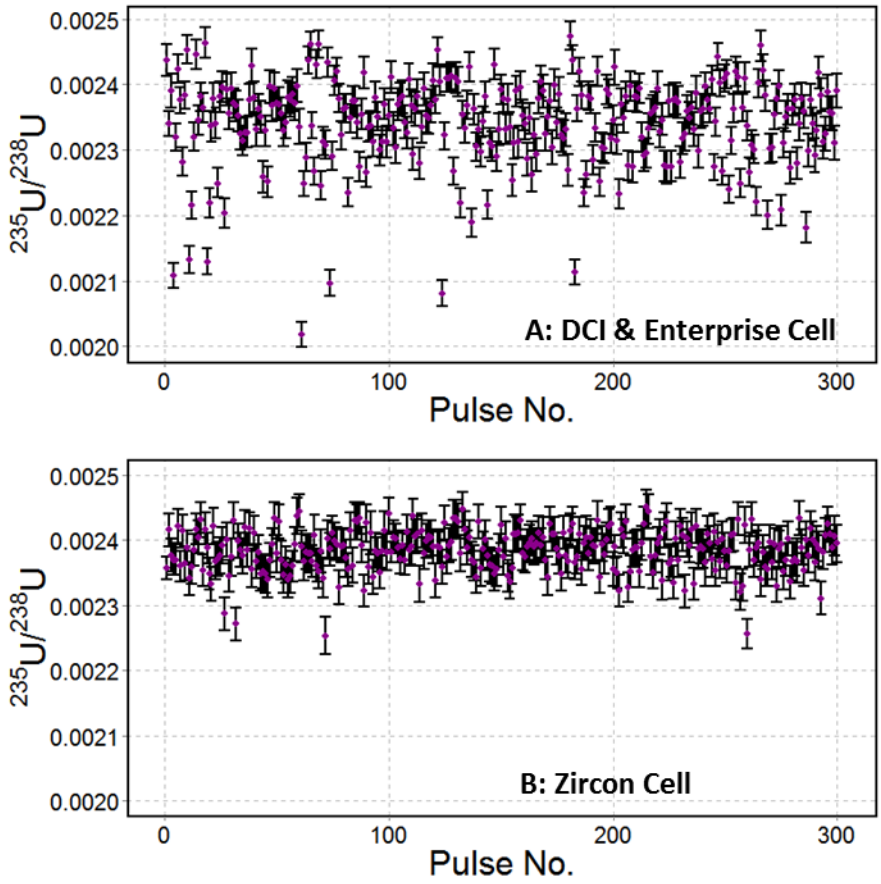

Figure 33 – $^{235}U/^{238}U$ for 300 single shot ablations of SRM611, error bars are 1σ. A. DCI & Enterprise Cell. B. Zircon Cell.

Looking closer at the $^{235}U/^{238}U$ ratios from the Zircon Cell it was determined there was also some tailing to lower $^{235}U/^{238}U$ values. In particular 4 of the 300 pulses gathered had $^{235}U/^{238}U$ ratios which isolated them from the main body of the distribution (Figure 33). Recalculating the RD and RSD values of the dataset with these 4 pulses removed accounted for more than half of the additional uncertainty on the Zircon Cell.

2.5.2 Identification of the Source of the Additional Uncertainty on the Isotope Ratio

Following the estimation of the size of the additional uncertainty on the $^{235}U/^{238}U$ ratio and the identification of an associated bias towards lower $^{235}U/^{238}U$ values, the next step was to try and identify the source of the additional uncertainty. The initial investigation focussed on the dead time of the ion counter used to measure ^{235}U. The number of ^{235}U counts measured was in the range of 8,000 to 15,000 counts, not normally sufficient to cause dead time effects. However with the DCI & Enterprise Cell these counts are delivered to the detector in a short time frame, perhaps only a few milliseconds. It was theorised therefore that at the apex of the pulse the rate at which the ions were delivered to the detector could be sufficient to cause dead time effects.

A scatterplot of ^{235}U against ^{238}U for the 300 TSI pulses (Figure 34) suggested a dead time effect on the ion counter was not responsible for the additional uncertainty. If a dead time effect was to blame the scatterplot would not be expected to match a linear fit, rather the responses would describe a smooth curve with the ^{235}U consistently depressed at higher count rates.

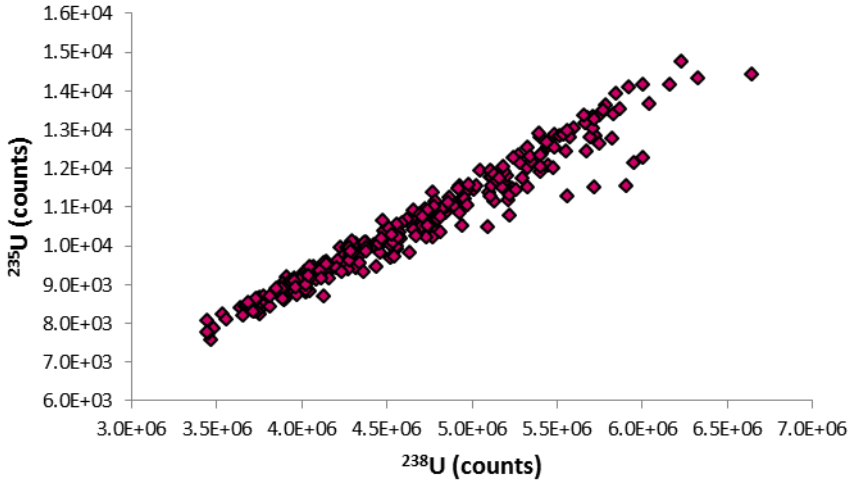

Figure 34 – ^{235}U (counts) plotted against ^{238}U (counts) for 300 TSI single shot ablations, DCI & Enterprise Cell.

In Figure 34 a significant number of the pulses fell below what was an otherwise strong linear trend in the data, suggesting the ^{235}U signal had been suppressed in those pulses. As these "suppressed" pulses seemed to occur more frequently at higher ^{238}U counts this seemed to suggest that the error was count rate dependent. In order to protect the ion counters the MC-ICP-MS is set to deflect away the signal to the ion counters if the signal intensity rises at a rate greater than 2,000 counts per millisecond (cpms) and it was theorised that the increase in S/N ratio achieved with the DCI & Enterprise Cell was great enough to allow the ^{235}U signal to breach this limit causing short duration 'trips' of the ion counters. The ablation of samples containing enriched uranium (see chapter 4) had certainly managed to breach this limit; however in doing so it was observed that when the ion counter "trips" the suppression of the ^{235}U signal was two orders of magnitude greater than that which had been observed for SRM611 and the suppression occurred on every ion counter. The difference in magnitude between the additional uncertainty under investigation and that which an ion counter trip would introduce, suggested this could not be the cause of the additional uncertainty. Unless there is another, softer, protective measure on the ion counters of which the author is not aware, the ion counter alone could not be responsible for the additional uncertainty.

2.5.3 Blind Time – A New Source of Additional Uncertainty for TRA MC-ICP-MS

The initial focus on the ion counter dead time and trip mechanism was due to the assumption that any error from poor ion counter and Faraday cup alignment had been eliminated by using TSI. Further work suggested this may not necessarily be true.

Instead of the 66ms integration time selected in the software, outputs were either 68ms or 69ms apart; an average extra time of 2.4ms added on to each integration. With the DCI & Enterprise Cell D. Douglas (2013)[6] had reported a similar discrepancy with the Element XR™ single collector ICP-MS. In the case of the single collector ICP-MS the extra time was due to the fly-back time of the electrostatic analyser voltage, but in the case of the MC-ICP-MS the electrostatic analyser voltage is fixed during the analysis.

By exporting the chart recorder built into the instrument panel of the MC-ICP-MS it was possible to get more information. The output of each integration was in three sections; a main 59ms section; a secondary 7ms section and the final 2 or 3ms residual time. When using the 8ms integration time the breakdown was; a 7ms main section; a 1ms secondary section and 3 or 4ms residual time.

An explanation of all three sections and how they relate to the system error was sourced[35]. During operation the Faraday cups generate an analogue current. In the Neptune Plus the current is digitized using voltage to frequency conversion (by an analogue-to-digital converter (ADC)). In this application rather than encoding the size of the signal the change in the signal is encoded instead (this removes any quantisation error). The current from the Faraday is therefore converted into a stream of digital pulses. For volt level signals on the Faraday the pulses occur at a frequency in the kHz range. If measured within a fixed time window in the millisecond range the next pulse could occur either in or outside of the window, limiting the precision to an integer unit per mille. To achieve the precision required the timing to a subsequent pulse needs to be measured against a fast, MHz, clock. It is this fast clock measurement which occurs in the secondary section of the integration. Once this section is complete a new integration can begin. However in order to actually begin the next integration the next pulse must be detected in order to start the clock. It is the delay in waiting for the next pulse on each channel which is responsible for the extra time, known here as “blind time”. During blind time the mass spectrometer is dead; no signal is recorded, on either the Faraday cups or ion counters. With the 66ms integration time, signal is being detected 96.5% of the time: at 8ms this drops to 71.6%.

The mechanism outlined above is ideal for applications where the signal is roughly steady and where the detectors respond over a similar timeframe. For extremely fast transient signals, such as those created by the DCI & Enterprise Cell, especially using a mixed array of Faraday cups and ion counters, blind time is a problem. In effect we do not have total signal integration as a significant part of the signal is missing.

To judge the effect of the blind time on the $^{235}U/^{238}U$ ratio for the DCI & Enterprise Cell and Zircon Cell 30 pulses for each coupling mechanism were merged to create an 'average' pulse profile for each isotope. The software Igor Pro (version 6.36, Wavemetrics, Oregon, USA) was used to calculate equations of curves which fitted to each pulse profile. The log-normal curves were fitted to each pulse profile in an iterative process; the software tried various unknown curve coefficients, determining the chi-squared of the fit each time. The output curve coefficients belonged to the curve fit which had the lowest chi-squared value.

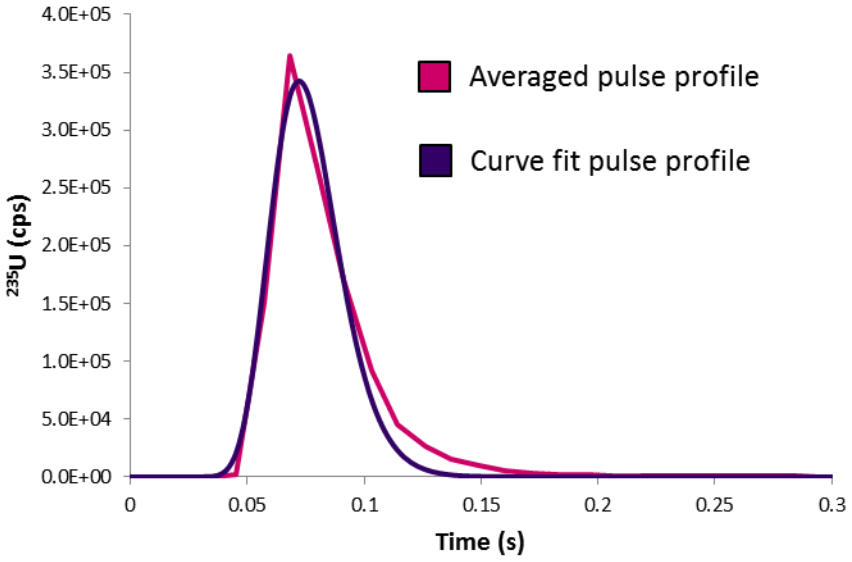

Figure 35 – Pulse profile of ^{235}U, created by averaging 30 experimental profiles on SRM 611, DCI & Enterprise Cell (pink). Pulse profile of ^{235}U created from the equation fitted to the averaged pulse profile by Igor Pro (purple).

Placing values of x (time) from 0 to 1 second into the equations from the curve fit, in intervals of 3 milliseconds, the pulse profiles were recreated as if the integration time selected on the mass spectrometer was 3ms. Assuming the blind time is equivalent also to 3 milliseconds, the number of counts lost if the blind time occurs at any point can be read.

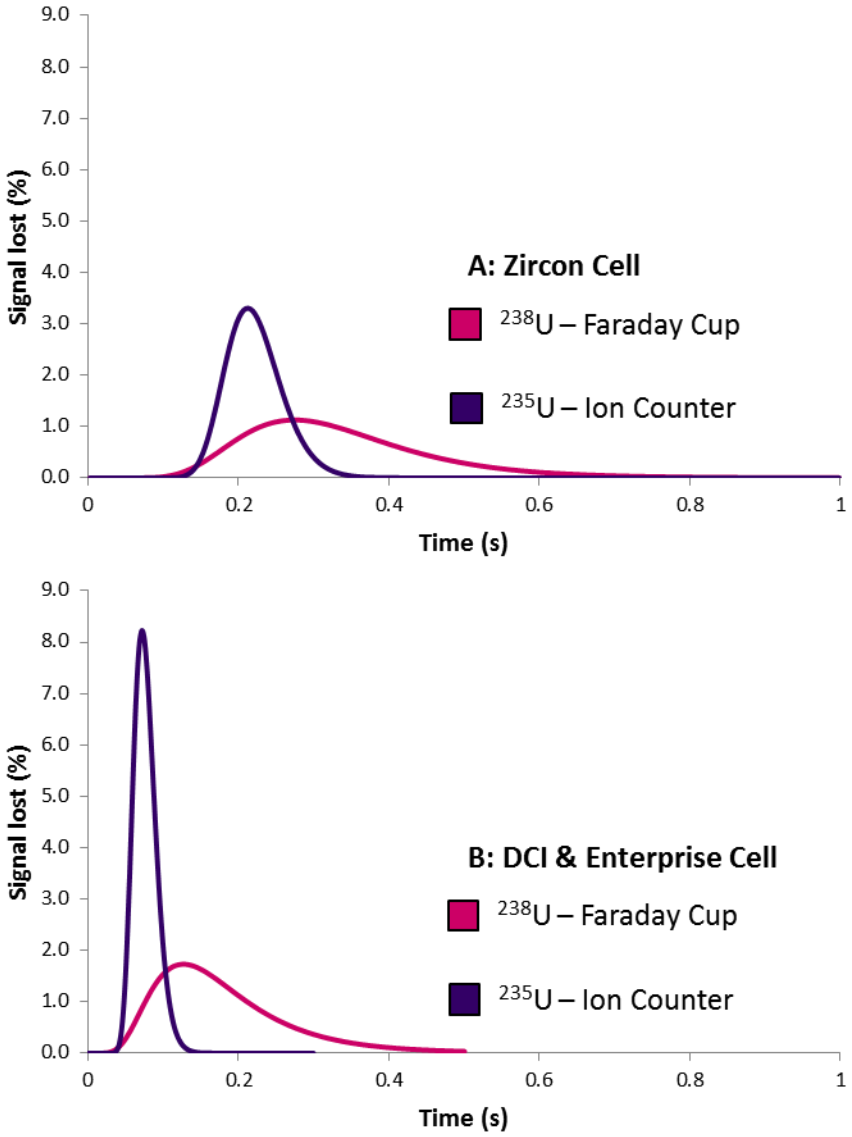

Figure 36 – A. Plot of percentage of signal lost to blind time against time for ^{238}U (pink) and ^{235}U (purple), Zircon Cell. B. Plot of percentage of signal lost to blind time against time for ^{238}U (pink) and ^{235}U (purple), DCI & Enterprise Cell.

In Figure 36 is given the percentage of total signal which would be lost if blind time was to occur at that particular moment in time. If the blind time were to occur at the apex of the pulse signal on the ion counter 8.2% of the total signal would be lost with the DCI & Enterprise Cell. With the Zircon Cell the maximum amount of signal which can be lost in a single blind time event is less, 3.3%. With both coupling mechanisms the proportion of ^{235}U signal which can potentially be lost in a single blind time event is greater than the corresponding loss on ^{238}U, due to the tau response of the Faraday detector.

The percentage of total signal which can potentially be lost in a single blind time event is greater on the ion counters than the Faraday cups, however with e.g. a 66ms integration time, as the integration time is less than the duration of the pulse, more than one blind time effect can occur

over the lifetime of the pulse. For a theoretical 66ms integration time the amount of signal lost was determined by adding together the percentage of signal lost for individual blind time events 66ms apart.

For the 66ms integration time the percentage of total signal lost using the Zircon Cell ranged: on the ion counter from 4.24% to 4.46% and on the Faraday cup from 4.36% to 4.35%. Due to the narrow range of signal which can be lost, on both types of detector, the model suggests the additional uncertainty contribution from blind time was only 0.08% RSD for the Zircon Cell. With the DCI & Enterprise Cell for the same 66ms integration time the percentage of total signal lost ranged: on the ion counter from 0.96% to 8.26% and on the Faraday cup from 4.29% to 4.40%. As the range of total signal which can be lost is wider for the DCI & Enterprise Cell, the additional uncertainty from blind time is correspondingly greater; 2.63% according to the model. The value from the model is broadly similar in size to the additional uncertainty of 1.93% reported in section 2.5.1. One final feature of the model is it predicts that, given the range of counts which can be lost in a given measurement, the DCI & Enterprise Cell will have some signals which are biased towards an enriched $^{235}U/^{238}U$ composition as well as having some biased towards low $^{235}U/^{238}U$. Examining the histograms of $^{235}U/^{238}U$ in Figure 32 does reveal some pulses which may exhibit this behaviour.

It was stated earlier in the chapter that using the 8ms integration data with the DCI and Enterprise Cell, 99% of the total signal collected on the ion counters was contained in a pulse duration of about 60ms. This is slightly less than the 66ms integration time used to collect the 300 shots demonstrated earlier. It is therefore also possible that almost the entire number of counts from the laser pulse could be captured within a single integration. For such a case no ^{235}U will be lost to blind time. According to the model a consistent percentage of the ^{238}U signal captured on the Faraday cup would be lost in the blind time, resulting in a slight consistent bias towards higher $^{235}U/^{238}U$ isotope ratios.

For the DCI & Enterprise Cell as the pulse duration measured on the ion counter averages about 60ms the ^{235}U signal is contained in at most two integrations. By measuring the proportion of signal contained in the 1^{st} integration relative to the whole and comparing to the isotope ratio, an indication can be made of the bias introduced by the blind time effect.

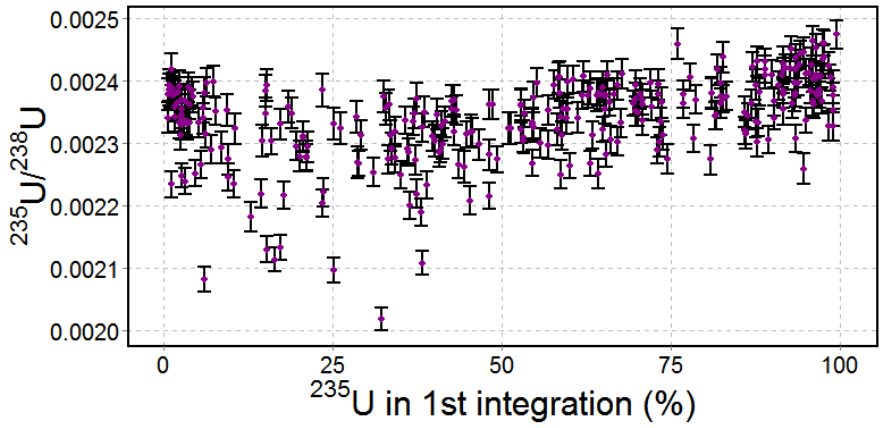

Figure 37 – $^{235}U/^{238}U$ plotted against the proportion of ^{235}U in the first integration (%). 300 single shot ablations of SRM611, DCI & Enterprise Cell, 66ms.

At either end of the plot (Figure 37), where almost all of the counts are contained within a single integration, the pulses are tightly grouped either around or above the expected value of 0.00239. Moving in towards the centre of the plot, where the measured ^{235}U counts are more evenly distributed between the two integrations, the $^{235}U/^{238}U$ ratios become more widely scattered and are biased towards depleted values. This behaviour is consistent with blind time being the source of the additional uncertainty in the data for the DCI and Enterprise Cell. At the far right of the plot, where nearly 100% of the ^{235}U signal is in the 1st integration, the average $^{235}U/^{238}U$ ratio is higher than the expected composition and the average composition at the far left of the plot where most of the signal is in the 2nd integration. This is likely due to the shape of the pulse profile; as the shape is log-normal rather than normal, if the blind time occurs near the front of the pulse a greater proportion of ^{235}U counts are lost than if it occurs in the tail.

After establishing the most probable source of the additional uncertainty with the DCI & Enterprise Cell coupling mechanism the next step was to try and either reduce or eliminate the blind time effect from the method. The most satisfactory and complete way to achieve this goal would be to change the way the MC-ICP-MS outputs integrations such that the blind time effect cannot occur. However this would require hardware modifications to the mass spectrometer which could not be achieved within the time remaining in the project. As time was limited the next best approach suggested was to increase the integration time. By increasing the integration time the frequency at which the ^{235}U signal would be affected by blind time would be reduced. On the MC-ICP-MS the available integration times under one second are 8ms, 66ms, 131ms, 262ms and 524ms. To investigate, further experiments, each consisting of 300 single shot ablations on SRM611, were carried out using each of the five integration times available.

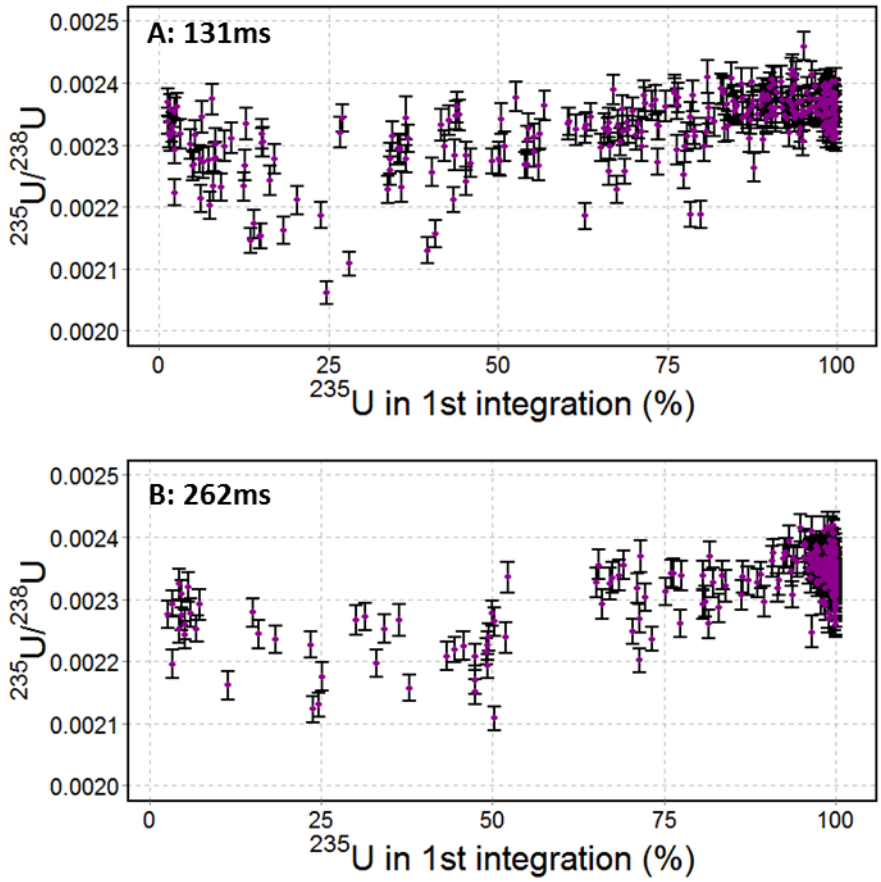

Figure 38 – $^{235}U/^{238}U$ plotted against the proportion of ^{235}U in the first integration (%). 300 single shot ablations of SRM611, DCI & Enterprise Cell. A. 131ms. B. 262ms.

By doubling the integration time to 131ms the number of blind time events should be halved for a fixed period of time. Choosing a threshold of 80% of the counts in the 1st integration, the number of acceptable pulses was only 84 out of 300 with the 66ms integration time. Indeed with the 131ms integration time the number of acceptable pulses increased to 159 and to 236 acceptable pulses with the 262ms integration time. As the number of blind time-afflicted pulses decreased there was a corresponding improvement in precision for $^{235}U/^{238}U$. Returning to the model of blind time behaviour, doubling the integration time to 131ms halved the proportion of ^{238}U counts lost on the Faraday cup due to blind time. If the ion counter signal is unaffected by blind time, every count lost on the Faraday cup signal should cause a bias towards an enriched $^{235}U/^{238}U$ ratio relative to the expected composition. Increasing the integration time should therefore improve both the accuracy and precision of the isotope ratio analysis. Although this would indicate a desire for the integration time to be as long as possible, increasing the integration time also decreases the S/N ratio and makes it harder to resolve signal pulses for separate particles. Of the five integration times tested 131ms and 262ms appeared to offer the best compromise between reducing the blind time effect while still keeping sufficient S/N ratio and ability to resolve signal pulses for individual particles.

Although increasing the integration time reduced the frequency of blind time effects, they were not removed completely. The next approach was to filter the data based on the proportion of counts in the 1st integration. Lacking a mathematical model[35], a reasonable limit of 80% of the ^{235}U counts in the 1st integration was selected based on the plots generated.

Table 14 – Mean uranium isotope ratios of SRM611, DCI & Enterprise Cell. Of the 300 pulses collected, only pulses with more than 80% of the ^{235}U counts in the 1st integration were used.

Method	n = 159	$^{234}U/^{238}U$	$^{235}U/^{238}U$	$^{236}U/^{238}U$
DCI & Enterprise Cell	R_{mean}	1.05E-05	2.34E-03	4.56E-05
TSI, 131ms	**(RSD)**	(15.2%)	(1.18%)	(7.56%)
	RD	9.86	0.02	8.19
	Limiting (RSD)	(14.8%)	(0.96%)	(7.02%)

By removing those pulses deemed to have been affected most by blind time the $^{235}U/^{238}U$ RSD was reduced in-line with the Zircon Cell, but at the cost of discarding almost half of the pulses collected. With a rare and important particle sample, where only a few particles may be indicative of an entire composition, such a rate of loss would not be acceptable.

2.6 Conclusion

Compared to the Zircon Cell, the DCI & Enterprise Cell prototype coupling mechanism achieved a fivefold improvement in S/N ratio by accelerating the transportation of the ablation plume to the torch. A smaller but significant improvement in detection efficiency, spot size depending, was also achieved, with over 5% of the atoms sampled being detected as ions by the mass spectrometer. The previous best reported detection efficiency with the Neptune *Plus™* MC-ICP-MS for uranium was 4%, by the manufacturer. The increased speed of transportation came at the cost of exaggerating the different response times of the Faraday cups and ion counters to the input ion signal. This limited the data evaluation strategy available to the DCI & Enterprise Cell to total signal integration. Using TSI requires that for a single particle an associated uncertainty cannot be reported for the isotope ratio, except by calculation from counting statistics. During isotope ratio analysis of single shot pulses of SRM611 an additional source of uncertainty (blind time) was identified for both coupling mechanisms. The magnitude of the additional uncertainty was significantly greater for the DCI & Enterprise Cell relative to the Zircon Cell. Modelling of the blind time effect suggested a way by which the impact could be reduced for a series of analysis, although the potential effect on any single analysis could not be removed. A method to screen out analysis which had been strongly

affected by blind time was developed at the cost of filtering out close to half of the pulses which had been collected.

Table 15 - Mean uranium isotope ratios of SRM611 for both the DCI & Enterprise Cell and Zircon Cell. The best results achieved with both coupling mechanisms, from Tables 9 and 13, are reported.

Method	n = 159	$^{234}U/^{238}U$	$^{235}U/^{238}U$	$^{236}U/^{238}U$
DCI & Enterprise Cell	**R_{mean}**	1.05E-05	2.34E-03	4.56E-05
TSI, 131ms	**(RSD)**	(15.2%)	(1.18%)	(7.56%)
	RD	9.86	0.02	8.19
	Limiting (RSD)	(14.8%)	(0.96%)	(7.02%)
	n = 300			
Zircon Cell	**R_{mean}**	1.04E-05	2.35E-03	4.55E-05
TSI, 66ms	**(RSD)**	(17.0%)	(1.34%)	(7.66%)
	RD	9.64	-1.50	5.29
	Limiting (RSD)	(16.8%)	(1.11%)	(8.18%)

Contrasting and comparing the best performance of both coupling mechanisms (Table 15) it is possible to conclude the DCI & Enterprise Cell has not achieved the improvements in accuracy and precision it was hoped new ultrafast laser ablation cells could achieved over current low-volume, single-volume ablation cells. Even discounting the complicating factor of blind time, the limiting uncertainties show the improvement in detection efficiency with the DCI & Enterprise Cell has not been large enough to merit a significant reduction in RSD over the Zircon Cell. For most systems an improvement in detection efficiency is not required to improve the precision, merely improving the S/N ratio is sufficient. The close agreement of the RSDs from the Zircon Cell to the calculated limiting uncertainty shows that any improvements gained by increasing the S/N ratio are minimal at best. This is due to the very low noise (essentially only dark noise) for the uranium isotopes with the LA-MC-ICP-MS system used. Measuring background on ^{235}U with the Zircon Cell averaged 0.026 counts per second, or one count every 38 seconds. For an isotope ratio analysis where the background noise was elevated then the DCI & Enterprise Cell with its higher S/N ratio could prove to be much more effective than the Zircon Cell, provided the additional uncertainty from blind time could be overcome.

2.7 References

1. H. A. O. Wang, D. Grolimund, C. Giesen, C. N. Borca, J. R. H. Shaw-Stewart, B. Bodenmiller, and D. Günther, *Anal. Chem.*, 2013, **85**, 10107–10116.

2. S. J. M. Van Malderen, J. T. van Elteren, and F. Vanhaecke, *J. Anal. At. Spectrom.*, 2015, **30**, 119–125.

3. D. Bleiner and D. Gunther, *J. Anal. At. Spectrom.*, 2001, **16**, 449–456.

4. D. Autrique, A. Bogaerts, H. Lindner, C. C. Garcia, and K. Niemax, *Spectrochim. Acta Part B At. Spectrosc.*, 2008, **63**, 257–270.

5. H. Lindner, D. Autrique, C. C. Garcia, K. Niemax, and A. Bogaerts, *Anal. Chem.*, 2009, **81**, 4241–4248.

6. D. N. Douglas, PhD Thesis, Loughborough University, 2013.

7. H. Lindner and A. Bogaerts, *Spectrochim. Acta Part B At. Spectrosc.*, 2011, **66**, 421–431.

8. A. J. Managh, presented in part at the 12th European Workshop on Laser Ablation, London, July, 2014.

9. *Product Specifications Thermo Scientific Jet Interface*, Thermo Scientific PS30222-E01/11G, Thermo Fisher Scientific, Bremen, 2010.

10. *Inductively Coupled Plasma Spectroscopy and its Applications*, ed. S. J. Hill, Blackwell Publishing, Oxford, 2nd edn., 2007.

11. K. Newman, *J. Anal. At. Spectrom.*, 2012, **27**, 63–70.

12. J. Neuhoff, *Certificate of Analysis CRM 112-A Uranium (normal) Metal Assay and Isotopic Standard*, New Brunswick Laboratory, Argonne IL, 2010.

13. J. Neuhoff, *Certificate of Analysis CRM U010 Uranium Isotopic Standard (5 mg Uranium as U_3O_8)*, New Brunswick Laboratory, Argonne IL, 2008.

14. M. Zimmer, W. Kinman, A. Kara, and R. Steiner, *Minerals*, 2014, **4**, 541–552.

15. M. S. A. Horstwood, G. L. Foster, R. R. Parrish, S. R. Noble, and G. M. Nowell, *J. Anal. At. Spectrom.*, 2003, **18**, 837–846.

16. S. E. Jackson, *SC40: Laser Ablation ICP-MS in the Earth Sciences: Current Practices and Outside Issues*, ed. P. Sylvester and R. Raeside, Mineralological Association of Canada, Vancouver, 2008, pp. 169–188.

17. C. H. Ebert, PhD Thesis, Iowa State University, 2012.

18. *Neptune Plus Multicollector ICPMS, Another step ahead in MC-ICP-MS*, Thermo Scientific BR30197-E01/12G, Thermo Fisher Scientific, Bremen, 2011.

19. T. Pettke, F. Oberli, A. Audétat, U. Wiechert, C. R. Harris, and C. A. Heinrich, *J. Anal. At. Spectrom.*, 2011, **26**, 475–492.

20. M. Aghaei, H. Lindner, and A. Bogaerts, *Spectrochim. Acta Part B At. Spectrosc.*, 2012, **76**, 56–64.

21. S. Kappel, S. F. Boulyga, L. Dorta, D. Günther, B. Hattendorf, D. Koffler, G. Laaha, F. Leisch, and T. Prohaska, *Anal. Bioanal. Chem.*, 2013, **405**, 2943–2955.

22. Z. Hu, Y. Liu, S. Gao, S. Xiao, L. Zhao, D. Günther, M. Li, W. Zhang, and K. Zong, *Spectrochim. Acta Part B At. Spectrosc.*, 2012, **78**, 50–57.

23. J. M. Cottle, M. S. A. Horstwood, and R. R. Parrish, *J. Anal. At. Spectrom.*, 2009, **24**, 1355–1363.

24. S. Bürger and L. R. Riciputi, *J. Environ. Radioact.*, 2009, **100**, 970–976.

25. S. Richter, H. Kühn, Y. Aregbe, M. Hedberg, J. Horta-Domenech, K. Mayer, E. Zuleger, S. Bürger, S. Boulyga, A. Köpf, J. Poths, and K. Mathew, *J. Anal. At. Spectrom.*, 2011, **26**, 550–564.

26. M. Kraiem, S. Richter, H. Kühn, and Y. Aregbe, *Anal. Chim. Acta*, 2011, **688**, 1–7.

27. C.-G. Lee, D. Suzuki, Y. Saito-Kokubu, F. Esaka, M. Magara, and T. Kimura, *Int. J. Mass Spectrom.*, 2012, **314**, 57–62.

28. P. Lach, J. Mercadier, J. Dubessy, M.-C. Boiron, and M. Cuney, *Geostand. Geoanalytical Res.*, 2013, **37**, 277–296.

29. S. Yongyang, W. Wei, L. Zhiming, D. Hu, Z. Guoqing, X. Jiang, and R. Xiangjun, *J. Anal. At. Spectrom.*, 2014, **30**, 1184–1190.

30. J. Fietzke, V. Liebetrau, D. Gunther, K. Gurs, K. Hametner, K. Zumholz, T. H. Hansteen, and A. Eisenhauer, *J. Anal. At. Spectrom.*, 2008, **23**, 955–961.

31. S. Johnston, G. Gehrels, V. Valencia, and J. Ruiz, *Chem. Geol.*, 2009, **259**, 218–229.

32. A. Gourgiotis, S. Bérail, P. Louvat, H. Isnard, J. Moureau, A. Nonell, G. Manhès, J.-L. Birck, J. Gaillardet, C. Pecheyran, F. Chartier, and O. F. X. Donard, *J. Anal. At. Spectrom.*, 2014, **29**, 1607–1617.

33. A. M. Duffin, G. L. Hart, R. C. Hanlen, and G. C. Eiden, *J. Radioanal. Nucl. Chem.*, 2013, **296**, 1031–1036.

34. D. C. Baxter, I. Rodushkin, and E. Engstrom, *J. Anal. At. Spectrom.*, 2012, **27**, 1355–1381.

35. N. Lloyd, J. Schwieters, C. Bouman, Personal Communication.

Chapter 3 – Utilisation of the Geometric Mean for Isotope Ratio Analysis

3.1 Introduction

This chapter describes the advantages and necessity of calculating isotope ratios by geometric distribution rather than the conventional arithmetic distribution. A basic mathematical rationale will be outlined for replacement by the geometric distribution of the arithmetic distribution and the advantages explained by application to experimental data. The potential for incorporating the geometric mean into common LA-ICP-MS data handling software is also discussed.

3.2 Disadvantages of the Arithmetic Distribution to Isotope Ratio Analysis

To calculate the mean isotope ratio (R_{mean}) for a series of data points the sum of the values is determined and then divided by the number of samples, represented by the following equation[1]:

$$\bar{r} = \frac{1}{n}\sum_{i}^{n}\frac{x_i}{y_i}$$

This is commonly known as the arithmetic mean. Alongside the arithmetic mean was reported the associated uncertainty, calculated from the standard deviation (SD) via[2]:

$$\sigma = \sqrt{\frac{1}{n-1}\sum_{i}^{n}\left(\frac{x_i}{y_i} - \bar{r}\right)^2}$$

These two functions (the arithmetic distribution functions) together describe a dataset which is normally distributed. This distribution is commonplace in isotope ratio analysis, both in geochronology and nuclear forensic applications. It is however, not without its problems. All of the isotope ratios reported so far have had the minor isotope as the numerator and the major isotope as the denominator, e.g. $^{234}U/^{238}U$, $^{235}U/^{238}U$ and $^{236}U/^{238}U$. But, what if the values were compared to another dataset where the major isotope was the numerator?

Table 16 - Uranium Isotope Ratios for SRM 611, Zircon Cell, P2P+1integration, n=100. Recalculated as $^{238}U/^{235}U$ and $^{238}U/^{236}U$. Arithmetic Distribution.

Method		$^{235}U/^{238}U$	$^{236}U/^{238}U$	$^{238}U/^{235}U$	$^{238}U/^{236}U$
P2P+1	**R_{mean}**	2.46e-03	4.63e-05	4.82e+02	2.92E+04
Arithmetic	**(RSD)**	(7.0%)	(12.7%)	(9.9%)	(30.0%)
	RD	3.2%	7.4%	15.0%	26.1%

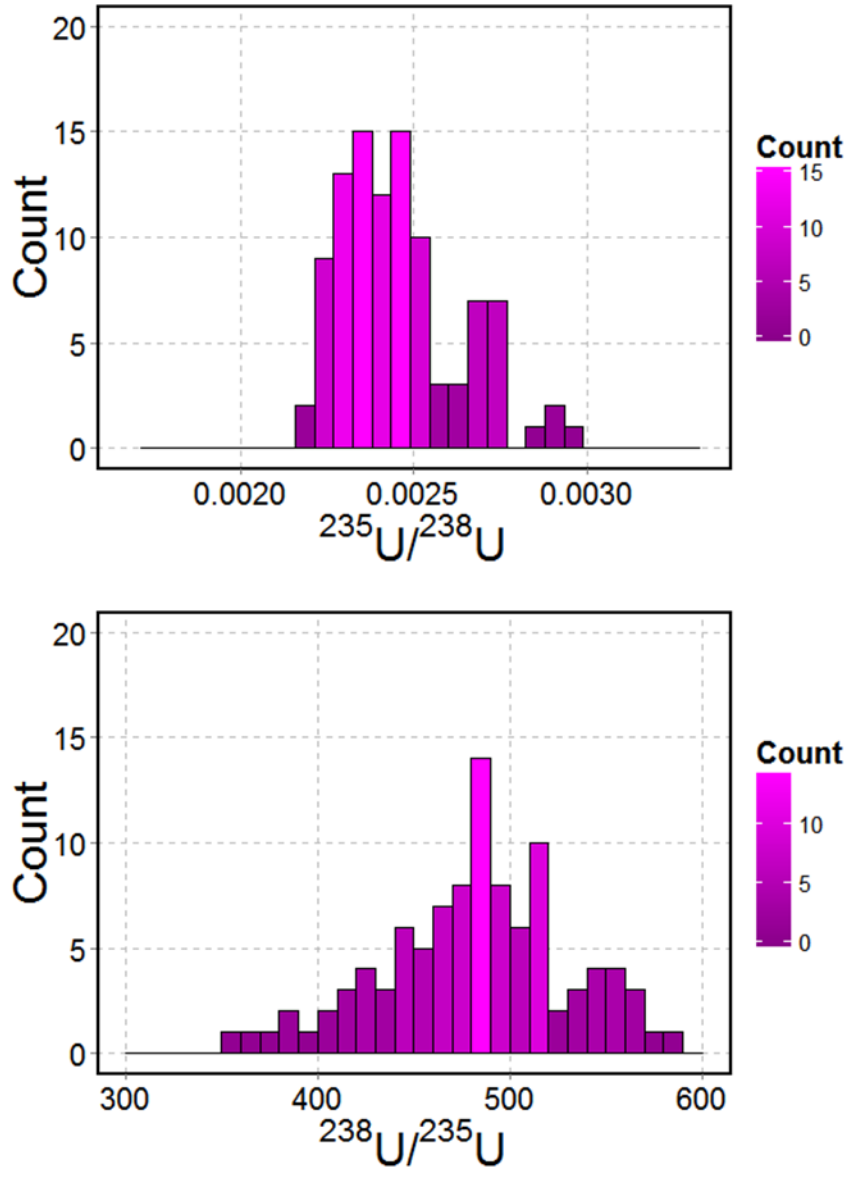

Figure 39 – Histograms of $^{235}U/^{238}U$ and $^{238}U/^{235}U$ for SRM611, Zircon Cell, P2P+1integration, n=100, arithmetic distribution. The range of both histograms was selected to be equivalent. Bandwidths are the range/30.

To show the consequences of swapping the numerator and denominator in isotope ratio analysis a dataset from Chapter 2 (100 single pulses on SRM 611, section 2.4.1, Zircon Cell, data evaluation

strategy = P2P, ^{238}U signal moved forward in time by one integration) was taken and recalculated with ^{238}U as the numerator. Ideally $^{238}U/^{235}U$ and $^{238}U/^{236}U$ should be the inverse of $^{235}U/^{238}U$ and $^{236}U/^{238}U$ but, the values of RD in Table 16 highlight that, using the dataset selected, this is not true. Not only were the RD values changed by switching the order of the isotopes; the RSD's had been similarly altered (Figure 39). An extra source of uncertainty has now been introduced to the isotope ratio analysis as it is unclear which set of results are correct, if indeed either set is truly representative of the isotopic composition. Improving the precision of the data reduces the difference, both in RD and RSD between the two ways of reporting an isotope ratio, but does not remove it entirely.

Another issue with the arithmetic distribution is best illustrated with datasets with RSD's greater than 50%. When quoting an arithmetic mean and RSD we are assuming that the distribution of values around the mean is Gaussian. However plotting the distribution of an *isotope ratio* arithmetic mean with a RSD greater than 50%, the distribution predicts some of the isotope ratio values would have been negative, an impossibility. This suggests the real distribution of isotope ratio values cannot actually be Gaussian. These two factors best illustrate why another way of reporting isotope ratios is required.

3.3 Compositional Analysis and Definitions of Distance

The two problems highlighted above come from failing to realise that isotope ratio analysis operates under a constraint[3]. As the isotope ratios describe a compositional data set the sum of all of the fractional components is equal to 1, or 100%. It is this constraint which makes the arithmetic distribution invalid for isotope ratio analysis. A full explanation as to why was provided by Aitchison for the geological community[4–8], but, as much of this explanation is for concepts not required in this work, and has still not been implemented for isotope ratio analysis to its fullest extent, a brief synopsis is included below.

3.3.1 Isotope Ratios as a Composition

In uranium isotope ratio analysis we primarily wish to look at three isotope ratios, $^{236}U/^{238}U$, $^{235}U/^{238}U$ and $^{234}U/^{238}U$. For a real sample we cannot simply look at any one of the isotope ratios in isolation, as they share the same denominator and therefore a relationship exists between them. Indeed in this case a closed number system can be assumed i.e. addition of all the isotopes will arrive at 100% of the uranium in the system[4]. There are therefore 10 possible different *components* to compare including ^{234}U, ^{235}U, ^{236}U, ^{238}U, $^{236}U/^{238}U$, $^{235}U/^{238}U$ and $^{234}U/^{238}U$ in this closed *set*. To compare these *components,* their analysis must take place in a metric space, a space where the

distance between the *components* is defined. The most familiar metric space is the Euclidean space (see Glossary). The same definitions of *distance* which apply to miles and kilometres should therefore also apply to the counts from the uranium isotopes. Only equations (functions) which describe a metric space can be used to analyse isotope ratio data.

3.3.2 The Definitions of Distance

In a closed *set* the functions used must have a statistical distance which is scalar in order to be considered valid. There are five criteria which must be passed in order for the statistical distance to be considered scalar[5].

1. Positivity.
   $f(x,y) > 0$ if x and y are not equivalent.
2. Zero difference between equivalent compositions.
   $f(x,y) = 0$ if $x = y$.
3. Interchangeability of compositions.
   $f(x,y) = f(y,x)$.
4. Scale Invariance.
   $f(ax,ay) = f(x,y)$ for every $a > 0$.
5. Triangular Inequality.
   $f(x,y) + f(y,z) \geq f(x,z)$.

Of the criteria listed above, the functions which describe the arithmetic distribution approach to calculating isotope ratios, only satisfy one of the five criteria. To satisfy criterion 3, the interchangeability of compositions, it must be possible to swap x and y and still achieve the same outcome. The experimental example reported in Table 16 and Figure 39 confirm the arithmetic distribution functions do not satisfy the interchange of x and y when calculating isotope ratios. This reason alone is sufficient to confirm the functions which describe an arithmetic distribution should not be used in isotope ratio analysis.

To satisfy the first criterion, positivity, none of the functions used can output a negative value. None of the individual isotope ratios calculated will ever have a negative value, however trying to fit an arithmetic distribution to an isotope ratio mean near zero with a high uncertainty can predict negative values. This prediction is an outcome of the normal distribution on which the arithmetic functions are based assigning probability over all real numbers, positive and negative[3].

To meet the criterion of scale invariance multiplying both x and y by the same value should have no impact on the output of the function. This is the one of the five criteria which the arithmetic

distribution satisfies for isotope ratio analysis as multiplying both the numerator and denominator by the same value does not affect the final result.

For the 2nd criterion, zero difference between equivalent compositions, the output of all of the functions must be equal to 0 if x is equal to y. For an isotope ratio calculated using the arithmetic mean if x and y are equivalent then the isotope ratio will be equal to 1, not 0.

The final criterion, triangular inequality, is the principle that there are no short cuts. In Euclidean space the sum of the two shortest sides of a triangle is always greater or equal to the longest side; the shortest distance between two points is always achieved by drawing a straight line between them. For our analysis if we assign ^{238}U as x, ^{235}U as y and ^{236}U as z, to satisfy triangular inequality the sum of $^{238}U/^{235}U$ and $^{235}U/^{236}U$ must be greater or equal to $^{238}U/^{236}U$. Using the R_{mean} values for the same dataset in section 3.2 the sum of 480 and 53 should be greater than or equal to 29,000. As 533 is less than 29,000 using the arithmetic distribution functions for isotope ratio analysis triangular inequality is not upheld.

3.3.3 The Geometric Distribution

As the arithmetic distribution does not describe a metric space for isotope ratio analysis, Aitchison (1984)[4] suggested that the log-ratio transformation, the geometric distribution, should be used instead. The mean of an isotope ratio in the geometric distribution is determined by:

$$\tilde{r} = \frac{1}{n}\sum_{i}^{n}(|\ln x_i - \ln y_i|)$$

The associated standard deviation (SD) is calculated via:

$$= \sqrt{\frac{1}{n-1}\sum_{i}^{n}(|\ln x_i - \ln y_i|)^2}$$

Unlike the arithmetic distribution, for isotope ratio analysis the geometric distribution is able to pass all five criteria to successfully define the distance and describe a metric space. The geometric, or log-normal, distribution can only describe positive real values and so meets the first criterion required. The 2nd criterion, zero difference between equivalent compositions is also met by the geometric distribution functions; if *x* is equal to *y* then the output from the function is zero.

Table 17 – Uranium Isotope Ratios for NIST611, Zircon Cell, P2P+1integration. Recalculated as $^{238}U/^{235}U$ and $^{238}U/^{236}U$. Geometric Distribution.

Method		$^{235}U/^{238}U$	$^{236}U/^{238}U$	$^{238}U/^{235}U$	$^{238}U/^{236}U$
P2P+1	**R_{mean}**	6.092	10.109	6.092	10.109
Geometric	**(RSD)**	(8.3%)	(17.0%)	(8.3%)	(17.0%)
	RD	5.4%	5.8%	5.4%	5.8%

For the 3rd criterion, the interchangeability of composition, recalculating $^{235}U/^{238}U$, $^{236}U/^{238}U$, $^{238}U/^{235}U$ and $^{238}U/^{236}U$ for the dataset in section 3.2 with the log-ratio transformation demonstrates x and y are now interchangeable with the geometric distribution. For the mean the outcome could be predicted from the function as:

$$\frac{1}{n}\sum_{i}^{n}(|\ln x_i - \ln y_i|) = \frac{1}{n}\sum_{i}^{n}(|\ln y_i - \ln x_i|)$$

$$\frac{1}{n}\sum_{i}^{n}(|\ln x_i - \ln y_i|) = \frac{1}{n}\sum_{i}^{n}(\lfloor -1(-\ln y_i + \ln y_i)\rfloor)$$

$$\frac{1}{n}\sum_{i}^{n}(|\ln x_i - \ln y_i|) = \frac{1}{n}\sum_{i}^{n}(|\ln x - \ln y_i|)$$

The geometric mean can be recovered from the log-ratio transformed values by taking the exponential of (-)R_{mean}, 2.261e-03 for $^{235}U/^{238}U$ and 4.073e-05 for $^{236}U/^{238}U$. As the log-normal distribution is more representative of the true scatter in isotope ratio analysis the RD has been improved by using the geometric mean. The RSD did not improve, but instead fell between the two extremes reported for the arithmetic distribution.

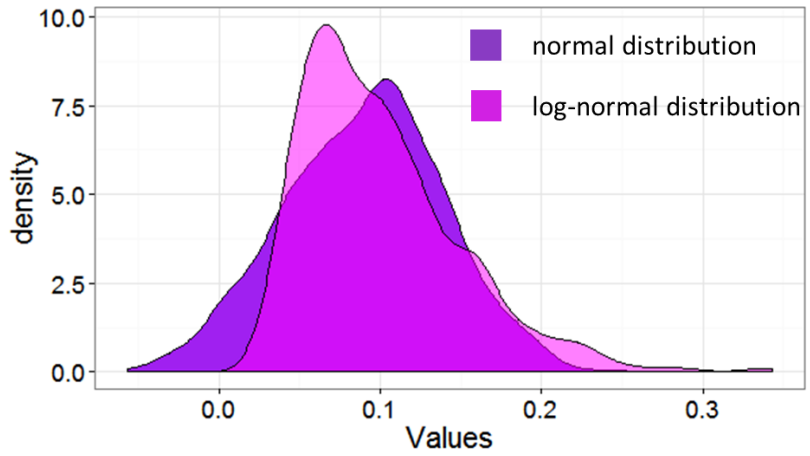

Figure 40 – Examples of a normal and log-normal distribution, produced by Monte Carlo simulation in R.

For the log-transformed data it is correct to only report a single RSD value (Table 17) as the log-transformation of a log-normal distribution produces a normal distribution[9]. However when the log-transformed data is converted back into arithmetic values, in order to keep the log-normal distribution, two RSD (one negative and one positive) values must be reported. In future all results will be reported with –RSD and +RSD. For high precision isotope ratio data the difference between the –RSD and +RSD is small such that the distribution would also fit a Gaussian profile. Even very good fits to a Gaussian distribution can be considered log-normal[9].

For similar reasons to the arithmetic distribution, the geometric mean meets the 4th criterion, scale invariance for isotope ratio analysis. The final criterion, triangular inequality, is met by the geometric mean as:

$$\frac{1}{n}\sum_{i}^{n}(|\ln x_i - \ln y_i|) + \frac{1}{n}\sum_{i}^{n}(|\ln y_i - \ln z_i|) \geq \frac{1}{n}\sum_{i}^{n}(|\ln x_i - \ln z_i|)$$

$$\frac{1}{n}\sum_{i}^{n}(|\ln x_i - \ln y_i + \ln y_i - \ln z_i|) \geq \frac{1}{n}\sum_{i}^{n}(|\ln x_i - \ln z_i|)$$

$$\frac{1}{n}\sum_{i}^{n}(|\ln x_i - \ln z_i|) \geq \frac{1}{n}\sum_{i}^{n}(|\ln x_i - \ln z_i|)$$

The geometric mean satisfies the condition of triangular inequality for isotope ratios as the sum of $f(x,y)$ and $f(y,z)$ is equal to $f(x,z)$. As the sum of $f(x,y)$ and $f(y,z)$ is equal to $f(x,z)$ the means (but not RSDs) of isotope ratios can be determined algebraically from the means of other

isotope ratios. For example the isotope ratio $^{236}U/^{235}U$ can be found by subtracting $^{238}U/^{236}U$ from $^{235}U/^{238}U$.

3.3.4 Covariance and Correlation

As stated above, the three isotope ratios $^{236}U/^{238}U$, $^{235}U/^{238}U$ and $^{234}U/^{238}U$ form part of a *set*. As such the ratios shouldn't be treated in isolation as a relationship exists between them. Both covariance and correlation can be used to test the strength of a relationship between two variables[1]. More correctly a numerical index, the correlation coefficient, *r*, is defined which can have values from -1 to 1. By definition *r* is a measure of how good *X* is at predicting *Y*[2].

$$r = \frac{\operatorname{cov}(X, Y)}{\sqrt{\operatorname{var}(X)\operatorname{var}(Y)}}$$

A value of +1 indicates a perfect positive correlation, -1 a perfect negative correlation and 0 no correlation. Calculating *r* requires the covariance value for the two distributions*, cov (X, Y)*, and also denoted σ_{xy}. This is calculated by[10]:

$$\operatorname{cov}(X, Y) = \sum_{i=1}^{n} \frac{(X_i - \bar{X})(Y_i - \bar{Y})}{n - 1}$$

The covariance and variance values are often reported in a covariance matrix. For $^{236}U/^{238}U$, $^{235}U/^{238}U$ and $^{234}U/^{238}U$ the matrix is:

$$\begin{bmatrix} {}^{234}\mathrm{U}/{}^{238}\mathrm{U} \\ {}^{235}\mathrm{U}/{}^{238}\mathrm{U} \\ {}^{236}\mathrm{U}/{}^{238}U \end{bmatrix} \begin{bmatrix} \sigma_{^{234}\mathrm{U}/^{238}\mathrm{U}} & \sigma_{^{234}\mathrm{U}/^{238}\mathrm{U},^{235}\mathrm{U}/^{238}\mathrm{U}} & \sigma_{^{234}\mathrm{U}/^{238}\mathrm{U},^{236}\mathrm{U}/^{238}\mathrm{U}} \\ \sigma_{^{234}\mathrm{U}/^{238}\mathrm{U},^{235}\mathrm{U}/^{238}\mathrm{U}} & \sigma_{^{235}\mathrm{U}/^{238}\mathrm{U}} & \sigma_{^{235}\mathrm{U}/^{238}\mathrm{U},^{236}\mathrm{U}/^{238}\mathrm{U}} \\ \sigma_{^{234}\mathrm{U}/^{238}\mathrm{U},^{236}\mathrm{U}/^{238}\mathrm{U}} & \sigma_{^{235}\mathrm{U}/^{238}\mathrm{U},^{236}\mathrm{U}/^{238}\mathrm{U}} & \sigma_{^{236}\mathrm{U}/^{238}\mathrm{U}} \end{bmatrix}$$

Determining the correlation and covariance between the isotope ratios is useful for isolating individual compositions within a mixture. If a possible 2nd composition only varies from the bulk in one isotope ratio, and neither of the other isotope ratios alters in tandem, then the variation is far more likely be due to another factor than any 2nd composition.

3.4 Application to LA-ICP-MS Data Handling Software

3.4.1 Iolite v2.5

Iolite v2.5 is a non-commercial download software package written by the Melbourne Isotope and trace element group[11], which is designed for the processing of LA-ICP-MS data. It is an add-on to Igor

Pro with a strong emphasis on data visualisation. Recently v2.5 stopped being supported and has been replaced with the commercial v3.

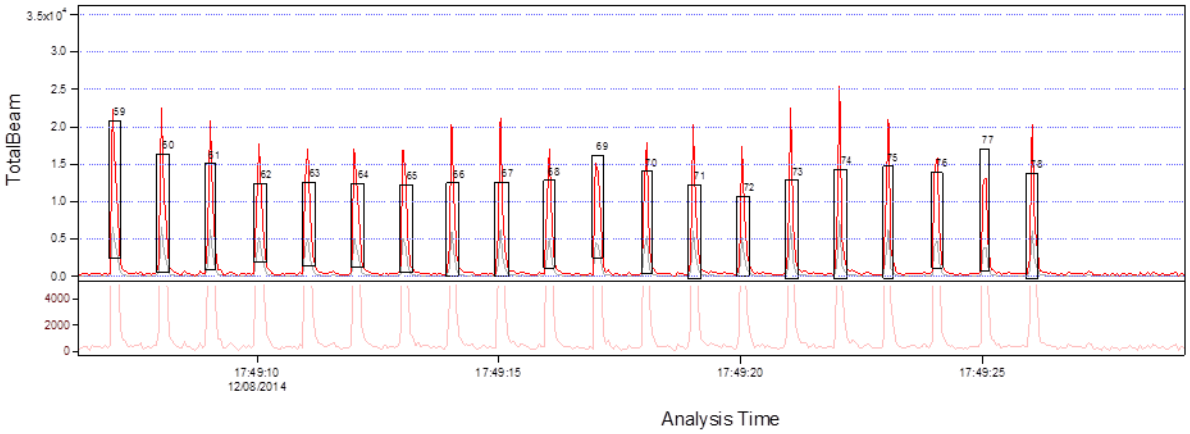

Figure 41 – Pulses ablated onto SRM611 uploaded into Iolite v2.5. Signal integration windows are in black.

Raw data files are uploaded into Iolite, whereupon signal integration windows are selected either manually in the graphical interface or automatically by signal intensity. Depending on the model of laser used, laser log files can also be uploaded and used to automatically assign the integration windows.

The data are interrogated via a Data Reduction Scheme (DRS), a set of instructions for the manipulation of the data[12]. A new DRS can be easily created and manipulated by the user and as such it was possible to create a DRS which used the geometric mean. Unfortunately Iolite has been setup in a way that only the P2P approach to data evaluation can be used within a DRS and therefore Iolite v2.5 could not be used for the data collected from the Neptune *Plus* MC-ICP-MS where a TSI approach was required.

3.4.2 R

R[13] (free-to-download) is a software environment for carrying out statistical computing and graphics. Within the software environment scripts written in the R programming language can carry out a wide variety of data analysis. The core functions can be extended by the addition of downloadable packages.

Within R a script was created to mimic many of the functions of the DRS created for Iolite v2.5. However in R it was possible to change the data evaluation method from P2P to TSI. Furthermore the R script incorporated the output of a correlation factor and correlation matrix, missing from the Iolite DRS. Signal integration windows were created either from the signal intensity or manually in a basic graphical interface, selecting start and end points from a plot of the data. However, accurately

selecting the start and end points was difficult for large datasets and tended to crash the software environment.

3.4.3 CoDaPack

CoDaPack is a freeware software download created by the Girona Compositional Data Group at the University of Girona. Making use of the work of Aitchison[5] outlined above, it can generate log-ratio data from the raw counts and then use higher functions to graphically display the data[14].

The software is limited; arithmetic functions, such as applying correction factors, are not possible within the software environment (for this reason the original MSEXCEL add-on would be better for ICP-MS data) and instead these have to be performed in another software environment. However from the raw counts the software automatically performs the log-ratio transformation, calculates the mean isotope ratio and associated SD, as well as the correlation and covariance matrix. Once calculated various biplots and ternary diagrams showing the relationships between the different isotope ratios can be plotted. The data can also be *centred*, useful for more clearly showing the relationships in various plots.

3.5 Determination and Application of Correction Factors

Moving to the geometric mean requires a modification of how some of the correction factors were calculated and applied in Chapter 2. The first correction factor (CF) required, for the UH/U ratio, is now calculated as:

$$CF_{\frac{UH}{U}} = \exp\left(\frac{1}{n}\sum\left(\ln \quad {}^{239}U_{CRM112} - \ln {}^{238}U_{CRM112}\right)\right)$$

The same modifications were required for the CF's for abundance at 1 and 2 amu.

$$CF_{1amu} = \exp\left(\frac{1}{n}\sum\left(\ln {}^{237}U_{CRM112} - \ln {}^{238}U_{CRM112}\right)\right)$$

$$CF_{2amu} = \exp\left(\frac{1}{n}\sum\left(\ln\left({}^{236}U_{CRM112} - {}^{235}U_{CRM112} \times CF_{\frac{UH}{U}}\right) - \ln {}^{238}U_{CRM112}\right)\right)$$

For the CF accounting for mass bias and detector response for each isotope, using the geometric mean changes how it is applied to the data. Due to the log-ratio transformation they are now a subtractive function rather than a division function.

$$CF_{\frac{234U}{238U}} = \ln\left({}^{234}U/{}^{238}U_{CRM010,\text{certified}}\right) - \frac{1}{n}\sum\left(\ln\left({}^{234}U_{CRM010} - {}^{235}U_{CRM010} \times CF_{1amu}\right) - \ln {}^{238}U_{CRM010}\right)$$

$$CF_{\frac{235U}{238U}} = \ln\left({}^{235}U/{}^{238}U_{CRM010,\text{certified}}\right) - \frac{1}{n}\sum\left(\ln{}^{235}U_{CRM010} - \ln{}^{238}U_{CRM010}\right)$$

$$CF_{\frac{236U}{238U}} = \ln\left({}^{236}U/{}^{238}U_{CRM010,\text{certified}}\right) - \frac{1}{n}\sum\left(\ln\left({}^{236}U_{CRM010} - {}^{235}U_{CRM010} \times CF_{\frac{UH}{U}} - {}^{238}U_{CRM010} \times CF_{2amu}\right) - \ln{}^{238}U_{CRM010}\right)$$

All of the CFs correct the laser ablation data in the following manner:

$${}^{234}U/{}^{238}U = \ln\left({}^{234}U - {}^{235}U \times CF_{1amu}\right) - \ln{}^{238}U - CF_{\frac{234U}{238U}}$$

$${}^{235}U/{}^{238}U = \ln{}^{235}U - \ln{}^{238}U - CF_{\frac{235U}{238U}}$$

$${}^{236}U/{}^{238}U = \ln\left({}^{236}U - {}^{235}U \times CF_{\frac{UH}{U}} - {}^{238}U \times CF_{2amu}\right) - \ln{}^{238}U - CF_{\frac{236U}{238U}}$$

3.6 Conclusion

The work of Aitchison[4–8] has conclusively shown that for compositional analysis, of which isotope ratio analysis is part, using the geometric mean is superior to the arithmetic mean. By using both the geometric and arithmetic approach to carry out isotope ratio analysis on experimental data the advantages of the geometric approach for this project were demonstrated. As such all subsequent isotope ratios reported in this thesis have been calculated using the geometric mean. Furthermore for identifying different compositions a correlation and covariance matrix will be reported alongside the individual isotope ratios. It is recommended the work of Aitchison be used throughout the isotope ratio community.

3.7 References

1. D. Rowntree, *Statistics without Tears*, Penguin, London, 3rd edn., 2000.
2. W. C. Krumbein and F. A. Graybill, *An Introduction to Statistical Models in Geology*, McGraw-Hill Inc., New York, 1965.
3. N. M. Mclean, PhD Thesis, Massachusetts Institute of Technology, 2012.
4. J. Aitchison, *Math. Geol.*, 1984, **16**, 531–564.
5. J. Aitchison, *Math. Geol.*, 1992, **24**, 365–379.
6. J. Aitchison, *Math. Geol.*, 1999, **31**, 563–580.
7. J. Aitchison, C. Barcel, and J. A. Mart, *Math. Geol.*, 2000, **32**, 271–275.

8. J. Aitchison, *A Concise Guide to Compositional Data Analysis*, Unverisity of Glasgow, Glasgow, 2003.

9. E. Limpert, W. A. Stahel, and M. Abbt, *Bioscience*, 2001, **51**, 341-252.

10. D. Marsal, *Statistics for Geoscientists*, Pegamon Press, Oxford, 1987.

11. C. Paton, J. Hellstrom, B. Paul, J. Woodhead, and J. Hergt, *J. Anal. At. Spectrom.*, 2011, **26**, 2508–2518.

12. J. D. Woodhead, J. Hellstrom, J. M. Hergt, A. Greig, and R. Maas, *Geostand. Geoanalytical Res.*, 2007, **31**, 331–343.

13. R Core Team, R: A language and enviroment for statistical computing (Version 3.12 “Pumpkin Helmet”), R Foundation for Statsitical Computing, Vienna, Austria, 2008.

14. S. Thió-Henestrosa and J. a. Martín-Fernández, *Math. Geol.*, 2005, **37**, 773–793.

Chapter 4 – Isotope Ratio Analysis of sub-micron UO_x particles by Laser Ablation Multi Collector Inductively Coupled Plasma Mass Spectrometry

4.1 Introduction

In this chapter the application of the methods developed in Chapters 2 and 3 is reported for the analysis of sub-micrometer (micron) uranium oxide particles. The particle samples were produced as part of an inter-laboratory comparison and as such the expected isotopic compositions are known. One of the sample planchets was expected to have particles of two different compositions, which should be satisfactorily resolved.

4.2 NUSIMEP Particles, an IRMM Inter-Laboratory Comparison

The particles analysed were obtained by NIGL through previous participation in an inter-laboratory comparison exercise as part of the Institute for Reference Materials and Measurements (IRMM) Nuclear Signatures Inter-laboratory Measurement Evaluation Program (NUSIMEP).

The measurement of the isotopic composition of nuclear materials is of not only scientific, but political and legal relevance[1]. As a consequence nuclear analytical laboratories have a requirement to test their capability, to determine the isotopic composition of nuclear materials, on a regular basis. One method by which laboratories can test their capability is by participating in inter-laboratory comparisons, where their capability is compared to other peer laboratories.

Environmental sampling of sites under the Additional Protocol is a vital tool in the monitoring of un-declared nuclear activities. Given the possible consequences, political and legal, of any determination made from environmental samples, a rigorous quality management system is required[2]. To ensure the reliability and comparability of a determination of the isotopic composition in uranium particles, the results need to be guaranteed and monitored using reference materials and quality control tools[3]. In order to overcome a lack of correct reference materials the NUSIMEP series of inter-laboratory comparisons were setup, with the objective of providing the required materials in suitable environmental matrices[2].

Of the eight NUSIMEP rounds which have been completed, two, NUSIMEP-6 and NUSIMEP-7, consisted of sub-micron UO_x particles on 2.5cm round carbon planchets[2]. NUSIMEP-6, which had only 1 planchet, was considered a pilot inter-laboratory comparison, and as such feedback from NUSIMEP-6 was used to help optimise NUSIMEP-7, which had two planchets. One of the NUSIMEP-7

planchets, similar to NUSIMEP-6, was manufactured to have particles of only a single uranium isotopic composition, however the other planchet was created to have a mix of particles with two different compositions.

The particles created for the study were produced from certified uranium hexafluoride (UF_6) reference materials[2–4]. The UF_6, contained in a glass vial and six carbon planchets were placed at either end of an aerosol deposition chamber. By breaking the glass vial the UF_6 was released to hydrolyse and condense gaseous UF_6 into solid UO_2F_2 particles onto the planchet's surface. Once formed the particles were baked at 350°C to produce U_3O_8 particulate. Particle morphology and size were confirmed by SEM. For the NUSIMEP-7 double composition planchet the procedure was completed twice, once for the 1st composition and then again to add the 2nd composition.

One of the major variations from NUSIMEP-6 to NUSIMEP-7 was the removal of a "smear" of uranium material noted in feedback from NUSIMEP-6[2]. This smear consisted of tiny nanometer (nm) sized particles which had precipitated alongside their larger sub-micron cousins. One consequence of the smear was that a uranium signal could be expected for ablation anywhere on the surface of the planchet.

As the particles were produced from certified reference materials the expected uranium isotopic compositions were known.

Table 18 – Certified Uranium Isotope Compositions of the NUSIMEP particles.

Planchet		**$^{234}U/^{238}U$**	**$^{235}U/^{238}U$**	**$^{236}U/^{238}U$**
NUSIMEP-6[3]		4.9817e-05	7.0439e-03	5.2048e-07
NUSIMEP-7(single composition)[4]		7.4365e-05	9.0726e-03	8.0205e-06
NUSIMEP-7(dual composition) [4]	**1st**	7.4365e-05	9.0726e-03	8.0205e-06
	2nd	3.4514e-04	3.4148e-02	1.0327e-04

The inter-laboratory comparison participants were asked to report for each planchet, the isotopic composition based on 10 particle results per composition. Subsequent measurement of the $^{235}U/^{238}U$ isotope ratio of the NUSIMEP particles has also been reported using LA-ICP-MS[5–7] but none have thus far been able to quantify the $^{234}U/^{238}U$ or $^{236}U/^{238}U$ isotope ratios. The aim therefore in this section was to, if possible, determine all three isotope ratios for the NUSIMEP uranium oxide particles.

4.3 Mapping of the Size and Distribution of UO_x particles on the surface of NUSIMEP planchets

Before undergoing laser ablation, the size and distribution of the uranium oxide particles on the carbon planchets was measured by SEM-EDX. The instrument used was a LEO 435VP fitted with an Oxford Instruments™ INCAx-sight energy-dispersive x-ray spectrometer (EDX) available at the British Geological Survey (BGS). The EDX was used for elemental analysis (confirming the particles on the surface were indeed uranium) by analysing the x-rays generated by the electron bombardment. Two planchets underwent analysis, the NUSIMEP-6 planchet and one of the two NUSIMEP-7 planchets.

4.3.1 NUSIMEP-6

For NUSIMEP-6 a particle detection sequence was used to scan a thin strip 0.37x4.55mm for particles. Using the backscatter detector, particles were identified if they exceeded a luminosity threshold, calibrated earlier. Detected particles were automatically interogated with the EDX and if any percentage of U was detected they were assigned as UO_x. The thin strip was scanned as 148 fields of 92x123µm.

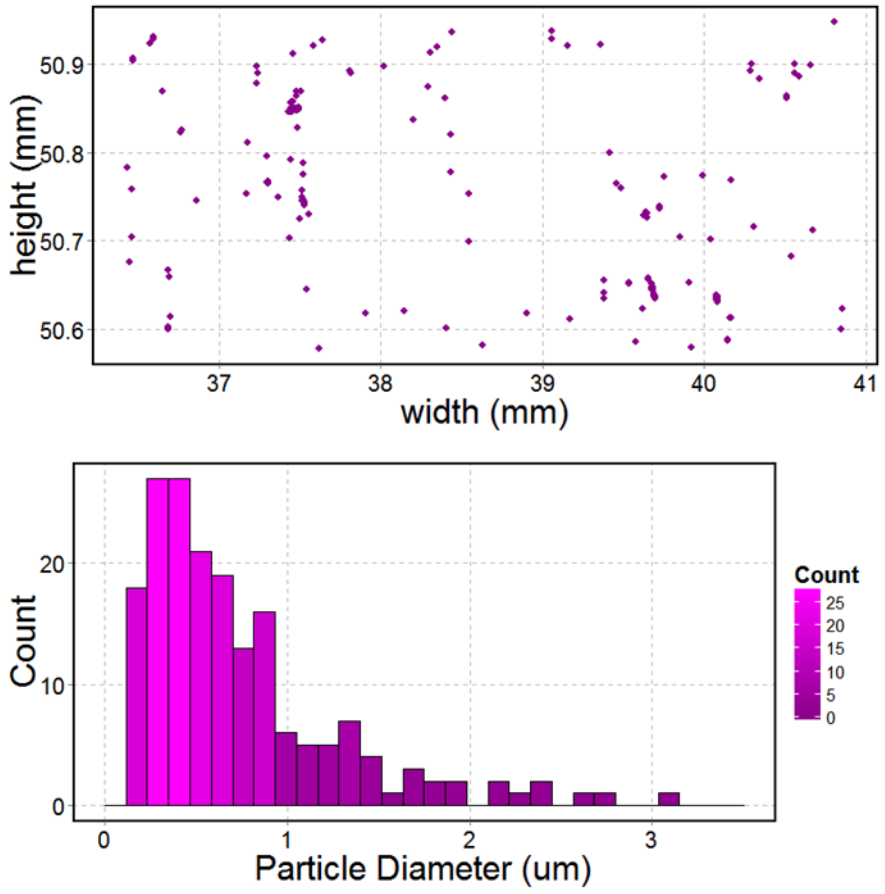

Figure 42 – Distribution of NUSIMEP-6 U particles within a rectangular strip 0.37x4.55µm (top). Histogram of particle diameter, bin width = 50µm (bottom).

In total, 184 uranium containing particles were detected across the strip with the size averaging 0.64±0.43µm. The particles were not evenly distributed across the surface, but instead were concentrated in clusters and/or lines.

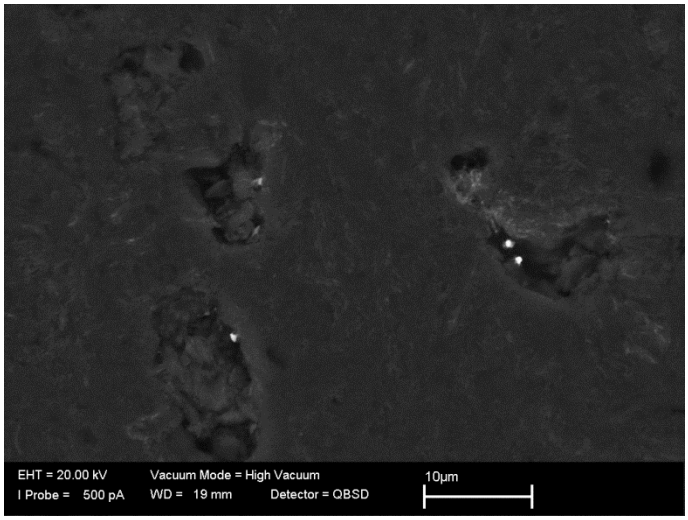

Figure 43 – SEM field on NUSIMEP-6, backscatter detector. U particles (white) are concentrated in features on the planchet surface.

By switching between the secondary electron and backscatter detectors of the SEM it was observed that the particles were mainly located within features (Figure 43) on the carbon planchet surface. It can be theorised that the edges of the features in the surface provided nucleation sites during the hydrolysis of the UF_6 to solid UO_2F_2.

4.3.2 NUSIMEP-7

An almost identical procedure to that used to analyse NUSIMEP-6 under the SEM, was used to analyse the surface of the NUSIMEP-7 (single composition) planchet. The same particle detection sequence was used although two larger strips, one 0.28x33mm, top to bottom, and another 0.28x25.5mm, left to right, were scanned.

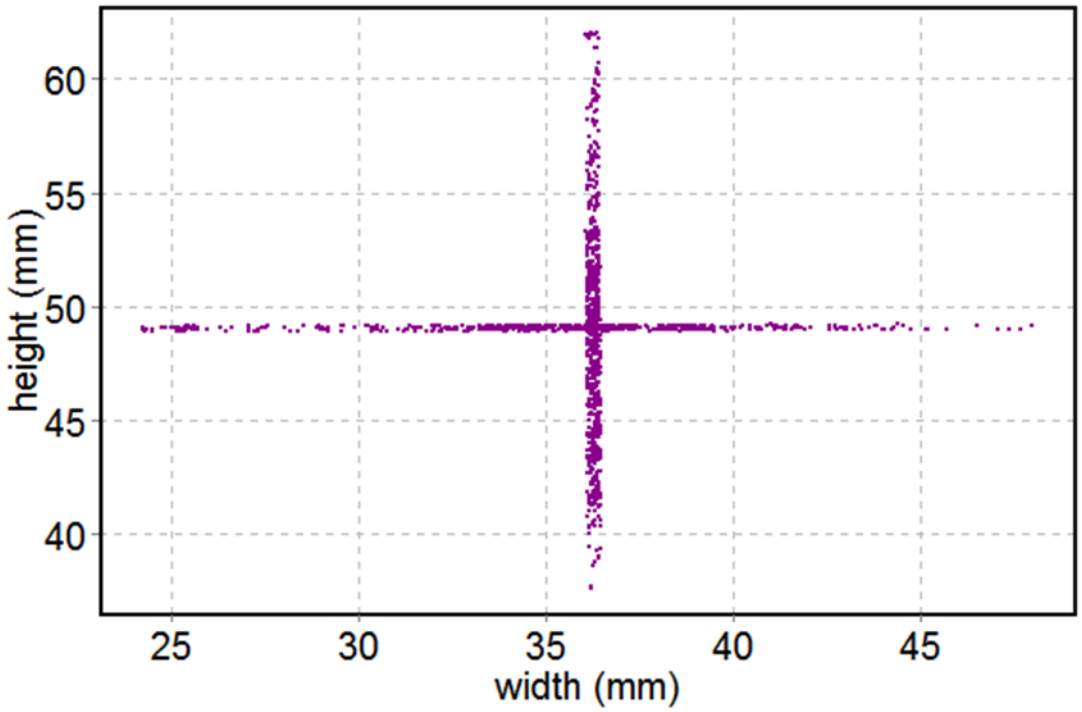

Figure 44 – Distribution of NUSIMEP-7 U particles within two narrow strips. The area of maximum particle density was at the centre of the planchet.

In the 1407 fields scanned, 1712 uranium containing particles were detected, averaging a size of 0.41±0.12 µm, top to bottom, and 0.36±0.11 µm, left to right. Smaller than NUSIMEP-6, the size distribution of these particles compare well to a previously reported size[4] of 0.327±0.139 µm for NUSIMEP-7. By combining both strips a density map of the planchet surface can be created, showing most particles were located in the centre of the planchet, with the density of particles decreasing towards the rim.

4.4 Analysis of NUSIMEP Planchets by Laser Ablation Multi Collector Inductively Coupled Plasma Mass Spectrometry

The NUSIMEP sample planchets were analysed using the same instrumentation and methods developed on SRM611 in Chapter 2, unless otherwise stated. Both the DCI & Enterprise Cell and Zircon Cell were used to connect the ESI® New Wave Research™ UP-193FX excimer laser ablation system to the Thermo Scientific™ Neptune *Plus*™ multi-collector inductively coupled plasma mass spectrometer (MC-ICP-MS) and the results from both coupling mechanisms are reported.

Table 19 – Typical laser ablation conditions for NUSIMEP particles.

UP-193FX excimer laser	Parameter
Ablation mode	Single spot
Fluence	6 J cm^{-2}
Repetition rate	1 Hz
Spot size	5 µm

Correction factors were generated by the same liquid aspiration of reference materials used for analysis of SRM611. Ablation analysis of SRM611 on the same day as the NUSIMEP particles allowed a further normalisation to the solid reference material if required. As the target particles were expected to be under 1µm in diameter and the uranium concentration that much greater for the UO_x particles, the spot size was reduced to 5µm from the 20µm primarily used on SRM611.

4.4.1 NUSIMEP-6

Consistent with the "smear" which had been previously reported for NUSIMEP-6, amost every ablation onto the surface returned at least some uranium signal. It is therefore difficult to report that each and every one of these signals has been caused by a single, discrete, particle, as many may have been due to ablation of a smear of nanometer-sized particles instead.

4.4.1.1 NUSIMEP-6 measured with the Zircon Cell

Based on the particle distribution from the SEM analysis, 300 5µm single shot ablations were carried out near the centre of the carbon planchet, in order to maximise the likelihood of hitting a particle with each ablation. Out of the 300 shots, 296 returned sufficient uranium signal for the $^{234}U/^{238}U$ and $^{235}U/^{238}U$ ratios to be determined. The signal from the average pulse on NUSIMEP-6 was insufficient to determine the $^{236}U/^{238}U$ ratio: for the expected isotope ratio of $^{236}U/^{238}U$ of 5.2048e-07 the average ^{238}U signal per pulse of five million counts only corresponds to 2.5 counts of ^{236}U. Ablating a particulate sample lightly held on a substrate surface is different from ablating a crater into a solid material, such as SRM611. When the pulse from the laser strikes the particle surface the particle can either be ablated, i.e. all or part of the particle is destroyed with the resulting material condensing into a plume of smaller particles, or the particle can be ejected, i.e. the particle leaves the substrate surface whole and travels intact towards the plasma. If the particle is ablated the pulse profile detected on the mass spectrometer is similar, both in shape and duration, to the pulse profile for SRM611. However if the particle is ejected whole into the plasma the pulse profile is significantly different.

In single particle ICP-MS (sp-ICP-MS) whole nanoparticles in a dilute solution are introduced into the plasma[8], either by aspiration with a spray chamber and nebuliser[9], or via a droplet generator[10,11,8,12]. SP-ICP-MS is a growing field, primarily providing size and compositional information of engineered nanoparticles, however the same approach has been applied to the isotope ratio analysis of single particles in suspension[13]. When a particle is added whole into the plasma, the signal width detected by the mass spectrometer is equal to the residence time of the particle in the plasma, between 200 and 500µs[10]. As the smallest integration time of the MC-ICP-MS was 8ms, the ion counter output from a particle added whole into the plasma would be contained within a single integration. As has been discussed in Chapter 2, due to the tau decay of the amplifier circuit the output signal from the Faraday cups will be longer in duration. To analyse the NUSIMEP particles on the mixed detector array of the MC-ICP-MS it is preferred that the particles are ablated rather than ejected whole from the substrate surface. For ^{235}U on an IC, compressing the signal from a large 600µm UO_x particle into 200-500µs could lead to suppression of the output signal from dead time and blind time effects, or by the deflection away of the input beam to protect the ion counter.

For the 300 shots collected on NUSIMEP-6 with the Zircon Cell, all of the pulse durations were greater than one integration on the ion counters, suggesting the particles were ablated from the planchet rather than ejected. A single laser ablation shot at the fluence selected was insufficient to ablate an entire particle. By firing multiple shots at the same location, repetition rate 1 Hz, it took an average of 3 shots to consume the average particle. The first shot contained the majority (three-quarters) of the total signal collected.

Table 20 – Mean U isotope ratios for 300 shots on NUSIMEP-6, Zircon Cell. The RSD for the $^{234}U/^{238}U$ was less than the RSD for $^{235}U/^{238}U$. Using counting statistics the $^{235}U/^{238}U$ RSD would be estimated at less than 20 times the reported value.

Method		**$^{234}U/^{238}U$**	**$^{235}U/^{238}U$**
Zircon Cell	**R_{mean}**	4.89E-05	6.50E-03
TSI	**(−RSD)**	(7.95%)	(12.15%)
	(+RSD)	(8.63%)	(13.83%)
	RD	-1.91	-8.07
	(−RSE)	(0.46%)	(0.71%)
	(+RSE)	(0.50%)	(0.80%)
	Limiting (RSD)	(6.80%)	(0.60%)

Despite the higher count rate on ^{235}U compared to ^{234}U, for the 296 NUSIMEP-6 signal pulses both the %RSD and RD were higher for $^{235}U/^{238}U$ than $^{234}U/^{238}U$. This suggested at least one additional

source of uncertainty unrelated to counting statistics was present in the dataset, for at least $^{235}U/^{238}U$.

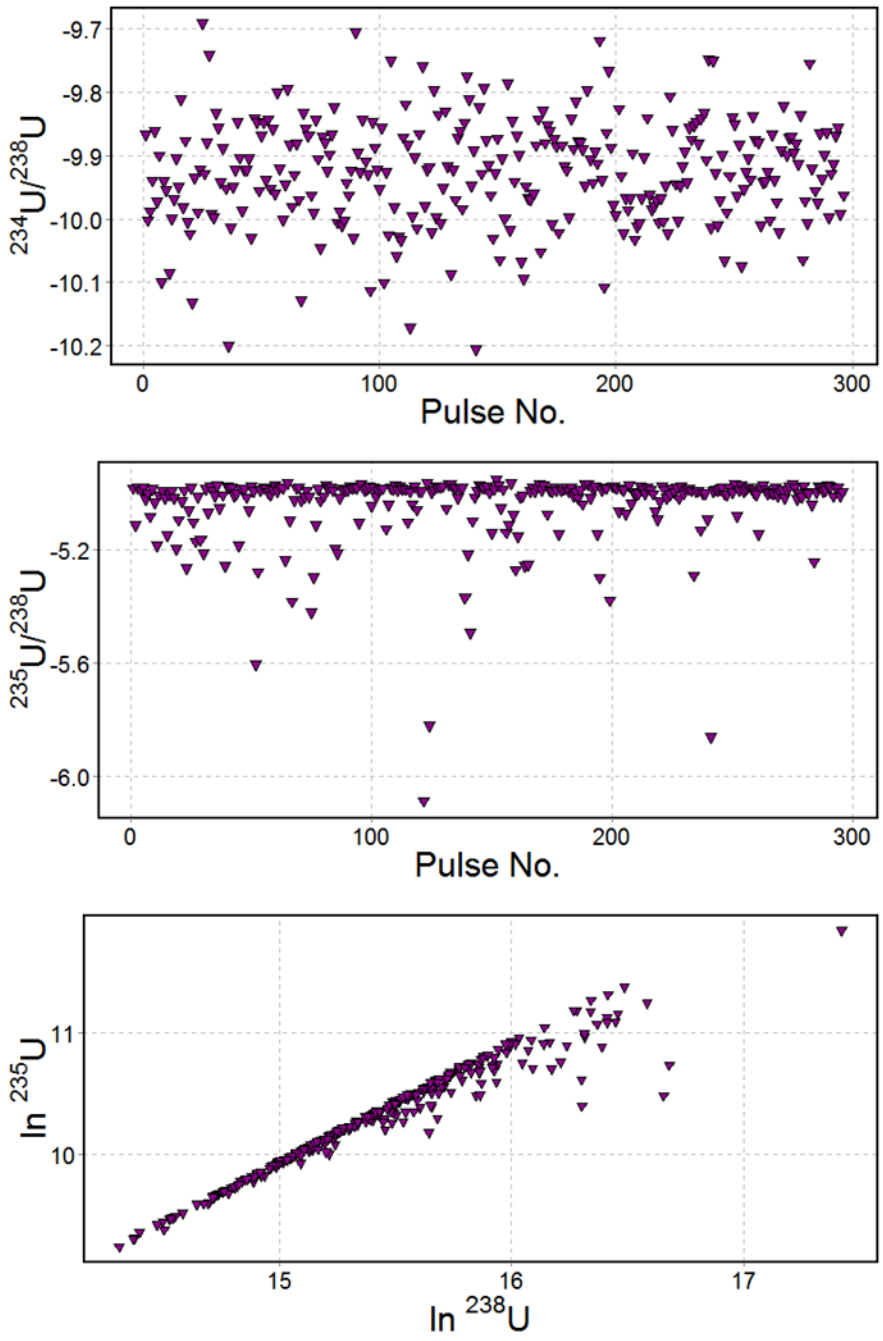

Figure 45 – Scatterplot of $^{234}U/^{238}U$, NUSIMEP-6, Zircon Cell (Top). Scatterplot of $^{235}U/^{238}U$, NUSIMEP-6, Zircon Cell (Middle). Plot of ln ^{235}U against ln ^{238}U, NUSIMEP-6, Zircon Cell (Bottom).

Plotting all $^{234}U/^{238}U$ and $^{235}U/^{238}U$ values a pattern similar to the blind time plots noticed in Chapter 2 for the DCI & Enterprise Cell was revealed (Figure 45). The affected signals were concentrated at higher count rates, between 1 and 4V total signal on ^{238}U. If the pulse profile for ^{235}U was similar to the profile with SRM611 on the Zircon Cell then the affected signals were unlikely to be due to blind

time, given how the ^{235}U signal on SRM611 was hardly affected by blind time. However closer analysis of the affected signals revealed a commonality in pulse profile, with strong, single integration, spikes in intensity.

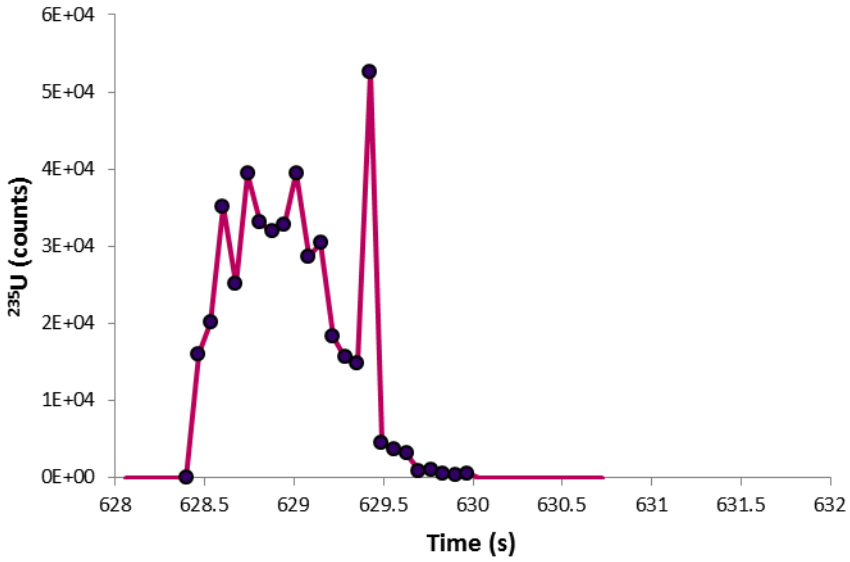

Figure 46 – ^{235}U pulse profile of the ablation of a NUSIMEP-6 particle, Zircon Cell. The standard profile is interrupted by a large single integration spike in signal.

The strong signal spikes were present across all four isotopes, not uniquely on ^{235}U. The spikes, being one integration in duration, are consistent with the response of particles which have been introduced whole into the plasma. Ideally the ablation plume would consist only of nanometer particles in a narrow size distribution; however the spikes suggest the NUSIMEP particles in question have not ablated cleanly. In one possible scenario most of the particle is ablated, but a remaining large fragment is ejected from the surface and is responsible for the spike in the pulse profile. Another possibility would be the shockwave, generated by the laser pulse, propagating across the planchet surface away from the target location, imparting sufficient energy to a particle, only lightly bound to the substrate surface, to knock it off the surface and into the plasma. This particle, located outside the 5µm spot ablated would be responsible for the spike in the pulse profile.

While the normal Zircon Cell ablation is only lightly affected by blind time, the spikes are more transient in nature, at least on the order of or more likely much faster than the DCI & Enterprise Cell. As a consequence they can be affected by blind time, and if they are as suspected much shorter in duration than the pulses profiles generated by the DCI & Enterprise Cell, the percentage of total counts lost on the ion counter could approach 100%. The additional uncertainty on the SRM611 $^{235}U/^{238}U$ isotope ratio for the DCI & Enterprise Cell which was attributed to blind time was between 2 and 3%. The additional uncertainty on NUSIMEP-6 is between 11 to 13%. Not all of the additional

uncertainty on NUSIMEP-6 from the strong transient spikes may be due to blind time, other effects such as ion counter dead time could contribute to the total additional uncertainty.

The best method for reducing the additional uncertainty from the transient spikes in the pulse profile would be to eliminate the transient spikes by changing how the particles were mounted for ablation. Pointurier *et al* (2011)[5], when analysing NUSIMEP-6 by LA-ICP-MS, transferred the UO_x particles off the carbon planchet and reaffixed them to a polycarbonate disc using a several micron thick collodion layer. By using such a procedure the risk of ejecting non-ablated particles from the sample surface would reduce. A new method for securely mounting particles for laser ablation has been developed as part of this project and is discussed in Chapter 6.

To gauge what could be achieved for NUSIMEP-6 with the additional uncertainty from the transient spikes removed, a method for filtering the affected pulses from the dataset was required. The simplest approach would be to set a threshold, below which the pulses would be removed from the dataset. However it would be very easy to be over-zealous in selecting the threshold and therefore a more objective, data-based solution was sought. Kappel *et al* (2013)[7] reported the use of Flexmix, a package in R, which uses linear regression to identify and separate out individual clusters within a dataset. Flexmix, with the same conditions used by Kappel, was applied to the dataset with the aim of filtering out the transient spike affected signals as one or more unique clusters.

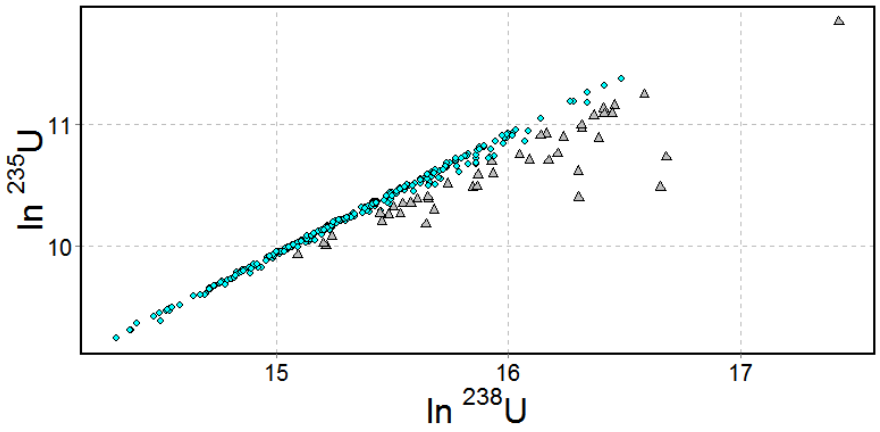

Figure 47 – Plot of ln ^{235}U against ln ^{238}U, NUSIMEP-6, Zircon Cell, clusters assigned by Flexmix.

Flexmix successfully isolated the majority of the transient spike affected pulses into a separate cluster from the rest of the dataset. Of the 296 total pulses, 43 or 14.5% were removed into the separate cluster. Recalculating the isotope ratio for the remaining 253 pulses, the RSD for the $^{235}U/^{238}U$ ratio dropped to 3% and the RD to -4.05% (Table 21).

Table 21 – Mean U isotope ratios for 300 shots on NUSIMEP-6, Zircon Cell, filtered by Flexmix. The 253 remaining pulses demonstrated a fourfold improvement in the $^{235}U/^{238}U$ RSD over the unfiltered dataset.

Method		$^{234}U/^{238}U$	$^{235}U/^{238}U$
Zircon Cell	**R_{mean}**	4.92E-05	6.76E-03
TSI	**(−RSD)**	(7.66%)	(2.93%)
	(+RSD)	(8.29%)	(3.01%)
	RD	-1.21	-4.05
	(−RSE)	(0.45%)	(0.17%)
	(+RSE)	(0.48%)	(0.18%)
	Limiting (RSD)	(7.07%)	(0.61%)

4.4.1.2 NUSIMEP-6 with the DCI & Enterprise Cell

A similar laser ablation procedure to that used for the Zircon Cell was employed with the DCI & Enterprise Cell; using the 66ms integration time on the mass spectrometer over 500 5µm shots across the surface of the planchet produced 491 signal responses. Once blind time had been established as a possible source of additional uncertainty with the DCI & Enterprise Cell the experiment was repeated with a similar number of 5µm shots measured with the 131ms as well as the 66ms integration time.

Table 22 – Mean U isotope ratios for 491 shots on NUSIMEP-6, DCI & Enterprise Cell. Integration time = 66ms. The RSD on $^{235}U/^{238}U$ was ten times higher than the estimated $^{235}U/^{238}U$ RSD from counting statistics.

Method		$^{234}U/^{238}U$	$^{235}U/^{238}U$
DCI & Enterprise Cell	**R_{mean}**	4.75E-05	6.80E-03
TSI	**(−RSD)**	(9.70%)	(6.46%)
66ms	**(+RSD)**	(10.7%)	(6.90%)
	RD	-4.73	-3.55
	(−RSE)	(0.44%)	(0.29%)
	(+RSE)	(0.48%)	(0.31%)
	Limiting (RSD)	(7.85%)	(0.65%)

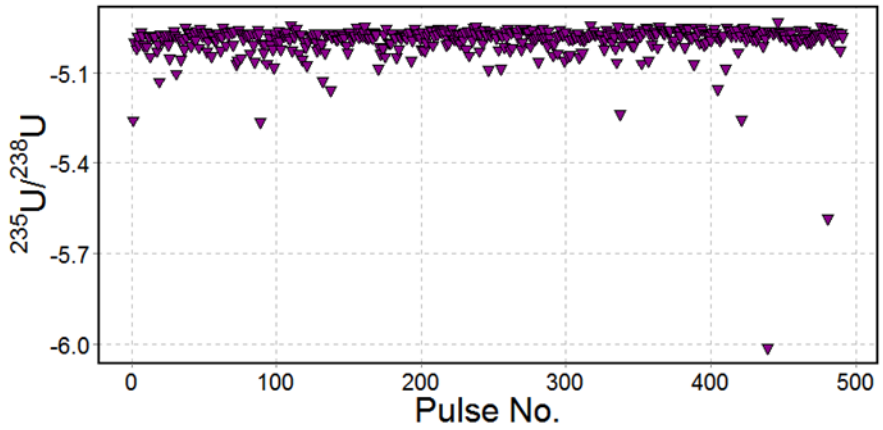

Figure 48 – Scatterplot of $^{235}U/^{238}U$, NUSIMEP-6, DCI & Enterprise Cell, integration time=66ms.

From the isotope ratio results in Table 22, given the additional uncertainty on the RSD it can be assumed that, like with the Zircon Cell, the $^{235}U/^{238}U$ ratio had been biased by transient spikes and plotting the $^{235}U/^{238}U$ pulses as a scatterplot (Figure 48) did reveal a bias towards lower $^{235}U/^{238}U$ ratios for some pulses. As well as additional uncertainty from transient spikes, using the DCI & Enterprise Cell it could also be assumed some component of the additional uncertainty would be due to blind time affected signals. The same $^{235}U/^{238}U$ threshold, -5.10, which had been determined for the Zircon Cell dataset using the Flexmix package, was applied to the 66ms integration time data collected with the DCI & Enterprise Cell. The threshold removed 2% of the total pulses.

Table 23 – Mean U isotope ratios for 480 filtered shots on NUSIMEP-6, DCI & Enterprise Cell. Integration time = 66ms. The Flexmix filtering reduced the $^{235}U/^{238}U$ RSD to less than half the unfiltered value.

Method		**$^{234}U/^{238}U$**	**$^{235}U/^{238}U$**
DCI & Enterprise Cell	**R_{mean}**	4.76E-05	6.80E-03
TSI	**(−RSD)**	(9.54%)	(2.79%)
66ms	**(+RSD)**	(10.6%)	(2.87%)
	RD	-4.49	-2.84
	(−RSE)	(0.44%)	(0.13%)
	(+RSE)	(0.48%)	(0.13%)
	Limiting (RSD)	(7.85%)	(0.65%)

The application of the threshold to the dataset (Table 23) improved the RSD and RD of the $^{235}U/^{238}U$ ratio with the DCI & Enterprise Cell to better than that which was achieved with the Zircon Cell, but considering the limiting uncertainty from counting statistics more improvement in the precision on both $^{234}U/^{238}U$ and $^{235}U/^{238}U$ should be possible. A large component of the remaining uncertainty on

the isotope ratios with the DCI & Enterprise Cell could be attributed to blind time effects: the threshold applied to the dataset may not have been zealous enough to filter out these signals from the dataset. A method to filter out blind time affected signals by comparing the percentage of total counts in the first integration was developed in Chapter 2, but this method could not be employed for NUSIMEP-6. The NUSIMEP-6 particle pulse profiles were longer in duration than for SRM611 and as such spread out over more than two integrations. By increasing the integration time from 66ms to 131ms the frequency of blind time events could be reduced.

Table 24 – Average U isotope ratios for 442 filtered shots on NUSIMEP-6, DCI & Enterprise Cell. Integration time = 131ms.

Method		$^{234}U/^{238}U$	$^{235}U/^{238}U$
DCI & Enterprise Cell	R_{mean}	4.97E-05	6.84E-03
TSI	**(−RSD)**	(9.35%)	(2.53%)
66ms	**(+RSD)**	(10.3%)	(2.59%)
	RD	-0.28	-2.93
	(−RSE)	(0.44%)	(0.12%)
	(+RSE)	(0.49%)	(0.12%)
	Limiting (RSD)	(8.49%)	(0.72%)

For the NUSIMEP-6 data collected with the 131ms integration time the same threshold on $^{235}U/^{238}U$ from Flexmix was applied. As with the 66ms integration time 2% of the total pulses were removed by the threshold from the dataset. The improvements in RSD achieved by moving to the 131ms integration time were less than 0.3% for both isotope ratios.

A $^{235}U/^{238}U$ threshold has been applied to filter all of the dataset collected for NUSIMEP-6. The best outcome which any filter based on a $^{235}U/^{238}U$ threshold value could achieve would be to have a perfect normal distribution around the mean. To estimate the RSD which could theoretically be achieved with such a robust threshold the $^{235}U/^{238}U$ threshold was set to achieve as normal a distribution as possible for the remaining values. The RSD achieved when filtering with the new threshold was 2%.

4.4.1.3 Comparison to Published Work

The results in Table 24 were judged the best which could be achieved for NUSIMEP-6 with the LA-MC-ICP-MS coupling mechanisms and system used. The potential utility of the LA-MC-ICP-MS setup used, to the capability of determining the isotopic composition of sub-micron particles, was assessed by comparison to other analyses of NUSIMEP-6 in the scientific literature. The only contribution in

the scientific literature which measures NUSIMEP-6 by LA-ICP-MS, used a quadrupole-based ICP-MS[5]. By using as a quadrupole based mass spectrometer the detection efficiency of the LA-ICP-MS was limited compared to the LA-MC-ICP-MS used in this project. As a consequence only the $^{235}U/^{238}U$ ratio was reported, with an RSD of 24.2% and an RD of 11.5% for 19 particles. Therefore with LA-MC-ICP-MS an order of magnitude improvement in the RSD has been achieved over the quadrupole based analysis. In the report produced by the original inter-laboratory comparison, in addition to NIGL, one other laboratory analysed the planchet by LA-ICP-MS. Although the results reported by the other laboratory look initially superior to values in Table 24, the laser conditions used (spot size= 35-100µm, repetition rate = 2Hz, raster pattern) suggested much more material than a single particle was collected for each analysis.

The results from analyses by SIMS and TIMS as well as LA-ICP-MS are also reported in the original inter-laboratory comparison[3] and subsequently Kraiem *et al* (2011)[14] further analysed NUSIMEP-6 by TIMS. For nine particles by TIMS the RSD of $^{234}U/^{238}U$ and $^{235}U/^{238}U$ were 30.3% and 0.95% respectively, RD 40.4 and 1.9%. RD and RSD values for $^{234}U/^{238}U$ were high as the count rate for ^{234}U was reported as close to background level. For 30 NUSIMEP-6 particles analysed by SIMS, Pointurier *et al* (2011)[5] reported an RSD of 0.7% and an RD of 0.5% for the $^{235}U/^{238}U$ ratio. No results for the $^{234}U/^{238}U$ ratio were reported.

4.4.2 NUSIMEP-7 (single composition)

Unlike for the NUSIMEP-6 planchet, not every ablation on the surface of the NUSIMEP-7 planchet resulted in a uranium signal. It was therefore much more likely that each pulse which was detected was caused by the ablation of a single discrete particle rather than potentially from a 'smear' of uranium material. As the particle size of NUSIMEP-7 was rougly half the size of NUSIMEP-6 this was reflected in the average total number of counts for each pulse detected by the MC-ICP-MS. Not every pulse profile collectedhad sufficient counts of ^{234}U or ^{236}U (likely those describing particles at the lower end of the size distribution) for the $^{234}U/^{238}U$ and $^{236}U/^{238}U$ isotope ratios to be determined. In order to report $^{234}U/^{238}U$ and $^{236}U/^{238}U$ for NUSIMEP-7 a signal threshold was used to exclude the smallest signals. In this case pulses with more than 10 total counts of ^{234}U was set as the signal threshold as this was the minimum number of counts at which the Monte Carlo simulation, used to determine the limiting uncertainty, would output a valid number.

4.4.2.1 NUSIMEP-7 (single composition) with the Zircon Cell

The data from NUSIMEP-7 (single composition) was processed in the same fashion as NUSIMEP-6. Of the total 360 particle signals collected with the Zircon Cell from the NUSIMEP-7 (single composition)

planchet, 11 had to be excluded for strong, single integration, spikes akin to those demonstrated for NUSIMEP-6.

Table 25 – Mean U isotope ratios for 349 shots on NUSIMEP-7 (single composition), Zircon Cell, filtered for transient spikes in the pulse profile. The reported RSD for all three isotope ratios approached counting statistics: with RD within uncertainty.

Method		$^{234}U/^{238}U$	$^{235}U/^{238}U$	$^{236}U/^{238}U$
Zircon Cell	**R_{mean}**	7.97E-05	8.97E-03	1.18E-05
TSI, 66ms	**(−RSD)**	(21.5%)	(3.63%)	(44.0%)
	(+RSD)	(27.4%)	(3.76%)	(78.6%)
	RD	6.91	-1.19	38.3
	(−RSE)	(1.15%)	(0.19%)	(2.35%)
	(+RSE)	(1.47%)	(0.20%)	(4.20%)
	Limiting (RSD)	(21.8%)	(2.19%)	(61.4%)

4.4.2.2 NUSIMEP-7 (single composition) with the DCI & Enterprise Cell

For NUSIMEP-6 about 20% of pulses collected with the Zircon Cell were affected by strong single integration spikes likely caused by ejection of particle material whole from the planchet surface. With the DCI & Enterprise Cell the proportion of NUSIMEP-6 pulses affected by transient signal spikes reduced to only 2% of pulses rejected under the same criteria. For NUSIMEP-7 (single composition) the coupling mechanism most strongly affected by transient spikes was reversed, with the DCI & Enterprise Cell losing a much greater proportion of its signals to transient spikes than the Zircon Cell (Figure 49). A probable rationale would be the number of transient spikes generated is based on the location of the ablation on the planchet surface. In an area more densely populated by particles, the potential for the ablation shockwave to 'knock' particles off the planchet surface would increase. The general area ablated on the NUSIMEP-7 single composition planchet with the DCI & Enterprise Cell was more densely populated with particles, it took approximately ¼ of the time required to ablate the same quantity of particles as was collected for the Zircon Cell.

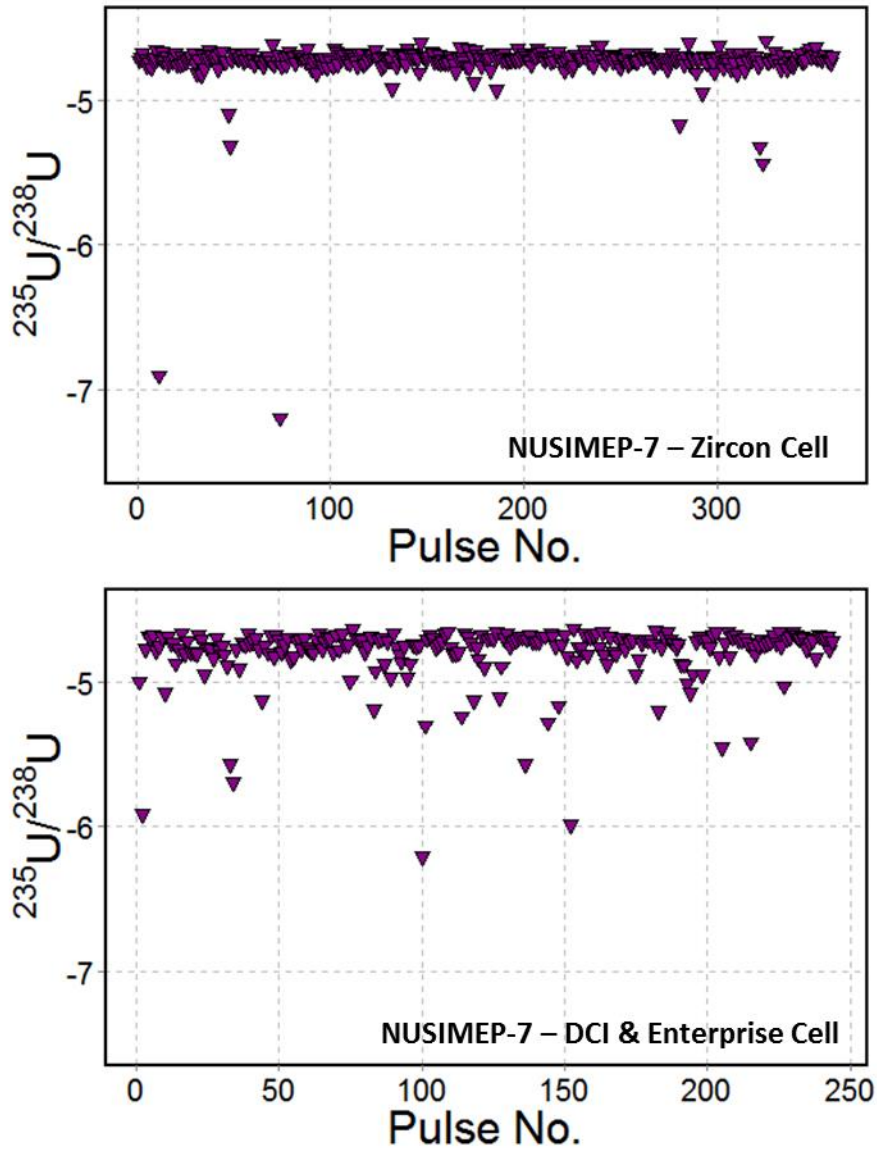

Figure 49 – Scatterplots of the $^{235}U/^{238}U$ ratio against pulse number, NUSIMEP-7 (single composition). Zircon Cell (top) and DCI & Enterprise Cell (bottom). The degree of scatter was greater with the DCI & Enterprise Cell.

The results for the minor isotope ratios, $^{234}U/^{238}U$ and $^{236}U/^{238}U$, with the DCI & Enterprise Cell (Table 26) were similar to the values achieved with the Zircon Cell. The RSD and RD for $^{235}U/^{238}U$ were both worse with the DCI & Enterprise Cell, by roughly the same proportion. With SRM611 the RSD and RD also were worse for $^{235}U/^{238}U$ by the same proportion with the DCI & Enterprise Cell and this was attributed to blind time.

Table 26 – Average U isotope ratios for 202 shots on NUSIMEP-7 (single composition), DCI & Enterprise Cell, filtered for transient spikes.

Method		$^{234}U/^{238}U$	$^{235}U/^{238}U$	$^{236}U/^{238}U$
DCI & Enterprise Cell	**R_{mean}**	7.78E-05	8.86E-03	9.59E-06
TSI	**(−RSD)**	(21.6%)	(4.77%)	(43.8%)
	(+RSD)	(27.6%)	(5.01%)	(78.0%)
	RD	4.47	-2.36	17.8
	(−RSE)	(1.52%)	(0.34%)	(3.08%)
	(+RSE)	(1.94%)	(0.35%)	(5.49%)
	Limiting (RSD)	(21.4%)	(2.09%)	(62.5%)

The pulses which had been collected on NUSIMEP-6 with the DCI & Enterprise Cell had been too wide in order to use the same blind time filter method which had been developed in Chapter 2, however the particle pulse durations for NUSIMEP-7 were narrower and the blind time filter could be adopted. The data for NUSIMEP-7 was filtered such that only those pulses with 80% of the signal in the 1st integration were retained. Employing the blind time filter to the data reduced the number of particles retained by nearly half, for small improvements in the $^{235}U/^{238}U$ RSD and RD (Table 27).

Table 27 – Average U isotope ratios of NUSIMEP-7 (single composition), DCI & Enterprise Cell. Of the 249 pulses collected, only pulses with more than 80% of the ^{235}U counts in the 1st integration were used.

Method		$^{234}U/^{238}U$	$^{235}U/^{238}U$	$^{236}U/^{238}U$
DCI & Enterprise Cell	**R_{mean}**	8.01E-05	9.05E-03	9.51E-06
TSI	**(−RSD)**	(22.1%)	(3.96%)	(43.4%)
	(+RSD)	(28.4%)	(4.12%)	(76.5%)
	RD	7.38	-0.21	17.0
	(−RSE)	(2.03%)	(0.36%)	(3.97%)
	(+RSE)	(2.61%)	(0.38%)	(7.02%)
	Limiting (RSD)	(20.2%)	(2.09%)	(62.1%)

4.4.3 NUSIMEP-7 (dual composition)

Although the NUSIMEP-7 (dual composition) planchet had not been analysed by SEM-EDX it was assumed the size and distribution of particles on the surface was identical to the single composition planchet as they had been produced at the same time.

4.4.3.1 NUSIMEP-7 (dual composition) with the Zircon Cell

To initially assess the NUSIMEP-7 (dual composition) planchet (unique identifier NU7-043), 290 particle pulses containing sufficient uranium signal (see threshold (section 4.4.2)) were ablated from an area near the centre of the planchet. After calculating all the uranium isotope ratios for all 290 pulses it was apparent that only one of the two expected compositions could be detected (Figure 50).

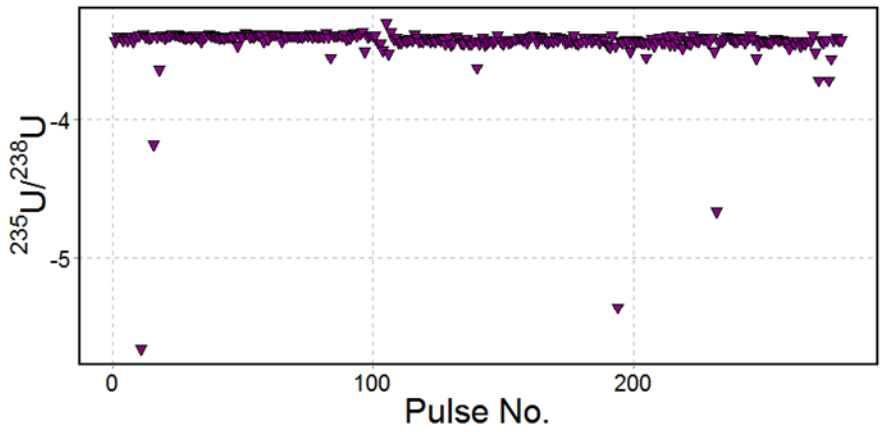

Figure 50 – Plot of $^{235}U/^{238}U$ for 280 particle pulses on the centre of the planchet, NU7-043, Zircon Cell. Only one composition is identifiable.

Potentially only one of the two compositions could be identified if the distribution of the compositions were not even across the planchet, and therefore ablation at a different location on the planchet may yield the other composition. To test the hypothesis a further 600 pulses were collected at nine different locations on the planchet surface. Eight of the test sample locations were located at points evenly distributed along the circumference of the planchet, the ninth was at the centre. Of the 890 total pulses collected only one potentially had the isotopic signature of the missing composition. By calculating the degree of correlation between the three isotope ratios (Table 29) they were found to be only weakly correlated, confirming the lack of a second composition.

Table 28 – Average uranium isotope ratios of 280 pulses on NU7-043, Zircon Cell. Only one composition (the 2nd shown in Table 18) is reported.

Method		$^{234}U/^{238}U$	$^{235}U/^{238}U$	$^{236}U/^{238}U$
Zircon Cell	**R_{mean}**	3.41E-04	3.28E-02	1.04E-04
TSI	**(−RSD)**	(10.0%)	(3.44%)	(18.2%)
	(+RSD)	(11.1%)	(3.56%)	(22.3%)
	RD	-1.22	-4.16	1.00
	(−RSE)	(0.60%)	(0.21%)	(1.09%)
	(+RSE)	(0.67%)	(0.21%)	(1.33%)
	Limiting (RSD)	(9.49%)	(0.99%)	(17.3%)

Table 29 – Covariance and correlation for uranium isotope ratios of 280 pulses on NU7-043, Zircon Cell.

Covariance Matrix	$^{234}U/^{238}U$	$^{235}U/^{238}U$	$^{236}U/^{238}U$	Correlation Coefficient	
$^{234}U/^{238}U$	1.11E-02	5.67E-04	2.77E-03	($^{234}U/^{238}U$, $^{235}U/^{238}U$)	0.15
$^{235}U/^{238}U$	5.67E-04	1.22E-03	9.60E-04	($^{234}U/^{238}U$, $^{236}U/^{238}U$)	0.13
$^{236}U/^{238}U$	2.77E-03	9.60E-04	4.04E-02	($^{235}U/^{238}U$, $^{236}U/^{238}U$)	0.14

It was therefore concluded that only one of the isotopic compositions, the 2nd composition (Table 18), could be identified. The results for the identifiable composition are given in Table 28. As the particles analysed were enriched in ^{234}U and ^{236}U relative to the particles from the single composition NUSIMEP-7 planchet, the RSD and RD values improved for the $^{234}U/^{238}U$ and $^{236}U/^{238}U$ ratios. However, the precision of the $^{235}U/^{238}U$ ratio, despite ^{235}U also being enriched compared to the single composition planchet, was not improved. The same Flexmix program in R had been used to filter out signals which had been affected by transient spikes in the pulse profile. However the Flexmix program did not identify every particle with a significantly depleted $^{235}U/^{238}U$ ratio, relative to the mean. By using the limiting uncertainty applied to each particle a new rejection criterion was used, particle compositions deviating by more than 2 times the RSD were excluded. The new filtering mechanism nearly doubled to 19, the number of particles removed from the dataset of 290 particles. For $^{235}U/^{238}U$ the results improved a little to 2.38% for the –RSD, 2.44% for the +RSD and -3.75% for the RD compared to the results in Table 28.

To investigate whether the inability to see the 2nd composition was an artefact of either the planchet or the LA-MC-ICP-MS analysis the NIGL planchet, NU7-043, was swapped for another NUSIMEP-7 dual composition planchet, NU7-021, kindly donated by another laboratory which had initially taken

part in the NUSIMEP-7 inter-laboratory comparison. Replacing the old NUSiMEP-7 dual composition planchet with the new planchet, NU7-021, another similarly sized dataset was collected by LA-MC-ICP-MS using the Zircon Cell. The area ablated on the new planchet was located near the centre of the planchet.

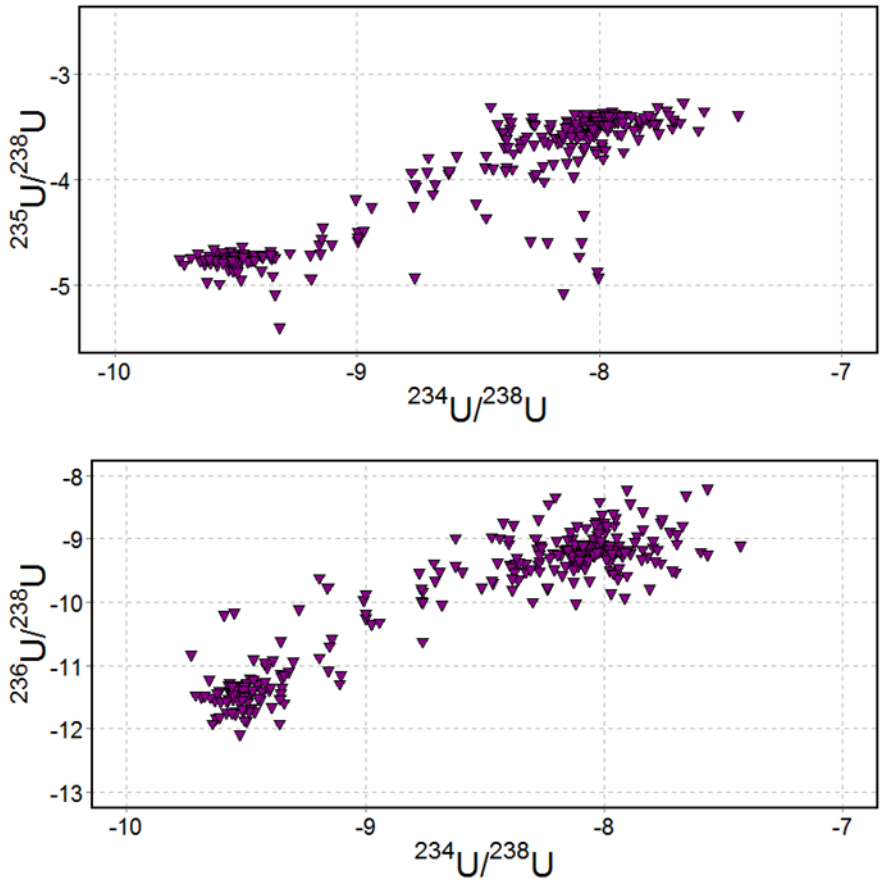

Figure 51 – Scatterplot of $^{235}U/^{238}U$ against $^{234}U/^{238}U$ for 303 pulses on planchet NU7-021, Zircon Cell (top). Scatterplot of $^{236}U/^{238}U$ against $^{234}U/^{238}U$ for 303 pulses on planchet NU7-021, Zircon Cell (bottom). Using both coupling mechanisms two discrete compositions are identified.

Unlike for NU7-043, with the NU7-021 planchet the two expected compositions could be readily identified in the data. However as the planchet was made with one composition laid down on top of the other, the two compositions are not discrete. Instead by plotting two of the isotope ratios of the particles against each other (Figure 51) in a scatterplot a mixing line was visible between the two compositions. For the $^{235}U/^{238}U$ isotope ratio, as well as the two compositions and the mixing line between them, some particles with depleted $^{235}U/^{238}U$ values are shown in the scatterplot. The Flexmix package, used to identify compositions, had to successfully isolate four groups, one for each composition, one group consisting of particles containing a mixture of the two compositions and a final group isolating particles with $^{235}U/^{238}U$ values depleted relative to the expected composition(s)

or their mixtures. Due to the complexity of the clusters to be resolved, the Flexmix package had difficulty isolating each composition to a high degree of precision.

Table 30 – Average uranium isotope ratios of 192 pulses on NU7-021, Zircon Cell, two compositions isolated from 303 pulses. The RSD of all three isotope ratios was less for the 1st composition than the 2nd composition, representative of the counting statistics of both compositions.

1st Composition	n=73	$^{234}U/^{238}U$	$^{235}U/^{238}U$	$^{236}U/^{238}U$
Zircon Cell	**R_{mean}**	7.43E-05	8.72E-03	1.12E-05
TSI	**(−RSD)**	(8.49%)	(3.27%)	(30.0%)
	(+RSD)	(9.27%)	(3.38%)	(42.1%)
	RD	-0.04	-3.97	33.10
	(−RSE)	(0.99%)	(0.38%)	(3.51%)
	(+RSE)	(1.09%)	(0.40%)	(5.02%)
	Limiting (RSD)	(7.92%)	(0.83%)	(22.4%)

2nd Composition	n=119	$^{234}U/^{238}U$	$^{235}U/^{238}U$	$^{236}U/^{238}U$
Zircon Cell	**R_{mean}**	3.35E-04	3.12E-02	1.10E-04
TSI	**(−RSD)**	(16.7%)	(6.76%)	(26.9%)
	(+RSD)	(20.1%)	(7.25%)	(36.9%)
	RD	-2.96	-8.99	6.02
	(−RSE)	(1.53%)	(0.62%)	(2.47%)
	(+RSE)	(1.84%)	(0.66%)	(3.38%)
	Limiting (RSD)	(15.4%)	(1.69%)	(28.3%)

Table 31 – Covariance and correlation for uranium isotope ratios of 303 pulses on NU7-021, Zircon Cell. The three isotope ratios are strongly correlated to each other, but $^{235}U/^{238}U$ were less strongly correlated to $^{234}U/^{238}U$ and $^{236}U/^{238}U$ than they were to each other.

Covariance Matrix	$^{234}U/^{238}U$	$^{235}U/^{238}U$	$^{236}U/^{238}U$	Correlation Coefficient	
$^{234}U/^{238}U$	5.15E-01	5.10E-01	7.39E-01	($^{234}U/^{238}U$, $^{235}U/^{238}U$)	0.73
$^{235}U/^{238}U$	5.10E-01	9.41E-01	7.47E-01	($^{234}U/^{238}U$, $^{236}U/^{238}U$)	0.94
$^{236}U/^{238}U$	7.39E-01	7.47E-01	1.21E+00	($^{235}U/^{238}U$, $^{236}U/^{238}U$)	0.70

To judge the success of Flexmix in isolating the two compositions from the dataset the values for the 1st composition can be compared to the single composition NUSIMEP-7 planchet and the 2nd composition to the first dual composition planchet NUSIMEP-7 planchet. For both the single

composition NUSIMEP-7 planchet and, presumably, NU7-043, the isotope ratio the RSD and RD values are unaffected by mixing of a second composition. Therefore the RSDs and RDs in Tables 26 and 28 are the best which could hope to be achieved for the two compositions isolated from the dual composition planchet. For the isolated 1st composition the RSD and RD results were actually better than the RSD and RD results of the individual single composition NUSIMEP-7 planchet. This improvement in precision was down to the increased count rate for the dual composition planchet, the limiting uncertainty of which for each isotope ratio was less than half the single composition planchet. However for the isolated 2nd composition on NU7-021 the count rate was less than on NU7-043 and hence the RSD and RD values were not improved, but instead were elevated. Not all of the increase in RSD and RD for $^{235}U/^{238}U$ was attributable to the count rate; the Flexmix package incorporated some $^{235}U/^{238}U$ depleted signals into the 2nd composition affecting the RSD and RD. The depleted $^{235}U/^{238}U$ signals, mostly due to transient signal spikes in the pulse profile, also explain the reduced correlation to $^{234}U/^{238}U$ and $^{236}U/^{238}U$, relative to the high degree of correlation between these two isotope ratios.

Although not exactly 50:50 in distribution, from the small area analysed on NU7-021 it appeared particles of both the expected compositions were present in high numbers on the planchet, in contrast to NU7-043 where only a single composition was identified. Published LA-MC-ICP-MS analysis of another dual composition planchet[7] reported only 29 particles of the 1st composition compared to 633 of the 2nd, but the reported contamination of that particular planchet with another set of particles could have introduced a bias. These results alone are not enough information to explain why one of the compositions was seemly missing from NU7-043.

4.4.3.2 NUSIMEP-7 (dual composition) with the DCI & Enterprise Cell

The dual composition planchet, NU7-021, was analysed further by LA-MC-ICP-MS using the DCI & Enterprise Cell coupling mechanism. For the area on the planchet sampled with the DCI & Enterprise Cell a high degree of mixing between the two compositions (Figure 52) was observed. As was reported for the Zircon Cell this made it difficult for Flexmix to isolate the two compositions from the dataset.

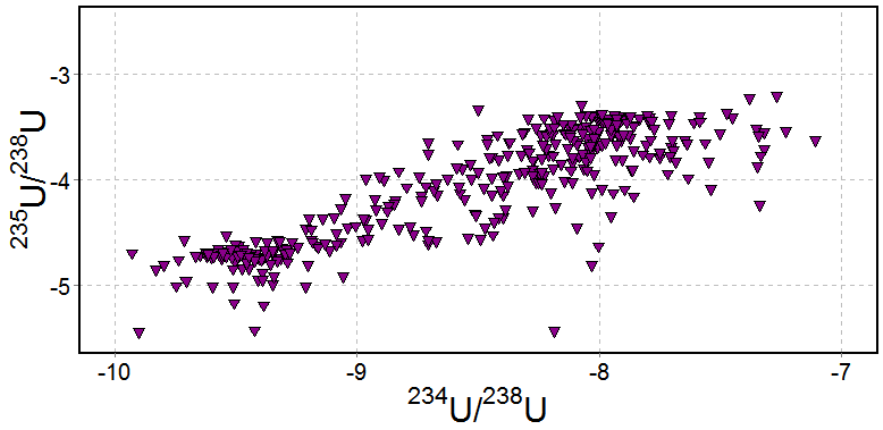

Figure 52 – Scatterplot of $^{235}U/^{238}U$ against $^{234}U/^{238}U$ for 393 pulses on planchet NU7-021, DCI & Enterprise Cell. A greater degree of mixing between the two compositions occurred than with the Zircon Cell.

Table 32 – Average uranium isotope ratios of 174 pulses on NU7-021, DCI & Enterprise Cell, two compositions.

1st Composition	**n=104**	**$^{234}U/^{238}U$**	**$^{235}U/^{238}U$**	**$^{236}U/^{238}U$**
DCI & Enterprise Cell	**R_{mean}**	7.75E-05	9.05E-03	1.40E-05
TSI	**(−RSD)**	(12.8%)	(6.80%)	(35.6%)
	(+RSD)	(14.7%)	(7.30%)	(55.3%)
	RD	4.14	-0.23	55.83
	(−RSE)	(1.26%)	(0.67%)	(3.49%)
	(+RSE)	(1.44%)	(0.72%)	(5.43%)
	Limiting (RSD)	(14.7%)	(1.36%)	(22.4%)

2nd Composition	**n=70**	**$^{234}U/^{238}U$**	**$^{235}U/^{238}U$**	**$^{236}U/^{238}U$**
DCI & Enterprise Cell	**R_{mean}**	3.57E-04	3.10E-02	1.20E-04
TSI	**(−RSD)**	(22.4%)	(7.73%)	(37.9%)
	(+RSD)	(28.9%)	(8.37%)	(60.9%)
	RD	3.25	-9.52	14.72
	(−RSE)	(2.68%)	(0.92%)	(4.52%)
	(+RSE)	(3.46%)	(1.00%)	(7.28%)
	Limiting (RSD)	(18.7%)	(2.08%)	(32.5%)

Table 33 – Covariance and correlation for uranium isotope ratios of 393 pulses on NU7-021, DCI & Enterprise Cell. As for the Zircon Cell the three isotope ratios are strongly correlated to each other, but $^{235}U/^{238}U$ were less strongly correlated to $^{234}U/^{238}U$ and $^{236}U/^{238}U$ than they were to each other.

Covariance Matrix	$^{234}U/^{238}U$	$^{235}U/^{238}U$	$^{236}U/^{238}U$	Correlation Coefficient	
$^{234}U/^{238}U$	5.07E-01	3.96E-01	6.31E-01	($^{234}U/^{238}U$, $^{235}U/^{238}U$)	0.69
$^{235}U/^{238}U$	3.96E-01	6.44E-01	5.86E-01	($^{234}U/^{238}U$, $^{236}U/^{238}U$)	0.84
$^{236}U/^{238}U$	6.31E-01	5.86E-01	1.11E+00	($^{235}U/^{238}U$, $^{236}U/^{238}U$)	0.69

Compared to the dataset collected on NU7-021 with the Zircon Cell, the uncertainty on all three isotope ratios has increased, for both compositions. This is likely a reflection of the increased degree of mixing, increasing the difficultly of isolating each composition. In the original inter-laboratory comparison each laboratory was asked to report an average and uncertainty for 10 particles in each composition. As the two compositions had been difficult to isolate with the DCI & Enterprise Cell dataset 10 particles were selected from the heart of each composition (based on $^{235}U/^{238}U$). The results from these selected particles were used to compare to the results reported in the original inter-laboratory comparison (Table 34).

Table 34 – Average uranium isotope ratios of 10 pulses on NU7-021, DCI & Enterprise Cell, two compositions. The 10 pulses were selected from the centre of each cluster.

1st Composition	n=10	$^{234}U/^{238}U$	$^{235}U/^{238}U$	$^{236}U/^{238}U$
DCI & Enterprise Cell	**R_{mean}**	7.27E-05	8.93E-03	1.15E-05
TSI	**(−RSD)**	(9.47%)	(0.40%)	(26.8%)
	(+RSD)	(10.5%)	(0.41%)	(36.6%)
	RD	-2.33	-1.61	36.12
	(−RSE)	(2.99%)	(0.13%)	(8.46%)
	(+RSE)	(3.31%)	(0.13%)	(11.6%)
	Limiting (RSD)	(14.7%)	(0.85%)	(23.8%)

2nd Composition	n=10	$^{234}U/^{238}U$	$^{235}U/^{238}U$	$^{236}U/^{238}U$
DCI & Enterprise Cell	**R_{mean}**	3.74E-04	3.36E-02	1.20E-04
TSI	**(−RSD)**	(14.6%)	(0.45%)	(27.5%)
	(+RSD)	(17.6%)	(0.45%)	(37.9%)
	RD	7.91	-1.59	14.93
	(−RSE)	(4.63%)	(0.14%)	(8.69%)
	(+RSE)	(5.44%)	(0.14%)	(12.0%)
	Limiting (RSD)	(12.9%)	(1.41%)	(22.7%)

4.4.3.3 NUSIMEP-7 (dual composition) with the DCI & Enterprise Cell – ^{235}U measured on a Faraday cup

Apart from the difficulty in isolating the two compositions, due to a high degree of compositional mixing, another reason for the poor RD and %RSD for NU7-021 with the DCI and Enterprise Cell was that many of the larger pulse signals had to be discarded as the enriched ^{235}U signal and increased signal-to-noise ratio of the DCI & Enterprise Cell tripped the ion counters, turning off all the ion counter detectors. As such the signals from these particles had clearly spurious isotopic compositions and had to be discarded. The 2nd, more enriched composition would be more likely to trip the ion counters and as such the remaining smaller pulses, may not be representative of the real proportion of particles of each composition. One possible solution to prevent the higher number of ^{235}U counts tripping all of the ion counters was to change to using a Faraday detector for ^{235}U. This required a change in cup configuration with ^{236}U placed on the axial ion counter, and ^{235}U and ^{238}U measured on the Faraday cups either side of the axial detector. The main disadvantage of this approach was measurement of ^{234}U was no longer possible as no ion counter at the correct mass

was available. Apart from the change in cup configuration all other instrument settings were kept the same as in section 4.4.3.2.

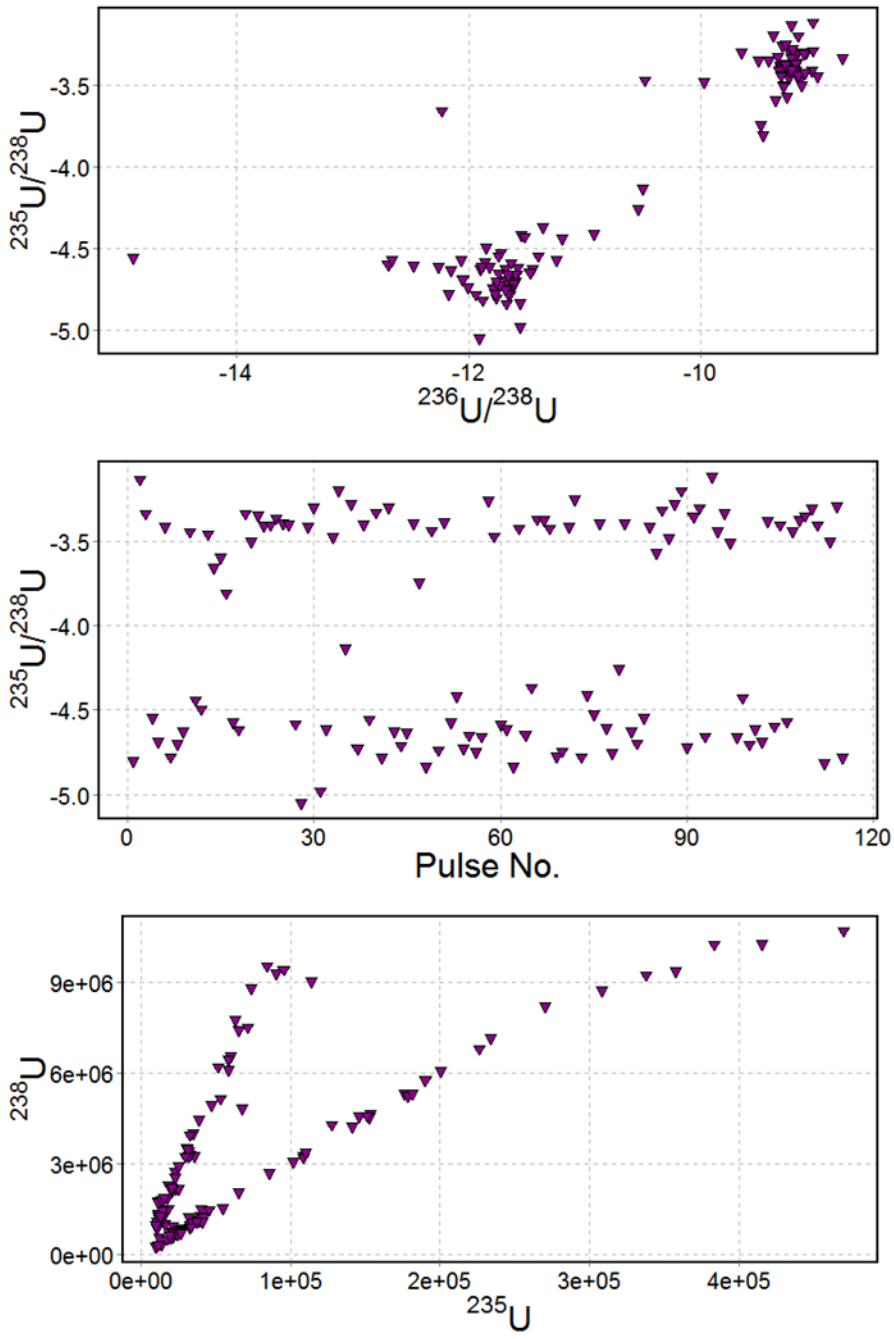

Figure 53 – Data from 115 pulses on planchet NU7-021, DCI & Enterprise Cell, ^{235}U measured on a Faraday cup. Scatterplot of $^{235}U/^{238}U$ against $^{236}U/^{238}U$ (top). Plot of $^{235}U/^{238}U$ (middle). Plot of ^{238}U against ^{235}U (bottom). Two distinct compositions are identifiable in all three plots. Plotting ^{238}U against ^{235}U demonstrates the deviation of the isotope ratio at higher count rates.

By ablation, 115 uranium signal pulses were collected for NU7-021 using the new cup configuration. The two expected compositions were easily identified, either as clusters, by plotting two isotope ratios against each other, or by the linear regression data evaluation strategy (Figure 53). Using the

linear regression data evaluation strategy it was noted that at least one of the compositions did not fit a straight line for its entire extent, but instead, above a certain count rate, the response changed to describe a curve. A reason for the change in behaviour at higher count rates has not yet been arrived at and more work is needed to resolve it.

The high count rate linear sections of the regression were extracted and the particle pulses used to calculate the average isotope ratios for the two compositions (Table 35). The results for $^{236}U/^{238}U$, due to the higher count rates now detectable without tripping the ion counter, were far superior to those achieved when using the previous cup configuration. For $^{235}U/^{238}U$, the results, RSD and RD for the 2nd composition were improved by moving to the new configuration. This was likely due to two factors, the elimination of any possible blind time effects, as both isotopes are measured on the same type of detector and the inclusion of higher count rate signals, now detectable without tripping the ion counter. For the 1st composition the change of cup configuration did not improve the precision of the measurement, compared to measuring ^{235}U on an ion counter. With the less enriched 1st composition the number of ^{235}U counts from the average NUSIMEP-7 particle was low, equivalent to a 1-2 millivolt pulse height on the Faraday cup detector. The difficulty in resolving the pulse from the background noise of the amplifier is reflected in the poor $^{235}U/^{238}U$ RSD for the 1st composition.

Table 35 – Average uranium isotope ratios of 54 pulses on NU7-021, DCI & Enterprise Cell, two compositions.

1st Composition	**n=35**	**$^{235}U/^{238}U$**	**$^{236}U/^{238}U$**
Zircon Cell	**R_{mean}**	9.51E-03	8.60E-06
TSI	**(−RSD)**	(11.5%)	(25.9%)
	(+RSD)	(13.1%)	(34.9%)
	RD	4.69	6.96
	(−RSE)	(1.95%)	(4.37%)
	(+RSE)	(2.21%)	(5.90%)
2nd Composition	**n=19**	**$^{235}U/^{238}U$**	**$^{236}U/^{238}U$**
Zircon Cell	**R_{mean}**	3.32E-02	9.55-05
TSI	**(−RSD)**	(3.16%)	(5.15%)
	(+RSD)	(3.26%)	(5.43%)
	RD	-2.93	-7.86
	(−RSE)	(0.72%)	(1.18%)
	(+RSE)	(0.75%)	(1.24%)

4.4.3.4 Comparison to Published Work

The measurement of the single composition NUSIMEP-7 planchet by LA-ICP-MS has been reported twice in the scientific literature. Pointurier *et al* (2012)[6] analysed the particles in a similar fashion to their previously reported work on NUSIMEP-6 and achieved, for 7 particles, an RSD of 9.6% and an RD of 2.9%. In Table 25, using the Zircon Cell a (–) RSD of 3.63%, a (+) RSD of 3.76% and a RD of -1.19% are reported and compare favourably to the work of Pointurier *et al*. Kappel *et al* (2013)[7] using a linear regression data evaluation strategy for LA-MC-ICP-MS reported an RSD of 5% and an RD of -1.0 for the single composition NUSIMEP-7 planchet. The results achieved with both the Zircon Cell and DCI & Enterprise cell were broadly similar to those reported by Kappel *et al*.

Also reported in Pointurier *et al* (2012) were the results from the analysis of particles from the NUSIMEP-7 single composition planchet by TIMS and SIMS. For TIMS the RSD and RD reported were 3.0% and -2.7% and for SIMS the RSD and RD were 3.0% and -2.6%. The improvement in precision for TIMS and SIMS over LA-ICP-MS was due to an increase in count rate, up 10 times and 20 times respectively for TIMS and SIMS. Comparing the average count rate per particle achieved by LA-MC-ICP-MS (Zircon Cell) to the count rates per particle reported by Pointurier *et al* the detection efficiency of the LA-MC-ICP-MS system was similar to TIMS.

Using the linear regression data evaluation strategy, Kappel *et al* (2013)[7] reported the $^{235}U/^{238}U$ ratios for the dual composition NUSIMEP-7 planchet by LA-MC-ICP-MS with both ^{235}U and ^{238}U measured on a Faraday cup. The RSD's of the $^{235}U/^{238}U$ ratios were 12.2% for the 1st composition and 3.0% for the 2nd composition. With the DCI & Enterprise Cell, measuring both ^{235}U and ^{238}U on Faraday cups comparable RSDs of (-) 11.54%/(+) 13.05% and (-) 3.16%/(+) 3.26% were determined for the two compositions respectively. A fourfold improvement in the RSD for the 1st composition was achieved when measuring ^{235}U on an ion counter, but at the cost of more than doubling the RSD on the 2nd composition (Table 32).

In the original inter-laboratory comparison three laboratories other than NIGL reported using LA-ICP-MS. Of the three laboratories one, identical to NU7-043, reported only the 2nd composition, with an RSD of 7.69% and an RD of -16.13%. For the second laboratory the values inferred strongly the analysis was the same as Kappel *et al*. The final laboratory identified both compositions, but with high RSD's of 50% for the 1st composition and 28% for the 2nd compositions, RD's 17.3% and -0.8% respectively. For a comparable 10 particle dataset, RSD's of under 0.5% and RD's of fewer than 2% were achieved with the DCI & Enterprise Cell (Table 34).

4.5 Conclusion

The isotope ratios of the NUSIMEP particles could be analysed by LA-MC-ICP-MS, with results approaching the limiting RSD constraints imposed by count rates. Two different compositions could be isolated on a single planchet and the minor isotope ratios $^{234}U/^{238}U$ and $^{236}U/^{238}U$ determined by LA-MC-ICP-MS, which has not been published previously in the scientific literature for the NUSIMEP particles. As $^{234}U/^{238}U$ and $^{236}U/^{238}U$ results have not been published for NUSIMEP particles by LA-ICP-MS, comparisons can only be made for $^{235}U/^{238}U$. It can be argued that better $^{235}U/^{238}U$ results for NUSIMEP-7 have been achieved by measuring both isotopes on Faraday cups and employing linear regression and this may indeed be the best approach for that particular isotope pair. However to simultaneously measure the $^{234}U/^{238}U$ and $^{236}U/^{238}U$ ratios another entirely different approach would need to be used concurrently, almost certainly using TSI. The method used would benefit from better ablation of the sample as ejected material interfered with overall analysis. This will be discussed later in Chapter 6.

The inability of LA-ICP-MS to find the 1st expected uranium isotopic composition on the NU7-043 planchet, despite measuring at 9 different locations on the surface, could not be explained. Numerous plausible causes may have occurred. For example during production how the inter-laboratory planchets were seeded with particles may have produced planchets with non-uniform distribution of particles. According to the NUSIMEP-7 report the missing composition should have been seeded first and therefore NU7-043 could not be a miss labelled single composition planchet. Perhaps the planchet was seeded with particles twice, but on the first seeding was located in the chamber such that very few particles formed on its surface. Regardless, for the NUSIMEP-7 inter-laboratory comparison exercise, where the utility of different instrumentation for UO_x particle analysis was under investigation, the lack of consistency from the planchets may have implications on the conclusions reported.

The main advantages of LA-ICP-MS for the analysis of single UO_x particles compared to SIMS and TIMS are the reduced sample preparation required and the speed at which the sample can be analysed. Pointurier *et al* (2011)[5] estimated for a given number of UO_x particles the time taken for TIMS, SIMS and LA-ICP-MS to perform the isotope measurements only was 6, 3 and 1.5 days respectively. Due to the slow measurement rate with TIMS the particles are often prepared with the fission track (FT) technique to pre-filter for particles of highly enriched uranium only. However FT itself is a slow process and was estimated to add 10 days to the overall analysis time. The decision by the community to use LA-ICP-MS for the analysis of single UO_x particles should therefore be based on whether any loss in accuracy and precision with the technique is worth the increase in sample

throughput. As the LA-MC-ICP-MS detection efficiency reported here compare favourably with respect to the literature, the limiting uncertainties calculated for each isotope ratio could be used as a guide to what could be potentially achieved with LA-MC-ICP-MS if perfected.

4.6 References

1. S. Richter, A. Alonso, J. Truyens, H. Kühn, A. Verbruggen, and R. Wellum, *Int. J. Mass Spectrom.*, 2007, **264**, 184–190.

2. J. Truyens, E. a Stefaniak, and Y. Aregbe, *J. Environ. Radioact.*, 2013, **125**, 50–55.

3. Y. Aregbe, J. Truyens, R. Kips, S. Richter, E. Stefaniak, H. Kühn, and M. Kraiem, *NUSIMEP-6 : Uranium isotope amount ratios in uranium particles*, IRMM Report EUR 23702EN, IRMM, Geel, 2008.

4. J. Truyerns, E. Stefaniak, S. Mialle, and Y. Aregbe, *NUSIMEP-7 : Uranium isotope amount ratios in uranium particles*, IRMM Report EUR 25179EN, IRMM, Geel, 2011.

5. F. Pointurier, A. Pottin, and A. Hubert, *Anal. Chem.*, 2011, **83**, 7841–7848.

6. F. Pointurier, A. Hubert, and A.-C. Pottin, *J. Radioanal. Nucl. Chem.*, 2012, **296**, 609–616.

7. S. Kappel, S. F. Boulyga, L. Dorta, D. Günther, B. Hattendorf, D. Koffler, G. Laaha, F. Leisch, and T. Prohaska, *Anal. Bioanal. Chem.*, 2013, **405**, 2943–2955.

8. O. Borovinskaya, S. Gschwind, B. Hattendorf, M. Tanner, and D. Günther, *Anal. Chem.*, 2014, **86**, 8142–8148.

9. F. Laborda, J. Jiménez-Lamana, E. Bolea, and J. R. Castillo, *J. Anal. At. Spectrom.*, **28**, 2013, 1220–1232.

10. O. Borovinskaya, B. Hattendorf, M. Tanner, S. Gschwind, and D. Günther, *J. Anal. At. Spectrom.*, 2013, **28**, 226–233.

11. P. E. Verboket, O. Borovinskaya, N. Meyer, D. Günther, and P. S. Dittrich, *Anal. Chem.*, 2014, **86**, 6012–6018.

12. O. Borovinskaya, M. Aghaei, L. Flamigni, B. Hattendorf, M. Tanner, A. Bogaerts, and D. Günther, *J. Anal. At. Spectrom.*, 2014, **29**, 262–271.

13. Y. Su, W. Wang, Z. Li, H. Deng, G. Zhou, J. Xu, and X. Ren, *J. Anal. At. Spectrom.*, 2015. DOI:10.1039/C4JA00339J

14. M. Kraiem, S. Richter, H. Kühn, and Y. Aregbe, *Anal. Chim. Acta*, 2011, **688**, 1–7.

Chapter 5 – Application of the DCI & Enterprise Cell Interface to Laser Ablation with a Fast Scanning Sector Field Inductively Coupled Plasma Mass Spectrometer

5.1 Introduction

In this chapter will be described the application of the DCI & Enterprise Cell to couple the ESI UP-193SS (solid state) laser ablation system to the Nu Instruments™ AttoM® ICP-MS (Nu Instruments™, Wrexham, UK). The utility of the system for the isotope ratio analysis of a glass solid standard and uranium oxide particles was determined.

According to Günther *et al* (2000)[1], the ideal detection system for short transient signals in laser ablation would be an 'all-collecting' sector-field instrument, where a detector is placed in the space and time focus that collects all isotopes simultaneously. Therefore for the short transient signals generated by the DCI & Enterprise Cell an MC-ICP-MS was preferred as, although not 'all-collecting', all of the isotopes of uranium could be detected simultaneously by its mixed detector array. The same mixed detector array however was shown in Chapter 2 to introduce a form of spectral skew, whereby whilst the *input* signal was detected simultaneously the *output* signal was not simultaneous for the two types of detectors, ion counters (IC) and Faraday cups. The spectral skew, referred to as Blind Time, in the output of the mass spectrometer led to different proportions of counts being lost on each detector and correspondingly an additional source of uncertainty on the measurement. Partly due to the spectral skew the improvement in precision and accuracy expected, for the isotope ratio analysis of single UO_x particles, using the DCI & Enterprise Cell over the Zircon Cell, an older design low-volume, single volume ablation cell, did not occur with the MC-ICP-MS.

Although not an "ideal" detection system for transient signals, a single collector ICP-MS, with a single solitary ion counter detector would not be affected by the Blind Time on a mixed detector array. With a single detector it is necessary to measure each isotope sequentially (only one *m/z* value is detected at any one time)[2]. This introduces a form of spectral skew (an error in relative signal between isotopes measured across a transient signal) as the need arises to scan the mass spectrum while the input concentration is constantly changing. To reduce the impact of spectral skew for transient signals with a scanning mass spectrometer it is recommended that the dwell time on each isotope and the time taken to switch between the isotopes is as short as possible. Quasi-simultaneous measurement has been reported with ICP-TOF-MS[3,4] and has been used for multi-element analysis of single droplets/particles with transient signals of only hundreds of microseconds

(µs) in duration. The isotope ratio analysis of single sub-micron sized particles will require good detection efficiency, greater than can be achieved by ICP-TOF-MS. The highest detection efficiency is achieved with a double focussing sector field ICP-MS. The dwell and settling time of a double focussing sector field ICP-MS would be expected to introduce significant spectral skew to the isotope ratio analysis of a fast transient signal, however the AttoM® from Nu Instruments™ can use ion optics, positioned either side of the magnet, to scan the mass range rather than the ESA. Relative to the ESA, the ion optics significantly reduce the minimum dwell time and settling time of the mass spectrometer. It was therefore decided to test the performance of using the DCI & Enterprise Cell to couple an ESI® UP-193SS™ laser ablation system to the AttoM® single collector ICP-MS.

5.2 Experimental

5.2.1 Coupling of the DCI to the Nu AttoM HR-ICP-MS

In order to couple the laser ablation system to the single collector ICP-MS with the DCI & Enterprise Cell some modification was required. The prototype DCI had been designed to only fit into the semi-demountable torch of ICP-MS available from another manufacturer. As the single collector AttoM® ICP-MS did not have a semi-demountable torch, the approach adopted was to replace the existing ICP torch with the semi-demountable torch from the other manufacturer. In order to fit the replacement torch into the AttoM® ICP-MS torch housing, a bracket used to both hold the Peltier spray chamber in place and to help guide the torch orientation, relative to the sampler cone, had to be removed. With the bracket removed the replacement torch and DCI still not fit into the matchbox of the ICP-MS. The replacement torch was longer than the original, and thus needed to be modified to fit. The extra length of the replacement torch was due to an increased distance between the end of the injector and the end of the torch. On the replacement torch the distance was 5mm longer. The end of the replacement torch was therefore shortened by 5 mm. The shortened torch and DCI could be then be used to couple the laser ablation system to the mass spectrometer. The original bonnet supplied with the AttoM® ICP-MS was not replaced.

5.2.2 Configuration of the LA-ICP-MS

The configuration of the LA-ICP-MS system using the single collector ICP-MS was similar to that which had been employed with the MC-ICP-MS. Unlike the MC-ICP-MS configuration the desolvator used was not a CETAC™ Aridus™ I but a DSN-100™ supplied by the manufacturer with the single collector ICP-MS.

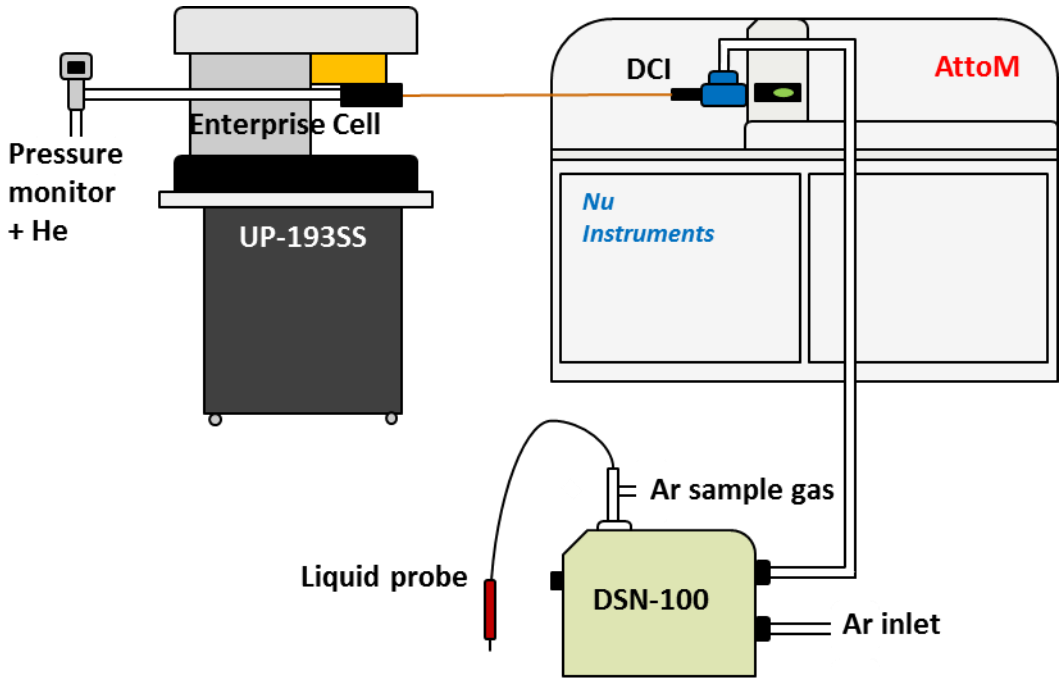

Figure 54 – Schematic of the single collector LA-ICP-MS setup with the DCI/Enterprise Cell. Due to spatial constraints the fused silica line was >1m. DCI sheath gas provided by outlet of a DSN-100 desolvator allowing the aspiration of liquid reference materials.

The same spatial constraints which had prevented a short direct line between the Enterprise Cell and the DCI with the MC-ICP-MS still applied for the single collector ICP-MS. As such the fused silica line used to couple the laser to the mass spectrometer was 1.5m in length. Using the desolvator to introduce the sheath gas to the DCI allowed liquid reference materials to be aspirated into the plasma. The aspirated liquid reference materials were used to tune the ICP-MS for maximum detection efficiency and, using a reference material of known isotopic composition, to calculate a correction factor (CF) for the mass bias and mass response curve of the mass spectrometer.

A second LA-ICP-MS setup using the Zircon Cell and ¼" Tygon® tubing was used as a comparison to the DCI & Enterprise Cell setup. The outflow from the Zircon Cell was mixed with the Ar outflow from the desolvator with a y-piece. Unlike with the DCI & Enterprise Cell, where the torch had to be replaced, the Zircon Cell used the original torch designed for the ICP-MS. Typical operating parameters for the LA-ICP-MS systems using both coupling mechanisms are given in Table 36.

Table 36 – Typical operating parameters of the single collector LA-ICP-MS setups.

	Zircon Cell	DCI & Enterprise Cell
Nu Instruments DSN-100 Desolvator		
Nebuliser Pressure (psi)	25	24
Hot Gas Flow (L min^{-1})	0.15	0.15
Membrane Gas Flow (L min^{-1})	3.2	4.3
Spray chamber temperature (°C)	110	110
Membrane temperature (°C)	120	120
Nu Instruments AttoM SF-ICPMS		
RF forward power (W)	1300	1300
RF reflected power (W)	8	8
Cool gas (L min^{-1})	13	15
Aux. gas (L min^{-1})	0.8	0.8
Argon gas (L min^{-1})	0	0
Helium gas (L min^{-1})	0.8	0.04
Resolution *m/Δm*	300	300
Cell pressure (psi)	0	11
Tubing	¼" Tygon®	250µm id fused silica

The cones used were nickel. For the Zircon Cell setup, which used the original ICP torch, the cool gas flow was set to 13 L min^{-1}, the typical operating condition for the AttoM® ICP-MS. The replacement torch used with the DCI & Enterprise Cell was designed for an ICP-MS typical operating with a higher cool gas flow of 15L min^{-1}. It was therefore deemed prudent to use 15 L min^{-1}, the cool gas flow rate with which the torch would typically operate.

5.2.3 Method Development

The AttoM® ICP-MS was selected over other sector field ICP-MS due ion optics which reduced the minimum dwell time and settling time of the mass spectrometer. Placed either side of the magnet, the ion optics allowed a minimum dwell time of 200µs for each isotope, with a 40µs switch delay between masses to be selected. These minimum dwell and switch delay times were used in order to minimise the spectral skew effect expected for the short transient. Although 200 µs was the minimum dwell time of the ICP-MS, it was not the minimum output integration time; a minimum of

10 sweeps (dwell times) are integrated into each single output (cycle) of the mass spectrometer. To maximise the amount of data output by the mass spectrometer, and to keep the S/N ratio high, the minimum of 10 sweeps was included in the method. In order to have sufficient analysis time 10,000 integration times (cycles) were collected for each method run.

Table 37 – Method settings for $^{235}U/^{238}U$ analysis by LA-ICP-MS with a single collector sector field ICP-MS.

Setting	Parameter
Analysis Mode	Deflector JUMP
Isotopes	^{235}U, ^{238}U
Dwell Time (µs)	200
Switch Delay (µs)	40
Number of Sweeps	10
Number of Cycles	10000

Only two isotopes, ^{235}U and ^{238}U, not four were included in the method. By only measuring the two major isotopes the spectral skew should be reduced, as the duty cycle on each isotope (42%) is more than doubled. Furthermore the detection efficiency of the single-collector LA-ICP-MS system was certain to be less than the multi-collector LA-ICP-MS system, probably by at least an order of magnitude. Given the known average count rate for the minor ^{234}U and ^{236}U isotopes with the LA-MC-ICP-MS system a loss of detection efficiency of an order of magnitude would render both isotopes undetectable.

With the DCI & Enterprise Cell the rate of increase in the ^{238}U signal was sufficient to activate a 'trip' which acts to prevent damaging large ion beams reaching the detector. On 'tripping' the ion beam is attenuated by switching it through a grid or 'filter'. This was applied to the ^{238}U signal, which reduced the amount of signal experienced by the detector. The average signal reduction is calibrated and at the time of analysis was set to 349: that is, for every 349 ^{238}U ions passing into the detection assembly, only one reached the detector. In this way the attenuation filter increases the count range which can be measured on the ion counter, although the attenuation filter has an associated uncertainty which is introduced into the measurement. With the DCI & Enterprise Cell each pulse collected 'tripped' the attenuation filter which was then reset at the end of the pulse. The consistent turning on and off of the attenuation filter had a negative impact on the analysis; before the end of each 10,000 cycle analysis the mass spectrometer would stop collecting data. To allow data to be

collected with the DCI & Enterprise Cell the method in Table 37 was altered; when measuring the ^{238}U signal the attenuation filter was used for the entire 10,000 cycle measurement.

5.3 Analysis of SRM611 Certified Reference Material

Before applying the LA-ICP-MS system to the analysis of the NUSIMEP UO_x particles, the utility of the system for isotope ratio analysis was tested by ablation of the NIST SRM611 certified reference material. The expected $^{235}U/^{238}U$ ratio of SRM611 was 2.386e-03[5]. Craters were ablated into the surface of SRM611 using the laser conditions, unless stated, in Table 38. For isotope ratio analysis 10 runs of 30 shots each were ablated using both the Zircon Cell and DCI & Enterprise Cell coupling mechanisms.

Table 38 – Laser ablation conditions for isotope ratio analysis of SRM611 glass. Isotope ratios were determined for 30 shots ablated at a single spot. For the determination of detection efficiency, 50 shots were ablated at a single location to generate a pit of sufficient depth for volume analysis.

Setting	Parameter
Ablation Mode	Spot
Fluence (J cm^{-2})	2.5-3.5
Dwell Time (s)	30 (50 for detection efficiency)
Repetition rate (Hz)	1
Spot Size	20

5.3.1 Comparison of Signal Pulse Profiles

As for the MC-ICP-MS, the DCI & Enterprise Cell should have an increased S/N ratio compared to the Zircon Cell for coupling to the single collector ICP-MS. To evaluate the difference in S/N ratio 300 shots were ablated into the surface of SRM611 using both coupling mechanisms. Typical pulse profiles for both coupling mechanisms are given in Figure 55.

The average pulse duration of SRM611 with the Zircon Cell was 360ms, 19% RSD. As the DCI & Enterprise Cell had average pulse duration of 29ms, 21% RSD, for the 300 pulses this would suggest an increase in S/N ratio of 12 times over the Zircon Cell, provided the signal intensity remained the same. However using the pulse maxima to calculate the difference in S/N ratio the DCI & Enterprise Cell had only an average 4.6 times improvement over the Zircon Cell, 51,400 counts against 11,200 counts for the DCI & Enterprise Cell and Zircon Cell respectively. The discrepancy in the difference in S/N ratio between the pulse width and pulse maxima is due to a decrease in signal intensity when using the DCI & Enterprise Cell. The average ^{238}U signal intensity for 300 shots was 275,000 counts

pulse area for the Zircon Cell, but only 194,000 counts pulse area with the DCI & Enterprise Cell. To confirm the decrease in efficiency of the LA-ICP-MS with the DCI & Enterprise coupling mechanism the detection efficiency was determined (section 5.3.2).

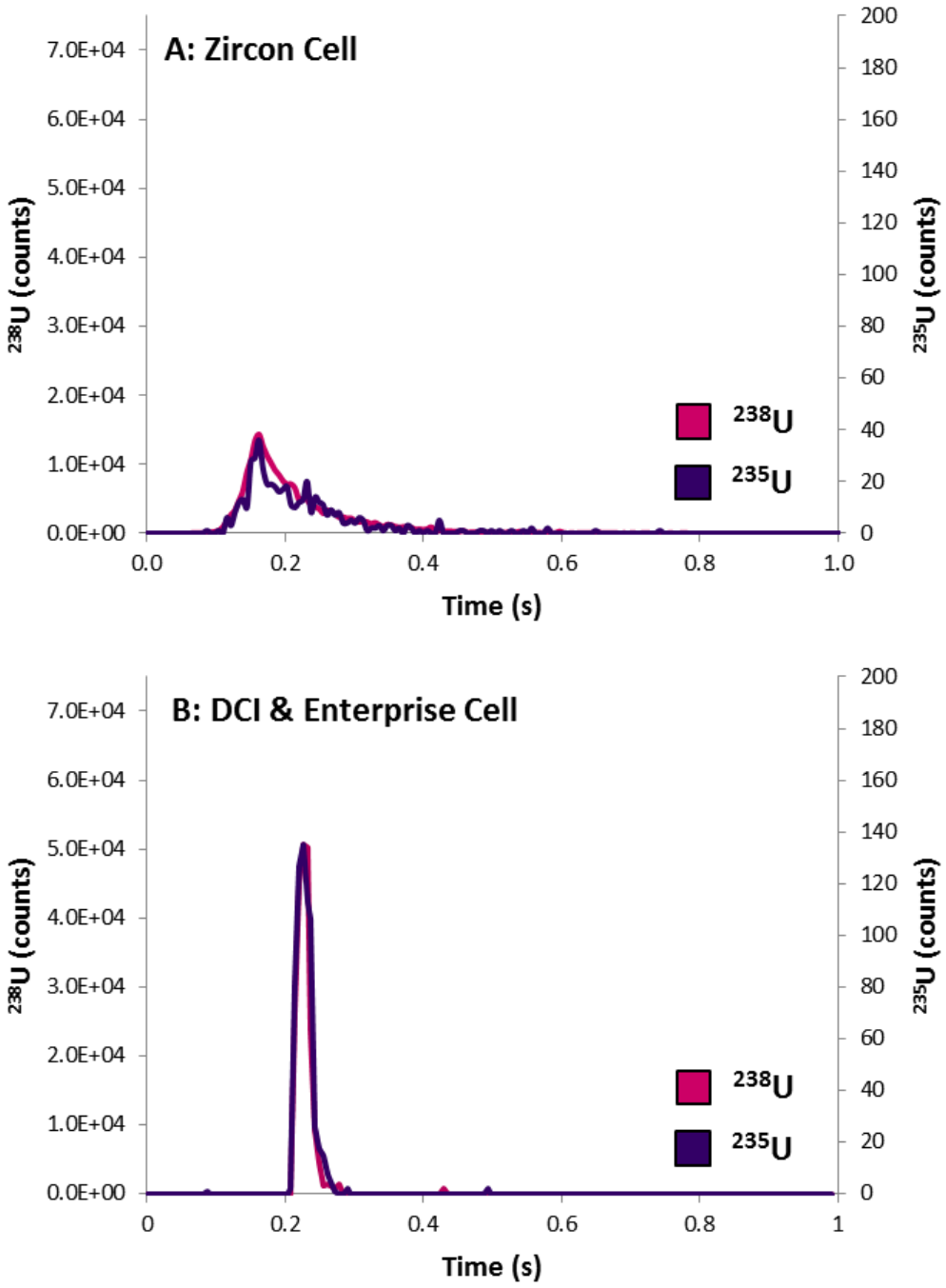

Figure 55 – Pulse profiles of ^{235}U (purple) and ^{238}U (pink) for SRM611, Zircon Cell and DCI & Enterprise Cell. Integration time = 5.8 ms. Laser conditions: Fluence = 3 J cm^{-2}, Spot size = 20 µm, Ablation type – spot. A. Zircon Cell. B. DCI & Enterprise Cell. The signal for the DCI & Enterprise was compressed into a narrow timeframe, increasing the S/N ratio.

For both the Zircon Cell and the Enterprise Cell the pulse profiles of ^{235}U and ^{238}U were closely aligned. The close alignment between the two profiles suggested any spectral skew was sufficiently

constraint to prevent disassociation of the ^{235}U and ^{238}U signals. Despite average pulse duration of 29ms for the DCI & Enterprise Cell the mean isotope ratio should be accurately determined.

5.3.2 Evaluation of the Detection Efficiency by Laser Ablation

From the signal intensity a decrease in detection efficiency was expected for the DCI & Enterprise Cell relative to the Zircon Cell. To determine the detection efficiency by laser ablation the same approach to Chapter 2 for the LA-MC-ICP-MS system was adopted. Deep craters were ablated into the surface of the SRM 611 by firing 50 shots at a rate of 1 Hz with a fluence of 3 J cm^{-2}. Spot sizes of 20, 25, 35 and 50 µm were used to form an identifiable geometric pattern on the SRM 611 glass surface. The volume of the craters was then measured using an Aliconia InfiniteFocus™ 3D microscope from the Metrology Unit within the School of Mechanical and Manufacturing Engineering at Loughborough University. From the volume, given that the concentration and isotopic composition of the reference material is known, it was possible to calculate the number of atoms sampled and by comparing to the number of ions detected, determine the detection efficiency.

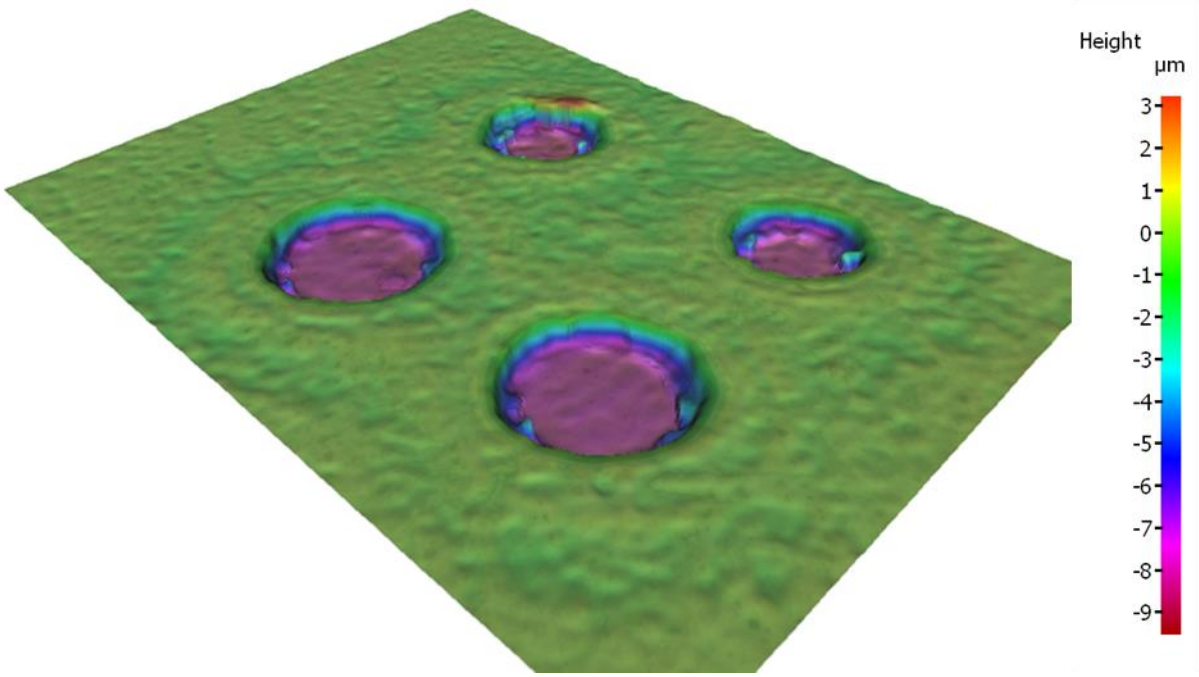

Figure 56 – 3D Image of 2x50 µm and 2x35 µm craters ablated into NIST SRM611, created with the Aliconia InfiniteFocus™ Microscope. The area imaged was 286.99 µm by 217.72 µm. The surface plane of the SRM611 glass was set to 0 µm height.

From the determined detection efficiencies (Table 39) it was possible to conclude there was a drop in both signal intensity and detection efficiency when using the DCI & Enterprise Cell compared to the Zircon Cell. This was in direct contrast to the LA-MC-ICP-MS setup in Chapter 2, where the signal intensity and detection efficiency had been higher with the prototype coupling mechanism. While no firm reason for the discrepancy has been discovered a possible explanation can be proposed. The

Enterprise Cell, as a prototype, was not without its flaws. One of those flaws was the seal of the cell lid to the main body, over time the thread of the screws holding the lid down deteriorated, affecting the seal and perhaps ultimately the crucial gas flow within the cell. When used with the single collector ICP-MS the seal of the Enterprise Cell was in poor repair, had deteriorated compared to its state when previously couple to the MC-ICP-MS, and attendant to the analysis failed completely.

Table 39 – Detection efficiency values for the LA-ICP-MS system for 4 different spot sizes, DCI & Enterprise Cell and Zircon Cell. The number of ions detected was determined from the volume; given the concentration of uranium in the SRM611 glass is known. The detection efficiency was consistently greater for the Zircon Cell than with the DCI & Enterprise Cell.

Spot Size	Volume (μm^3)		No. Atoms Sampled		No. Ions Detected		Detection Efficiency (%)	
	DCI & Enterprise	Zircon Cell	DCI & Enterprise	Zircon Cell	DCI & Enterprise	Zircon Cell	DCI & Enterprise	Zircon Cell
50 µm	6.7E+03	7.1E+03	2.0E+10	2.1E+10	5.4E+07	8.5E+07	**0.28**	**0.41**
50 µm	6.9E+03	5.9E+03	2.0E+10	1.7E+10	5.7E+07	8.5E+07	**0.28**	**0.49**
35 µm	3.9E+03	4.6E+03	1.1E+10	1.4E+10	3.3E+07	5.1E+07	**0.29**	**0.38**
35 µm	4.3E+03	4.7E+03	1.3E+10	1.4E+10	3.3E+07	5.6E+07	**0.26**	**0.41**
25 µm	1.7E+03	2.0E+03	5.1E+09	5.8E+09	1.7E+07	2.4E+07	**0.33**	**0.42**
25 µm	1.7E+03	1.9E+03	5.0E+09	5.6E+09	1.6E+07	2.4E+07	**0.33**	**0.44**
20 µm	1.0E+03	1.1E+03	3.1E+09	3.4E+09	1.1E+07	1.5E+07	**0.35**	**0.46**
20 µm	1.2E+03	1.2E+03	3.6E+09	3.5E+09	1.1E+07	1.5E+07	**0.30**	**0.44**

With the LA-MC-ICP-MS setup in Chapter 2, the detection efficiency of the DCI & Enterprise Cell coupling mechanism varied with spot size, the smaller the spot sizes the greater the detection efficiency measured. The change in detection efficiency with spot size was mirrored by changes in the shape of the pulse. For the two spot sizes above 25µm, 35µm and 50µm, the height of the pulse did not increase, but instead the extra counts were expressed by an increase in the pulse duration. For the single collector LA-ICP-MS setup the analysis summarised in Table 39 did not exhibit a change in detection efficiency with spot size; however the shape of the pulse did change with spot size (Figure 57).

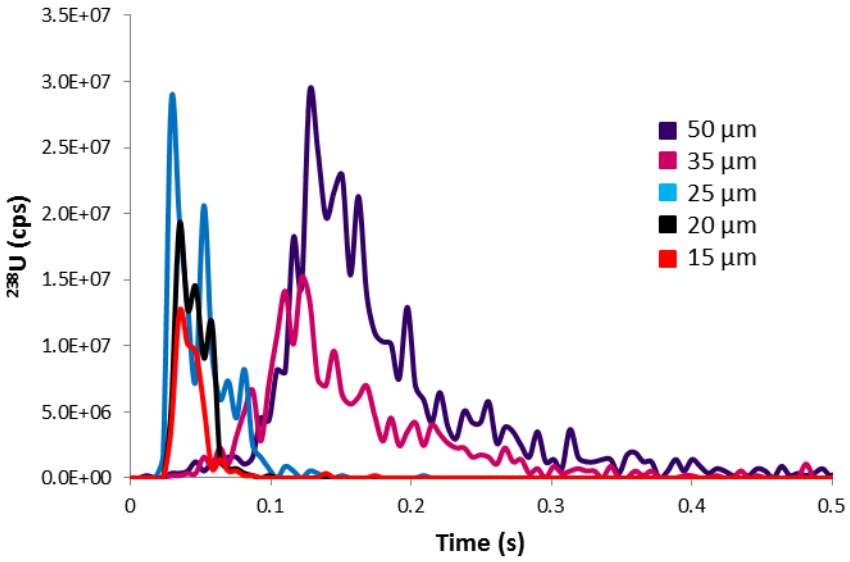

Figure 57 - Typical pulse profiles of different spot sizes on SRM611 using the DCI & Enterprise Cell. The three smallest spot sizes generated pulse profiles less than 100ms in duration. At larger spot sizes the pulse profiles altered, broadening to over 200ms.

At 15, 20 and 25µm spot sizes, the pulses have the same general profile and develop over approximately the same period of time. However at 35µm and 50µm spot sizes the pulse profile changed, broadening to a time frame and shape similar to the pulse profiles generated by the Zircon Cell. Compared to the smaller spot sizes, at 35µm and 50µm the pulse maximum is delayed relative to the start of the pulse. Possible rationales for the changing behaviour of the DC & Enterprise Cell at larger spot sizes are discussed in Chapter 2.

Table 40 – Detection efficiency values for the LA-ICP-MS system for 6 different spot sizes, DCI & Enterprise Cell only. The detection efficiency was dependent on the spot size, with higher detection efficiency achieved at smaller spot sizes.

Spot Size	Volume (µm^3)	No. Atoms Sampled	No. Ions Detected	Detection Efficiency (%)
50 µm	1.1E+04	3.2E+10	4.6E+07	0.14
50 µm	1.0E+04	2.9E+10	4.6E+07	0.15
35 µm	6.2E+03	1.7E+10	3.0E+07	0.16
35 µm	6.4E+03	1.8E+10	3.0E+07	0.16
25 µm	2.3E+03	6.3E+09	1.5E+07	0.23
25 µm	2.6E+03	7.1E+09	1.5E+07	0.20
20 µm	1.5E+03	4.3E+09	1.1E+07	0.23
20 µm	1.5E+03	4.3E+09	1.1E+07	0.25
15 µm	7.1E+02	2.0E+09	6.1E+06	0.30
15 µm	7.2E+02	2.0E+09	6.1E+06	0.29
10 µm	2.4E+02	6.8E+08	2.1E+06	0.30
10 µm	2.6E+02	7.1E+08	2.4E+06	0.32

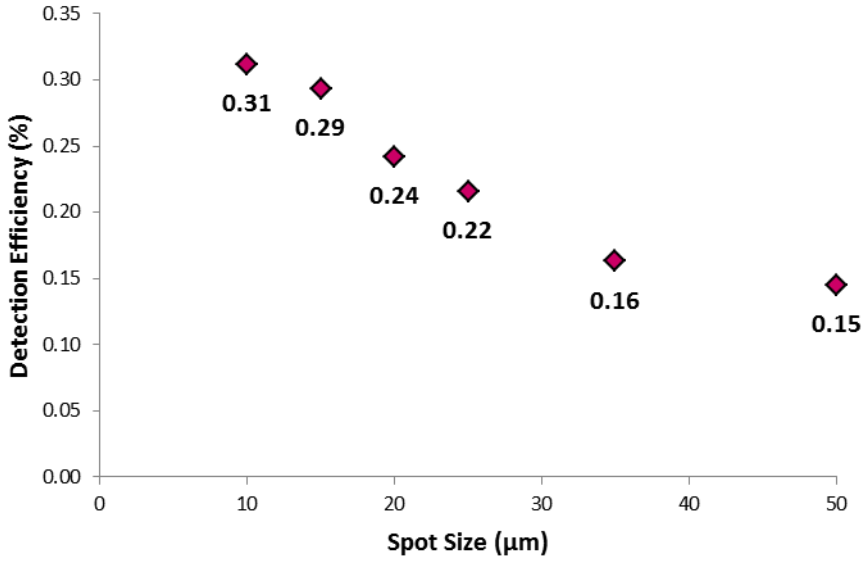

Figure 58 – Detection efficiency plotted against spot size for single collector LA-ICP-MS, coupled with the DCI & Enterprise Cell. For each spot size the average detection efficiency was calculated from the values reported in Table 40.

Subsequent determination of the detection efficiency with the DCI & Enterprise Cell demonstrated the same dependence between the detection efficiency and spot size which was seen with the MC-ICP-MS (Table 40 and Figure 58). At the point of writing no hypothesis as to why no correlation was observed in the analysis from Table 39 has been developed.

5.3.3 Determination of $^{235}U/^{238}U$ for SRM611, Data Evaluation Strategies

Due to the different response times of the ion counters and Faraday cups in the mixed detector array of the MC-ICP-MS used in Chapter 2, only one data evaluation strategy, total signal integration (TSI) was deemed suitable for isotope ratio analysis. However the single collector mass spectrometer only has one detector. Due to the pseudo-simultaneous nature of the measurement, the response time of both isotopes, ^{235}U and ^{238}U, should be nearly identical. As the pulse profiles of the two isotopes were shown to track one another (Figure 55, section 5.3.1) other data evaluation strategies, point-to-point (P2P) and linear regression may also be adopted alongside TSI.

The P2P data evaluation strategy is historically the method by which isotope ratios have been determined in ICP-MS. The isotope ratio is determined at each integration point, in a selected period of time, and from the isotope ratio values a mean and uncertainty are derived. As an alternative to P2P, linear regression was developed[6] for LA-MC-ICP-MS with the aim of improving precision. In linear regression the isotopes are plotted against one another as an x-y scatter plot and a linear fit

plotted through the points using the least squared method, with the isotope ratio equivalent to the gradient of the linear fit.

Given that one of the stated aims of this project was to determine the isotope ratio of a single particle, the "ideal" data evaluation strategy was considered to be P2P. Linear regression requires multiple data points, and hence multiple particles to successfully determine a composition. For a successfully identified composition the uncertainty on the measurement is the uncertainty on the population, not of the measurement of a single particle. Using TSI the isotope ratio is determined for each individual particle; however the uncertainty of the measured isotope ratio for each particle cannot be reported, except that which can be determined from counting statistics. Therefore if the requirement is for an isotope ratio measurement for each particle with an associated uncertainty on the measurement, then P2P is the only solution out of the three data evaluation strategies.

5.3.3.1 Determination of $^{235}U/^{238}U$ using the P2P Data Evaluation Strategy

For the 300 laser ablation pulses generated with the DCI & Enterprise Cell the $^{235}U/^{238}U$ isotope ratio was determined using the P2P data evaluation strategy. The analysis was carried out in Iolite (version 2.5)[7], a non-commercial download software package add-on in Igor Pro™ (version 6.46) developed for LA-ICP-MS. A data reduction scheme (DRS) was written which determined the isotope ratio by two different methods. The first used the arithmetic approach currently widely used in the isotope ratio analysis community and the second used the geometric approach, discussed and recommended in Chapter 3. The signal integration windows were selected automatically by the software package based on the ^{235}U signal intensity. An integration window was created if the ^{235}U signal was greater than 1,000cps (2 true counts) for more than three concurrent integrations of 5.8ms.

Although 300 pulses were ablated using SRM611, not every pulse returned what was deemed sufficient signal. Unlike the UP193FX laser used earlier in Chapter 2, the solid-state based laser ablation system, UP193SS, required some time to "heat up" and therefore the first one or two pulses on to the surface of the glass had much less energy than the subsequent pulses.

Unlike with the TSI data evaluation strategy it is now necessary to differentiate between the uncertainty of the isotope ratio on each measurement and the uncertainty on the isotope ratio for the population. Using the terminology of Pointurier *et al* (2011)[8] the average uncertainty on each measurement has been termed the uncertainty and the average uncertainty of the population, the reproducibility of the measurement.

Table 41 – Mean $^{235}U/^{238}U$ values for 294 pulses, DCI & Enterprise Cell, P2P calculated using both the arithmetic and geometric approach. For both approaches the mean isotope ratio was within uncertainty to the certified composition. The uncertainty and reproducibility were similar for both the approaches.

Method	n = 294	$^{235}U/^{238}U$, P2P (Arithmetic)	$^{235}U/^{238}U$, P2P (Geometric)
DCI & Enterprise Cell	**R_{mean}**	2.31E-03	2.24E-03
	Uncertainty		
	(-RSE)	(10.7%)	(10.4%)
	(+RSE)	(10.7%)	(11.6%)
	Reproducibility		
	(-RSD)	(11.2%)	(10.9%)
	(+RSD)	(11.2%)	(12.2%)
	RD	-3.13	-6.29
	(-RSE)	(0.65%)	(0.64%)
	(+RSE)	(0.65%)	(0.71%)

Table 42 – Mean $^{235}U/^{238}U$ values for 284 pulses, Zircon Cell, P2P calculated using both the arithmetic and geometric approach. In contrast to the DCI & Enterprise Cell (Table 41) the mean $^{235}U/^{238}U$ differs between the arithmetic and geometric approaches. Only the geometric mean is within uncertainty of the certified isotopic composition (RD).

Method	n = 284	$^{235}U/^{238}U$, P2P (Arithmetic)	$^{235}U/^{238}U$, P2P (Geometric)
Zircon Cell	**R_{mean}**	3.08E-03	2.37E-03
	Uncertainty		
	(-RSE)	(12.4%)	(9.43%)
	(+RSE)	(12.4%)	(10.4%)
	Reproducibility		
	(-RSD)	(12.6%)	(9.08%)
	(+RSD)	(12.6%)	(9.99%)
	RD	25.8	-0.26
	(-RSE)	(0.75%)	(0.54%)
	(+RSE)	(0.75%)	(0.59%)

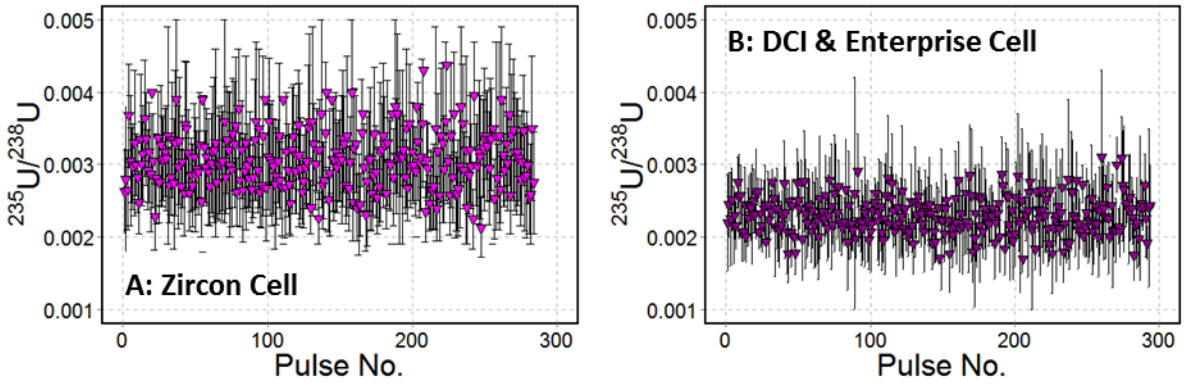

Figure 59 – $^{235}U/^{238}U$ isotope ratio determined using the arithmetic approach plotted against pulse number, error bars are 2SE. A. Zircon Cell, 284 pulses. B. DCI & Enterprise Cell, 294 pulses. The reproducibility (error bars) on each pulse is improved with the DCI & Enterprise Cell. The mean $^{235}U/^{238}U$ isotope ratio for the Zircon Cell is biased higher relative to both the certified value and the DCI & Enterprise Cell.

When using the arithmetic approach to calculate $^{235}U/^{238}U$ the relative difference (RD) – $100\left(\frac{measured}{true}-1\right)$ – values calculated for the Zircon Cell and the DCI & Enterprise Cell differ by nearly 30%. The majority of the difference is due to the R_{mean} for the Zircon Cell being biased towards higher $^{235}U/^{238}U$ ratios (Figure 59). Without the work of Aitchison[9–12] it would be possible to conclude the improved S/N ratio of the DCI & Enterprise Cell had significantly improved the potential of using the single collector ICP-MS to determine isotope ratios for transient signals.

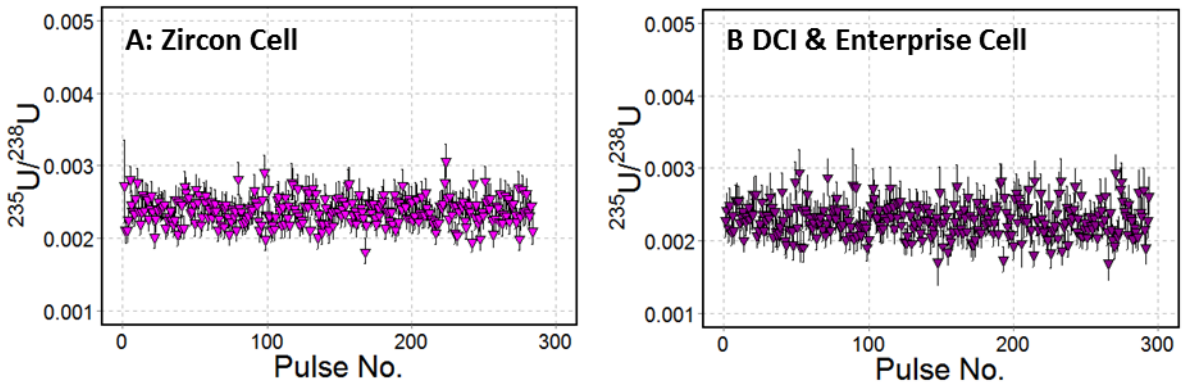

Figure 60 – $^{235}U/^{238}U$ isotope ratio determined using the geometric approach plotted against pulse number, error bars are 2SE. A. Zircon Cell, 284 pulses. B. DCI & Enterprise Cell, 294 pulses. In contrast to the arithmetic approach (Figure 59), the reproducibility and mean isotope ratio are similar for both cells.

However using the geometric approach to determine the $^{235}U/^{238}U$ isotope ratio instead of the arithmetic approach; the bias with the Zircon Cell towards isotope ratio values higher than the expected composition, was eliminated (Figure 60). The average uncertainty on each measurement for the two coupling mechanisms, reported as RSE in Tables 41 and 42, appear broadly similar. However by converting the RSE to RSD, calculated by $\mathrm{SD} = \mathrm{SE} \times \sqrt{\mathrm{n}}$, where n is the number of data points, the two coupling mechanisms are no longer similar. The pulse duration with the Zircon Cell is

nearly 12 times greater than the pulse duration with the DCI & Enterprise Cell. Hence by converting the RSE to RSD for both cells it becomes apparent the RSD on each measurement for the Zircon Cell is actually approximately 3.5 times greater than for the DCI & Enterprise Cell. The difference in the isotope ratio using the arithmetic or geometric approach is more pronounced for measurements with larger uncertainties and low absolute ratios[13]. Therefore due to the large measurement uncertainty with the Zircon Cell the geometric approach to isotope ratio analysis is crucial to prevent bias.

The performances of both coupling mechanisms using the geometric approach are broadly similar, with the RD of the Zircon Cell better than the DCI & Enterprise Cell. As has already been stated however, the uncertainty on the measurement for each pulse was less with the DCI & Enterprise Cell. As one of the stated aims of the project is to determine the isotope ratio of a single particle, this is a powerful reason in favour of the improved S/N ratio delivered by the DCI & Enterprise Cell.

5.3.3.2 Determination of $^{235}U/^{238}U$ using the Linear Regression Data Evaluation Strategy

Although contrary to the aim of determining the isotope ratio for a single particle, an attempt was made to find the isotope ratio using the linear regression data evaluation strategy, following the method laid out in Fietzke *et al* (2008)[6].

Table 43 – $^{235}U/^{238}U$ isotope ratio results for SRM611, determined for both the Zircon Cell and DCI & Enterprise Cell, using the linear regression data evaluation strategy. The accuracy and precision were improved by approx. 3 times using the DCI & Enterprise Cell over the Zircon Cell.

Parameter	Zircon Cell	DCI & Enterprise Cell
R_{mean}	1.90E-03	2.21E-03
(RSD)	(77.9%)	(25.4%)
RD	-20.2	-7.20
(RSE)	(0.25%)	(0.08%)

The linear regression data evaluation strategy for isotope ratio analysis was developed with the aim of improving the accuracy and precision of the measurement relative to P2P. Compared to the P2P data evaluation strategy neither aim was achieved for the SRM611 dataset using either the Zircon Cell or DCI & Enterprise Cell. Similar to P2P the improved S/N ratio when using the DCI & Enterprise Cell resulted in significant improvements both in the RD and RSD of 13% and 52.5% respectively, compared to with the Zircon Cell. Even with the DCI & Enterprise Cell the RSD on the $^{235}U/^{238}U$ ratio determined by linear regression was more than twice what had been determined by P2P with the same dataset.

5.3.3.3 Determination of $^{235}U/^{238}U$ by the Total Signal Integration Data Evaluation Strategy

In the third data evaluation strategy, the isotope ratios are not calculated for each integration, but are instead calculated from the sum of the total number of counts for each isotope (TSI). TSI was the only data evaluation strategy which could be used to determine the uranium isotope ratios with the mixed detector array on the MC-ICP-MS. By calculating the isotope ratio using TSI on the single collector ICP-MS a direct comparison could be made to previous analyses on the MC-ICP-MS.

Table 44 – $^{235}U/^{238}U$ isotope ratio results for SRM611, determined for both the Zircon Cell and DCI & Enterprise Cell, using the TSI data evaluation strategy. Of the two coupling cells the Zircon Cell analysis was more accurate, with reduced uncertainty.

Parameter	Zircon Cell	DCI & Enterprise Cell
R_{mean}	2.37E-03	2.28E-03
n	284	294
(-RSD)	(7.52%)	(9.58%)
(+RSD)	(8.13%)	(10.6%)
RD	-0.26	-4.09
(-RSE)	(0.45%)	(0.56%)
(+RSE)	(0.48%)	(0.62%)

Unlike either the P2P or linear regression data evaluation strategies, the improved S/N ratio with the DCI & Enterprise Cell compared to the Zircon Cell does not improve the $^{235}U/^{238}U$ isotope ratio analysis. By summing all of the counts for each isotope the crucial factor in determining the RD and RSD of the isotope ratio was no longer the S/N ratio, but the detection efficiency which was achieved with each coupling mechanism. For this analysis the detection efficiency of the Zircon Cell was demonstrated in section 5.3.2 to be superior to that of the DCI & Enterprise Cell.

For the same number of pulses on SRM611, the RSD on the $^{235}U/^{238}U$ ratio with the Zircon Cell was 1.34% using the MC-ICP-MS, compared to 7.82% on the single collector ICP-MS. For the DCI & Enterprise Cell the corresponding RSD values on the $^{235}U/^{238}U$ ratio were 2.93% (MC-ICP-MS) and 10.1% (single collector ICP-MS). Although the LA-ICP-MS analysis with the single collector mass spectrometer was not affected with the same spectral skew from the mixed detector array experienced by the LA-MC-ICP-MS analysis, this did not translate into higher precision. Due to the decreased detection efficiency, the limiting uncertainty on the $^{235}U/^{238}U$ isotope ratio with the single collector ICP-MS (Zircon Cell) setup, calculated by counting statistics, was 3.97%. Discounting any other sources of addition uncertainty the reduced count rate achieved with the single collector ICP-

MS alone was sufficient cause to prevent the $^{235}U/^{238}U$ ratio having higher precision than on the multi-collector.

5.4 Analysis of NUSIMEP UO_x particles

Following analysis of SRM611 the LA-ICP-MS system, with both the DCI & Enterprise Cell and Zircon Cell coupling mechanisms, was used to analyse NUSIMEP UO_x particles on both the NUSIMEP-6 and NUSIMEP-7 dual composition planchet, NU7-021. The expected $^{235}U/^{238}U$ ratios of the NUSIMEP particles are given in Table 46. To increase the likelihood of only ablating a single particle with each shot of the laser, the spot size was reduced from 20µm on SRM611 to 5µm on the NUSIMEP planchets.

Table 45 – Laser conditions on UP-193SS for isotope ratio analysis of NUSIMEP UO_x particles.

Setting	Parameter
Ablation Mode	Single shot
Fluence (J cm^{-2})	2.5-3.5
Repetition rate (Hz)	1
Spot Size	5

Table 46 – Certified Uranium Isotope Compositions of the NUSIMEP particles.

Planchet		$^{235}U/^{238}U$
NUSIMEP-6[14]		7.0439e-03
NUSIMEP-7(dual composition) [15]	**1st**	9.0726e-03
	2nd	3.4148e-02

5.4.1 Analysis of NUSIMEP-6 Planchet

The first planchet analysed was the single composition planchet, NUSIMEP-6. Likely as a consequence of the "smear" of uranium material reported on the surface of the NUSIMEP planchet[16], almost every ablation of the surface returned some signal. With the Zircon Cell coupling mechanism as many pulses as could be fitted into 15, 10,000 cycle, runs were collected and for the DCI & Enterprise Cell 10 runs of 10,000 cycles were collected. As the pulse duration with the DCI & Enterprise Cell was shorter than with the Zircon Cell, less time between shots was required and therefore more pulses could be collected in the same period of time.

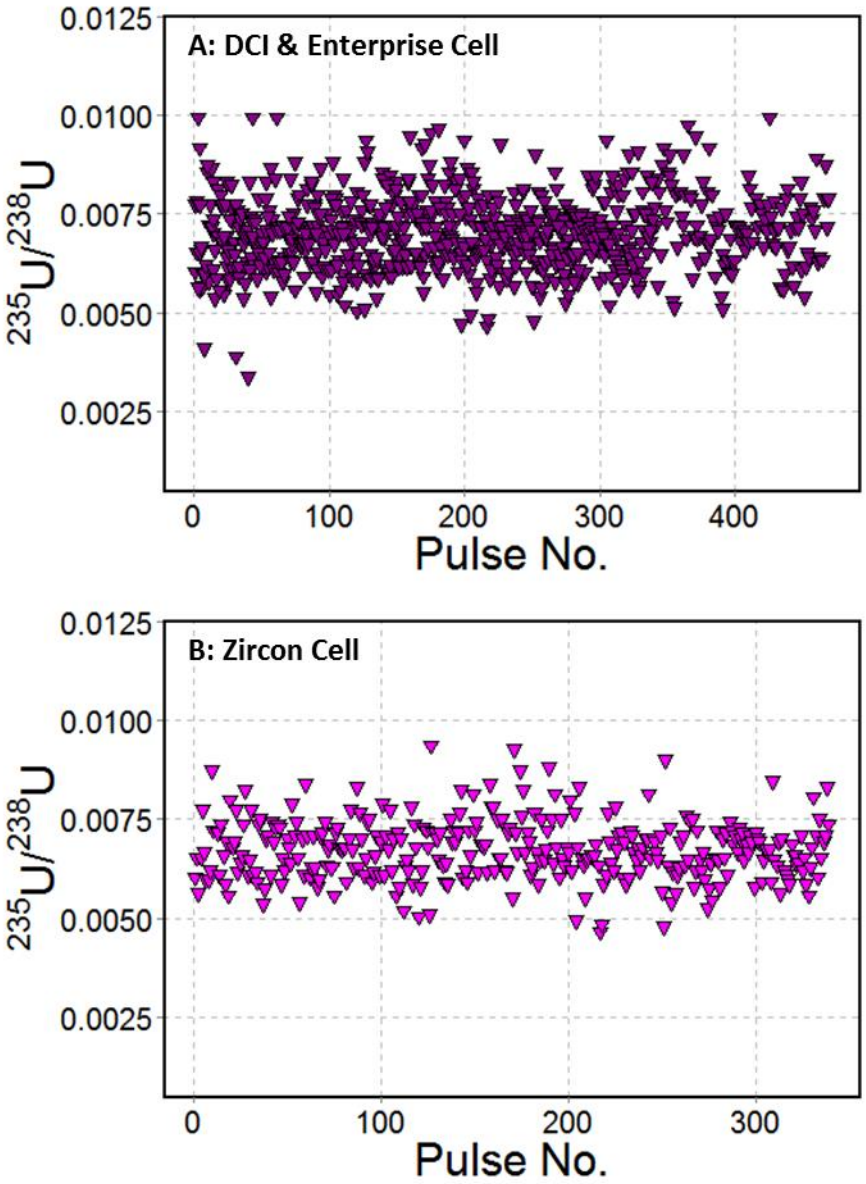

Figure 61 – $^{235}U/^{238}U$ isotope ratio determined using P2P (Geometric) plotted against pulse number. A. DCI & Enterprise Cell, 469 pulses. B. Zircon Cell, 339 pulses. The reproducibility of the $^{235}U/^{238}U$ ratio was better with the Zircon Cell, than with the DCI & Enterprise Cell.

As for SRM611, using the arithmetic approach with the Zircon Cell to calculate the $^{235}U/^{238}U$ ratio (Table 48) resulted in a bias towards an enriched isotope ratio relative to the expected composition. Using the geometric approach instead of the arithmetic approach on the same dataset improved not only the RD, but the uncertainty (RSE) and reproducibility (RSD). Using the P2P (Geometric) data evaluation strategy the reproducibility of the Zircon Cell was 2.4-3.0% better than the DCI, mainly due to the presence of some outliers in the dataset collected with the DCI & Enterprise Cell (Figure 61A, bottom left).

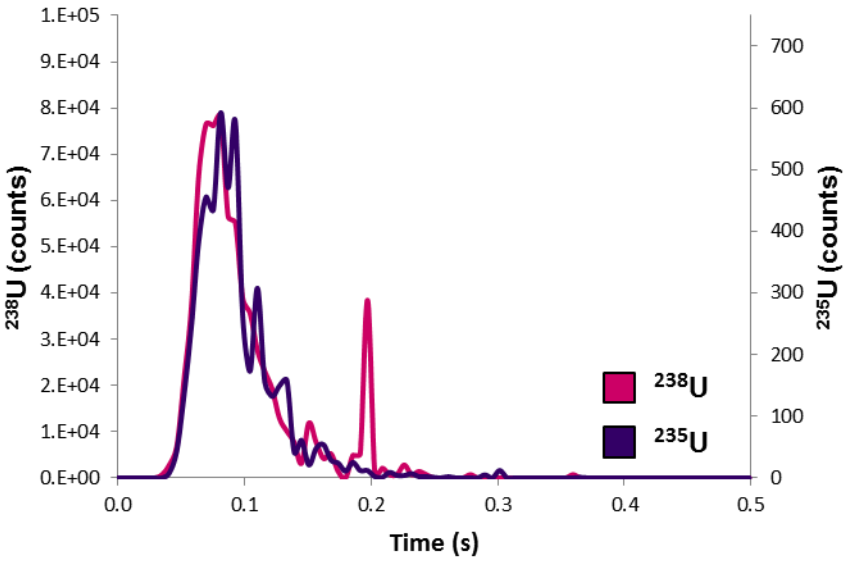

Figure 62 – Pulse profiles of ^{235}U (purple) and ^{238}U (pink) for NUSMEP-6, DCI & Enterprise Cell. Integration time = 5.8 ms. The ^{238}U pulse profile has a single integration, transient, spike in the tail the pulse. Addition of these counts to the integrated ^{238}U signal, results in a bias on the calculated $^{235}U/^{238}U$ ratio.

The outliers in the dataset collected with the DCI & Enterprise Cell were due to single sharp integration spikes in the pulse profile (Figure 62). The same transient spikes were first identified as a source of additional uncertainty in Chapter 4, although the cause of the addition uncertainty on the MC-ICP-MS was different to the cause on the single collector ICP-MS. On the MC-ICP-MS the detector array measures simultaneously and therefore the single integration spike occurred on every isotope; the source of the additional uncertainty was down to the different response times of the Faraday cups and ion counters in the mixed detector array. On a single collector ICP-MS the isotopes are not measured simultaneously, the dwell time on each isotope was 200 µs, with a settling time of 40 µs. As the cause of the single integration spike is a large particle entering the plasma whole, the width of the spike is 200-500 µs[3], the residence time of a particle in the ICP plasma. As the width of the spike is equal to the dwell time on each isotope, the single integration spike only occurs on one of the isotopes measured (Figure 62), introducing a bias.

Table 47 – $^{235}U/^{238}U$ isotope ratio results for NUSIMEP-6, DCI & Enterprise Cell. Two data evaluation strategies are reported, P2P (Geometric) and TSI.

Method	n = 469	$^{235}U/^{238}U$, P2P (Geometric)	$^{235}U/^{238}U$, TSI
DCI & Enterprise Cell	**R_{mean}**	7.17E-03	7.30E-03
	Uncertainty		
	(-RSE)	(11.3%)	-
	(+RSE)	(12.8%)	-
	Reproducibility		

	(-RSD)	(13.0%)	(7.64%)
	(+RSD)	(14.9%)	(8.27%)
	RD	1.70	3.50
	(-RSE)	(0.60%)	(0.35%)
	(+RSE)	(0.69%)	(0.38%)

Table 48 – $^{235}U/^{238}U$ isotope ratio results for NUSIMEP-6, Zircon Cell. Three data evaluation strategies are reported, P2P (Arithmetic), P2P (Geometric) and TSI. The P2P (Arithmetic) approach introduced a significant bias in the isotope ratio reported.

Method	**n = 339**	**$^{235}U/^{238}U$, P2P (Arithmetic)**	**$^{235}U/^{238}U$, P2P (Geometric)**	**$^{235}U/^{238}U$, TSI**
Zircon Cell	**R_{mean}**	9.56E-03	6.70E-03	6.72E-03
	Uncertainty			
	(-RSE)	(13.5%)	(9.93%)	-
	(+RSE)	(13.5%)	(11.0%)	-
	Reproducibility			
	(-RSD)	(16.7%)	(10.6%)	(12.2%)
	(+RSD)	(16.7%)	(11.9%)	(13.9%)
	RD	30.6	-5.02	-4.73
	(-RSE)	(0.90%)	(0.58%)	(0.66%)
	(+RSE)	(0.90%)	(0.65%)	(0.75%)

For the TSI data evaluation strategy the RD and RSD of the $^{235}U/^{238}U$ ratio were improved by using the DCI & Enterprise Cell rather than the Zircon Cell. This outcome is counter to the P2P (Geometric) results and highlights the importance the data evaluation strategy plays in the isotope ratio determined.

For 300 pulses on NUSIMEP-6, the RSD on the $^{235}U/^{238}U$ ratio with the Zircon Cell was 2.93-3.01% using the MC-ICP-MS. As for SRM611 the limiting uncertainty on the $^{235}U/^{238}U$ isotope ratio with the single collector instrumentation was greater than the experimental RSD achieved on the MC-ICP-MS. However when compared to the quadrupole-based LA-ICP-MS analysis of NUSIMEP-6 by Pointurier *et al* (2011)[8], the RSD and RD achieved were halved with the single collector sector field ICP-MS. The improvement in RSD and RD was most likely due to the increased sensitivity which can be achieved with sector field based ICP-MS compared to most quadrupole-based ICP-MS instruments.

5.4.2 Analysis of NUSIMEP-7 (Dual Composition) Planchet

Of the two NUSIMEP-7 planchets, only one, the dual composition planchet, was analysed using the single collector based LA-ICP-MS setups. In Chapter 4, it was shown experimentally that of the two expected isotopic composition on the original NIGL planchet, NU7-043, only the 2nd composition (Table 46) could be identified. This planchet was swapped for another dual composition planchet, NU7-021, obtained from another participant in the original NUSIMEP-7 inter-laboratory comparison (ILC). Unlike NU7-43, on NU7-021 particles of both expected compositions were easily identified. It was the 2nd planchet, NU7-021, which was analysed on the single collector ICP-MS.

Lacking the "smear" of uranium material identified on NUSIMEP-6, not every ablation pulse of the surface of NU7-021 returned uranium signal. With both the DCI & Enterprise Cell and Zircon Cell, analyses were continued until uranium signals from over 100 particles had been observed.

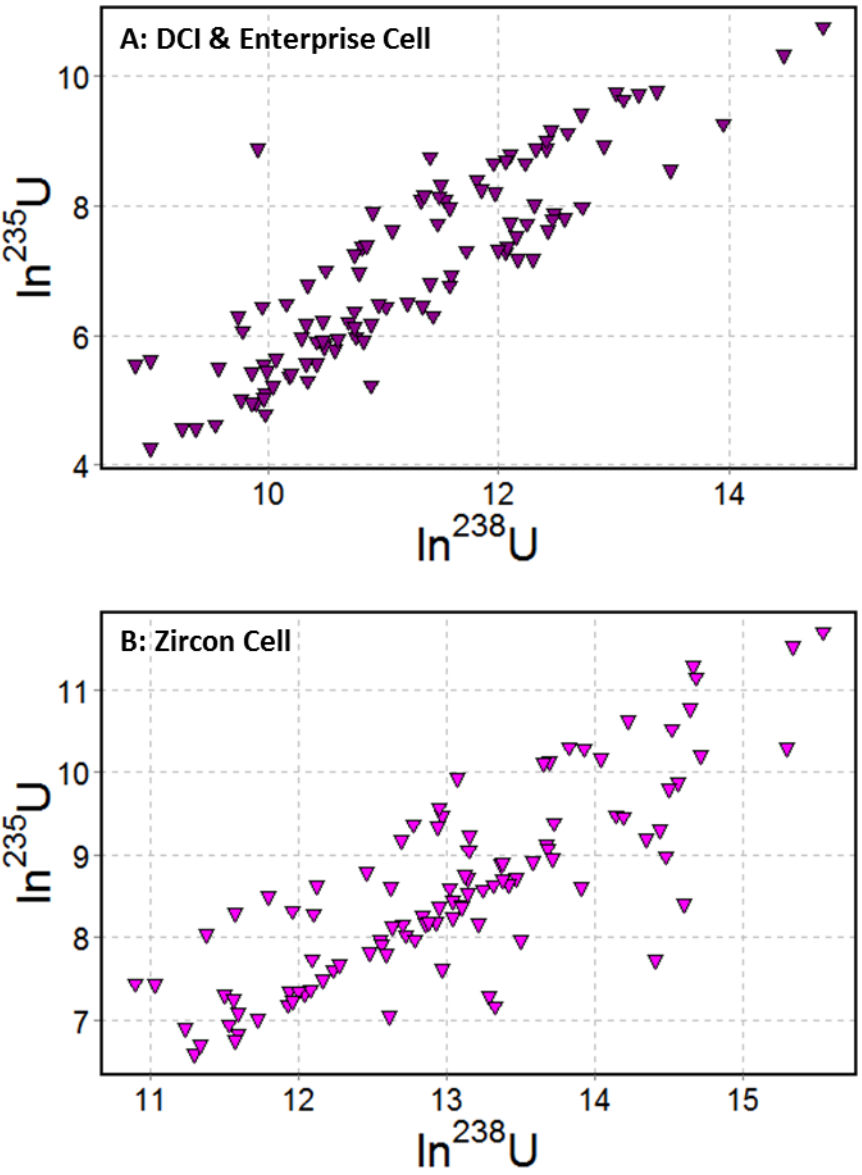

Figure 63 – plots of ln ^{235}U against ln ^{238}U for NUSIMEP-7 (dual composition), TSI. A. DCI & Enterprise cell. B. Zircon Cell. In both plots two separate regression lines can be identified.

Using the TSI data evaluation strategy, plotting the total number of ^{235}U counts against the total number of ^{238}U counts (Figure 63), two compositions could be identified within the more than 100 particles collected, for both DCI & Enterprise Cell and Zircon Cell. The Flexmix package in R, first used by Kappel *et al* (2013)[17] on NUSIMEP-7, was used to assign each particle to a cluster. Two of the clusters assigned were correlated to the two expected isotopic compositions. For both coupling mechanisms, particle signals which Flexmix had deemed not to be part of either cluster (outliers in the dataset) were assigned to a 3rd cluster. Only particles in the first two clusters were used in the isotope ratio analysis.

Table 49 – $^{235}U/^{238}U$ isotope ratio results for NUSIMEP-7 (dual composition), DCI & Enterprise Cell. Two data evaluation strategies are reported, P2P (Geometric) and TSI.

1st composition	**n = 61**	**$^{235}U/^{238}U$, P2P (Geometric)**	**$^{235}U/^{238}U$, TSI**
DCI & Enterprise Cell	**R_{mean}**	9.07E-03	9.25E-03
	Uncertainty		
	(-RSE)	(22.2%)	-
	(+RSE)	(28.6%)	-
	Reproducibility		
	(-RSD)	(22.5%)	(20.8%)
	(+RSD)	(29.1%)	(26.3%)
	RD	0.004	1.95
	(-RSE)	(2.85%)	(2.66%)
	(+RSE)	(3.66%)	(3.36%)
2nd composition	**n = 44**	**$^{235}U/^{238}U$, P2P (Geometric)**	**$^{235}U/^{238}U$, TSI**
DCI & Enterprise Cell	**R_{mean}**	2.95E-02	3.10E-02
	Uncertainty		
	(-RSE)	(18.8%)	-
	(+RSE)	(23.1%)	-
	Reproducibility		
	(-RSD)	(23.9%)	(23.0%)
	(+RSD)	(31.4%)	(29.8%)
	RD	-14.7	-9.84
	(-RSE)	(3.60%)	(3.46%)
	(+RSE)	(4.74%)	(4.49%)

Table 50 – $^{235}U/^{238}U$ isotope ratio results for NUSIMEP-7 (dual composition), Zircon Cell. Three data evaluation strategies are reported, P2P (Arithmetic), P2P (Geometric) and TSI.

1st composition	**n = 66**	**$^{235}U/^{238}U$, P2P (Arithmetic)**	**$^{235}U/^{238}U$, P2P (Geometric)**	**$^{235}U/^{238}U$, TSI**
Zircon Cell	**R_{mean}**	1.61E-02	9.69E-03	9.18E-03
	Uncertainty			
	(-RSE)	(23.2%)	(12.8%)	-
	(+RSE)	(23.2%)	(14.7%)	-
	Reproducibility			
	(-RSD)	(60.7%)	(23.5%)	(22.4%)
	(+RSD)	(60.7%)	(30.8%)	(28.9%)
	RD	57.6	6.58	1.21
	(-RSE)	(7.47%)	(2.90%)	(2.76%)
	(+RSE)	(7.47%)	(3.79%)	(3.56%)
2nd composition	**n = 30**	**$^{235}U/^{238}U$, P2P (Arithmetic)**	**$^{235}U/^{238}U$, P2P (Geometric)**	**$^{235}U/^{238}U$, TSI**
Zircon Cell	**R_{mean}**	5.51E-02	2.85E-02	2.72E-02
	Uncertainty			
	(-RSE)	(30.3%)	(12.8%)	-
	(+RSE)	(30.3%)	(14.6%)	-
	Reproducibility			
	(-RSD)	(81.9%)	(36.3%)	(21.2%)
	(+RSD)	(81.9%)	(57.0%)	(26.9%)
	RD	47.8	-18.1	-22.9
	(-RSE)	(15.0%)	(6.63%)	(3.87%)
	(+RSE)	(15.0%)	(10.4%)	(4.92%)

By comparing the performance of the DCI & Enterprise Cell and the Zircon Cell, with the preferred P2P (Geometric) data evaluation strategy, it was possible to conclude the best outcome was for the DCI & Enterprise Cell. For the 1st composition the RD to the expected composition with the DCI & Enterprise Cell was effectively zero, compared to 6.58% with the Zircon Cell. The RSD achieved on the DCI & Enterprise Cell was an improvement of 1-2% on the Zircon Cell, however for the 2nd composition the improvement in RSD had raised to 12.6-15.6%.The RSD of the 2nd composition

generally was higher than the first composition, a point reflected in the RD values of -14.7% and -18.1% for the DCI & Enterprise Cell and Zircon Cell respectively.

Using the arithmetic approach to calculate the $^{235}U/^{238}U$ isotope ratio for both compositions (Zircon Cell) the results were poor. For both compositions the RSD was over 50% and the mean ratios were biased towards higher values, with RD to the expected compositions of 57.6% and 47.8%. The original NIGL submission to the NUSIMEP-7 inter-laboratory comparison used the same single collector ICP-MS coupled to a similar laser ablation system. The same ablation cell (Zircon Cell), with Ar gas added via the same desolvator, was also used, and therefore the LA-ICP-MS setup was nearly identical to what was used in this chapter. Analysing the dual composition planchet, NU7-043, in the original NIGL submission the two $^{235}U/^{238}U$ isotopic ratio compositions identified were 3.27E-02 and 5.34E-02. The reasons why the original NIGL submission values were flawed are twofold and have now been identified. The first reason was unknown at the time; on NU7-043 only one composition, $^{235}U/^{238}U$ = 3.41E-02, was actually present. The 2nd reason was by calculating the isotope ratios using the P2P (Arithmetic) data evaluation strategy the one composition actually present on the planchet was identified with a high uncertainty and the mean biased towards enriched $^{235}U/^{238}U$ ratios. Knowing two compositions were expected the high uncertainty single composition was interpreted as two compositions of lower uncertainty, with a mixing line between them. The erroneous 5.34E-02 composition reported to the inter-laboratory comparison was therefore an artefact caused by the data evaluation strategy. If the P2P (Geometric) or TSI data evaluation strategies had been adopted instead it would have been more likely that the lack of a 2nd composition would have been identified.

On the MC-ICP-MS the RSD of both $^{235}U/^{238}U$ compositions was 3.27-3.38% and 6.76-7.25% respectively. Therefore compared to the LA-MC-ICP-MS analyses of NUSIMEP-7 in Chapter 4 and by Kappel *et al* (2013)[17], the mean RSD and RD achieved for both $^{235}U/^{238}U$ compositions were significantly higher with the single collector ICP-MS. However both compositions were clearly identifiable, not just manually by the user, but by an impartial software package and by using the geometric approach to calculate the $^{235}U/^{238}U$ ratio both were close to the expected compositions.

5.5 Conclusion

The reproducibility which could be achieved with the MC-ICP-MS, 1.34% on the $^{235}U/^{238}U$ ratio for SRM611 and 2.93-3.01% for NUSIMEP-6, could not be replicated with the single collector ICP-MS: limited to a reproducibly on the $^{235}U/^{238}U$ ratio of 7.82% for SRM611 and 7.64-8.27% for NUSIMEP-6 respectively. This was related to the difference in detection efficiency between the two mass spectrometers; the limiting uncertainty on the single collector ICP-MS due to count rate alone was consistently greater than the RSD which had been determined experimentally on the multi-collector

ICP-MS. A further consequence of the reduced detection efficiency with the single collector ICP-MS was measurement restricted to the $^{235}U/^{238}U$ isotope ratio only.

However with the single collector ICP-MS, as the ^{235}U and ^{238}U were measured on the same detector, it was possible to use the P2P data evaluation strategy to assign an uncertainty to each measurement, a key point as one of the stated aims of the project was to assign an isotope ratio composition based on a single particle. Using the DCI & Enterprise Cell rather than the Zircon cell reduced the uncertainty on each measurement due to the improved S/N ratio which was achieved with the prototype coupling mechanism. The high uncertainty on each measurement made using the Zircon Cell resulted in a bias towards higher $^{235}U/^{238}U$ ratios, unless the geometric approach to calculating isotope ratios outlined in Chapter 3 was applied. The failure to apply the geometric approach when using a similar LA-ICP-MS setup was part of the reason why NIGL reported the presence of an erroneous composition on one of the NUSIMEP-7 planchets in the original inter-laboratory comparison. By using the geometric approach the erroneous composition was eliminated and the two compositions present on the NUSIMEP-7 planchet were successfully identified.

Although LA-MC-ICP-MS has been shown to be superior for the isotope ratio analysis of single particles than single collector sector field ICP-MS, MC-ICP-MS instrumentation is more specialised and less widely available than single collector sector field ICP-MS. Single collector sector field ICP-MS instruments are already used to determine the 'bulk' isotopic compositions of dissolved radionuclide particles collected on swabs and wipes[18–20], even isolated single particles have been dissolved and the isotopic composition measured by sector field ICP-MS[21]. For reasons of instrument availability alone, development of single collector sector field LA-ICP-MS methods to determine the isotope ratio composition of single particles may be of importance to the community.

5.6 References

1. D. Günther, I. Horn, and B. Hattendorf, *Fresenius J. Anal. Chem.*, 2000, **368**, 4–14.

2. Z. Hu, W. Zhang, Y. Liu, S. Gao, M. Li, K. Zong, H. Chen, and S. Hu, *Anal. Chem.*, 2015, **87**, 1152–1157.

3. O. Borovinskaya, B. Hattendorf, M. Tanner, S. Gschwind, and D. Günther, *J. Anal. At. Spectrom.*, 2013, **28**, 226–233.

4. O. Borovinskaya, S. Gschwind, B. Hattendorf, M. Tanner, and D. Günther, *Anal. Chem.*, 2014, **86**, 8142–8148.

5. M. Zimmer, W. Kinman, A. Kara, and R. Steiner, *Minerals*, 2014, **4**, 541–552.

6. J. Fietzke, V. Liebetrau, D. Gunther, K. Gurs, K. Hametner, K. Zumholz, T. H. Hansteen, and A. Eisenhauer, *J. Anal. At. Spectrom.*, 2008, **23**, 955–961.

7. C. Paton, J. Hellstrom, B. Paul, J. Woodhead, and J. Hergt, *J. Anal. At. Spectrom.*, 2011, **26**, 2508–2518.

8. F. Pointurier, A. Pottin, and A. Hubert, *Anal. Chem.*, 2011, **83**, 7841–7848.

9. J. Aitchison, *Math. Geol.*, 1984, **16**, 531–564.

10. J. Aitchison, *Math. Geol.*, 1992, **24**, 365–379.

11. J. Aitchison, *Math. Geol.*, 1999, **31**, 563–580.

12. J. Aitchison, C. Barcel, and J. A. Mart, *Math. Geol.*, 2000, **32**, 271–275.

13. N. M. Mclean, PhD Thesis, Massachusetts Institute of Technology, 2012.

14. Y. Aregbe, J. Truyens, R. Kips, S. Richter, E. Stefaniak, H. Kühn, and M. Kraiem, *NUSIMEP-6 : Uranium isotope amount ratios in uranium particles*, IRMM Report EUR 23702EN, IRMM, Geel, 2008.

15. J. Truyerns, E. Stefaniak, S. Mialle, and Y. Aregbe, *NUSIMEP-7 : Uranium isotope amount ratios in uranium particles*, IRMM Report EUR 25179EN, IRMM, Geel, 2011.

16. J. Truyens, E. a Stefaniak, and Y. Aregbe, *J. Environ. Radioact.*, 2013, **125**, 50–55.

17. S. Kappel, S. F. Boulyga, L. Dorta, D. Günther, B. Hattendorf, D. Koffler, G. Laaha, F. Leisch, and T. Prohaska, *Anal. Bioanal. Chem.*, 2013, **405**, 2943–2955.

18. X. Z. Zhang, F. Esaka, K. T. Esaka, M. Magara, S. Sakurai, S. Usuda, and K. Watanabe, *Spectrochim. Acta Part B At. Spectrosc.*, 2007, **62**, 1130–1134.

19. F. Esaka, M. Magara, C. G. Lee, S. Sakurai, S. Usuda, and N. Shinohara, *Talanta*, 2009, **78**, 290–294.

20. F. Esaka, M. Magara, D. Suzuki, Y. Miyamoto, C.-G. Lee, and T. Kimura, *Talanta*, 2010, **83**, 569–573.

21. F. Esaka, M. Magara, and T. Kimura, *J. Anal. At. Spectrom.*, 2013, **28**, 682–688.

Chapter 6 – Fast Mounting of Micron-sized Particles for Analysis by Laser Ablation Inductively Coupled Plasma Mass Spectrometry

6.1 Introduction

This chapter describes the development of a new method to prepare (mount) micrometre (micron) sized particles for laser ablation inductively coupled plasma mass spectrometry (LA-ICP-MS). A methodological approach was taken to discover the optimum conditions for the method to produce the best mounted particle samples for laser ablation analysis. The suitability of the prepared sample mounts will be determined experimentally using a variety of analytical techniques and subsequently demonstrated by LA-ICP-MS.

6.2 Preparation of Particulate Samples for LA-ICP-MS Analysis

One advantage of LA-ICP-MS when compared to some other mass spectrometry-based techniques, is that minimal sample preparation is usually required. For particulate samples, LA-ICP-MS studies so far have utilised particle sizes from hundreds of micrometres (micron) down to the sub-micron size with applications in environmental analysis[1], industrial pollution[2], forensic analysis[3] and nuclear safeguards[4–7]. In almost all cases the particles analysed were collected from the environment, however how the particles were collected has varied in many ways. These methods of collection have normally involved trapping the particles in a substrate, either by drawing aerosolised particles onto the substrate or by wiping the substrate onto a particle coated surface. The substrates used to trap the particles have ranged from membrane filters, cotton wipes, even spider silk[8]. Although one of the main advantages of laser ablation is a typical requirement for less sample preparation, particles are not generally analysed directly from the substrate used to collect the particles, but are instead transferred to a substrate more suitable for laser ablation. The primary aim of this Chapter is the development and optimisation of a new method by which environmentally collected particles can be transferred to a more appropriate substrate before undergoing LA-ICP-MS analysis.

6.2.1 Current Particle Mounting Techniques for LA-ICP-MS

One of the earliest methods developed for analysing particles by LA-ICP-MS involved pressing them into a pellet. The particles of interest to the analyst could comprise the entire pellet[9,10] or only a small proportion of the material mixed within a binder[11,12]. This method was not designed to analyse individual particles, but instead to analyse a material in bulk which happened to be particulate in

form. One advantage of using a pelleted powder rather than another form of bulk material is the capability to add reference components into the material as part of the pelleting process[13]. Tabersky *et al* (2014)[14] have taken this further and have managed to produce solid certified reference materials for LA-ICP-MS from liquid materials by using a flame spray technique to produce nano-powders which can be pressing into pellets. A related method to pressed pellets for producing reference materials from particles involves embedding the particles in epoxy resin; aiming to produce a homogeneous surface of the powdered material[15]. However, epoxy resin has also been used as a mounting agent for dispersed particles, enabling individual particles to be targeted for analysis. In geology, zircons, which are effectively large particles, are regularly mounted in epoxy resin for analysis by laser ablation[16,17]. Lloyd *et al* (2009)[5] used a similar approach to mount uranium oxide (UO_x) particles by mixing aliquots of particles, suspended in liquid, into the wet epoxy mix. In order to ablate material from the particles stuck within the resin, the face of the mount was polished to bring out suitable particle surfaces, which could then be targeted for laser ablation. Although effective for larger particles (>20μm), polishing of the epoxy mount to reveal particle surfaces suitable for laser ablation becomes more difficult if the particles are smaller (<10μm). Another material which has been used to embed particles for laser ablation, in a similar fashion to epoxy resin is gelatin. Due to its composition and density, doped gelatin has more commonly found use in LA-ICP-MS as a reference material for tissue sections[18], however UO_3 particles adhered in a gelatin matrix have been successfully analysed by LA-ICP-MS[19].

Although it is not impossible to ablate particles not bound to a matrix, usually particles are either embedded into a mount (epoxy resin, gelatin) or an adhesive or fixing agent is used to bind the particles to a substrate surface. In Chapters 4 and 5 the NUSIMEP particles analysed were created by the hydrolysis of UF_6 gas to solid UO_3 particle formed on the surface of a carbon planchet[20]; no adhesive or fixing agent was used. In laser ablation the particles which travel from the ablation site to be ionised in the plasma are formed from the nucleation and condensation of the plume of material released by the ablation. Most of the NUSIMEP particles underwent this mechanism however some of the particles did not; sharp, single integration, spikes in signal on the mass spectrometer correspond to particles which rather than being ablated had been ejected whole, off of the surface of the planchet. Of the two mechanisms, ablation or ejection, it is ablation which is most desired for analysis by ICP-MS. To prevent the laser shockwave ejecting rather than ablating particles, an adhesive or fixing agent is usually used to bind the particles to the substrate surface (as well as to prevent the particles leaving the substrate during transport). Particles can either be transferred to an adhesive surface or either coated in situ with an adhesive layer. A common adhesive surface, Scotch™ tape or Sellotape®, has been applied to the laser ablation of both

zircons[21] and environmental particles[22]. Sellotape® has also been used to help arrange particles before further mounting them in epoxy resin[23]. Kappel *et al* (2013)[24] reported adhering particles for laser ablation by coating a vacuum impactor target with a layer of 1:1 nail polish to acetone and by applying a vacuum, transferring particles onto the adhesive target. Similar to nail polish and acetone, cyanoacrylate glue is an easily available adhesive which has also been used to bind particles to a substrate for LA-ICP-MS analysis[3].

To overlay particles with an adhesive agent, collodion (a solution of nitrocellulose in either ether or alcohol) is an established binder for single particles, notably during the irradiation of particles for FT-TIMS. The application of collodion for particle analysis falls into two categories: particles suspended in collodion dropped onto a substrate[25] or collodion dropped over particles already present on the substrate[26]. As the solvent (either ether or alcohol) dries a nitrocellulose layer settles out of solution binding the particles in place. The thickness of the collodion layer over the particles has been reported from a few microns (μm)[27] to around 200 μm[8] and indeed the layer generated for FT-TIMS is sufficiently thick that it can be peeled off to extract the particle following irradiation. As a consequence of the thickness of the collodion layer multiple laser ablation pulses are often required to cut through the layer to reach the particle underneath. Messerly (2008)[19] reported requiring 30 laser pulses to cut through the collodion layer and Pointurier *et al* (2011)[27] reported firing 100 shots per particle analysed. Ebert (2012)[8] also used 100 shots to analyse each particle, however lower fluence *fs*-LA-ICP-MS had been used instead of *ns*-LA-ICP-MS.

Membranes (either of cellulose acetate, cellulose nitrate or polycarbonate) are a common substrate used to collect particles[28,29] from the environment. These membranes are often dissolved by common solvents and by doing so particles can be quickly transferred from the membrane surface and into a liquid suspension. Esaka *et al* (2012)[30] mounted particles for FT-SIMS analysis by dissolving a particle-coated polycarbonate membrane in a mix of 1,2-dichloroethane and dichloromethane. The resulting particle suspension was then poured onto a silica plate and left for the 1,2-dichloroethane and dichloromethane to evaporate away. This left the particles behind, trapped inside a polycarbonate film. Boulyga and Prohaska (2008)[31] also produced a film containing fixed particles by placing particle-coated cellulose acetate membranes within an atmosphere containing acetone vapour. The membrane reacted with the acetone vapour, becoming transparent and adhesive, but importantly did not lose its shape. Once the particles coating the membranes were adhered, the membranes were then dried to harden them.

6.2.2 An Ideal Particle Mounting Technique for LA-ICP-MS Analysis of Micron-sized Particles

The ESARDA (European Safeguards Research and Development Association) Working Group on Standards and Techniques for Destructive Analysis (WGDA) recommended a quality control standard for the analysis of radionuclide particles by LA-ICP-MS[32] which would contain particles of mixed isotopic and elemental composition varying in size from 0.5µm to 10µm; mounted on a transparent substrate. From this it can be inferred an ideal technique for mounting radionuclide particles for LA-ICP-MS analysis should be applicable to all particles of that given size range and should utilise a transparent substrate, such as clear glass. Furthermore an ideal particle mounting method for laser ablation would result in well-spaced particles adhered under or within a very thin transparent layer. The method should be rapid and easy to use with as few sample handling steps as possible to reduce the likelihood of sample loss or contamination.

Managh *et al* (2013)[33] reported the application of cytocentrifugation to prepare non-adherent tissue cells, ≈10µm in diameter, for LA-ICP-MS. Cytocentrifugation removed the cell culture medium the cells were suspended within and dispersed the cells evenly across a transparent slide, assisting the targeting of individual cells by laser ablation. Cytocentrifugation, the instrumentation for which is often referred to as a Cytospin™[34,35] is a well-established technique in cytology for spinning suspensions of cells onto a microscope slide, but to the knowledge of the author, following a comprehensive search of the scientific literature, has not been reported for mounting micron-sized inorganic particles for analysis. Cytocentrifugation was investigated to see if, as the original patent (US Patent 4,250,830) suggested[36], it could disperse particles instead of cells evenly across a slide and as such form the basis of a new method to prepare particle samples for LA-ICP-MS analysis.

6.3 Experimental

6.3.1 Principles of Cytocentrifugation

As the name suggests cytocentrifugation uses centrifugal force to coat the suspended cells/particles onto the substrate surface. The suspended cells/particles are placed within a well, formed from the substrate (the base) and a cylindrical chamber (the walls). A locking mechanism holds the chamber against the substrate to form the well. Between the chamber walls and the substrate is placed an absorbent filter. The well is placed within a holder positioned on the end of a rotor arm within the Cytocentrifuge, a modification of a centrifuge. Once the rotor starts to spin the well and holder move such that the centrifugal force acts to push the suspension in the well onto the substrate surface. The suspension media is absorbed into the filter, which thus far has acted as a gasket, but

the cells/particles remain inside the well, forced onto the surface of the substrate. Once the centrifugal force is removed the well and holder can be disassembled to leave a substrate coated in dispersed cells/particles.

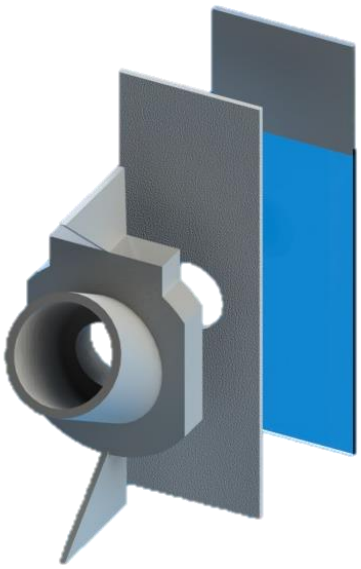

Figure 64 – 3D rendered image from Solidworks® of the three consumables placed within the cyto-chamber (exploded view). The suspended sample is placed within the well of the angled chamber (front). On application of the centrifugal force the sample is coated onto the surface of the glass slide. The solvent is absorbed by the filter card in the middle of the sandwich.

The cytocentrifuge used was a Universal 320R™ centrifuge (Hettich™, Tuttlingen, Germany) which had been modified with the Hettich Cyto System™. The cytocentrifuge had four holders, designed to operate with an angled, rather than straight, chamber. The angled chamber was placed atop a coated glass slide (Polysine™ Slides, Thermo Scientific™, Loughborough, UK), with a filter card sandwiched between. A 1 cm hole in the chamber and filter card allowed the sample access to that portion of the glass slide. The angled chamber could hold up to 1.2mL of liquid and could be spun at speeds of up to 4,000 revolutions per minute (rpm).

6.3.2 Optical Microscopy and Surface Metrology

Once the slides had been coated with particles in the cytocentrifuge the surface metrology of the particle-coated slides was investigated optically. Alongside a conventional microscope, two other optically-based surface metrology instruments were used to analyse the particle-coated slides. The instruments were used at the Metrology Unit within the School of Mechanical and Manufacturing Engineering at Loughborough University and were:

1. TalySurf™ CLI 2000 (Taylor Hobson, Leicester, UK)

The Talysurf™ CLI 2000 is a scanning topography measurement system, used to determine the roughness of a surface. It can operate with a variety of gauges, either contact (a stylus) or non-

contact (white light or laser). The gauge head is stationary and measures the altitude to the location directly underneath the gauge. As the gauge head positon is fixed it is the sample which moves via a stage positioned underneath the sample. The gauge used was non-contact and operated using the chromatic length aberration (CLA) principle.

Figure 65 – The Talysurf™ CLI 2000 scanning topography measurement system at the Metrology Unit within the School of Mechanical and Manufacturing Engineering at Loughborough University. The particle coated slides were placed on the mobile stage under the gauge.

In CLA a white light is directed by a beam splitter through a spectral aberration lens and from there to the surface of the sample. The spectral aberration lens splits the light into all of its different wavelengths, only one of which, depending on its altitude under the lens, is in focus on the sample surface. The light reflected from the sample surface passes through a pinhole, which acts to only allow the wavelength in focus to pass through. A spectrometer then deflects the light onto a CCD detector to interpolate the spatial position of the data point. The Talysurf™ CLI 2000 (serial number DS-51224) was used to scan across the particle-coated slides to generate a surface profile transect across the sample area. The range used was the CLA-300 (real range size 320 µm) at a measurement speed of 500 µm/s and a sampling rate of 100 Hz.

2. Zygo® NewView™ 5000 (ZYGO, Middlefield, CT, USA)

The Zygo® NewView™ 5000 is a non-contact 3D scanning white light interferometer (SWLI) and was used to investigate the sample surface of the particle-coated slides, specifically the boundary between the particle-coated area and the glass. It provides graphical and numerical analysis of the structure and topography of samples.

Figure 66 – The Zygo® NewView™ 5000 SWLI (serial number 00-28-50166) at the Metrology Unit within the School of Mechanical and Manufacturing Engineering at Loughborough University.

In scanning white light interferometry a beam from a white light source is split by a beam splitter into two beams, a measurement beam and a reference beam. The measurement beam is passed onto the sample surface and reflected back to the beam splitter, whilst the reference beam is reflected off a mirror back to the beam splitter. The beam splitter superimposes the measurement beam and the reference beam onto each other and the re-combined beam is imaged on a CCD detector. If at any pixel on the CCD the light from the measurement beam and the reference beam have the same optical path (travelled the same distance) then constructive interference occurs and the pixel will report high intensity. If the optical paths are different then destructive interference occurs and the pixel reports lower intensity. Therefore the bands of constructive and destructive interference are representative of the sample topography. By moving the reference mirror the interferometer changes the reference optical path, changing the location on the image where constructive and destructive interference will occur. Scanning with the reference mirror the resulting images are combined by the instrument software to reproduce the 3D shape of the sample surface.

6.3.3 Scanning Electron Microscopy

In order to confirm the composition, and therefore source, of the particles which had been coated onto the glass slides by the cytocentrifuge, the surface of the slides were analysed by SEM-EDX (SEM

- LEO 435VP, EDX – Oxford Instruments™ INCAx) at the British Geological Survey (BGS) using the same conditions described in Chapter 4. As well as the isotopic composition the size and distribution of the particles across the sample area was mapped, using a feature detection sequence to scan hundreds of fields for particles. Each field area was 44 x 58 µm. In order to be analysed by SEM-EDX the particle-coated slides were carbon coated prior to analysis and backed with conductive carbon tape.

6.3.4 Configuration of the LA-ICP-MS

After analysing the particle-coated slides by microscopy, LA-ICP-MS analysis was carried out at Loughborough University on a single collector sector-field Element 2XR™ (Thermo Scientific™, Bremen, Germany) coupled to a 213 nm New Wave™ UP-213 Nd:YAG laser (Electro Scientific Industries®, Cambridge, UK). The ablation cell used was the Zircon Cell with all the tubing consisting of ¼" Tygon® (S-50-HL), with an overall transport length from cell to injector of 70 cm. The overall transport volume was 9.75 cm^3. The Ar make-up gas was added via a y-piece half way between the cell and the injector. Unlike at NIGL the Ar did not come from a desolvator, instead pure Ar gas was sourced from the sample gas line of the mass spectrometer. In order to tune the system a certified reference material, SRM611 (National Institute of Standards and Technology, Gaithersburg, MD, USA)[37] was ablated at a high repetition rate in a raster pattern to give a smooth signal. The signal generated by the ablation of SRM611 was used to tune the settings on the mass spectrometer for optimum ^{238}U sensitivity, alongside maintaining a Th/U ratio of nearly 1 and keeping the UO/U ratio low.

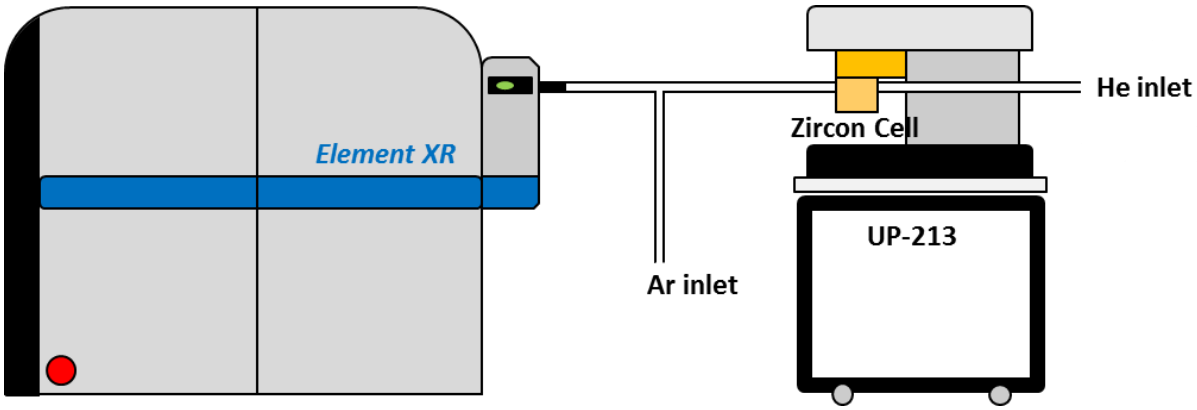

Figure 67 – Schematic of the LA-SF-ICP-MS setup with the Element 2XR™ mass spectrometer and UP-213 laser ablation system.

Typical operating conditions for the LA-ICP-MS system are given in Table 51. The laser was operated firing a single shot at a time on to the sample surface with a small spot size: to mimic the conditions used with the NUSIMEP particle analyses described in Chapters 4 and 5. The method used on the

mass spectrometer was limited to a single isotope with an integration time (segment duration) of 15ms.

Table 51 – Typical operating parameters for LA-ICP-MS, Element 2XR™ and UP213.

Parameter	Value
ESI® New Wave™ UP-213 Nd:YAG laser	
Ablation mode	Grid of spots
Fluence (J cm^{-2})	9
Repetition rate (Hz)	1
Spot size (µm)	8
He carrier gas (L min^{-1})	0.55
Thermo Scientific™ Element 2XR™ ICP-MS	
RF power (W)	1245
Cool gas (L min^{-1})	15.5
Aux. gas (L min^{-1})	0.95
Sample gas (L min^{-1})	0.96
X position (mm)	5.0
Y position (mm)	3.5
Z position (mm)	-2.3
Resolution	Low
Isotope	^{109}Ag
Mass Window (%)	5
Settling Time (ms)	1
Sample Time (ms)	3
Samples Per Peak	100
Segment Duration (ms)	15

6.3.5 Sample Preparation

Although the rapid particle mounting method for LA-ICP-MS using the cytocentrifuge was developed with the intention of applying it for UO_x particles, for reasons of cost and safety for method development the UO_x particles where exchanged for an alternative. The alternative particulate sample chosen for the method development and optimisation were purchased silver (Ag) particles of a reported size range of 2-3.5 µm (Sigma-Aldrich®, Gillingham, UK). The Ag particles were cheap, less valuable than the UO_x particles, easier to handle and readily available in large quantities. Ag particles

were also of a similar density to UO_x particles and so it was hypothesised would act similarly on the application of the centrifugal force.

The solvent chosen to suspend the particles was acetone as neither the Ag nor UO_x particles would readily dissolve in acetone and so was considered a safe solvent. Initially the particles were coated onto the slide surface with the cytocentrifuge in acetone only, but the requirement to better retain the particles on the slide surface lead to the addition of an adhesive agent. It was reported in section 6.2.1 that Kappel *et al* (2013)[24] had coated the surface of a vacuum impactor target in a 50:50 mix of commercial nail polish and acetone. Nail polish, a mix of cellulose nitrate (collodion), ethyl acetate, butyl acetate and ethanol, forms a hard thin film layer of cellulose nitrate on the nail when the solvent evaporates. A commercially available clear nail polish (Miss Beauty No.1, Wilkinsons, UK) was chosen as the adhesive agent.

The method by which the nail polish adhesive would be best applied had to be determined. Simply overlaying a particle-coated slide by dropping nail polish onto the surface was discarded as the literature suggested the cellulose nitrate layer would be too deep for the laser ablation system to easily cut through. Two methods were tested; in the first method nail polish was added to the Ag particle and acetone suspension prior to coating in the cytocentrifuge. In the second method the Ag particle and acetone suspension was spun in the cytocentrifuge onto a slide already coated with a layer of nail polish. Of the two methods, the first, adding the nail polish to the particle suspension prior to application was the most successful, creating a smooth clear film layer. The second method resulted in an uneven surface, with large air pockets trapped inside the film layer. Once a general method had been determined the next stage was to optimise the procedure.

6.4 Development and Optimisation of a Method to Mount Particulate Samples for Laser Ablation

6.4.1 Optimisation Methodology

In the original method described above the conditions used were 3.2 mg of Ag particles in 1 mL of a 50:50 mixture of nail polish and acetone. The mixture was spun onto the glass slide at the maximum rotation speed of 4,000 rpm for 25 minutes. These conditions were not ideal, the nail polish layer was too thick, and due to the concentration of particles they were densely packed, not dispersed. To find the ideal conditions for preparing a particle-coated slide for laser ablation an optimisation methodology was decided upon. The optimisation methodology involved four different conditions which were optimised sequentially. The order of optimisation was the concentration of the Ag particles, the rate and duration of cytocentrifugation, the ratio of nail polish to acetone and the

quantity of liquid added to the chamber. The optimum outcome desired was for a slide of well dispersed particles coated and held within a thin film layer of sufficient thickness that the particles upon laser ablation were analysed via the ablation mechanism rather than ejected from the sample surface.

6.4.2 Optimisation of the Method to Mount Particulate Samples for Laser Ablation

6.4.2.1 Optimisation of the Concentration of Ag Particles

Using the starting concentration condition of 3.2 mg of Ag particles suspended in 1 mL of a 50:50 mixture of nail polish and acetone the outcome was a layer consisting of densely packed particles. The particle density was such that the layer deposited on the glass slide was opaque. The mass of Ag added to 1 mL of 50:50 nail polish and acetone was reduced in turn by two orders of magnitude to 0.03 mg resulting in a transparent layer which under microscopy was shown to have a well dispersed scatter of particulate imbedded across the layer. Reducing the mass of Ag added to 1mL of solvent by a further order of magnitude resulted in too little material being present on the surface for easy analysis. The optimum quantity of material was therefore approximately 0.03 mg/ml.

6.4.2.2 Optimisation of the Rate and Duration of Cytocentrifugation

Using the starting cytocentrifugation conditions of 4,000 rpm for 25 minutes a smooth film layer of particles coated in nitrocellulose was produced. However the cytocentrifugation conditions were so vigorous the solvent, instead of being retained in the filter card, travelled through the card and deposited inside the well holder. Designed to operate with aqueous-based biological media the acetone passed quickly through the filter card to the well holder, which was made of a polymer which reacted with the acetone. The cytocentrifugation speed and time needed to be reduced to a point where all the solvent had been taken up by the filter card and still retained within. Not only would this prevent damage to the system, but would at the same time reduce the time taken to produce a particle mount for analysis.

The initial cytocentrifugation speed of 4,000 rpm was kept constant and the time reduced from 25 to 5 minutes, however the conditions were still too vigorous and the solvent was not retained within the filter card. A further reduction in time to 60 seconds and in speed to 2,000rpm however, were enough to ensure the solvent remained entirely within the filter card, whilst still forming a smooth and transparent layer of dispersed particles.

6.4.2.3 Optimisation of the Composition of the Solvent

To investigate the best ratio of nail polish to acetone in the solvent five different compositions were tested, composing 10%, 20%, 25%, 50% and 75% of nail polish to acetone by volume. With the compositions containing higher quantities of nail polish (50% and 75%) the Ag particles were less evenly dispersed across the layer, but instead tended to amalgamate into large aggregations. Using a composition containing only 10% nail polish, laser ablation (section 6.4.4) revealed the film layer was of insufficient strength to prevent particles from ejecting whole off of the slide surface. The optimum composition contained either 20% or 25% nail polish. With both 20% and 25% nail polish to acetone the film layer formed was thinner and contained a reduced population of particle aggregates than either 50% or 75% nail polish, but was of sufficient strength for particles to be analysed through an ablation mechanism. Of the two potential compositions, which performed similarly, 20% nail polish to 80% acetone by volume was selected as the optimum ratio.

6.4.2.4 Optimisation of the Quantity of the Suspension

So as not to change the concentration of particles optimised in section 6.4.2.1, the Ag particle suspension continued to be made up in 1 mL of solvent, however the quantity of suspension added to the well in the angled chamber required optimisation. In order to investigate the best quantity of suspension to use, multiple Ag particle-coated slides were created from volumes varying from 10 µl to 1000 µl. At volumes above 100 µl the film layer produced contained sufficient, well-dispersed particles, in a film layer of enough thickness to hold the particles on the sample surface for, ablation. Below 100 µl in volume, analysis by both microscopy and laser ablation could not identify sufficient Ag particles on the surface and those which were present were not tightly bound in a strong film layer. Indeed at below 75 µl the presence of a film layer could not be determined by microscopy. The optimum quantity of suspension was therefore chosen to be 100 µl, however to compensate for a reduction in the number of particles coated onto the surface by an order of magnitude, the concentration of particles (section 6.4.2.1) was increased to 0.3 mg in 1 ml of solution.

The optimum conditions for producing a particle-coated mount for laser ablation were 0.3mg of particles suspended in 1mL of 1:4 nail polish to acetone, with a 100 µl aliquot spun onto the glass slide in the cytocentrifuge at 2,000 rpm for 60 seconds. Unless stated otherwise these conditions were used to create each subsequent particle mount.

6.4.3 Analysis of Ag Particles Mounted by Cytocentrifugation using Surface Metrology and Scanning Electron Microscopy

The optimum conditions determined for producing a particle-coated slide for laser ablation analysis were used to produce an ‘ideal’ test mount. Analysis of the Ag particle mount producing using the

optimum conditions by microscopy showed (Figure 68) a well-distributed scatter of particles across the surface; ranging in size from approximately 1 µm to 20 µm.

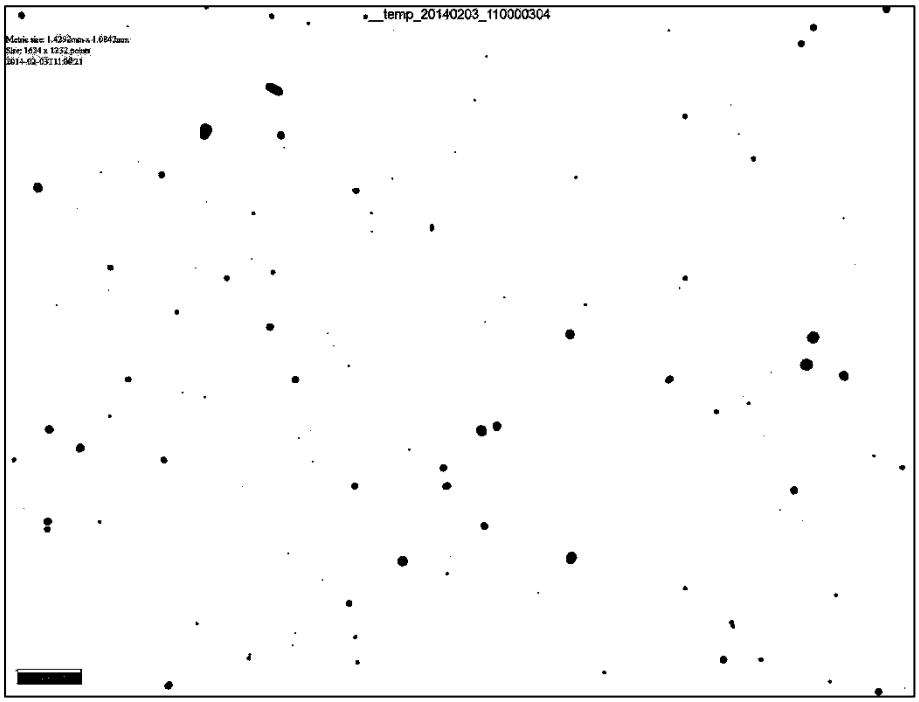

Figure 68 – Image of an area (1.43 x 1.08 mm) on an optimally produced Ag particle mount, captured on an InfiniteFocus 3D microscope. Scale bar (bottom left of the image) is 100µm across.

Subsequent analysis by laser ablation, which cut through the film layer of nail polish, revealed the film layer over each particle acted as a lens. When analysing the particles optically, such as under a microscope or using the camera in the laser ablation system, the 'lensing' effect of the film layer acted to make the particle under the layer appear significantly larger than its actual dimensions.

6.4.3.1 Analysis of Ag Particles Mounted by Cytocentrifugation using SEM-EDX

Two different Ag particle-coated slides which had been prepared using modified optimised conditions were imaged under the SEM. The two Ag particle-coated slides differed in the density of the particles coated in the film layer. On the slide less densely populated with particles, an area of 0.75x1.00mm was scanned using feature detection sequence and 43 Ag particles were detected with an average particle size of 1.30±1.04 µm. On the more densely populated slide 327 Ag particles of size range 1.23±0.88 µm, were detected in a feature detection sequenced area of 1.15x1.05 mm. For the more densely populated slide it was calculated the number of particles in the area corresponded to an average spacing of 60 µm between particles. The particle size and distribution determined on both Ag particle-coated slides were less than the particle size range stated by the manufacturer. In Figure 68, for an area similar in size to that which had been interrogated with the SEM, a greater quantity of large particles was identified. It has already been stated that due to a 'lensing' effect

many of the particle in Figure 68 are likely smaller than they appear, but even accounting for a lensing effect the particle size range determined optically and by SEM-EDX did not appear to align. This suggested agglomeration of small Ag particles was not responsible for the large particles detected in Figure 68, but instead the large particles likely come from a source other than the Ag powder. Targeted analysis of particles (LA-ICP-MS), at best only identified the particle as containing silver 55% of the time. Comparing fields collected with both the Secondary Electron (SE) and Backscatter Detector revealed particles, which did not contain high concentrations of a heavy element (ie. Ag) and therefore appeared dull (Figure 69). Interrogation with the EDX confirmed these contamination particle did not contain silver.

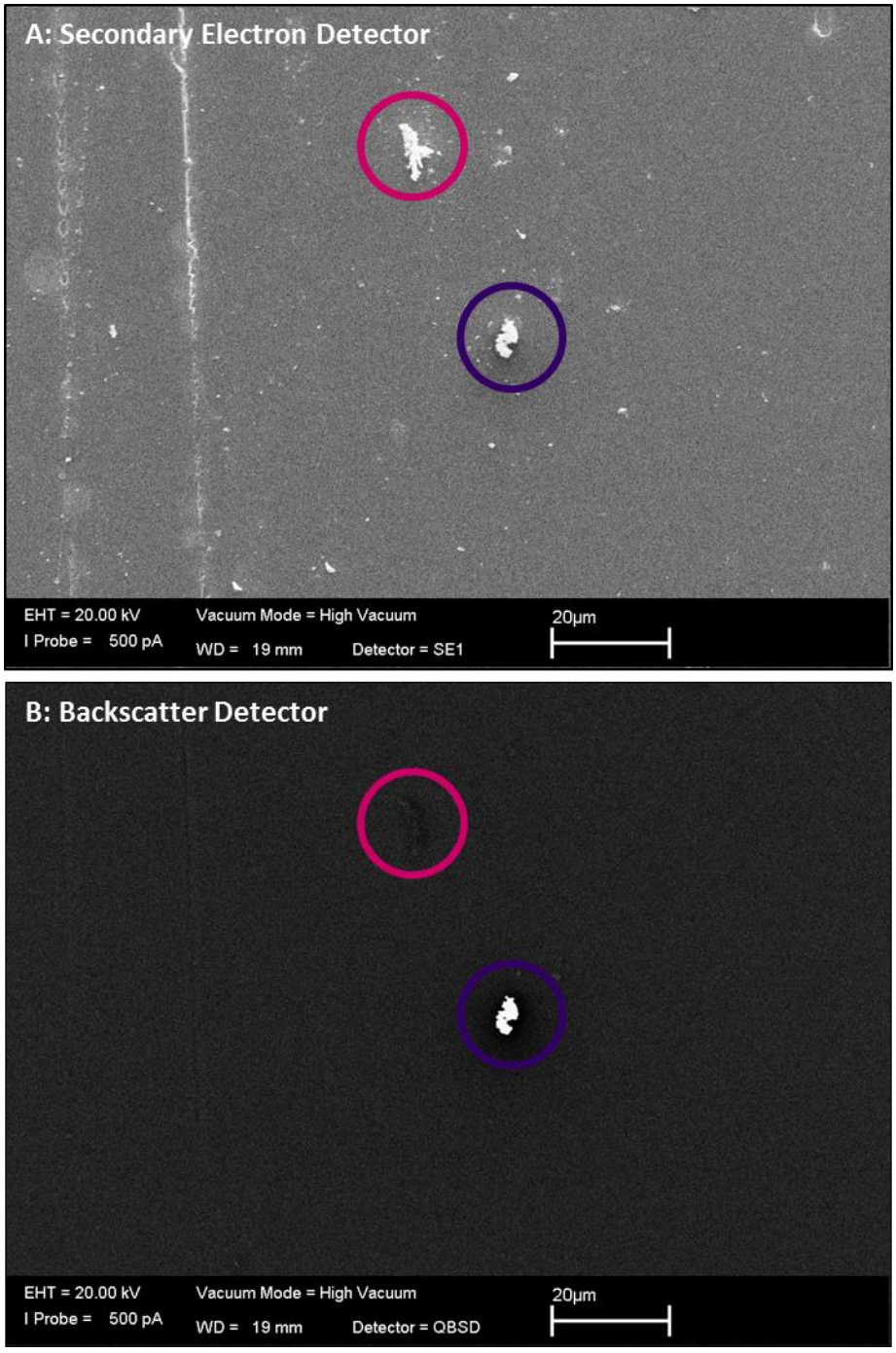

Figure 69 – Two images of two Ag particles on an optimally produced particle mount, magnification 1,990X. A. Particles imaged using the Secondary Electron Detector. B. Particles imaged using the Backscatter Detector. Of the two particles only one (circled in purple) contains silver. The other particle (circled in magenta) consists mainly of lighter, organic elements and therefore is fainter in the Backscatter electron image.

Away from the centre of the particle-coated slide, the SEM was also used to investigate the edge of the film layer, created at the interface of the glass slide to the filter card. Feature detection across the layer edge seemed to confirm the Ag particles were confined to inside the film layer.

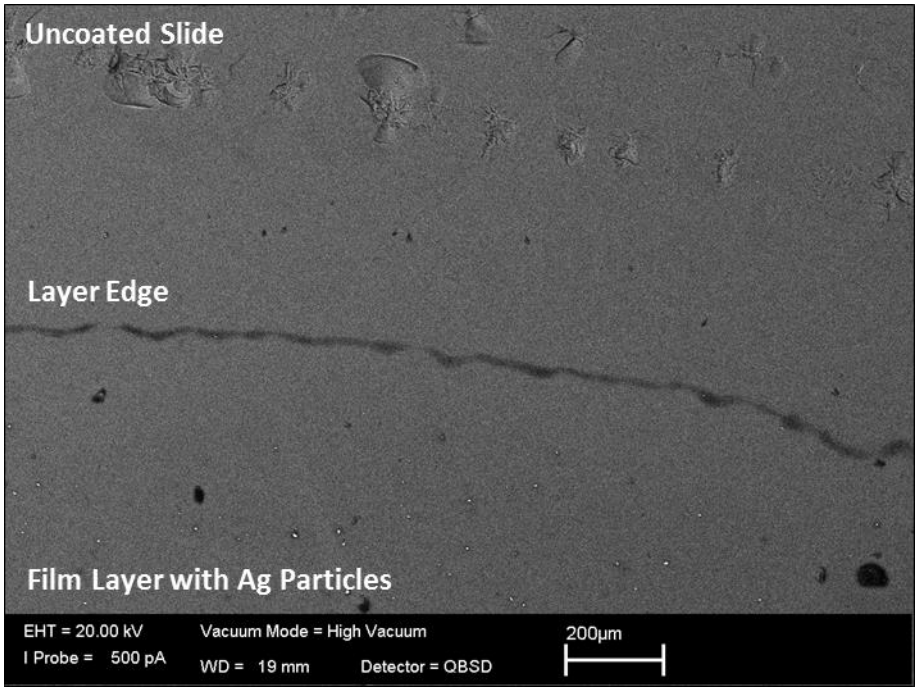

Figure 70 – Image of the film layer edge of an Ag particle coated slide, captured with the Backscatter detector of the SEM-EDX. The particles are confined within the film layer.

Figure 70 shows the layer edge as a dark line. Only to the inside of the film layer can any Ag particles (bright spots) be identified. The surface under the film is smoother than the uncoated glass slide, suggesting many of the imperfections on the glass surface have been filled in by the nail polish layer. Further investigation did reveal some particles beyond the edge, but after examination with the EDX examination were found to be composed of tungsten rather than silver.

SEM-EDX analysis could not be used to determine the thickness of the film layer, but in the literature particles coated in film layers produced by either, dropping liquid onto the surface or from a dissolved membrane, were not be analysed by SEM-EDX and instead rely on optical microscopy (although FT could be used to identify uranium bearing particles[25]). This is most likely a consequence of the film layers being of sufficient thickness that the SEM beam cannot penetrate to the depth required to analyse the particles. Esaka *et al* (2015)[38] reported that SEM-EDX was an improvement on optical microscopy for particles embedded in film layers as the improved resolution of SEM-EDX reduced the likelihood of two spatially close particles of differing isotopic compositions being mistakenly analysed as a single particle, however in order to analyse the particles by SEM-EDX the film layer first had to be removed by a plasma asher. As the particles embedded in the film layer produced using the cytocentrifuge can be analysed by SEM-EDX the layer must be significantly thinner than that which had been produced by the other reported methods.

6.4.3.12Analysis of Ag Particles Mounted by Cytocentrifugation using Surface Metrology

Microscopy and SEM-EDX analysis were used to investigate the size and distribution of the particles within the film layer coated onto the slides, but could give little information on the thickness of the film layer over the particles. To determine a measure of the thickness of the film layer the topography of the layers were investigated with the Talysurf™ CLI 2000 surface topography analyser and ZYGO® NewView™ 5000 scanning white light interferometer (SWLI).

Two of the Ag particle-coated slides were analysed using the surface topography analyser, the first slide was created with the original non-optimised conditions (3.2 mg Ag particles in 1ml of 50:50 of nail polish to acetone) and the second slide was created using the optimised conditions. On both slides a transect was analysed lengthwise across the film layer (Figure 71).

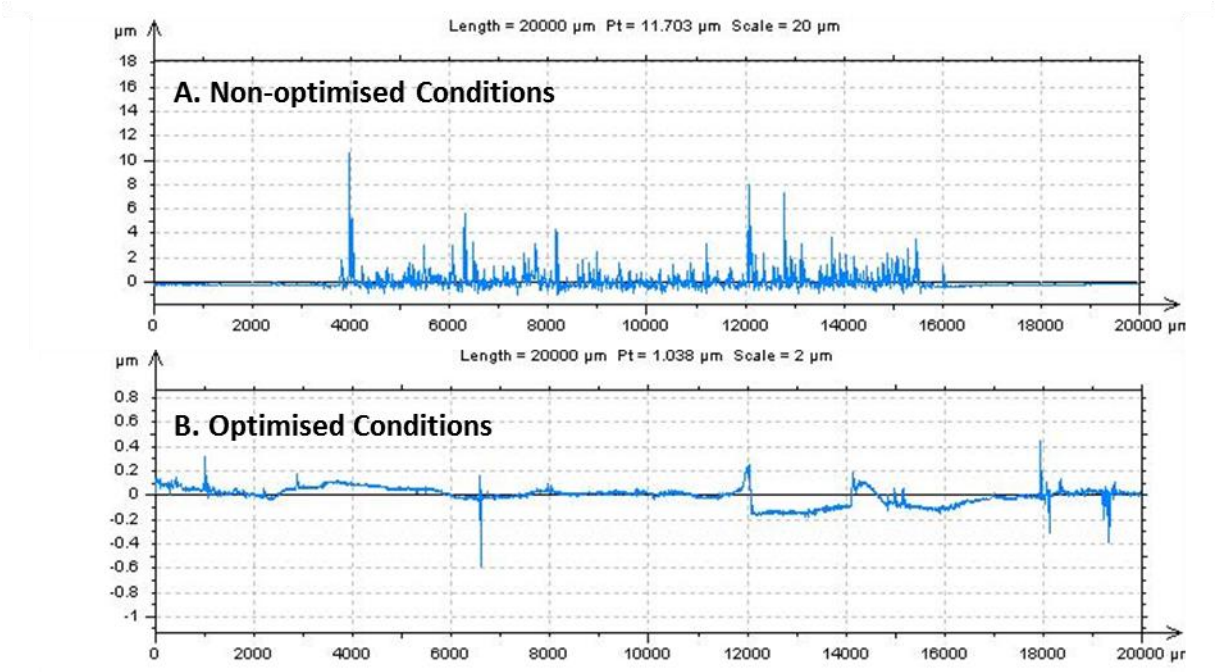

Figure 71 – Trace of two transects across Ag particle coated slides produced under A. Non-optimised conditions and B. Optimised conditions. Spikes associated with particles are visible for the thickly coated non-optimised conditions. No film layer is detected for either set of conditions.

For the slide produced using the original non-optimised conditions the Ag particles are densely packed and, as the transect went over many particles and aggregations, they resulted in many spikes in the signal, up to 11µm in height over the surface of the glass slide. For the slide produced using the optimised conditions, the transect appeared to show a trace consistent with the surface of the glass. This suggested the film layer, visible with the naked eye, was either indistinguishable in depth from the surface of the glass slide or was transparent to the investigative technique employed.

The film layer should not be transparent to the scanning white light interferometer as the presence of the film layer would change the optical path of the beam. Analysis of the film layer edge on the Ag particle-coated slide produced under optimised conditions with the scanning white light interferometer showed the layer edge as a ridge of 700 nm in height and less than 100 µm in width (Figure 72). Either side of the ridge (formed at the interface of the well chamber and the remainder of the glass slide) the slide surfaces are indistinguishable, suggesting either the film layer is extremely thin, or is undetectable away from the edge. As the layer edge is 700 nm thick it was assumed the film layer was at most the same thickness across the layer.

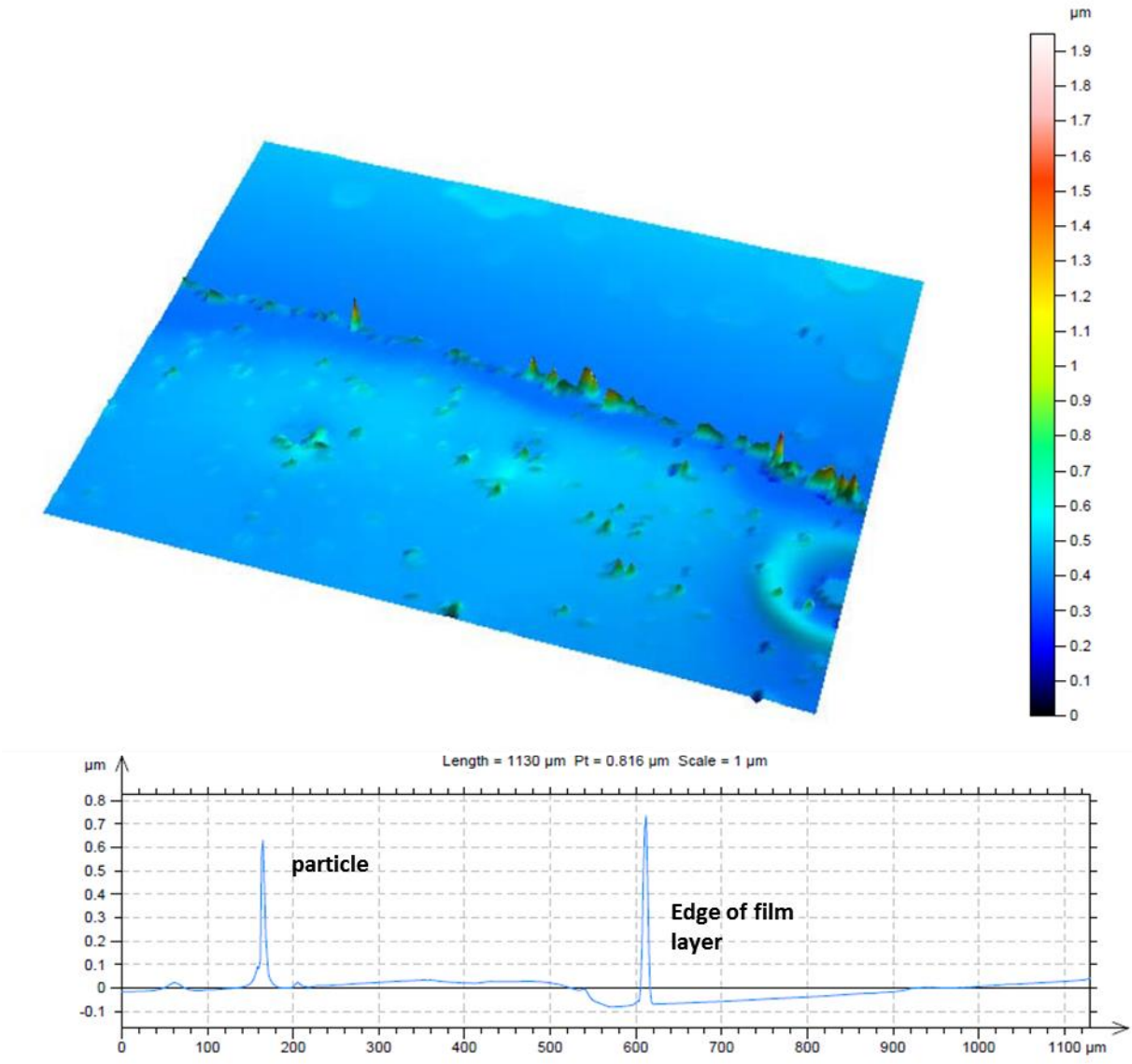

Figure 72 – Oblique plot of the edge of an Ag particle coated film layer created under optimum conditions produced using the ZYGO® NewView™ 5000 SWLI (top). Transect of the film layer edge showing the film edge as a peak approximately 700nm in height and 20µm in width (bottom). Settings: Objective L10X Michau, Image Zoom 0.5X, Scan Length 5 µm, FDA resolution high.

For the slide produced using the original non-optimised conditions the layer edge was approximately 1 µm in height from the glass surface and 100 µm wide. For this more densely particle-populated film layer a difference in surface height of about 200 nm was distinguishable between the uncoated glass slide and the film layer.

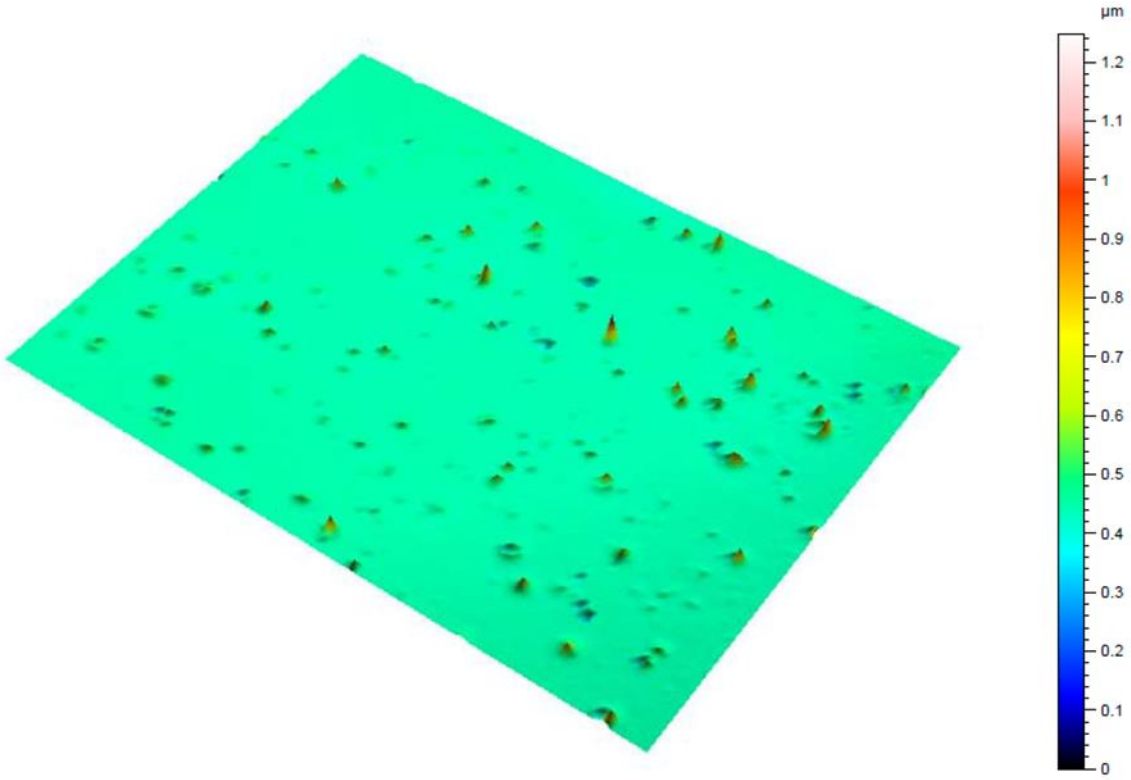

Figure 73 – Oblique plot of the centre of an Ag particle coated slide created under optimum conditions, produced using the ZYGO® NewView™ 5000 SWLI. It shows Ag particles as spikes in the topography of the surface. If the film layer is detectable then the particles are proud of the surface and available for laser ablation analysis. Settings: Objective L10X Michau, Image Zoom 0.5X, Scan Length 5 µm, FDA resolution high.

Analysis of the centre of the Ag particle-coated slide produced under optimised conditions (Figure 73) shows particles as spikes in the generally flat topography of the surface. If the film layer is indeed detectable by the ZYGO NewWave 5000 SWLI then this highlights particles embedded in the layer sit proud of the film layer surface. This suggests the laser ablation system will not have to cut through a thick layer of nitrocellulose in order to ablate a particle.

6.4.4 Analysis of Ag Particles Mounted by Cytocentrifugation using LA-ICP-MS

LA-ICP-MS analysis was used to ascertain the effectiveness of the film layer in holding the particles onto the surface of the glass slide. Two different Ag particle coated slides were analysed by LA-ICP-MS, one of the slides was produced using the optimised conditions, and the other slide was

produced from a suspension containing acetone only resulting in the formation of no nail polish based film layer.

Using the camera on the laser ablation system an image was captured before and after a single laser ablation pulse (fluence 20 Jcm^{-2}, spot size 25 µm) onto the slide surface. The freeware software download ImageJ (National Institutes of Health, USA) was used to subtract the pre-ablation image from the post-ablation image for both of the ablated slides (Figure 74). Black spots correspond to the locations where particles were present pre-ablation, but not post-ablation; white spots corresponded to locations on the slide surface where material was present post-ablation, but not pre-ablation. On the slide produced without using nail polish, the shockwave created by the laser ablation pulse removed not only the particle targeted, but all of the other particles within 75 µm of the ablation crater (Figure 74A). Even further out from the ablation site, the particles were not removed, but had moved across the surface from their original positions (black) to new locations (white). On the slide produced using nail polish under optimum conditions, the effect of the shockwave produced by the single laser ablation pulse was much more muted. The film layer was effective in holding particles distant from the site of the ablation (Figure 74B).

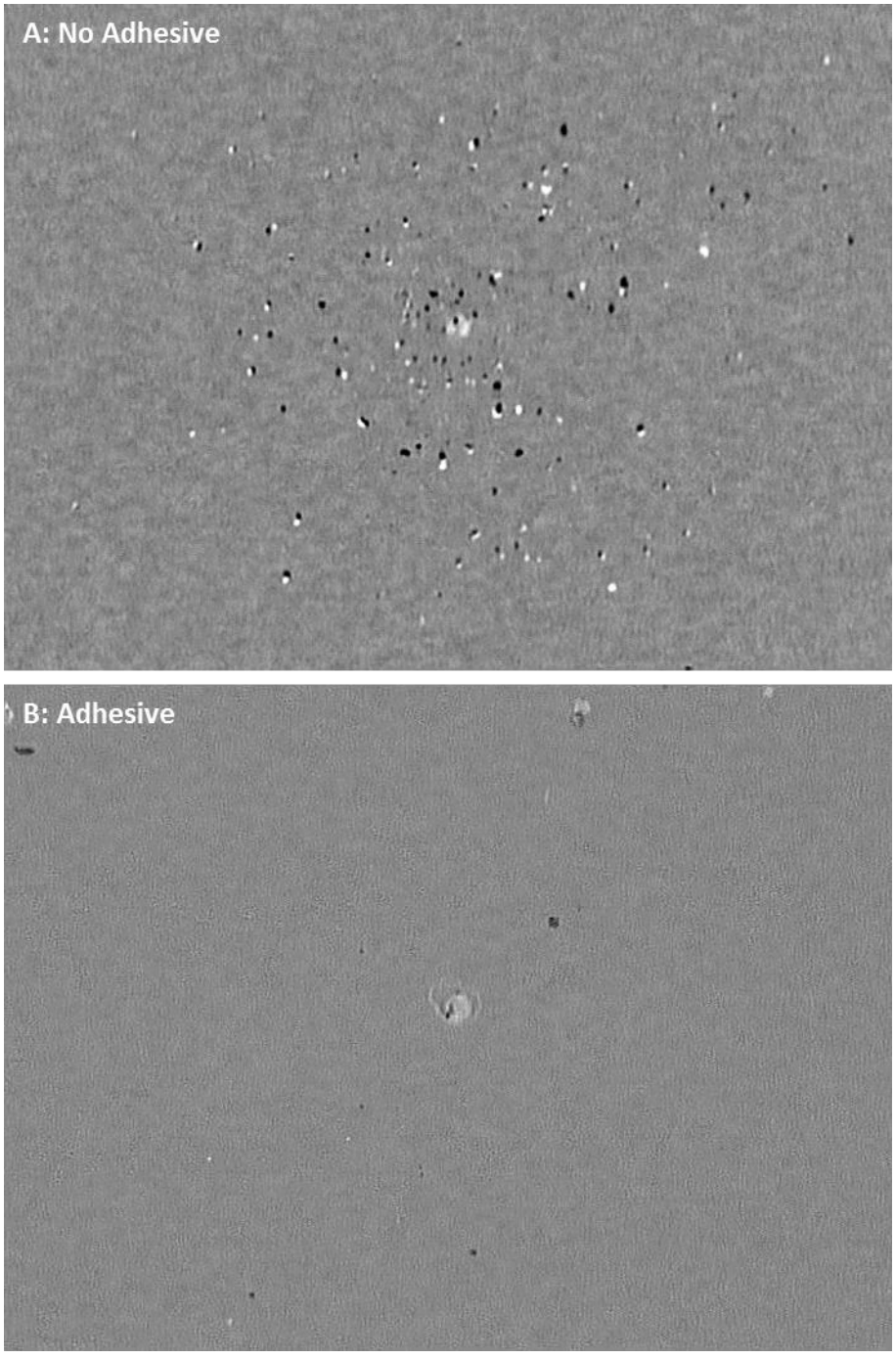

Figure 74 – Images of two Ag particle coated slides, produced by subtraction of images captured by the laser camera pre- and post-ablation, using ImageJ. Fluence 20 Jcm^{-2}, spot size 25 µm, single shot ablation. A. Ag particle coated slide with no nail polish adhesive. B. Ag particle coated slide with nail polish adhesive. Black spots are where material was present pre-ablation, but not post-ablation. White spots are the reverse, where material was present post-ablation, but not pre-ablation.

On the particle coated slide produced without nail polish, lowering the fluence of the single ablation pulse (<10 J cm^{-2}) reduced the effect of the shockwave on the surface, without the highly disruptive removal of particles around the ablation site. Using ablation conditions of 9 J cm^{-2} fluence and 8 µm spot size, repetition rate 1 Hz, dwell time 1 s, a direct comparison was made between ablating particles with or without the film layer.

Table 52 – LA-ICP-MS results of ablating two different Ag particle coated slides. The first slide was produced with using nail polish; the second slide was produced using the optimum conditions. The adhesive layer increased the proportion of particles which were successively ablated.

No adhesive layer	n	Mean ^{109}Ag counts	% of total signals
Ag particles ablated	23	3.48E+04	31.5
Ag particles ejected	36	1.51E+05	49.3
Ag particles exhibiting as ablated and ejected	14	2.81E+05	19.2
Total number of particles	73		
Adhesive layer	**n**	**Mean ^{109}Ag counts**	**% of total signals**
Ag particles ablated	88	1.13E+06	96.7
Ag particles ejected	1	1.43E+05	1.1
Ag particles exhibiting as ablated and ejected	2	1.67E+06	2.2
Total number of particles	91		

The particles analysed were determined to have been either 'ablated' or 'ejected'. Particles were assigned as ablated if the signal pulse profile was spread over multiple integrations and ejected if the signal pulse profile consisted of only a single integration spike. Signals profiles which had characteristics of both ablation mechanisms (a signal pulse profile interrupted by strong single integration spikes) were assigned separately. The total number of ^{109}Ag counts measured in each pulse was determined.

A summary of the LA-ICP-MS results (Table 52) showed a difference in preferred ablation mechanism between the two slides. The slide coated with the film layer by adding nail polish had significantly more particles which were ablated, the preferred mechanism, rather than ejected by the laser pulse. For the slide containing Ag particles embedded in the film layer the ^{109}Ag signal pulse duration was between 200-300 ms, however for the slide of Ag particles not bound in a film layer a majority of signal pulses were contained within a single, 15 ms integration (Figure 75).

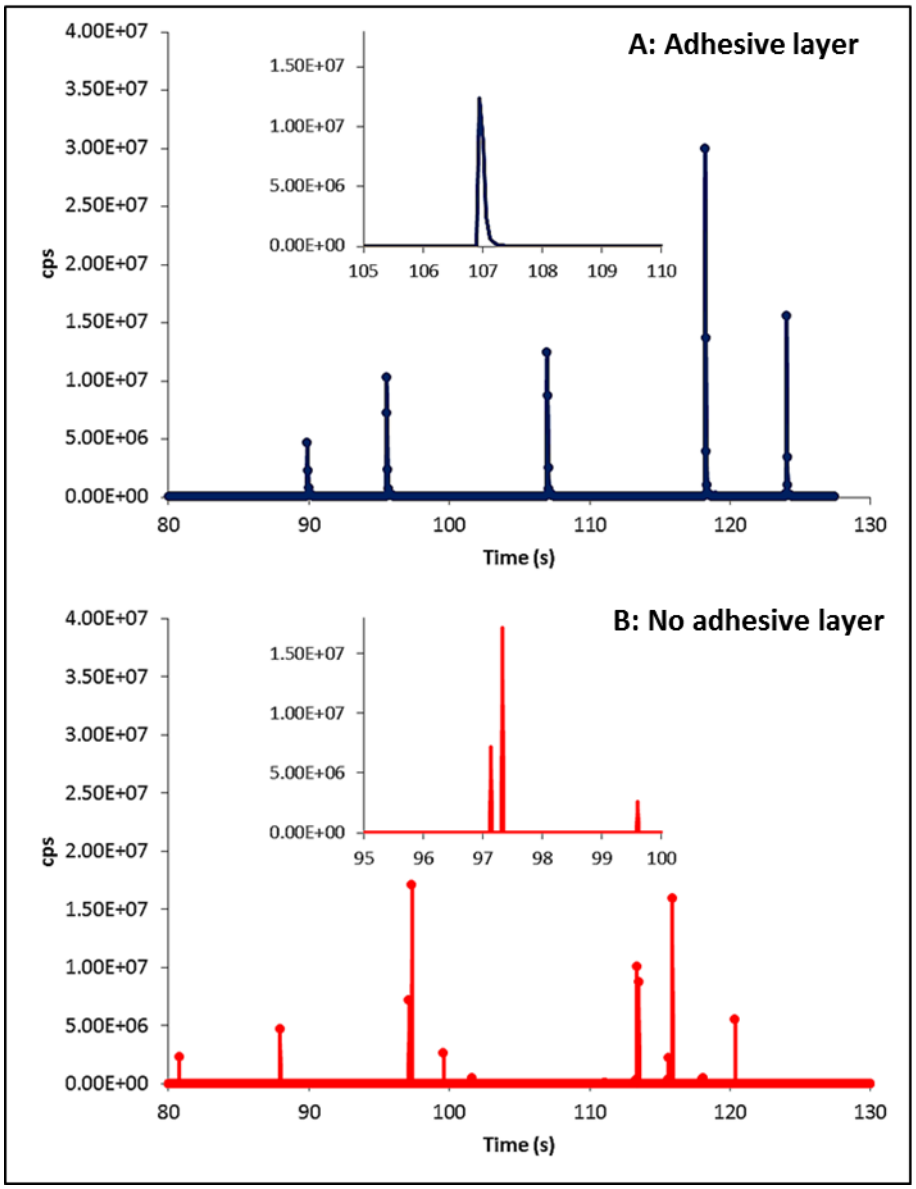

Figure 75 – Signal pulse profiles of ^{109}Ag collected using the single collector sector field LA-ICP-MS system. A. ^{109}Ag trace for particles ablated from a slide produced using the nail polish adhesive, optimum conditions. B. ^{109}Ag trace for particles ablated from a slide produced from a suspension containing acetone only. With the film layer the signal pulse profiles are over multiple integrations; without the film layer the signal pulse profiles consist of single integration spikes.

It was observed in Chapters 4 and 5 that the isotope ratio analysis of particles added whole into the plasma of an ICP-MS was difficult, with either mixed detector arrays or single collector instrumentation. In addition it has been reported that particles greater than 150 nm are not completely ionised within the plasma[39], and therefore the total signal which could be achieved for a particle larger than 150 nm would be reduced by adding it whole into the plasma. For LA-ICP-MS analysis of single particles it can be recommended that an adhesive agent be used to control the ablation mechanism of the particle.

6.5 Determination of the Background Signal from the Film layer and Polysine™ Coated Glass Slide

One potential concern with using a film layer over the particle of interest would be if the ablation of the film layer would add to the signal background at various masses. In order to determine if ablation of the film layer and the glass slide underneath would add to the background signal a glass slide and film layer prepared with no particles was ablated. The ablation setup used was a raster pattern of 9 J cm^{-2} fluence, 5 Hz repetition rate, an 8 µm spot size and a scan speed of 8 µm s^{-1}. The signal for 15 isotopes was measured, once without the surface undergoing any ablation and once with ablation. The signal associated with the film layer and glass slide was the difference between the two signals measured.

Table 53 – Average signal of 15 isotopes measured on the single collector sector field ICP-MS, with and without the laser ablation of a slide coated with a film layer of nail polish. The glass slide and nail polish did not contribute background on the majority of isotopes tested, with the exception of a small contribution, approx. 300cps, of lead.

Isotope	without ablation (cps)	with ablation (cps)	Background signal from film layer and glass slide (cps)
^{195}Pt	24.6	25.2	0.7
^{197}Au	48.1	52.7	4.6
^{204}Pb/^{204}Hg	460.1	452.9	-7.2
^{206}Pb	25.8	99.2	73.4
^{207}Pb	23.7	90.5	66.8
^{208}Pb	39.0	189.2	150.2
^{230}Th	13.8	12.2	-1.7
^{232}Th	14.5	43.4	28.9
^{234}U	12.8	11.4	-1.4
^{235}U	14.2	13.0	-1.2
^{236}U	13.9	13.8	-0.1
^{238}U	14.2	26.4	12.2
^{239}Pu	11.7	12.2	0.6
^{242}Pu	12.7	13.8	1.1
$^{238}U^{16}O$	38.7	40.9	2.1

For the 15 isotopes measured, ablation of the film layer and glass slide did not significantly increase the background signal, with the exception of the isotopes of lead. The effect of the ablation of the

film layer on the formation of polyatomic species in the plasma needs to be investigated in future work.

6.6 Analysis of Ag Particles Collected on a Cellulose Nitrate Membrane

For radionuclide particles collected in the environment, using the cytocentrifuge to mount the particles onto a slide in a suspension of acetone and nail polish requires a transfer step from the initial substrate used to collect the particles to the liquid suspension. Cellulose-based membranes have been used in the field as a substrate onto which radionuclide particles for analysis were collected[40]. The key component of the nail polish which produces the film layer is cellulose nitrate, which is also present alongside cellulose acetate in cellulose nitrate membranes. It was theorised that by dissolving a cellulose nitrate membrane in acetone a suspension would be produced which would also form a film layer of cellulose acetate on a glass slide when mounted using the cytocentrifuge. By using the cellulose nitrate membrane both to collect the particle from the environment and as the adhesive agent in the mounting process the transfer step could be eliminated.

To test the hypothesis a single 2.5 cm in diameter cellulose nitrate membrane (Whatman™, UK), was wiped onto a surface which had been contaminated with Ag particles. The cellulose nitrate membrane was placed into a vial into which 5 ml of acetone was added to dissolve the membrane. A 100 µl aliquot of the resulting suspension was then mounted onto a glass slide using the optimised conditions for the cytocentrifuge, 2,000 rpm for 60 seconds. A film layer similar to the one described for the nail polish was created, by the dissolved membrane, however the layer deposited was much thicker, suggesting the concentration of cellulose nitrate in the aliquot was higher than had been present in the nail polish. The thick layer from the membrane was less tightly fixed to the glass slide than that which had been produced with the nail polish, and gentle agitation of the layer with a cotton bud was all that was required to remove part of the surface.

A second cellulose nitrate membrane was wiped onto a Ag particle contaminated surface, but instead of dissolving the membrane entirely in acetone the membrane surface was ‘washed’ with 400µl of acetone to extract the particles. The 400 µl of acetone was extracted from the vial and 100µl of nail polish added. A 100µl aliquot of the resulting suspension was mounted onto a glass slide using the same conditions given previously. This approach to mounting the particles caught on the membrane was more successful, forming a stronger particle-containing film layer than with the dissolved membrane alone.

6.7 Conclusion

The particle coating of glass slides by cytocentrifugation of a particle suspension in a mixture of nail polish and acetone was demonstrated as a viable method by which to mount particulate samples for LA-ICP-MS analysis. The particles coating the glass slides, when produced under optimum conditions, were evenly dispersed across the surface, with sufficient distance between particles to reduce the likelihood of inadvertently ablating multiple particles in a single laser ablation pulse. The particles were embedded under a film layer of cellulose nitrate, which acted to ensure then particles were ablated by the laser ablation system rather than ejected whole from the surface by the action of the laser shockwave produced. The thickness of the film layer was estimated by surface metrology as under 500 nm. The particles appeared to be proud of the film layer surface and therefore the laser did not require a large number of pulses to cut through the layer to the particle beneath. The particle-coated slides were quick to prepare, requiring only 60 seconds to coat the particle suspension onto the surface.

Many of the methods described in the scientific literature to prepare radionuclide particles for laser ablation analysis are slow and labour intensive, involving the individual transfer of particles from one substrate to another by means of a micromanipulator, often inside a SEM. An alternative method would involve the particles collected being transferred from a cellulose nitrate membrane onto a glass slide using the cytocentrifugation method outlined. A map of the particles locations on all or part of the film layer, and their elemental composition, could be created using SEM-EDX or by graphite-assisted laser ablation (GALA) TOF-MS. The map created could then be fed into a modern laser ablation system and used to target particles for LA-ICP-MS analysis.

6.8 References

1. T. Punshon, B. P. Jackson, P. M. Bertsch, and J. Burger, *J. Environ. Monit.*, 2004, **6**, 153–9.

2. T. Okuda, J. Kato, J. Mori, M. Tenmoku, Y. Suda, S. Tanaka, K. He, Y. Ma, F. Yang, X. Yu, F. Duan, and Y. Lei, *Sci. Total Environ.*, 2004, **330**, 145–58.

3. C. J. Scadding, R. J. Watling, and A. G. Thomas, *Talanta*, 2005, **67**, 414–24.

4. J. S. Becker, H. Sela, J. Dobrowolska, M. Zoriy, and J. S. Becker, *Int. J. Mass Spectrom.*, 2008, **270**, 1–7.

5. N. S. Lloyd, R. R. Parrish, M. Horstwood, and S. R. N. Chenery, *J. Anal. At. Spectrom.*, 2009, **24**, 752–758.

6. S. Kappel, S. F. Boulyga, and T. Prohaska, *J. Environ. Radioact.*, 2012, **113**, 8–15.

7. A. Hubert, F. Claverie, C. Pécheyran, and F. Pointurier, *Spectrochim. Acta Part B At. Spectrosc.*, 2014, **93**, 52–60.

8. C. H. Ebert, PhD Thesis, Iowa State, 2012.

9. D. Hare, C. Austin, and P. Doble, *Analyst*, 2012, **137**, 1527–37.

10. J. Koch, I. Feldmann, B. Hattendorf, D. Günther, U. Engel, N. Jakubowski, M. Bolshov, K. Niemax, and R. Hergenroder, *Spectrochim. Acta Part B*, 2002, **57**, 1057–1070.

11. C. O. Connor, M. R. Landon, and B. L. Sharp, *J. Anal. At. Spectrom.*, 2007, **22**, 273–282.

12. M. Resano, K. S. McIntosh, and F. Vanhaecke, *J. Anal. At. Spectrom.*, 2012, **27**, 165–173.

13. B. Fernández, F. Claverie, C. Pécheyran, and O. F. X. Donard, *J. Anal. At. Spectrom.*, 2008, **23**, 367–377.

14. D. Tabersky, N. a. Luechinger, M. Rossier, E. Reusser, K. Hametner, B. Aeschlimann, D. a. Frick, S. C. Halim, J. Thompson, L. Danyushevsky, and D. Gunther, *J. Anal. At. Spectrom.*, 2014, **29**, 955–962.

15. M. E. Shaheen and B. J. Fryer, *Spectrochim. Acta Part B At. Spectrosc.*, 2011, **66**, 627–636.

16. S. E. Jackson, N. J. Pearson, W. L. Griffin, and E. a. Belousova, *Chem. Geol.*, 2004, **211**, 47–69.

17. J. M. Cottle, A. R. Kylander-Clark, and J. C. Vrijmoed, *Chem. Geol.*, 2012, **332-333**, 136–147.

18. A. Izmer, D. Gholap, K. De Houwer, F. Cuyckens, and F. Vanhaecke, *J. Anal. At. Spectrom.*, 2012, 27, 413–418.

19. J. Messerly, PhD Thesis, Iowa State, 2008.

20. J. Truyerns, E. Stefaniak, S. Mialle, and Y. Aregbe, *NUSIMEP-7 : Uranium isotope amount ratios in uranium particles*, IRMM Report EUR 25179EN, IRMM, Geel, 2011.

21. J. M. Cottle, M. S. a. Horstwood, and R. R. Parrish, *J. Anal. At. Spectrom.*, 2009, **24**, 1355–1363.

22. S. Rauch, G. M. Morrison, and M. Moldovan, *Sci. Total Environ.*, 2002, **286**, 243–51.

23. J. Košler, J. Sláma, E. Belousova, F. Corfu, G. E. Gehrels, A. Gerdes, M. S. a. Horstwood, K. N. Sircombe, P. J. Sylvester, M. Tiepolo, M. J. Whitehouse, and J. D. Woodhead, *Geostand. Geoanalytical Res.*, 2013, **37**, 243–259.

24. S. Kappel, S. F. Boulyga, L. Dorta, D. Günther, B. Hattendorf, D. Koffler, G. Laaha, F. Leisch, and T. Prohaska, *Anal. Bioanal. Chem.*, 2013, **405**, 2943–2955.

25. F. Pointurier, A. Hubert, and A.-C. Pottin, *J. Radioanal. Nucl. Chem.*, 2012, **296**, 609–616.

26. I. Choi, K. Song, Y. J. Park, J.-Y. Kim, and H.-S. Yoo, *Microchem. J.*, 2010, **95**, 38–42.

27. F. Pointurier, A. Pottin, and A. Hubert, *Anal. Chem.*, 2011, **83**, 7841–7848.

28. S. Gligorovski, J. T. Van Elteren, and I. Grgić, *Sci. Total Environ.*, 2008, **407**, 594–602.

29. L. Arroyo, T. Trejos, T. Hosick, S. Machemer, J. R. Almirall, and P. R. Gardinali, *Environ. Forensics*, 2010, **11**, 315–327.

30. F. Esaka, C.-G. Lee, M. Magara, and T. Kimura, *Anal. Chim. Acta*, 2012, **721**, 122–128.

31. S. F. Boulyga and T. Prohaska, *Anal. Bioanal. Chem.*, 2008, **390**, 531–539.

32. Y. Aregbe, T. Prohaska, Z. Stefánka, E. Szeles, A. Hubert, and S. F. Boulyga, *ESARDA Bull.*, 2011, **46**, 136–145.

33. A. J. Managh, S. L. Edwards, A. Bushell, K. J. Wood, E. K. Geissler, J. A. Hutchinson, R. W. Hutchinson, H. J. Reid, and B. L. Sharp, *Anal. Chem.*, 2013, **85**, 10627–10634.

34. B. O. Stokes, *Lab. Med.*, 2003, **35**, 434–437.

35. E. R. J. Jackson, J. C. Vickerman, and N. P. Lockyer, *Surf. Interface Anal.*, 2011, **43**, 290–293.

36. *US Pat.*, US4250830, 1981.

37. S. A. Wise and R. L. Watters, *National Institute of Standards & Technology Certificate of Analysis Standard Reference Material® 611 Trace Elements in Glass*,NIST, Gaithersburg MD, 2012.

38. F. Esaka, D. Suzuki, and M. Magara, *Anal. Chem.*, 2015, **87**, 3107–3113.

39. H.-R. Kuhn, M. Guillong, and D. Günther, *Anal. Bioanal. Chem.*, 2004, **378**, 1069–1074.

40. D. Donohue, *J. Alloys Compd.*, 1998, **271-273**, 11–18.

Chapter 7 – Analysis of a Soil Sample Containing Uranium Oxide Particles Collected from Colonie, New York

7.1 Introduction

In this chapter the isotope ratio analysis of uranium oxide (UO_x) particles by laser ablation (LA-) multi-collector (MC-) inductively coupled plasma (ICP-) mass spectrometry (MS) is described, as developed in Chapters 2 and 4. The UO_x particles were extracted from a soil sample collected at the town of Colonie, New York, USA and mounted for laser ablation analysis using the cytocentrifugation method developed in Chapter 6.

7.2 A Uranium Contaminated Soil Sample from Colonie, NY

7.2.1 Previous Analysis of UO_x Particles

From 1958 to 1984 in the town of Colonie, NY, a plant operated by National Lead Industries (NLI) processed U metal (mostly depleted uranium (DU), but also some enriched uranium (EU)) and used the DU to manufacture kinetic energy projectiles, counterweights and radiation shielding[1]. The manufacturing process created quantities of scrap uranium metal, a hazard due to uranium metal's pyrophoric properties when finely divided. Therefore before its disposal the scrap metal was converted to uranium oxide by combustion in a furnace, as a result of which UO_x particles were released into the environment, sometimes via an unfiltered stack[2]. Over the lifetime of the plant an estimated *ca.* 4.8 tonnes of uranium was emitted, with prevailing winds acting to disperse the UO_x particles across the town of Colonie and suburban Albany[3]. The evidence of the uranium contamination from the plant has been found in air filters, reservoir sediments, urine of former plant employees, dusts and soils[1–4]. The morphology of UO_x particles isolated in soil samples collected at Colonie, 25 years after the plant was closed down, was found to be as they were emitted from the plant, with only some evidence of weathering[1]. Due to their low solubility and non-bioaccessability, UO_2 with variable amounts of U_3O_8 dominated the composition of the particles[1].

Lloyd *et al* (2009)[3] determined by LA-MC-ICP-MS, the $^{235}U/^{238}U$ and $^{236}U/^{238}U$ uranium isotope ratios of individual UO_x particles sourced from Colonie. The method used to extract the particles from the soil limited the size to approximately 20 µm or greater; analysis by SEM-EDX confirmed a mean uraniferous grain size of 36µm. Conical pits of 25x14x1µm were ablated into the UO_x particles at a repetition rate of 1 Hz with a large volume ablation cell to give a smooth signal. The uranium isotope ratios, calculated from 30, 1 second integrations for each particle, were, for all 115 particles analysed, consistent with DU; the $^{235}U/^{238}U$ ratio was less than 2.4E-03.

EU was known to have been processed at the Colonie plant (and was found in the urine of at least one worker[4]) and it was theorised that, as DU and EU may have been processed differently, particles of EU could be found by looking at a different particle size fraction, perhaps under 5 µm or the sub-micron fraction. To this end a further soil sample was collected at Colonie by Dr N. Lloyd and sent to NIGL. This chapter describes attempts to isolate uraniferous particles of the desired particle size range from this soil sample, prepare them for LA-MC-ICP-MS analysis and therefore determine the uranium isotope ratios.

7.2.2 Particle Size Analysis of the Untreated Colonie Soil Sample

Before handling, the soil sample from Colonie was autoclaved in order to render it biologically inert. Once rendered inert the first step was to determine if the soil sample contained any particles in the desired size ranges of fewer than 5 µm and under 1 µm. A quantity of the untreated soil sample was added to the Beckman Coulter™ LS 13 320 Series laser diffraction particle size analyser at the British Geological Survey (BGS). The soil sample was dispersed into a stream of DI water which was constantly pumped through the detector. The particle size distribution of the dispersed soil sample was determined via the Mie Approximation of Light Scattering.

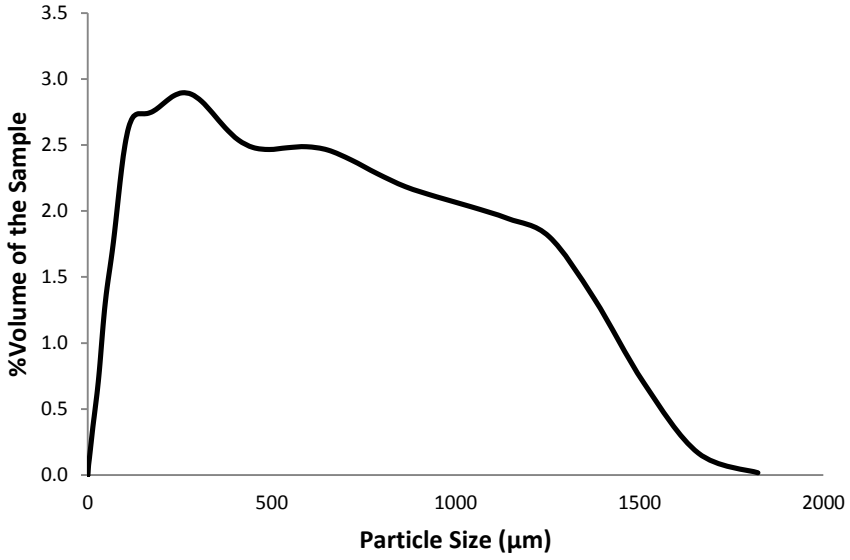

Figure 76 – Percentage of the total volume of the soil sample plotted against particle size. 98.56% of the total volume of the sample was comprised of particles greater than 5µm in diameter. 99.87% of the total volume of the sample was comprised of particles greater than 1µm in diameter.

Of the total sample volume, 0.13% was composed of particles less than 1 µm in diameter, 1.44% was composed of particles under 5 µm in diameter. The volume of a perfectly spherical 1 µm diameter particle is 10,000 times less than the volume of a perfectly spherical 100 µm diameter particle. Therefore despite only comprising 0.13% and 1.44% of the total sample the number of sub-1 µm and

sub-5 µm was thought to be sufficient for LA-ICP-MS analysis if they could be extracted from the remainder of the soil sample volume.

7.3 Extraction of a Size Fraction from the Colonie Soil Sample onto an Alumina Membrane

7.3.1 Dense Liquid Separation

The methodology used by Lloyd *et al* (2009)[2] to concentrate the number of UO_x particles in the soil and dust samples used a six stage process (Table 54), at each stage removing a fraction of unwanted material from the sample.

Table 54 – Methodology reported in Lloyd *et al* (2009) for concentrating uranium oxide grains from a soil and dust sample and the fractions removed.

Process	Criteria	Fraction Removed
Dry	60°C	Moisture
Sieve	<250 µm	Coarse grains
Hand magnet	magnetic	Magnetite, Iron
Dense liquid (di-iodomethane)	$\rho > 3.3$ g cm^{-3}	Fine particulate, silica and silicates
Isodynamic magnetic separation (Franz LB-1)	0.1 – 1 A	Iron-oxides, some zircons
Sieve	40 µm	Coarse and fine fractions

Initial attempts to extract the <1 µm fraction from the soil sample were not based on the methodology in Table 54, but instead aqueous suspensions of the soil sample were passed through a 1 µm Titan 2™ (Fisher Scientific, Loughborough, UK) PTFE membrane (polypropylene housing) syringe filter. The filtrate which passed through the syringe filter was further filtered through a cellulose acetate membrane (pore size 0.1 µm) to trap any particles. This and other aqueous suspension based attempts to concentrate and mount <1 µm particles for laser ablation analysis met with failure. Subsequently a method more closely followed the methodology described in Table 54 was used.

In the new method a proportion of the Colonie soil sample was wet sieved in acetone through a series of nylon filters of pore size 200 µm, 40 µm and 20 µm[5]. The resulting pale yellow filtrate was transferred into a 50 ml falcon tube and spun in a centrifuge at 6000 rpm for 30 minutes. Following centrifugation the filtrate had separated, producing a smear of particulate material at the bottom of the falcon tube. The remaining liquid was decanted off and the smear of particulate material re-suspended in a small quantity of acetone. The resulting mixture was evaporated down to 0.25 mL

under a heat lamp and then mixed with 3-4 mL of iodomethane and divided into 2 x 2 mL centrifuge tubes. Iodomethane is a dense liquid, ρ 2.28 g mL^{-1} and low density particulate such as silica and silicates should float on its surface. The soil fraction/iodomethane/acetone mixture was subsequently spun for 90 minutes at 3,500 rpm in a centrifuge.

7.3.2 Stokes Law

The time for which the soil fraction/iodomethane/acetone mixture was centrifugally spun was determined by Stokes Law. George Gabriel Stokes proposed an equation for the drag force (F_d) acting on a particle moving through a fluid[6]:

$$F_d = -3\pi\mu D v$$

Where μ is the shear viscosity of the fluid; D is the diameter of the particle and v is the constant velocity of the particle. The force felt by the particle due to its weight (F_g) is expressed by[7]:

$$F_g = (\rho_p - \rho_f)gV$$

Where ρ_p is the density of the particle; ρ_f is the density of the fluid; g is the acceleration due to gravity and V the volume of the particle. If the particle is falling through the fluid at terminal velocity:

$$F_g = -F_d$$

By substitution:

$$3\pi\mu D v = (\rho_p - \rho_f)gV$$

As the volume of a perfectly spherical particle can be calculated from the diameter by:

$$V = \frac{\pi D^3}{6}$$

Then an equation can be derived for the terminal velocity of a spherical particle in a fluid.

$$v = \frac{(\rho_p - \rho_f)gD^2}{18\mu}$$

This equation is known as the Stokes Formula for Terminal Velocity and particles which obey it are referred to as Stokesian particles[8]. Stokes law does require perfect spheres and therefore modifications to the Law have been attempted in order to account for deviations from the ideal[7–9], based on the largest possible surface area being projected in the direction of fall[7]. However for <1

µm particles the difference between the velocity calculated from the modified Law and the Stokes Law is sufficiently small that <1 µm can be said to obey Stokes Law.

The lengths of the centrifuge tubes were measured and, assuming a UO_x density of 10.3 g cm^{-3}, used to calculate the time taken for a 1 µm particle to fall to the bottom of the tube under the applied centrifugal force. As the aim was to mount only the fraction of particles which made it to the bottom of the tube, this was the minimum time for which the centrifugal force was applied.

7.3.3 Mounting Particles onto an Alumina Membrane

Following centrifugation the soil sample in the iodomethane/acetone containing 2x2mL centrifuge tubes was found to have split into fractions. One fraction was material which had collected on the bottom of the tube and another fraction was the material floating on the surface of the iodomethane. Under microscopy however a further fraction of material was observed moving within the iodomethane/acetone. The three fractions where extracted separately and mounted for further analysis.

Prior to the development of the rapid method for preparing particulate samples onto glass slides for LA-ICP-MS described in Chapter 6 other approaches to mounting UO_x particles for analysis were considered. Becker *et al* (2008)[10] collected UO_2 particles and subsequently ablated them from a filter. The iodomethane and acetone mixture in which the soil sample fractions resided was found to dissolve most commercially available filters with a pore size much less than 1 µm. Membranes made of alumina, however were available which were inert to the iodomethane and acetone. Therefore all three soil sample fractions collected were each vacuum filtered through an alumina membrane, pore size 0.2 µm. No adhesive agent was applied to the filters.

7.3.4 SEM Analysis of Particles on an Alumina Membrane

The alumina membranes were used as they were inert to the iodomethane and acetone mixture, but they were not an ideal substrate material for the particles. The membranes were brittle and prone to shattering into shards on transfer. Intended to strengthen the membrane and make transport easier, a clear film support ring surrounded the alumina which reacted with the acetone to form a glue which acted to make transferring the membrane intact more difficult. Without an adhesive agent in the protocol, great care had to be taken in transferring the brittle membranes in order to prevent particles being aerosolised from the membrane surface.

The three alumina membranes coated with the three soil fractions collected were attached to three 25 mm SEM stubs by carbon tape and then carbon coated. The three membranes were then analysed by SEM-EDX (SEM - LEO 435VP, EDX – Oxford Instruments™ INCAx) at BGS. A feature

detection sequence was used to scan hundreds of fields for particles in the centre of each membrane. Of the three soil fractions only the membrane associated with the fraction which was suspended in the iodomethane/acetone was found to have any uraniferous particle, the other two membranes were clean of particles. Whether particles had been present in these fractions and were lost during transfer was unclear.

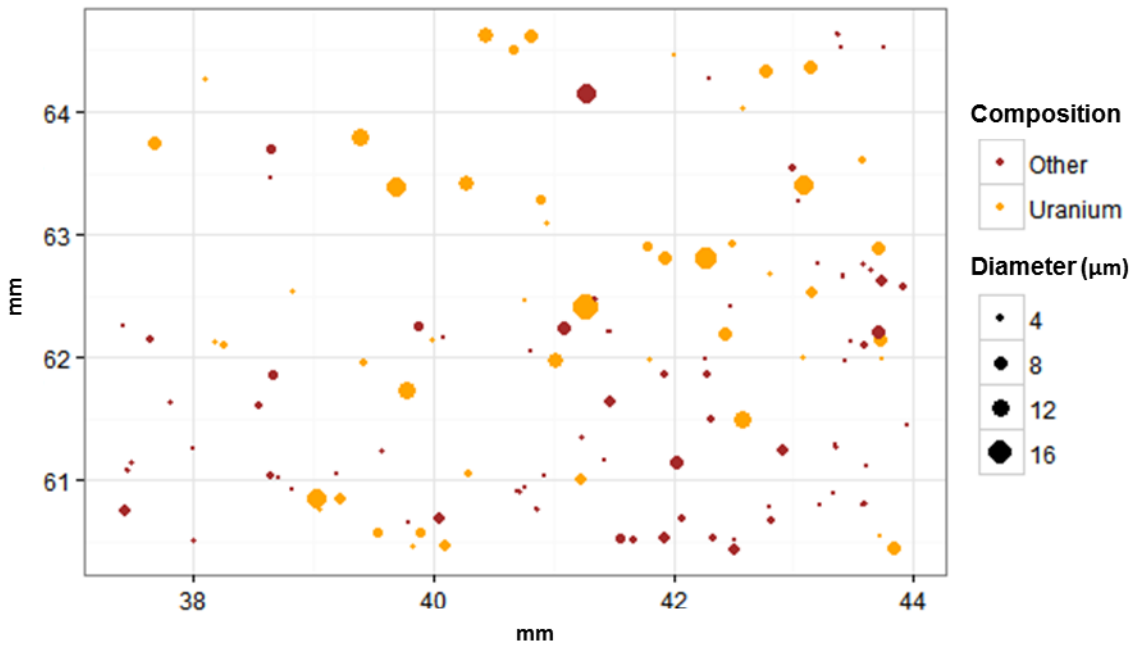

Figure 77 – Distribution map of particles on an area of an alumina membrane, 44 mm^2. The particles were from the soil fraction suspended within the iodomethane and acetone. 54 uraniferous particles were detected and ranged in size from 0.3 to 20 µm in diameter. Map not to scale.

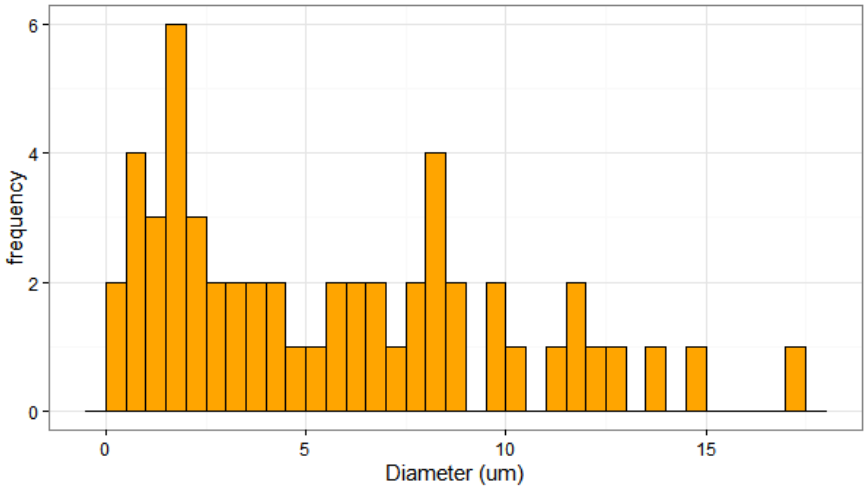

Figure 78 – Histogram of 54 uraniferous particles located on 44mm^2 of alumina membrane. The particles were from the soil fraction suspended within the iodomethane and acetone.

On the alumina membrane on which uraniferous particles were found, an area of 44mm^2 was scanned with a feature detection sequence. 54 uraniferous particles, ranging in size from 0.3 µm to 20 µm in diameter (the size of the smallest filter), were identified within the scanned area. Particles of other compositions, mainly magnetite and barite were also present in the soil sample. A subsequent attempt to ablate the particles on the alumina membrane for isotope ratio analysis by LA-MC-ICP-MS met with failure, likely due to the lack of an adhesive agent to bind the particles to the fragile alumina surface. Following the failure of the method for LA-ICP-MS analysis, the particle mounting method employing cytocentrifugation described in Chapter 6 was optimised. Subsequently this new method was used on fractions extracted from the Colonie soil sample.

7.4 Extraction of a Size Fraction from the Colonie Soil Sample onto a Glass Slide

7.4.1 Mounting the Colonie Soil Sample onto a Glass Slide using Cytocentrifugation

To prepare a glass slide coated with particles from the Colonie Soil sample, 2 grams of the untreated Colonie soil sample was suspended in ultraclean acetone. The suspended soil sample was then passed through two nylon filters in series, pore size 50 µm and 20 µm. The nylon filters were washed with fresh ultraclean acetone before being discarded. The retained pale-yellow filtrate was then passed and washed through a further series of nylon filters, pore size 10 µm and 5µm. The remaining filtrate was collected in a 50 mL centrifuge tune and made up to 50 mL with ultraclean acetone.

Centrifugal force was then applied to the filtrate, spun at 2,000 rpm for 25 minutes. The outcome was a small quantity of precipitate particles at the bottom of the centrifuge tube. The majority of the liquid was discarded, what remained and the precipitated particles were transferred to a 2 mL centrifuge tube. The 2 mL centrifuge tube was then spun at 10,000 rpm for 15 minutes, to re-precipitate the particles to the bottom of the tube. All of the liquid was removed and replaced with 400 µl of fresh ultraclean acetone and 100 µl of nail polish.

A vortex mixer was used to suspend the particles at the bottom of the tube in the acetone and nail polish mixture. Once suspended four 100 uL aliquots were taken and coated onto four glass slides using a cytocentrifuge. The cytocentrifuge was spun at 2,000 rpm for 60 seconds to prepare the slides.

7.4.2 SEM-EDX analysis of a Colonie Soil Sample on a Glass Slide

A slide prepared using the method described in section 7.4.1 was analysed under the SEM-EDX. Before analysis the slide was carbon coated and backed with carbon tape.

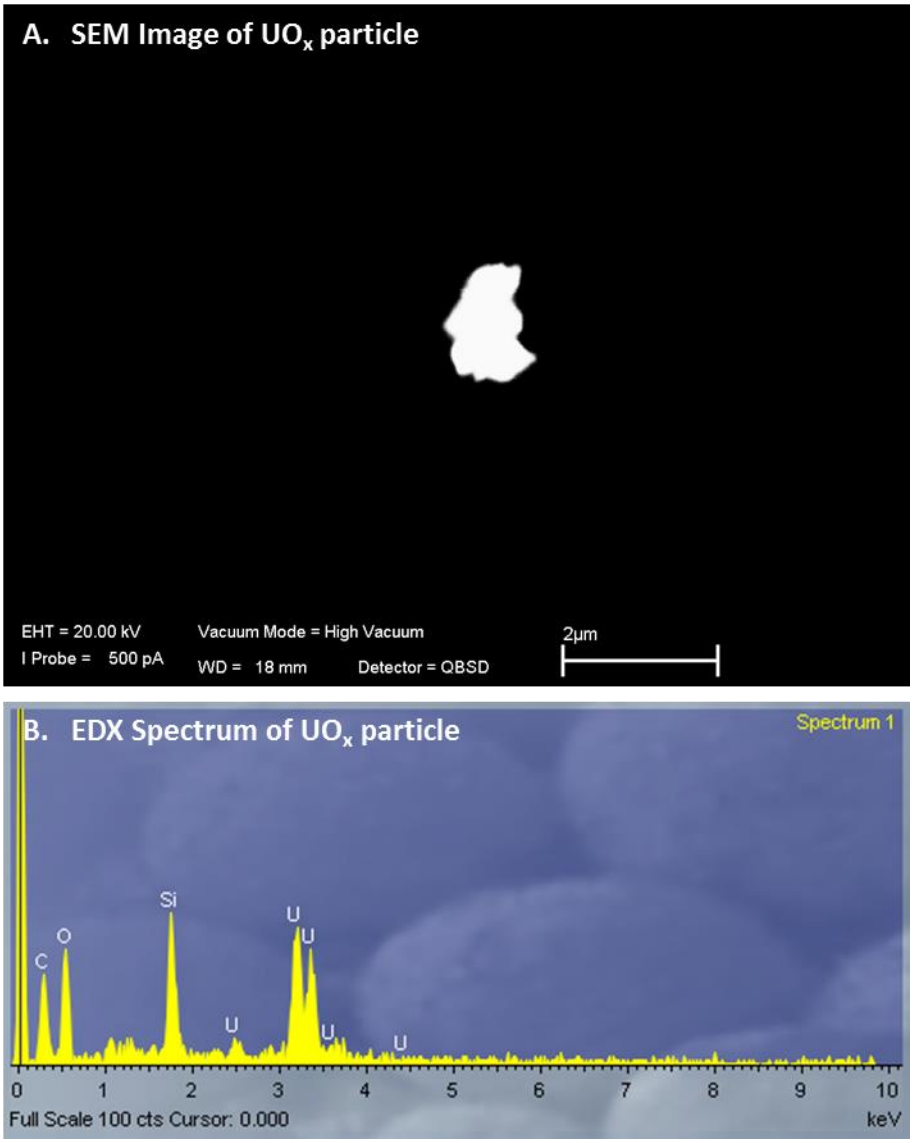

Figure 79 – SEM-EDX of a single UO_x particle from Colonie soil sample, mounted in a film layer on a glass slide. A. SEM image of UO_x particle, magnification 10,000X. B. EDX spectrum of UO_x particle, Si contribution is from the glass slide.

A manual search of the particle containing film layer on the glass slide revealed particles which EDX analysis confirmed contained a significant proportion of uranium (Figure 79). Once uranium-bearing particles were identified a rectangle of 4 mm by 8 mm inside the 12 mm diameter film layer was scanned for more particles using a feature detection sequence. In total 339 particles were detected by the feature detection sequence, 186, or 55% of the total, were identified as uraniferous. 5% seems high compared to Lloyd *et al* (2009)[2] who reported for the mounts they produced only 2.5%

of the particles were uraniferous, however the feature detection sequence was biased towards particles containing heavy elements. Particles which contained only light elements would have been rejected by the sequence. The particles not identified as uraniferous contained identifiable quantities of either lead, zinc, tin or barium.

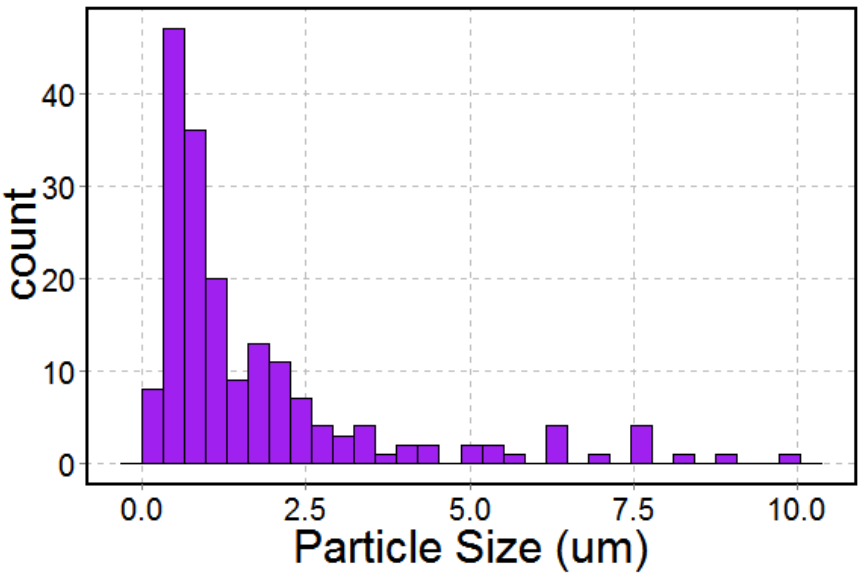

Figure 80 – Histogram of particle size (Diameter) in microns of UO_x particles identified by particle detection sequence using SEM-EDX. Area scanned 8mm^2. The median particle size occurs at 1.00 µm.

The distribution of the 339 particles in the 8 mm^2 area is mapped in Figure 81. For the 186 uranium bearing particles identified, the particle size, quoted as the average diameter, ranged up to 10 µm. Consistent with the pore size of the most restrictive filter used, the majority of the particles were under 5 µm. The median particle size was 1.00 µm and the mean particle size was 1.12 µm.

The SEM-EDX analysis of the Colonie soil sample fraction, mounted onto a glass slide by cytocentrifugation, confirmed the utility of the method to prepare an environmental sample containing radionuclide particles for LA-ICP-MS analysis. The uraniferous particles were spread out across the surface, rather than aggregating or concentrating together on a single area of the substrate. A distribution map, like Figure 81, could be uploaded into current generation laser ablation systems and, provided there are visible points of reference for triangulation, used to target particles for LA-ICP-MS analysis. This could not be achieved if the film layer had been produced by dropping adhesive over the particles[11] or by dissolution of a polycarbonate membrane[12] as the layer would be thicker than the penetration depth of the SEM. The cytocentrifugation method developed for mounting particles also has utility for other forms of analysis. Fission track (FT) analysis of particle samples requires the particles to be held in place, often within a film layer of polycarbonate[13,12,14] or collodion[11] atop a glass slide. By stacking a fission track detector of 20 µm thickness onto the

cytocentrifuge particle-coated slide and irradiating, FT analysis could be used to identify uranium bearing particles in the film layer[12]. These particles could then be targeted for LA-ICP-MS analysis or instead removed from the layer. Small squares around each particle could be cut out using a micro-handling device and transferred to a high purity rhenium filament for TIMS, or a micromanipulator with a small drop of acetone used to dissolve the layer over a particle to extract it for analysis by solution ICP-MS[11].

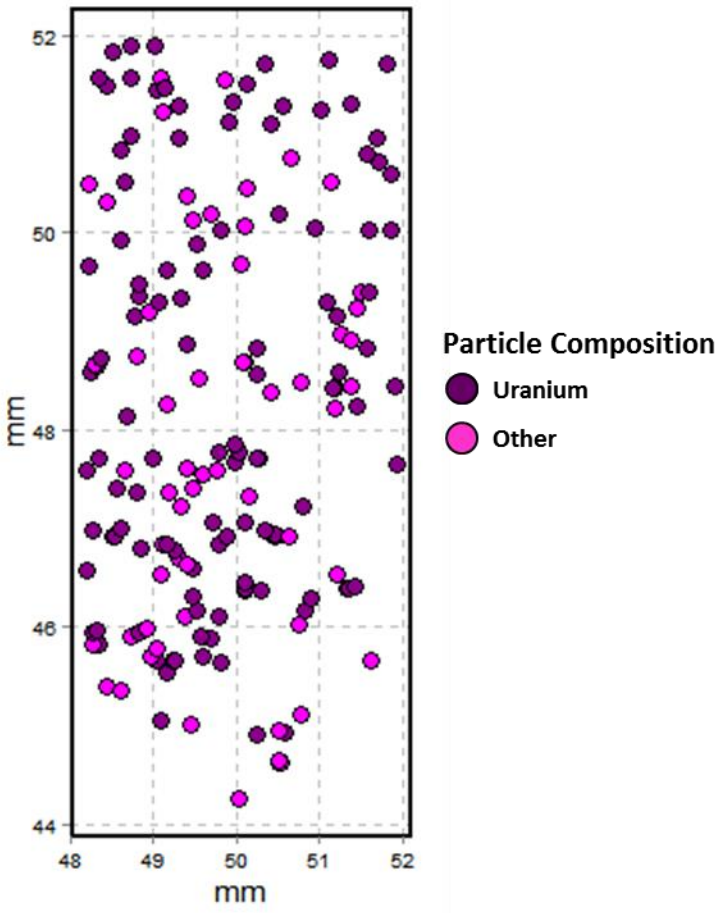

Figure 81 – Distribution map of particles identified in an area 8mm^2 by SEM-EDX by a feature detection sequence. 186 uraniferous particles (purple) were detected across the surface alongside 153 particles of other compositions (magenta). Particles not to scale.

7.5 Uranium Isotope Ratio Analysis of UO_x particles from the Colonie Soil Sample by LA-MC-ICP-MS

7.5.1 Experimental

Following analysis by SEM-EDX, glass slides coated with the Colonie soil sample were analysed by LA-MC-ICP-MS. The instrumentation used was the ESI® New Wave Research™ UP-193FX excimer laser ablation system and the Thermo Scientific™ Neptune *Plus*™ MC-ICP-MS coupled with the DCI &

Enterprise Cell. The configuration of the LA-ICP-MS setup used for the Colonie soil sample was identical to the configuration reported in Chapters 2 and 4.

Table 55 – Operating parameters of LA-MC-ICP-MS setup coupled with the DCI & Enterprise Cell for analysis of Colonie soil sample.

	Parameter
ESI® New Wave Research™ UP-193FX excimer laser	
Ablation mode	Single spot
Fluence (J cm^{-2})	6
Repetition rate (Hz)	1
Spot size (µm)	10
He carrier gas (L min^{-1})	0.05
CETAC™ Aridus™ I	
Nebulizer	PFA 50
Sweep gas (L min^{-1})	5.70
N_2 add gas (L min^{-1})	0.09
Spray chamber temperature (°C)	95
Membrane temperature (°C)	160
Thermo Scientific™ Neptune Plus™ HR MC-ICP-MS	
RF power (W)	1171
Cool gas (L min^{-1})	15
Aux. gas (L min^{-1})	0.8
Skimmer cone	X (Ni)
Sampler cone	Jet (Ni)
Sample Gas (L min^{-1})	0.725
Extraction (V)	-2000
Resolution m/Δm	300
Cell pressure (psi)	11.3
Tubing length (m)	1.5

The Ar sweep gas was supplied by the outflow of a desolvator, which allowed correction factors to be generated by the liquid aspiration of reference materials. The method by which the correction factors were used to correct the isotope ratios is described in Chapter 3. A solid reference material, SRM611 was ablated prior to the analysis of the Colonie soil sample. The analysis of SRM611 was

used to confirm the detection efficiency of the LA-MC-ICP-MS system and as potential further normalisation to the liquid reference material derived correction factors.

The cup configuration used on the MC-ICP-MS was the same as Method 1 (section 2.2.2); ^{238}U was measured on a Faraday cup, ^{236}U & ^{235}U on ion counters and ^{234}U on a compact discrete dynode, a miniaturised ion counter. The integration time selected was 131 ms based on the investigation into reducing the blind time additional uncertainty identified in Chapter 2.

7.5.2 Uranium isotope ratio analysis of Colonie soil sample

Using the DCI & Enterprise Cell to couple the MC-ICP-MS setup, as has already been reported in Chapter 2, the signal pulse profiles from the Faraday cup and the ion counters do not align (Figure 82), and as such the TSI data evaluation strategy was required.

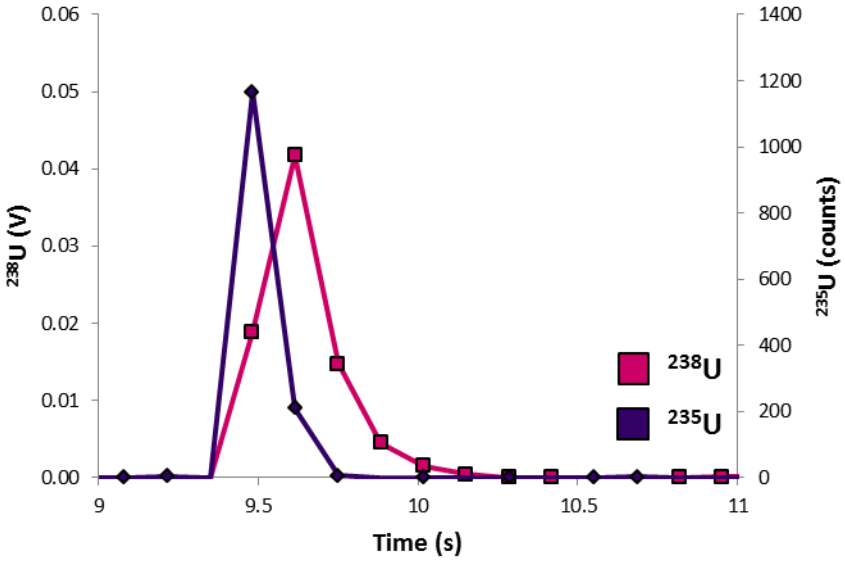

Figure 82 – typical signal pulse profile of ^{238}U and ^{235}U for Colonie soil sample collected with LA-MC-ICP-MS coupled with DCI & Enterprise Cell. Integration time 131 ms. Pulse profiles do not align and so TSI data evaluation strategy required.

The Colonie soil sample was ablated using single shot mode, allowing the operator the greatest amount of control. Rather than ablated randomly across the surface of the thin layer, particles visible within the layer were deliberately targeted. Most of the particles visible were shades of dull brown in colour, however a few looked gloss black. Deliberate targeting of the few gloss black particles returned a much higher likelihood of detecting uranium signal (UO_2 and U_3O_8 grains are black in colour[15]). Due to the 'lensing' effect of the film layer, it was difficult to identify the size of the particle analysed prior to ablation. Both the pore size of the filter and the SEM-EDX analysis suggest most were less than 5 µm in diameter, although following the initial ablation some were clearly larger, up to 20 µm in diameter.

With the NUSIMEP-6 UO_x particles, average size 0.64±0.43 µm, a single laser pulse was shown to be insufficient to consume the entire particle; uranium signal was returned for 2nd and 3rd ablation pulses. For the Colonie soil sample, the much larger UO_x particles could, size depending, return strong uranium signals for multiple pulses. Due to both time constraints and the relative rarity of UO_x particles coated on the slide, the number of signal pulses collected was increased by ablating each particle, if it continued to return sufficient signal, more than once.

A total of 822 uranium signal pulses were collected from material on a Colonie soil sample coated slide. Plotting the Ln ^{235}U against Ln ^{238}U for each pulse (Figure 83A) only one major composition was identified. The methodology for identifying uranium compositions by linear regression using Flexmix (a downloadable package for the freeware R) described in Kappel *et al* (2013)[16] was used to assign the main composition identified in Figure 83A to its own cluster. The mean isotope ratios were subsequently calculated for the main composition.

Table 56 – Mean uranium isotope ratios for Colonie soil sample, measured by LA-ICP-MS with the DCI & Enterprise Cell. Dataset has been filtered for the main composition using Flexmix package in R.

Method	**n = 760**	**$^{234}U/^{238}U$**	**$^{235}U/^{238}U$**	**$^{236}U/^{238}U$**
DCI & Enterprise Cell	**R_{mean}**	9.76E-06	2.24E-03	3.87E-05
TSI, 131ms	**(−RSD)**	(35.5%)	(6.91%)	(21.6%)
	(+RSD)	(55.0%)	(7.42%)	(27.5%)
	(−RSE)	(1.29%)	(0.25%)	(0.78%)
	(+RSE)	(1.99%)	(0.27%)	(1.00%)
	Limiting (RSD)	(36.5%)	(2.37%)	(18.0%)

Lloyd et al (2009)[2] identified two main uranium isotope composition clusters at Colonie from the $^{235}U/^{238}U$ and $^{236}U/^{238}U$ values. The main cluster was tightly clustered around 2.0E-03 $^{235}U/^{238}U$ and 2.7E-05 $^{236}U/^{238}U$. The mean isotope ratio for the second cluster was not reported, but the values were more diffuse than the main cluster and ranged between 2.0E-03 &2.4E-03 $^{235}U/^{238}U$ and 3.0E-05 & 5.0E-05 $^{236}U/^{238}U$. The mean isotope ratios reported in Table 56 are more consistent with mean values for the second, more scattered, cluster from Lloyd *et al*. The uncertainty on the measurement for all three isotope ratios is sufficiently large however such that, assuming both clusters previously identified are present, the two compositions could not be resolved.

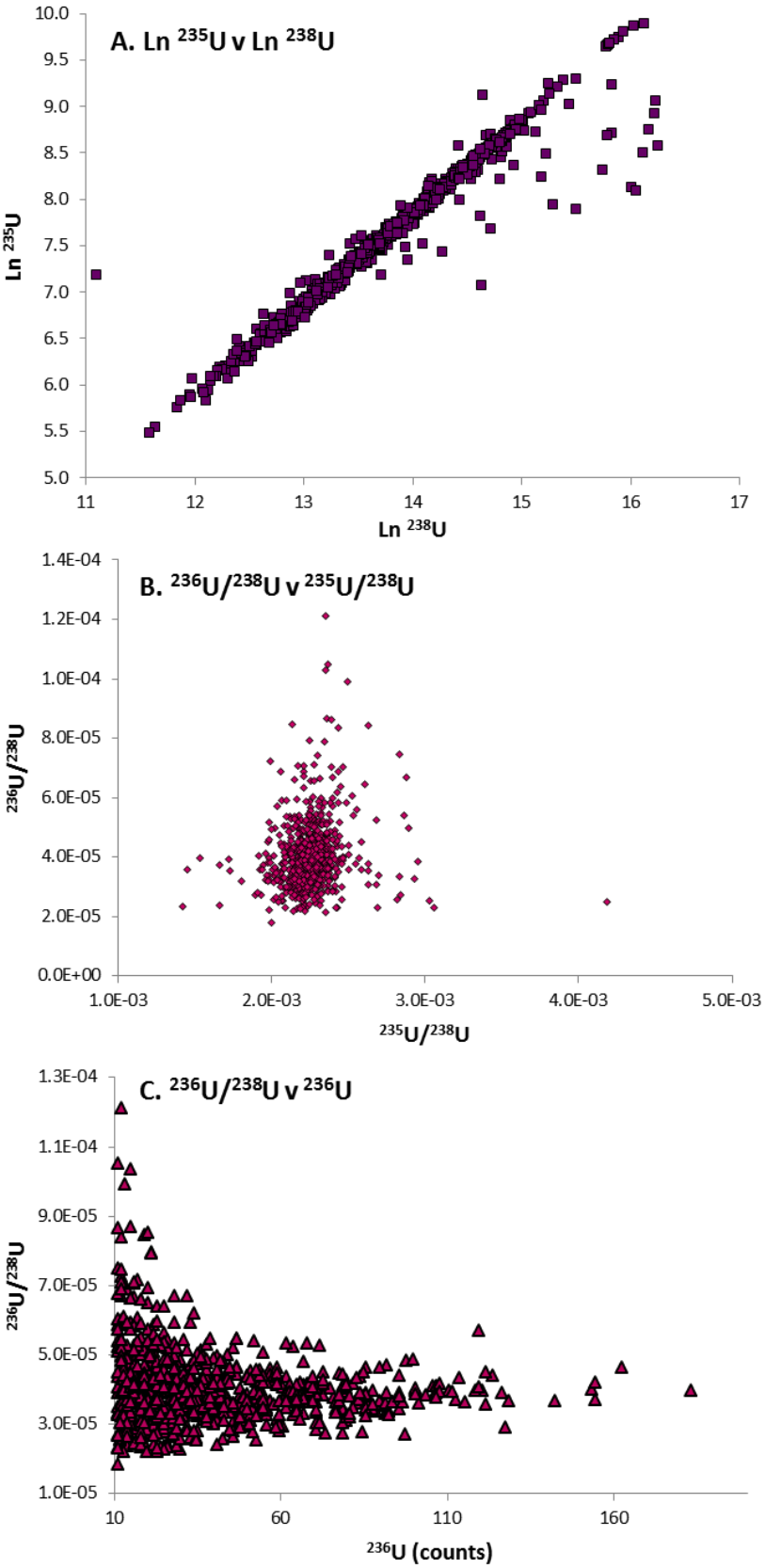

Figure 83 – Plots from the LA-MC-ICP-MS of UOx particles from the Colonie soil sample. A. Plot of Ln ^{235}U against Ln ^{238}U, identifying only one major composition. B. Plot of ^{236}U/^{238}U against ^{235}U/^{238}U. C. Plot of ^{236}U/^{238}U against ^{236}U, the scatter on the ^{236}U/^{238}U ratio decreases as the signal of the minor isotope increases.

Following Lloyd *et al* (2009) a plot of $^{236}U/^{238}U$ against $^{235}U/^{238}U$ was constructed (Figure 83B). It was hypothesised[15] at Colonie the DU feedstock emitted had $^{236}U/^{238}U$ ratios up to 6.0E-05. In Figure 83B the $^{236}U/^{238}U$ had even greater scatter, up to 1.2E-04. Plotting $^{236}U/^{238}U$ against the total number of counts of ^{236}U counts confirmed the increased scatter on $^{236}U/^{238}U$ was dependent on the count rate (Figure 83C). For higher count rate signals, total ^{236}U greater than 30 counts, the $^{236}U/^{238}U$ ratio for each pulse was more constrained to the range described by Lloyd *et al*.

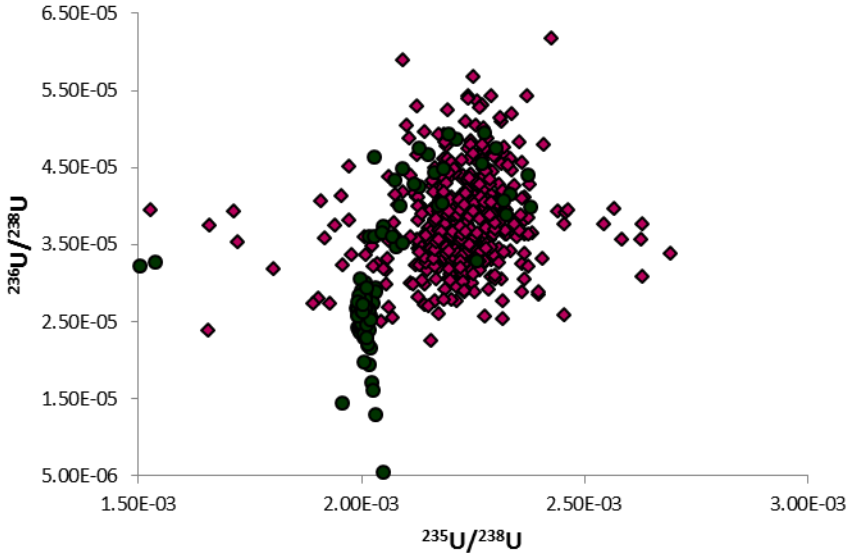

Figure 84 – Scatterplot for 448 pulses of $^{236}U/^{238}U$ against $^{235}U/^{238}U$ for the Colonie soil sample (purple diamonds), the dataset has been filtered for the highest value signals $^{236}U \geq 30$ counts. Suberimposed onto the particle analysis by Lloyd *et al* (2009), reproduced with permission (green circles). The majority of the 448 pulses collected correspond with the second cluster identified by Lloyd *et al* (2009).

The mean uranium isotope ratios for the dataset restricted to pulses of total ^{236}U signal greater than 30 are reported in Table 57. For the $^{235}U/^{238}U$ ratio the RSDs were significantly greater than the limiting uncertainty determined from the counting statistics. As the coupling mechanism used was the DCI & Enterprise Cell a proportion of the additional uncertainty could be attributed to a blind time mixed detector effect, however other causes could not be discounted. In Figure 83B the scatter on $^{236}U/^{238}U$ against $^{235}U/^{238}U$ was such that two distinct uranium isotopic compositions could not be identified, but restricting the dataset to higher count rate signals (Figure 84) a potential dividing line between two clusters on the $^{235}U/^{238}U$ ratio emerges, more consistent with the results of Lloyd *et al* (2009).

Table 57 – Mean uranium isotope ratios for Colonie soil sample, measured by LA-ICP-MS with the DCI & Enterprise Cell. Dataset has been filtered for the highest value signals $^{236}U \geq 30$ counts.

Method	n = 448	$^{234}U/^{238}U$	$^{235}U/^{238}U$	$^{236}U/^{238}U$
DCI & Enterprise Cell	**R_{mean}**	9.52E-06	2.22E-03	3.76E-05
TSI, 131ms	**(−RSD)**	(26.0%)	(6.58%)	(14.9%)
	(+RSD)	(35.1%)	(7.05%)	(17.6%)
	(−RSE)	(1.23%)	(0.31%)	(0.71%)
	(+RSE)	(1.66%)	(0.33%)	(0.83%)
	Limiting (RSD)	(27.2%)	(1.75%)	(13.9%)

Assuming the line in Figure 84 did represent a divide between two distinct isotope ratio compositions, the mean isotope ratios of the 1st composition was determined for 15 pulses. For the 15 pulses isolated as the 1st composition, the mean uranium isotope ratios differ from the 2nd composition not just in terms of $^{235}U/^{238}U$, but also $^{234}U/^{238}U$ and $^{236}U/^{238}U$. The mean $^{235}U/^{238}U$ value 1.98E-03 is consistent with the value reported by Lloyd *et al* (2009), but the $^{236}U/^{238}U$ mean value 3.33E-05 is significantly greater than the 2.7E-05 previously reported.

Table 58 – Mean uranium isotope ratios for Colonie soil sample, measured by LA-ICP-MS with the DCI & Enterprise Cell. 15 pulses assigned to be of the 1st composition predicted by the work of Lloyd *et al*.

Method	n = 15	$^{234}U/^{238}U$	$^{235}U/^{238}U$	$^{236}U/^{238}U$
DCI & Enterprise Cell	**R_{mean}**	7.69E-06	1.98E-03	3.33E-05
TSI, 131ms	**(−RSD)**	(26.1%)	(3.25%)	(14.2%)
	(+RSD)	(35.3%)	(3.36%)	(16.5%)
	(−RSE)	(6.74%)	(0.84%)	(3.66%)
	(+RSE)	(9.12%)	(0.87%)	(4.26%)
	Limiting (RSD)	(22.6%)	(1.49%)	(11.7%)

7.6 Conclusion

It was originally hypothesised a new uranium isotopic composition (potentially of enriched uranium) could be potentially identified at Colonie by analysis of UO_x particles recovered from a soil sample, by analysing particles of a smaller size fraction than in previous analyses. Using a series of nylon filters a soil sample collected at Colonie was sieved to obtain the size fraction of grains less than 5 µm. The fraction extracted was subsequently mounted for LA-MC-ICP-MS using the cytocentrifugation method developed in Chapter 6. The resulting particle-coated slide was analysed

by SEM-EDX to confirm the presence and size of UO_x particles within the fraction. LA-MC-ICP-MS analysis was then applied to determine isotopic composition.

The uranium isotope ratios of the pulses generated did not confirm the presence of a uranium isotopic composition which had not been identified in the previous LA-MC-ICP-MS analysis by Lloyd *et al* (2009)[15] of larger uraniferous grains collected at Colonie. Of the two main isotopic composition clusters identified in Lloyd *et al*, only one of the compositions could be positively identified in this analysis. This composition was dominant in the analysis; the overwhelming majority of the pulses analysed were identified as being of that composition. However for the size fraction analysed by Lloyd *et al*, of 115 grains only 30 were assigned to this cluster. While a new uranium isotopic composition was not identified in the ≤5 μm size fraction there is at least some evidence that the prevalence of an isotopic composition within a population is dependent on the grain size. Further work on the Colonie soil sample, extracting different size fractions for analysis, would contribute towards an understanding of this potential relationship.

7.7 References

1. N. S. Lloyd, J. F. W. Mosselmans, R. R. Parrish, S. R. N. Chenery, S. V. Hainsworth, and S. J. Kemp, *Mineral. Mag.*, 2009, **73**, 495–510.

2. N. S. Lloyd, R. R. Parrish, M. Horstwood, and S. R. N. Chenery, *J. Anal. At. Spectrom.*, 2009, **24**, 752–758.

3. N. S. Lloyd, S. R. N. Chenery, and R. R. Parrish, *Sci. Total Environ.*, 2009, **408**, 397–407.

4. R. R. Parrish, M. Horstwood, J. G. Arnason, S. Chenery, T. Brewer, N. S. Lloyd, and D. O. Carpenter, *Sci. Total Environ.*, 2008, **390**, 58–68.

5. R. R. Parrish, Personal Communication

6. G. G. Stokes, *Trans. Cambridge Philos. Soc.*, 1850, **9**, 8–92.

7. W. E. Dietrich, *Water Resour. Res.*, 1982, **18**, 1615–1626.

8. A. V Nguyen, H. Stechemesser, G. Zobel, and H. J. Schulze, *Int. J. Miner. Process.*, 1997, **50**, 53–61.

9. K. G. Tsakalakisq and G. A. Stamboltzis, *Miner. Eng.*, 2001, **14**, 349–357.

10. J. S. Becker, H. Sela, J. Dobrowolska, M. Zoriy, and J. S. Becker, *Int. J. Mass Spectrom.*, 2008, **270**, 1–7.

11. F. Pointurier, A. Hubert, and A.-C. Pottin, *J. Radioanal. Nucl. Chem.*, 2012, **296**, 609–616.

12. F. Esaka, M. Magara, and T. Kimura, *J. Anal. At. Spectrom.*, 2013, **28**, 682–688.

13. F. Esaka, C.-G. Lee, M. Magara, and T. Kimura, *Anal. Chim. Acta*, 2012, **721**, 122–128.

14. F. Esaka, D. Suzuki, and M. Magara, *Anal. Chem.*, 2015, **87**, 3107–3113.

15. N. S. Lloyd, PhD Thesis, University of Leicester, 2009.

16. S. Kappel, S. F. Boulyga, L. Dorta, D. Günther, B. Hattendorf, D. Koffler, G. Laaha, F. Leisch, and T. Prohaska, *Anal. Bioanal. Chem.*, 2013, **405**, 2943–2955.

Conclusion

The aim of this thesis, as a body of work, has been to improve the utility of laser ablation inductively coupled plasma mass spectrometry (LA-ICP-MS) for determining the isotopic composition of single micron-sized (μm) uranium oxide (UO_x) particles. To achieve the primary aim of the thesis, four objectives were identified. The objectives were: to improve the sensitivity of the LA-ICP-MS system; compare different data evaluation strategies for isotope ratio LA-ICP-MS; develop a new method for preparing UO_x particles for laser ablation analysis and to demonstrate a capability to perform UO_x particle analysis on an environmental sample.

Objective 1: Improve the sensitivity of the LA-ICP-MS system

The first objective, to improve the sensitivity of the LA-ICP-MS system, was addressed in Chapter 2. A prototype injector and ablation cell (DCI & Enterprise Cell), developed previously at Loughborough University, was used to couple a 193 nm excimer laser ablation system to a multi-collector (MC-) ICP-MS. The MC-ICP-MS was fitted with a high efficiency interface in order to maximise sensitivity. The detection efficiency (the number of ions detected as a percentage of atoms ablated) of the system, a measure of sensitivity, was determined by ablating craters into the glass surface of the standard reference material, SRM611. As the concentration of uranium in the reference material was known, the number of uranium atoms sampled by the mass spectrometer could be calculated from the volume of material ablated. Using the DCI & Enterprise Cell a detection efficiency of over 7% was achieved, double the 3.5% detection efficiency achieved with the comparison, Zircon Cell based, coupling mechanism. At 7% detection efficiency the LA-ICP-MS analysis of a pure uranium particle of 1 μm diameter containing 10^{10} atoms[1], with a hypothetical isotopic composition of 1% ^{235}U, 0.01% ^{234}U and 0.0001% ^{236}U, assuming it is totally consumed, would be expected to return 7,000,000 counts of ^{235}U, 70,000 counts of ^{234}U and 700 counts of ^{236}U. From counting statistics a 1-5% uncertainty on ^{234}U and ^{236}U could be expected, providing there were no other sources of uncertainty.

By LA-MC-ICP-MS the three isotope ratios, $^{234}U/^{238}U$, $^{235}U/^{238}U$ and $^{236}U/^{238}U$ were determined for 300 single shot ablations of SRM611, using both the DCI & Enterprise Cell and Zircon Cell coupling mechanisms. With the Zircon Cell the uncertainties on the average isotope ratios were similar to the limiting uncertainties determined via counting statistics (Table 1). However the experimental uncertainty (RSD) of the $^{235}U/^{238}U$ ratio measured using the DCI & Enterprise Cell, 2.93%, was significantly higher than the 0.99% expected from counting statistics. It was concluded the use of the DCI & Enterprise Cell had introduced an additional source of uncertainty into the isotope ratio

analysis. The additional uncertainty, referred to as 'blind time', was a consequence of the accelerated transmission of the ablation plume from the ablation cell to the plasma; improving the signal-to-noise ratio as well as the detection efficiency. The resulting short transient signals were a problem for the mixed detector array of Faraday cups and ion counters used in the multi-collector mass spectrometer. Equations of the pulse profiles collected on each detector were used to produce a model of the effect of blind time on isotope ratio analysis. The output of the model corresponded well to the additional uncertainty observed experimentally.

Table 1 - Mean uranium isotope ratios of SRM611 for the DCI & Enterprise Cell and Zircon Cell, taken from Tables 12 and 13, section 2.5.1.

Method	**n = 300**	**$^{234}U/^{238}U$**	**$^{235}U/^{238}U$**	**$^{236}U/^{238}U$**
DCI & Enterprise Cell	**R_{mean}**	1.05E-05	2.34E-03	4.56E-05
TSI	**(RSD)**	(14.1%)	(2.93%)	(7.92%)
	RD	10.4	-1.93	5.53
	Limiting (RSD)	(15.1%)	(0.99%)	(7.28%)
	n = 300			
Zircon Cell	**R_{mean}**	1.04E-05	2.35E-03	4.55E-05
TSI, 66ms	**(RSD)**	(17.0%)	(1.34%)	(7.66%)
	RD	9.64	-1.50	5.29
	Limiting (RSD)	(16.8%)	(1.11%)	(8.18%)

The additional uncertainty from blind time could not be eliminated, but approaches to filter out affected pulses were developed. Applying a filter for blind time, results comparable, but not superior, to the Zircon Cell were achieved with the DCI & Enterprise Cell. As the noise on the uranium isotopes was very low, less than 1 count every 30 seconds on an ion counter, the improvement in signal-to-noise ratio from the DCI & Enterprise Cell could not deliver an improvement in accuracy or precision on the isotope ratios.

In Chapter 4 the LA-MC-ICP-MS setup, with both coupling mechanisms, was applied to the analysis of sub-micron uranium oxide particles. The particle samples used were produced for two inter-laboratory comparisons, NUSIMEP-6 and NUSIMEP-7. The NUSIMEP-6 particles had a nearly natural uranium isotopic composition and an average particle size of 0.64±0.43 µm, measured by SEM-EDX. The $^{235}U/^{238}U$ and $^{234}U/^{238}U$ mean isotope ratios were successfully determined with a precision of 3% RSD and 8% RSD respectively. One NUSIMEP-7 sample planchet, average particle size 0.38±0.11 µm, contained particles of only a single isotopic composition, another planchet contained particles with

two distinct uranium isotopic compositions. The two distinct uranium compositions were successfully resolved by LA-MC-ICP-MS (Table 2).

Table 2 – Average uranium isotope ratios of 192 pulses on NU7-021, Zircon Cell, two compositions isolated from 303 pulses. Results taken from Table 30, section 4.4.3.1.

1st Composition	**n=73**	**$^{234}U/^{238}U$**	**$^{235}U/^{238}U$**	**$^{236}U/^{238}U$**
Zircon Cell	**R_{mean}**	7.43E-05	8.72E-03	1.12E-05
TSI	**(−RSD)**	(8.49%)	(3.27%)	(30.0%)
	(+RSD)	(9.27%)	(3.38%)	(42.1%)
	RD	-0.04	-3.97	33.10
	Limiting (RSD)	(7.92%)	(0.83%)	(22.4%)

2nd Composition	**n=119**	**$^{234}U/^{238}U$**	**$^{235}U/^{238}U$**	**$^{236}U/^{238}U$**
Zircon Cell	**R_{mean}**	3.35E-04	3.12E-02	1.10E-04
TSI	**(−RSD)**	(16.7%)	(6.76%)	(26.9%)
	(+RSD)	(20.1%)	(7.25%)	(36.9%)
	RD	-2.96	-8.99	6.02
	Limiting (RSD)	(15.4%)	(1.69%)	(28.3%)

The detection efficiency achieved with the LA-MC-ICP-MS, and its demonstrated application to the NUSIMEP inter-laboratory comparison samples, highlighted the potential utility of LA-ICP-MS in the analysis of sub-micron uranium oxide particles. LA-MC-ICP-MS has the potential to be a complementary technique to SIMS and TIMS for single UO_x particle analysis. However as a consequence of the additional uncertainty on the isotope ratios from blind time effects, the full potential of simultaneous detection by MC-ICP-MS for short transient signals was not realised. As the addition uncertainty from blind time was a consequence of a mixed detector array, the utility of LA-ICP-MS with a single collector mass spectrometer (Chapter 5) was investigated. The single collector ICP-MS was an order of magnitude less sensitive than the MC-ICP-MS. Due to the lower sensitivity of the single collector ICP-MS, only $^{235}U/^{238}U$ could be measured, with a higher uncertainty than the MC-ICP-MS. Despite the higher uncertainty, accurate mean $^{235}U/^{238}U$ ratios were detected for the NUSIMEP particles, and the two compositions on the dual composition planchet were resolved. As MC-ICP-MS instrumentation is less widely available than single collector sector field ICP-MS, the utility of single collector LA-ICP-MS instruments to determine the isotopic compositions of individual particles, may be of importance to the community.

Objective 2: Compare different data evaluation strategies for isotope ratio LA-ICP-MS

Three different data evaluation strategies were investigate for their utility to the LA-MC-ICP-MS analysis of single UO_x particles (Chapter 2). The method by which isotope ratios are typically determined is point-to-point (P2P), where the isotope ratio is determined for each data point within a signal window of interest. In a mixed detector array the outputs from the ion counters and Faraday cups are not simultaneous. Consequently the isotope ratio was not consistent over the duration of the analysis, affecting the precision of the measurement. Neither the P2P nor linear regression evaluation strategies could be used to evaluate the LA-MC-ICP-MS data. The only data evaluation strategy which could be employed was total signal integration (TSI), where the isotope ratio is calculated from the sum number of counts of each isotope. This was problematic for the stated aim of identifying an isotopic composition from a single particle, as the only uncertainty which can be associated with each measurement is derived from counting statistics. In Chapter 5, the application of LA-ICP-MS with a single collector sector field mass spectrometer P2P was used to evaluate the data, as well as TSI. Using P2P the uncertainties on the isotopic composition of each particle were evaluated. Compared to TSI, the P2P evaluation strategy was shown to bias the $^{235}U/^{238}U$ ratio determined (Zircon Cell). However if the isotope ratio was calculated using the geometric mean, rather than the arithmetic mean, the bias was eliminated.

The mathematical rationale behind using the geometric mean rather than the arithmetic mean for isotope ratio analysis, first described by Aitchison[3–6], was described in Chapter 3. The reasons given are sufficient to recommend the use of the geometric mean rather than the arithmetic mean to calculate isotope ratios, not just for single particle analysis, or ICP-MS, but for mass spectrometry generally.

Objective 3: Develop a new method for preparing UO_x particles for laser ablation analysis

Chapter 6 described the development of a new method of preparing a particulate sample for laser ablation analysis. The method developed was based on cytocentrifugation, typically used to disperse biological cells, to instead provide a rapid way of dispersing particles, suspended in liquid, evenly onto a glass slide. By using as the solvent, a mixture of nail polish and acetone, the dispersed particles could be held in a film layer, of sufficient strength to prevent the laser ablation shockwave dislodging particles from the surface. The final optimised method produced an even dispersion of particles, under a film layer thin enough (<500 nm) to allow the particles to be imaged by SEM-EDX. The particle-coated slides could be prepared rapidly, requiring only 60 seconds of cytocentifugation; many of the methods described in the scientific literature to prepare radionuclide particles for laser

ablation analysis are slow and labour intensive. The substrate is transparent, a recommendation of the ESARDA Workshop on Direct Analysis of Solid Samples Using Laser Ablation-Inductively Coupled Plasma-Mass Spectrometry[7] for further inter-laboratory comparisons (ILC) of radionuclide particles. As SEM-EDX was able to locate particles under the film layer, a map of the particles locations could be created. Such a map, loaded into a laser ablation system, can be used to target particles. The reasons stated suggest the method developed for preparing UO_x particles was almost ideal for LA-ICP-MS analysis.

Objective 4: Demonstrate a capability to perform UO_x particle analysis on an environmental sample

The outcomes of the first three objectives were then applied to the analysis of UO_x particles from an environmental sample (Chapter 7). The sample selected was a soil sample from Colonie, NY, USA, an area known to be contaminated with UO_x particles. A series of nylon filters was used to obtain the sub-5 µm size fraction of the soil sample, which was then mounted for analysis. SEM-EDX was used to estimate the size and distribution of UO_x particles on the sample mount prior to LA-MC-ICP-MS. The uranium isotopic compositions determined for the particles, matched closely the results of prior analysis at Colonie by Lloyd *et al* (2009).

By demonstrating the determination of the isotopic composition of single micron-sized (µm) uranium oxide (UO_x), from an environmental sample, by LA-ICP-MS, it was concluded significant progress had been made in meeting the stated aim of the research.

1. *Safeguards Techniques and Equipment: 2011 Edition International Nuclear Verification Series No.1 (Rev. 2)*, IAEA, Vienna, 2011.

2. J. Aitchison, *Math. Geol.*, 1984, **16**, 531–564.

3. J. Aitchison, *Math. Geol.*, 1992, **24**, 365–379.

4. J. Aitchison, *Math. Geol.*, 1999, **31**, 563–580.

5. J. Aitchison, C. Barcel, and J. A. Mart, *Math. Geol.*, 2000, **32**, 271–275.

6. Y. Aregbe, T. Prohaska, Z. Stefánka, E. Szeles, A. Hubert, and S. F. Boulyga, *ESARDA Bull.*, 2011, **46**, 136–145.

7. N. S. Lloyd, R. R. Parrish, M. Horstwood, and S. R. N. Chenery, *J. Anal. At. Spectrom.*, 2009, **24**, 752–758.

Future Work

The detection efficiency of over 7% measured by MC-ICP-MS has implications beyond the isotope ratio analysis of single UO_x particles. The measured value is significantly greater than the 4% quoted by the manufacturer of the MC-ICP-MS. The figure of 7% which has been achieved with the DCI & Enterprise Cell coupling mechanism heavily suggests the previous detection efficiency figure of 4% is limited by the sample introduction system and not by the interface region of the mass spectrometer. Indeed the 7% figure achieved with the DCI & Enterprise Cell may be limited by the setup which was used; due to spatial constraints the length of tubing used was greater than optimal. The potential therefore exists that MC-ICP-MS analysis with detection efficiency of 10% can be achieved with the current generation mass spectrometers, if improvements can be made in the sample introduction system.

One modification which could be made to the design of the DCI and Enterprise Cell would be to have wider bore tubing, 500 µm rather than 250 µm internal diameter. If the reduced performance of the DCI & Enterprise Cell at larger spot sizes (Chapters 2 and 5) is due to a limit in the density of material which the tube diameter can accept, then moving to a larger diameter tubing would mitigate some of the effect. Reducing the length of tubing required to couple the laser ablation system to the mass spectrometer, would likely increase both the detection efficiency and signal-to-noise ratio further, however doing so would only be of advantage if the limitations due to blind time effects can be mitigated.

Further work is required in the investigation of blind time, which introduces additional uncertainty into LA-MC-ICP-MS analysis of short transient signals. If the effect of blind time cannot be eliminated, either by a modification to the mass spectrometer or mathematically, then this will place a limitation on the cell designs which can accommodate transient signal analysis by MC-ICP-MS.

It was concluded the geometric mean should be used to calculate isotope ratios, instead of the arithmetic mean currently used in much of the literature. The change to using the geometric mean is made more difficult by the entrenchment of the arithmetic mean in current data evaluation software. Future work to develop new data evaluation software which incorporates the geometric mean would be beneficial for isotope ratio analysis.

Appendix I – Personal Development and Conference Attendance

Table 1 – Staff Development, Training, Meetings and Seminars

Comment	Date	Days	RDF Domain	Activity
Training on Thermo Element 2 ICP-MS from Claire Camp	11 Jan 2012	0.5	A	Lab Training
Training on Eppendorf Transferman Micromanipulator from Carol Arrowsmith	26 Jan 2012	0.5	A	Lab Training
Training on New Wave UP-213 Laser Ablation System from David Douglas	13 Feb 2012	0.5	A	Lab Training
Training on Thermo Neptune Plus MC-IP-MS from Dr Matt Horstwood	24 Feb 2012	1	A	Lab Training
Training on Nu AttoM ICP-MS from Dr Matt Horstwood	14 May 2012	1	A	Lab Training
Training on Thermo Delta V IRMS from Pareen Patel	18 Sep 2012	0.5	A	Lab Training
Training on qNANO from Dr Matt Platt	22 Nov 2012	1	A	Lab Training
Training on SEM-EDX from Dr Jeremy Rushton	11 Feb 2013	1	A	Lab Training
Meeting with Dr Noah McLean (NIGL) to discuss statistics	18 Jun 2012	0.5	C	Meeting
Meeting with Professor Barry Sharp, Dr Helen Reid and Dr Matt Horstwood	02 Feb 2012	0.5	C	Meeting
Meeting with AWE to discuss collaboration, presentation of work made to Dr Sam Walton, Dr David Mitchell and Dr Terry Piper	06 Aug 2012	0.5	C	Meeting
Meeting and training on Heavy Liquid Separation from Prof Randall R. Parrish	02 Jul 2013	1	A/C	Meeting/Lab Training
Appearance on University Challenge	14 Mar 2013	2	B	Personal Development
Postgraduate Research Students Induction	17 Jan 2012	0.5	A/D	Seminar
QMX, Seminar new advances in sample preparation and sample introduction for ICP-MS	19 Apr 2012	0.5	A/D	Seminar
QMX, New Advances in laser ablation	20 Apr 2012	0.5	A/D	Seminar

BGS PhD Student Induction	12 Jun 2012	0.5	A/D	Seminar
R for Statistics, 3 day course	12 Mar 2013	3	A/C	Software Training
MATLAB software training course	05 Jun 2013	0.5	A/C	Software Training
Designing and Producing Conference Posters	25 Jan 2012	0.5	D	Staff Development
Chi-squared Tests (analysing two-way tables)	02 May 2012	0.3	A	Staff Development
Introduction to Analysis of Variance (ANOVA)	23 May 2012	0.3	A	Staff Development
Introduction to the Design of Multifactor Experiments	30 May 2012	0.3	A	Staff Development
Statistics User Group, Introduction to statistics for researchers	24 Jul 2012	0.3	A	Staff Development
Teaching Skills for those Supervising Practical Activities - 1	13 Mar 2012	0.5	D	Teaching
Teaching Skills for those Supervising Practical Activities – 2	20 Mar 2012	0.5	D	Teaching
Teaching Skills for those Supervising Practical Activities - 3	27 Mar 2012	0.5	D	Teaching

Table 2 – Conference Attendance

Comment	Date	Days	RDF Domain	Activity
BUFI Science Festival, submission of a poster	22 May 2012	1	D	Conference
BUFI Science Festival, submission of a poster	09 Apr 2013	1	D	Conference
Poster presentation at 2014 Winter Conference on Plasma Spectroscopy, Amelia Island, FL	06 Jan 2014	5	C/D	Conference
Presentation of a poster at Emerging Analytical Professionals 2014, Penrith, Cumbia	04 Apr 2014	3	C/D	Conference
Attendance at Analytical Research Forum 2014, RSC, London	07 Jul 2014	1	C	Conference
Oral presentation at European Workshop on Laser Ablation, Royal Holloway, London	08 Jul 2014	4	C/D	Conference

Table 3 – Safety Courses

Comment	Date	Days	RDF Domain	Activity
Introduction, good laboratory practice	13 Nov 2013		A	Safety Course
Flammable materials	22 Jan 2014		A	Safety Course
Liquefied gases, cryogenics	26 Feb 2014		A	Safety Course
Corrosive materials	12 Mar 2014		A	Safety Course
Pressurised gases	07 May 2014		A	Safety Course
Explosive and energetic materials	12 Nov 2014		A	Safety Course
Waste disposal	03 Dec 2014	1	A	Safety Course

Total number of days = 35

Appendix II – Data Tables

The data tables are for the results summarised in Table 34, section 4.4.3.2 NUSIMEP-7 (dual composition) with the DCI & Enterprise Cell.

Table 1 – Data Table of 10 pulses on NU7-021, DCI & Enterprise Cell, 1st composition, selected from the centre of the cluster. All isotope abundances are in counts. RSD on each pulse derived from counting statistics.

Pulse	^{234}U	^{235}U	^{236}U	^{238}U	$^{234}U/^{238}U$	RSD	$^{235}U/^{238}U$	RSD	$^{236}U/^{238}U$	RSD
1	394	4.73E+04	61	5.50E+06	7.54E-05	5.04	8.89E-03	0.46	1.20E-05	12.8
2	33	4.78E+03	8	5.56E+05	6.34E-05	17.3	8.89E-03	1.45	1.54E-05	35.6
3	148	1.97E+04	18	2.28E+06	6.84E-05	8.21	8.91E-03	0.71	8.32E-06	23.9
4	124	1.41E+04	18	1.64E+06	7.99E-05	8.97	8.92E-03	0.84	1.17E-05	23.8
5	107	1.27E+04	23	1.47E+06	7.70E-05	9.65	8.92E-03	0.89	1.67E-05	21.0
6	447	5.15E+04	40	5.97E+06	7.88E-05	4.73	8.92E-03	0.44	7.22E-06	15.8
7	46	6.35E+03	8	7.35E+05	6.65E-05	14.7	8.93E-03	1.26	1.16E-05	35.7
8	118	1.67E+04	14	1.93E+06	6.47E-05	9.19	8.94E-03	0.77	7.65E-06	27.1
9	91	9.84E+03	18	1.13E+06	8.49E-05	10.5	8.98E-03	1.01	1.70E-05	23.7
10	170	2.21E+04	29	2.54E+06	7.07E-05	7.66	9.00E-03	0.68	1.26E-05	18.4
	^{234}U	^{235}U	^{236}U	^{238}U	$^{234}U/^{238}U$		$^{235}U/^{238}U$		$^{236}U/^{238}U$	
mean	168	20493	24	2.38E+06	7.30E-05		8.93E-03		1.20E-05	
RSD	83.2	79.0	69.3	79.2	9.96		0.41		29.69	

Table 2 – Data Table of 10 pulses on NU7-021, DCI & Enterprise Cell, 2nd composition, selected from the centre of the cluster. All isotope abundances are in counts. RSD on each pulse derived from counting statistics.

Pulse	^{234}U	^{235}U	^{236}U	^{238}U	$^{234}U/^{238}U$	RSD	$^{235}U/^{238}U$	RSD	$^{236}U/^{238}U$	RSD
1	49	5.96E+03	19	1.85E+05	2.82E-04	14.2	3.34E-02	1.32	1.11E-04	23.0
2	255	2.27E+04	66	7.04E+05	3.82E-04	6.26	3.34E-02	0.67	1.01E-04	12.3
3	291	2.62E+04	60	8.10E+05	3.78E-04	5.86	3.34E-02	0.63	7.98E-05	12.9
4	121	1.15E+04	38	3.54E+05	3.61E-04	9.08	3.35E-02	0.95	1.16E-04	16.2
5	174	1.84E+04	61	5.66E+05	3.24E-04	7.57	3.36E-02	0.75	1.16E-04	12.8
6	26	2.68E+03	12	8.23E+04	3.26E-04	19.8	3.37E-02	1.96	1.57E-04	28.9
7	242	2.57E+04	79	7.89E+05	3.23E-04	6.42	3.37E-02	0.63	1.08E-04	11.3
8	332	3.60E+04	108	1.10E+06	3.17E-04	5.49	3.38E-02	0.54	1.06E-04	9.64
9	49	3.77E+03	14	1.15E+05	4.52E-04	14.2	3.38E-02	1.66	1.31E-04	26.8
10	101	9.81E+03	33	2.99E+05	3.57E-04	9.93	3.39E-02	1.02	1.19E-04	17.4
	^{234}U	^{235}U	^{236}U	^{238}U	$^{234}U/^{238}U$		$^{235}U/^{238}U$		$^{236}U/^{238}U$	
mean	164	16267	49	5.01E+05	3.50E-04		3.36E-02		1.15E-04	
RSD	67.4	69.0	63.8	68.9	13.45		0.58		17.60	

Appendix III – Applicability of Software Packages

This appendix contains further details and examples on the use of different software packages used throughout the thesis.

III.1 R

R[1] is a software environment for carrying out statistical computing and graphics. Within the software environment scripts written in the R programming language can carry out a wide variety of data analysis. Furthermore the core functions of the R environment can be extended by the addition of downloadable packages.

III.1.1 ggplot2

The downloadable package for R, ggplot2[2], was used extensively throughout this thesis to produce various figures, primarily scatterplots. An example script used to produce a scatterplot with ggplot2 is given below.

```
library("ggplot2")
Plot.1<-ggplot(myRatio, aes(x=Time, y=U235_U238))
Plot.1    + geom_point(size=3, colour="#108070", fill="black")
          + theme(axis.text = element_text(colour = "black",size=20),
                                  axis.title.x = element_text(colour = "black",size=30),
                                  axis.title.y = element_text(colour = "black",size=30),
                                  panel.background = element_rect(fill="white"),
                                  panel.grid.minor = element_blank(),
                                  panel.grid.major = element_line(colour = "grey",linetype="dashed"),
                                  panel.border = element_rect(colour = "black", fill=NA,size=1.2),
                                  plot.background = element_rect())
          + xlab("Time (s)")
          + ylab(expression(paste({}^"235","U/",{}^"238","U")))
```

III.1.2 Flexmix

In both Chapter 2 and Chapter 4, the R downloadable package Flexmix was used to group pulses within datasets into clusters. This approach was used to identify mixed compositions (pulses of different composition would be assigned to different clusters) and to filter out erroneous pulses. Flexmix uses linear regression, two variables (in the example below, ^{235}U and ^{238}U) are plotted and clusters assigned based on the best fit of straight lines through the scatterplot. An example script is

provided below, and is based on the electronic supplementary information provided with Kappel *et al* (2013)[3].

```
library("flexmix")
attach (NUSIMEP6)
modsimul <- stepFlexmix(U235~U238,
                data = NUSIMEP6,
                k=5,
                control = list(classify = "hard",minprior = 0.01),
                nrep = 10,
                model=FLXMRglmfix(varFix = TRUE))
p <- parameters(modsimul)
p
plot(U235~U238,
          data = NUSIMEP6,
          pch = modsimul@cluster)
legend("topleft", pch = c(2,1,3),
          legend = c("Cluster 1","Cluster 2","Cluster 3"))
Cluster<-clusters(modsimul)
NUSIMEP6_Clusters<-cbind(NUSIMEP6,Cluster)
write.csv(NUSIMEP6_Clusters, "NUSIMEP6_Clusters.csv")
detach (NUSIMEP6)
```

III.1.3 Monte Carlo

In Chapter 3, Figure 40 contains two overlapping plots of example normal and log-normal distributions. The example normal and log-normal distributions were produced in R using a Monte Carlo simulation.

```
Normal_distribution <- as.data.frame(matrix(rnorm(1*1000, mean = 2.5, sd = 0.3),
          ncol = 1000))
rownames(Normal_distribution) <- "sample"
colnames(Normal_distribution) <- paste("obs", 1:1000, sep = "")
```

The script above produces a normal distributed dataset of 1000 values around a mean value of 2.5, with a standard deviation of 0.3. The script to produce a similar log-normal distribution is given below.

```
Log_normal_distribution <- as.data.frame(matrix(rlnorm(1*100, meanlog = 2.5, sdlog = 0.3),
        ncol = 100))
rownames(Log_normal_distribution) <- "sample"
colnames(Log_normal_distribution) <- paste("obs", 1:100, sep = "")
```

III.2 IgorPro

Igor Pro (Wavemetrics, Oregon, USA) is similar to R, in that it is a software environment, with its own programming language, used for statistical computing and the production of graphics.

III.2.1 Curve Fitting

In Chapter 2 (section 2.5.3), IgorPro was used to fit curves to pulse profiles. The equations of the fitted curves were then used to produce a model of the effect of "blind time" on isotope ratios. Unlike the R software environment, IgorPro is supplied with a menu interface from which many functions can be selected without the use of a script.

Using the menu interface in IgorPro, a log-normal curve was fitted to the pulse profiles produced experimentally using the LA-MC-ICP-MS. The log-normal equation was of the form:

$$y = y_0 + A\exp\left\{-\left[\frac{\ln(x/x_o)}{width}\right]^2\right\}$$

The function returned for each fitted curve the coefficient values x_0, y_0, A, and $width$. The resulting equations were then used to produce the model pulse profiles reported in section 2.5.3.

III.2.2 Iolite v2.5

Iolite[4] is an add-on for the processing of LA-ICP-MS data, which has been produced in the Igor Pro software environment. A more detailed explanation is given in section 3.4.1. Iolite analyses LA-ICP-MS data in such a way that only the point-to-point data evaluation strategy can be used. The point-to-point results reported in Chapter 5 were produced in Iolite v2.5. In order to interrogate the data in Iolite a Data Reduction Scheme (DRS), a script, is required. None of the DRS supplied with Iolite v2.5 were appropriate for the isotope ratio analysis of uranium oxide particles. Therefore a new DRS was written, the script for which is supplied below.

```
    variable CurrentChannelNo=0,NoOfChannels=itemsinlist(ListOfInputChannels) //Create local variables to hold the current input channel number and the total number of input channels

    String NameOfCurrentChannel,CurrentElement //Create a local string to contain the name of the current channel, and its corresponding element

    Do //Start to loop through the available channels
```

```
		NameOfCurrentChannel=StringFromList(CurrentChannelNo,ListOfInputChannels) //Get the name of the nth channel from the input list

		CurrentElement=GetElementFromIsotope(NameOfCurrentChannel) //get name of the element

		if(cmpstr(CurrentElement,"Null")!=0 && cmpstr(NameOfCurrentChannel, IndexChannel)!=0) //if this element is not "null" (i.e. is an element), and it is not the index isotope, then..

			wave ThisChannelBLsub = $InterpOntoIndexTimeAndBLSub(NameOfCurrentChannel)		//use this external function to interpolate the input onto index_time then subtract it's baseline

			ListOfIntermediateChannels+=NameOfCurrentChannel+"_" + DefaultIntensityUnits +";" //Add the name of this new output channel to the list of outputs

		endif //Have now created a (baseline-subtracted channel) output wave for the current input channel, unless it was TotalBeam or index

		CurrentChannelNo+=1 //So move the counter on to the next channel..

	While(CurrentChannelNo<NoOfChannels) //..and continue to loop until the last channel has been processed.

	ListOfIntermediateChannels+=IndexChannel+"_"+DefaultIntensityUnits+";" //Add the name of the index channel to the list of intermediates

	//Replace "YourWaveName", and "LoopWaveName" will be in the form "[NameOfInputWave]_[DefaultIntensityUnits]"

	Wave U238 = $ioliteDFpath("CurrentDRS","U238_CPS")

	Wave U235 = $ioliteDFpath("CurrentDRS","U235_CPS")		//etc

	//Repeat for each input wave

	Wave LnU235=$MakeioliteWave("CurrentDRS","LnU235",n=NoOfPoints)

	LnU235=Ln(U235)

	Wave LnU238=$MakeioliteWave("CurrentDRS","LnU238",n=NoOfPoints)

	LnU238=Ln(U238)

	ListOfIntermediateChannels+="LnU235;LnU238;"

	Wave MaskBeam = $DRS_CreateMaskWave(IndexOut,MaskThreshold,MaskEdgeDiscardSeconds,"MaskBeam","StaticAbsolute")

	Wave U238_U235=$MakeioliteWave("CurrentDRS","U238_U235",n=NoOfPoints)

	U238_U235=LnU238-LnU235

	Wave U238_U235x=$MakeioliteWave("CurrentDRS","U238_U235x",n=NoOfPoints)

	U238_U235x=U235/U238
```

```
	//U238_U235=U238/U235*MaskBeam

	ListOfIntermediateChannels+="U238_U235;U238_U235x;"

	//DRSAbortIfNotWave(ioliteDFpath("Splines",StringFromList(0,ListOfIntermediateChannels)+"_"+Refe
renceStandard))  //Abort if there is not yet a spline of the expected standard type, for the first intermediate
channel

	//variable StdValue_238_235 = GetValueFromStandard("ln238U_235U",ReferenceStandard)

	//"NameOfParameter" could be Pb208Pb206 for instance, as long as it is in the file

	//Wave modU238_U235=$MakeioliteWave("CurrentDRS","modU238_U235",n=NoOfPoints)

	//modU238_U235=U238_U235-StdValue_238_235

	//ListOfOutputChannels+="modU238_U235;"

	ListOfOutputChannels+="U238_U235;"

	//Wave StdSpline_U238_U235=$InterpSplineOntoIndexTime("modU238_U235",ReferenceStandard)

	//Wave Ln_U238_U235=$MakeioliteWave("CurrentDRS","Ln_U238_U235",n=NoOfPoints)

	//Ln_U238_U235=U238_U235-StdSpline_U238_U235

	//ListOfOutputChannels+="Ln_U238_U235;”

	//Propagate_Errors("All", "Ln_U238_U235", "modU238_U235", ReferenceStandard)

	//Wave Check_U238_U235=$MakeioliteWave("CurrentDRS","Check_U238_U235",n=NoOfPoints)

	//Check_U238_U235=EXP(Ln_U238_U235)

	//ListOfOutputChannels+="Check_U238_U235;"

	//Propagate_Errors("All", "Ln_U238_U235", "Ln_U238_U235", ReferenceStandard)

End
```

III.3 MATLAB®

MATLAB® (MathWorks®, Natick, MA, USA) is another software environment for statistical computing and graphics, again with its own programming language. MATLAB was used to calculate the limiting uncertainty on isotope ratios throughout the thesis, using counting statistics. A Monti Carlo simulation was used to simulate a random Poisson distribution around the number of counts measured for each isotope. For each of the random Poisson distributions a standard deviation was determined. The standard deviation of the Poisson distribution was defined as the limiting uncertainty. An example script is given below.

```
nPulses = size(data,1);
nMC = 1e5;
```

```
slrMC = zeros(nPulses,3);
for iPulse = 1:nPulses
   i234 = data(iPulse,1);
   i234MC = random('Poisson', i234, [nMC 1]);
   i235 = data(iPulse,2);
   i235MC = random('Poisson', i235, [nMC 1]);
   i236 = data(iPulse,3);
   i236MC = random('Poisson', i236, [nMC 1]);
   i238 = data(iPulse,4);
   i238MC = random('Poisson', i238, [nMC 1]);
   lr48MC = log(i234MC./i238MC);
   slrMC(iPulse,1) = std(lr48MC);
   lr58MC = log(i235MC./i238MC);
   slrMC(iPulse,2) = std(lr58MC);
   lr68MC = log(i236MC./i238MC);
   slrMC(iPulse,3) = std(lr68MC);
   disp(num2str(iPulse))
end
```

III.4 Solidworks

In section 2.3.1 is reported the outcome of a model produced in Solidworks® 2011 (Dessault Systèmes SOLIDWORKS Corp, Waltham, MA, USA) 3D computer aided design (CAD) software using the Flow Simulation package. The full report of the model, detailing the input and output conditions is appended.

FULL REPORT

Table 1 - System Info

Product	**Flow Simulation 2011 5.0. Build: 1747**
Computer name	POWERPC
User name	Analytical_2
Processors	Intel(R) Xeon(R) CPU E5640 @ 2.67GHz(2 processors)
Memory	16367 MB / 8388607 MB
Operating system	Windows 7 Service Pack 1 (Build 7601)
CAD version	SolidWorks 2011 SP5.0
CPU speed	2661 MHz

Table 2 - General Info

Model	DCI_Sheath_Flow\Flow_Model.SLDASM
Project name	Flow Model
Project path	DCI_Sheath_Flow\1
Units system	SI (m-kg-s)
Analysis type	Internal
Exclude cavities without flow conditions	On
Coordinate system	Global coordinate system
Reference axis	X

INPUT DATA

Initial Mesh Settings

Automatic initial mesh: On

Result resolution level: 3

Advanced narrow channel refinement: Off

Refinement in solid region: Off

Geometry Resolution

Evaluation of minimum gap size: Manual

Minimum gap size: 1.000e-04 m

Evaluation of minimum wall thickness: Automatic

Computational Domain

Table 3 - Size

X min	-0.132 m
X max	0.157 m
Y min	-0.016 m
Y max	-0.006 m
Z min	-0.092 m
Z max	-0.012 m

Table 4 - Boundary Conditions

2D plane flow	**None**
At X min	Default
At X max	Default
At Y min	Default
At Y max	Default
At Z min	Default
At Z max	Default

Physical Features

Heat conduction in solids: Off

Time dependent: Off

Gravitational effects: Off

Flow type: Laminar and turbulent

High Mach number flow: Off

Humidity: Off

Default roughness: 0 micrometer

Default wall conditions: Adiabatic wall

Table 5 - Initial Conditions

Thermodynamic parameters	**Static Pressure: 101325.00 Pa** **Temperature: 293.20 K**
Velocity parameters	Velocity vector Velocity in X direction: 0 m/s Velocity in Y direction: 0 m/s Velocity in Z direction: 0 m/s
Turbulence parameters	Turbulence intensity and length Intensity: 2.00 % Length: 4.054e-04 m

Material Settings

Fluids

Argon

Boundary Conditions

Table 6 - Static Pressure 1

Type	Static Pressure
Faces	Face <1LID4-1@Imported1>
Coordinate system	Face Coordinate System
Reference axis	X
Thermodynamic parameters	Static pressure: 101325.00 Pa
	Temperature: 293.20 K
Turbulence parameters	Turbulence intensity and length
	Intensity: 2.00 %
	Length: 4.054e-04 m
Boundary layer parameters	Boundary layer type: Turbulent

Table 7 - Inlet Volume Flow 1

Type	Inlet Volume Flow
Faces	Face <1LID6-1@Imported1>
Coordinate system	Face Coordinate System
Reference axis	X
Flow parameters	Flow vectors direction: Normal to face
	Volume flow rate normal to face: 1.4500 l/min
	Fully developed flow: No
Thermodynamic parameters	Inlet profile: 0
	Approximate pressure: 101325.00 Pa
	Temperature: 293.20 K
Turbulence parameters	Turbulence intensity and length
	Intensity: 2.00 %
	Length: 4.054e-04 m
Boundary layer parameters	Boundary layer type: Turbulent

Calculation Control Options

Table 8 - Finish Conditions

Finish conditions	If one is satisfied
Maximum travels	4.000
Goals convergence	Analysis interval: 0.500

Solver Refinement

Refinement: Disabled

Results Saving

Save before refinement	**On**

Advanced Control Options

Flow Freezing

Flow freezing strategy	**Disabled**

RESULTS

General Info

Iterations: 241

CPU time: 3151 s

Table 9 - Log

Mesh generation started		**14:39:07 , Jan 13**
Mesh generation normally finished		14:40:26 , Jan 13
Preparing data for calculation		14:40:27 , Jan 13
Calculation started	0	14:40:50 , Jan 13
Calculation has converged since the following criteria are satisfied:	240	15:34:02 , Jan 13
Goals are converged	240	
Calculation finished	241	15:34:32 , Jan 13

Calculation Mesh

Table 10 - Basic Mesh Dimensions

Number of cells in X	**160**
Number of cells in Y	6
Number of cells in Z	44

Maximum refinement level: 6

Table 11 - Number of Cells

Total cells	**376504**
Fluid cells	84341
Solid cells	144863
Partial cells	147300
Irregular cells	0
Trimmed cells	10

Table 12 - Min/Max Table

Name	**Minimum**	**Maximum**
Pressure [Pa]	101314.57	101934.99
Temperature [K]	293.09	293.20
Velocity [m/s]	0	11.009
X - Component of Velocity [m/s]	-11.009	2.613
Y - Component of Velocity [m/s]	-5.449	5.203
Z - Component of Velocity [m/s]	-5.430	5.775
Fluid Temperature [K]	293.09	293.20
Mach Number [ ]	0	0.03
Shear Stress [Pa]	0	54.08
Heat Transfer Coefficient [W/m^2/K]	0	0
Surface Heat Flux [W/m^2]	0	0
Density [kg/m^3]	1.66	1.67

1. R Core Team, R: A language and enviroment for statistical computing (Version 3.12 “Pumpkin Helmet”), R Foundation for Statsitical Computing, Vienna, Austria, 2008.

2. H. Wickham, *ggplot2: elegant graphics for data analysis*, Springer, New York, 2009.

3. S. Kappel, S. F. Boulyga, L. Dorta, D. Günther, B. Hattendorf, D. Koffler, G. Laaha, F. Leisch, and T. Prohaska, *Anal. Bioanal. Chem.*, 2013, **405**, 2943–2955.

4. C. Paton, J. Hellstrom, B. Paul, J. Woodhead, and J. Hergt, *J. Anal. At. Spectrom.*, 2011, **26**, 2508–2518.

Appendix IV – List of Reference Materials

Appendix IV contains a list of all certified reference materials, standards and inter-laboratory comparison samples used.

CRM 112A

CRM 112A[1] is a uranium metal assay and isotopic standard supplied by the New Brunswick Laboratory of the U.S. Department of Energy. It is distributed as a 1 g piece of uranium metal. In this study the CRM 112A used was dissolved in high purity 2% (w/w) nitric acid, at a concentration of between 0.5 – 20 ppb of uranium, depending on conditions. CRM 112A was used as a liquid certified reference material, aspirated via a desolvator into the ICP-MS. As CRM 112A has a certified natural uranium composition, it was used to determine correction factors for abundance sensitivity.

Table 1 – Certified uranium isotopic composition of CRM 112A

	$^{234}U/^{238}U$	$^{235}U/^{238}U$	$^{236}U/^{238}U$
CRM 112A[1]	5.2841e-05	7.2543e-03	-

CRM U010

CRM U010[2] is a uranium isotopic standard supplied by the New Brunswick Laboratory of the U.S. Department of Energy. It is distributed as 5 mg of U_3O_8. In this study the CRM U010 used was dissolved in high purity 2% (w/w) nitric acid, at a concentration of between 0.5 –10 ppb uranium, depending on conditions. CRM U010 was used as a liquid certified reference material, aspirated via a desolvator into the ICP-MS. As CRM U010 has a non-natural certified natural uranium composition, it was used to determine correction factors for gain and mass bias.

Table 2 – Certified uranium isotopic composition of CRM U010

	$^{234}U/^{238}U$	$^{235}U/^{238}U$	$^{236}U/^{238}U$
CRM U010[2]	5.4655e-05	1.0140e-02	6.8798e-05

SRM 611

Standard Reference Material® (SRM) 611[3] is a solid glass matrix (nominal composition of 72 % SiO_2, 14 % Na_2O, 12 % CaO, and 2 % Al_2O_3) which has been doped with 61 trace elements. SRM611 is supplied by the National Institute of Standards and Technology, Gaithersburg, Maryland, USA as a wafer, 1mm thick and between 12 mm and 14 mm in diameter. Uranium is one of the doped 61

trace elements, with a certified concentration of 461.5±1.5 ppm. The uranium isotopic composition of SRM611 is not certified; therefore the uranium isotopic composition was taken from Zimmer *et al* (2014)[4], who determined the uranium composition by MC-ICP-MS, MC-TIMS and SIMS.

Table 3 – Uranium isotopic composition of SRM611, from Zimmer *et al* (2014)

	$^{234}U/^{238}U$	$^{235}U/^{238}U$	$^{236}U/^{238}U$
SRM 611[4]	9.45e-06	2.38555e-03	4.314e-05

NUSIMEP-6

NUSIMEP-6[5] was an inter-laboratory comparison run by the Institute for Reference Materials and Measurements (IRMM). As part of the inter-laboratory comparison a sample, referred to here by the name of the inter-laboratory comparison, was distributed to the participants. The sample consisted of sub-micron uranium oxide particles which had been condensed onto the surface of a carbon planchet 25 mm in diameter. The particles were reported as having the same uranium isotopic composition as the uranium hexafluoride certified reference material, from which they had been manufactured. The certified values were given in the inter-laboratory comparison report.

Table 4 – Uranium isotopic composition of the NUSIMEP-6 particles

Planchet	$^{234}U/^{238}U$	$^{235}U/^{238}U$	$^{236}U/^{238}U$
NUSIMEP-6[5]	4.9817e-05	7.0439e-03	5.2048e-07

NUSIMEP-7 (single composition)

NUSIMEP-7[6] was a subsequent inter-laboratory comparison run by the Institute for Reference Materials and Measurements (IRMM). As part of the inter-laboratory comparison two samples, were distributed to the participants. Both samples consisted of sub-micron uranium oxide particles which had been condensed onto the surface of a carbon planchet 25 mm in diameter. The first sample had particles of only a single uranium isotopic composition and was therefore referred to as NUSIMEP-7 (single composition). Again the particles were reported as having the same uranium isotopic composition as the uranium hexafluoride certified reference material, from which they had been manufactured.

Table 5 – Uranium isotopic composition of the NUSIMEP-7 (single composition) particles

Planchet	$^{234}U/^{238}U$	$^{235}U/^{238}U$	$^{236}U/^{238}U$
NUSIMEP-7(single composition)[6]	7.4365e-05	9.0726e-03	8.0205e-06

NUSIMEP-7 (dual composition)

The second sample distributed as part of the NUSIMEP-7 inter-laboratory comparison had sub-micron uranium oxide particles of two different uranium isotopic compositions. Therefore the planchet was referred to as NUSIMEP-7 (dual composition). Again the particles were reported as having the same uranium isotopic composition as the uranium hexafluoride certified reference material, from which they had been manufactured.

Table 6 – Uranium isotopic composition of the NUSIMEP-7 (dual composition) particles

Planchet		$^{234}U/^{238}U$	$^{235}U/^{238}U$	$^{236}U/^{238}U$
NUSIMEP-7(dual composition)[6]	**1st**	7.4365e-05	9.0726e-03	8.0205e-06
	2nd	3.4514e-04	3.4148e-02	1.0327e-04

Two NUSIMEP-7 (dual composition) planchets were used in this study. NU7-043 was the original NUSIMEP-7 (dual composition) planchet supplied to NIGL as part of the inter-laboratory comparison. Another planchet, NU7-021, was obtained from another participant in the inter-laboratory comparison during the study.

1. J. Neuhoff, *Certificate of Analysis CRM 112-A Uranium (normal) Metal Assay and Isotopic Standard*, New Brunswick Laboratory, Argonne IL, 2010.

2. J. Neuhoff, *Certificate of Analysis CRM U010 Uranium Isotopic Standard (5 mg Uranium as U_3O_8)*, New Brunswick Laboratory, Argonne IL, 2008.

3. S. A. Wise and R. L. Watters, *National Institute of Standards & Technology Certificate of Analysis Standard Reference Material® 611 Trace Elements in Glass*,NIST, Gaithersburg MD, 2012.

4. M. Zimmer, W. Kinman, A. Kara, and R. Steiner, *Minerals*, 2014, **4**, 541–552.

5. Y. Aregbe, J. Truyens, R. Kips, S. Richter, E. Stefaniak, H. Kühn, and M. Kraiem, *NUSIMEP-6 : Uranium isotope amount ratios in uranium particles*, IRMM Report EUR 23702EN, IRMM, Geel, 2008.

6. J. Truyerns, E. Stefaniak, S. Mialle, and Y. Aregbe, *NUSIMEP-7 : Uranium isotope amount ratios in uranium particles*, IRMM Report EUR 25179EN, IRMM, Geel, 2011.